NASA/CR—2007-215006

A Microfabricated Segmented-Involute-Foil Regenerator for Enhancing Reliability and Performance of Stirling Engines

Phase II Final Report for the Radioisotope Power Conversion Technology NRA Contract NAS3-03124

Mounir Ibrahim and Daniel Danila
Cleveland State University, Cleveland, Ohio

Terrence Simon, Susan Mantell, and Liyong Sun
University of Minnesota, Minneapolis, Minnesota

David Gedeon
Gedeon Associates, Athens, Ohio

Songgang Qiu
Infinia Corporation, Kennewick, Washington

Gary Wood
Sunpower Incorporated, Athens, Ohio

Kevin Kelly and Jeffrey McLean
International Mezzo Technologies, Baton Rouge, Louisiana

December 2007

NASA STI Program . . . in Profile

Since its founding, NASA has been dedicated to the advancement of aeronautics and space science. The NASA Scientific and Technical Information (STI) program plays a key part in helping NASA maintain this important role.

The NASA STI Program operates under the auspices of the Agency Chief Information Officer. It collects, organizes, provides for archiving, and disseminates NASA's STI. The NASA STI program provides access to the NASA Aeronautics and Space Database and its public interface, the NASA Technical Reports Server, thus providing one of the largest collections of aeronautical and space science STI in the world. Results are published in both non-NASA channels and by NASA in the NASA STI Report Series, which includes the following report types:

- TECHNICAL PUBLICATION. Reports of completed research or a major significant phase of research that present the results of NASA programs and include extensive data or theoretical analysis. Includes compilations of significant scientific and technical data and information deemed to be of continuing reference value. NASA counterpart of peer-reviewed formal professional papers but has less stringent limitations on manuscript length and extent of graphic presentations.

- TECHNICAL MEMORANDUM. Scientific and technical findings that are preliminary or of specialized interest, e.g., quick release reports, working papers, and bibliographies that contain minimal annotation. Does not contain extensive analysis.

- CONTRACTOR REPORT. Scientific and technical findings by NASA-sponsored contractors and grantees.

- CONFERENCE PUBLICATION. Collected papers from scientific and technical conferences, symposia, seminars, or other meetings sponsored or cosponsored by NASA.

- SPECIAL PUBLICATION. Scientific, technical, or historical information from NASA programs, projects, and missions, often concerned with subjects having substantial public interest.

- TECHNICAL TRANSLATION. English-language translations of foreign scientific and technical material pertinent to NASA's mission.

Specialized services also include creating custom thesauri, building customized databases, organizing and publishing research results.

For more information about the NASA STI program, see the following:

- Access the NASA STI program home page at *http://www.sti.nasa.gov*

- E-mail your question via the Internet to *help@sti.nasa.gov*

- Fax your question to the NASA STI Help Desk at 301–621–0134

- Telephone the NASA STI Help Desk at 301–621–0390

- Write to:
  NASA Center for AeroSpace Information (CASI)
  7115 Standard Drive
  Hanover, MD 21076–1320

NASA/CR—2007-215006

A Microfabricated Segmented-Involute-Foil Regenerator for Enhancing Reliability and Performance of Stirling Engines

Phase II Final Report for the Radioisotope Power Conversion Technology NRA Contract NAS3-03124

Mounir Ibrahim and Daniel Danila
Cleveland State University, Cleveland, Ohio

Terrence Simon, Susan Mantell, and Liyong Sun
University of Minnesota, Minneapolis, Minnesota

David Gedeon
Gedeon Associates, Athens, Ohio

Songgang Qiu
Infinia Corporation, Kennewick, Washington

Gary Wood
Sunpower Incorporated, Athens, Ohio

Kevin Kelly and Jeffrey McLean
International Mezzo Technologies, Baton Rouge, Louisiana

Prepared under Contract NAS3–03124

National Aeronautics and
Space Administration

Glenn Research Center
Cleveland, Ohio 44135

December 2007

Acknowledgments

We are grateful for sponsorship of this effort by the NASA Headquarters Science Mission Directorate (SMD) and the Radioisotope Power System (RPS) Program and for the support of the NASA Glenn Research Center (GRC) under NASA Contract NAS3-03124. Dr. Roy Tew of NASA GRC is the Contracting Officer's Technical Respresentative. We wish to acknowledge the valuable guidance we received from our team of advisors: James Cairelli (retired, NASA GRC), Randy Bowman of NASA GRC and David Berchowitz at Global Cooling, Inc.

Level of Review: This material has been technically reviewed by NASA technical management.

Available from

NASA Center for Aerospace Information
7115 Standard Drive
Hanover, MD 21076–1320

National Technical Information Service
5285 Port Royal Road
Springfield, VA 22161

Available electronically at http://gltrs.grc.nasa.gov

Contents

1.0 Introduction 2
2.0 Nomenclature 4
2.1 Abbreviations 5
3.0 Program Overview 6
3.1 Objectives 6
3.2 Approach 6
3.3 Technical Challenges 6
3.4 Phase II Work Plan Review 7
3.5 Description of Technology 7
3.5.1 Regenerator Concepts 7
3.5.2 Selected Regenerator Concept 7
3.6 Summary of Phase II Accomplishments 8
3.6.1 Prototype Regenerator Fabrication (Mezzo) 8
3.6.2 Prototype Regenerator Testing (Gedeon Associates/Sunpower) 8
3.6.3 Large Scale Mockup (University of Minnesota, UMN) 20
3.6.4 Analysis Tools and CFD Results (CSU) 22
3.6.5 Analytic Support (Gedeon Associates) 23
3.6.6 Structural Analysis of Microfabricated Involute-Foil Regenerators (Infinia) 36
3.7 Summary of Expected Benefits of Segmented-Involute-Foil Regenerators 37
4.0 Mezzo Microfabrication Process 37
4.1 Background 37
4.2 LiGA-EDM 37
4.3 LiGA-Fabricated Regenerator 39
4.3.1 Manufacturing Process 39
4.3.2 Fabricated Regenerator 42
4.4 Microfabrication Process Conclusions 43
5.0 Large Scale Mockup (University of Minnesota, UMN) 43
5.1 Large Scale Mockup (LSMU) Design 43
5.2 The Operating Conditions 45
5.3 The LSMU Experiments Under Unidirectional Flow 47
5.3.1 The LSMU Experimental Setup 47
5.3.2 Traverse of the Hot Wire Probe Over the Area of a Sector of an Annulus 48
5.3.3 Friction Factor 49
5.3.4 Permeability and Inertial Coefficient 53
5.3.5 Friction Factor of Various LSMU-Plate Configurations 58
5.4 The Jet Penetration Study 60
5.4.1 The Jet Penetration Study for the Round Jet Generator 60
5.4.2 The Jet Penetration Study for the Slot Jet Generator 71
5.5 Unsteady Heat Transfer Measurements 78
5.5.1 Embedded Thermocouple 79
5.5.2 Experimental Procedure 80
5.5.3 LSMU Unsteady-Heat-Transfer-Measurement Results 82
6.0 Analysis Tools and CFD Results (Cleveland State University (CSU)) 87
6.1 Computational Fluid Dynamics (CFD) Summary 87
6.2 CFD Introduction 87
6.3 Establishing the Computational Domain 90
6.3.1 Radial Direction Periodicity 90
6.3.2 Angular Direction Periodicity 90
6.3.3 Flow Direction Periodicity 92

6.3.4 Computational Domains for Oscillatory-Flow Simulations 92
6.3.5 Two-Dimensional Computational Domains 94
6.4 Material Properties and Boundary Conditions 95
6.4.1 Material Properties 95
6.4.2 Dimensionless Quantities, Correlations and Boundary Conditions 96
6.5 Summary of All Cases Studied 97
6.6 CFD Grid-Independence Test and Code Validation 98
6.6.1 2-D CFD Grid-Independence-Study Results 98
6.6.2 CFD Code Validation 101
6.6.3 Summary: Number and Types of Cells used for Various 2- and 3-D CFD Cases 104
6.7 Results of Two-Dimensional (2-D) CFD Simulations of Involute-Foil Layers 104
6.7.1 2-D Steady-State Simulations 104
6.7.2 2-D Oscillatory-Flow Simulation 106
6.8 Results of 3-D CFD Straight-Channel-Layers Approximation of Involute-Foil Layers 116
6.8.1 Steady-Flow Simulation (3-D Straight-Channel Layers) 117
6.8.2 Oscillatory-Flow Simulation (3-D Straight-Channel Layers) 118
6.9 Results, 3-D Steady-Flow Simulation of Involute-Foil Layers 121
6.9.1 Summary of 3-D Involute-Foil Runs 121
6.9.2 Steady-State, Re = 50, Friction-Factor and Nusselt Number Comparisons 122
6.9.3 Summary: Steady 3-D Involute-Foil Friction-Factor Results for All Reynolds Numbers 123
6.9.4 Summary: Steady 3-D Involute-Foil Mean-Nusselt-Number Results for All Reynolds Numbers 126
6.10 CFD Simulation Conclusions 127
6.10.1 Conclusions: 2-D Parallel-Plate Simulations (Steady and Oscillating Flow) 127
6.10.2 Conclusions: 3-D Straight-Channel-Layer Simulations (Steady and Oscillating Flow) 128
6.10.3 Conclusions: 3-D Involute-Foil-Layer Simulations (Steady Flow Only) 129
6.10.4 Future CFD Work 129
7.0 Structural Analysis of Micro-Fabricated Involute-Foil Regenerators (Infinia) 130
7.1 Summary 130
7.2 Introduction 130
7.3 Finite Element Analysis 131
7.3.1 Material Properties of Stainless steel 316L Used in FEA 131
7.3.2 Geometric Model 131
7.3.3 FEA Model 131
7.3.4 Boundary and Loading Conditions 131
7.3.5 FEA Results for Cases 1, 2 and 3 133
7.4 Structural Analysis Summary and Conclusions 142
7.5 Further Structural Analysis Work 142
8.0 Phase II Conclusions and Recommendations for Future Work 142
References 143
Appendix A—Detailed Derivation of Radiation Heat Flux Through a Tube With a Small Cross-Section (Gedeon Associates) 145
A.1 Negative End Contribution 145
A.2 Positive End Contribution 145
A.3 Negative Wall Contribution 146
A.4 Positive Wall Contribution 147
A.5 Normalization 147
A.6 Programming 148

Appendix B—Regenerator Figure-Of-Merit Degradation With Intra-Regenerator Flow-Gap Variations (Gedeon Associates) 149
B.1 Background 149
B.2 Effects of Gap Variations 149
Appendix C—Potential 6 to 9% Power Increase for a Foil-Type "Microfab" Regenerator in the Sunpower ASC Engine (Gedeon Associates) 153
C.1 Details 153
Appendix D—EDM Regenerator Disks: Concentric Involute Rings (Gedeon Associates) 155
D.2 Packing a Cylinder 155
D.2 Dimensions 156
D.3 Central Holes 156
D.4 Alternating Sense Involutes 156
D.5 EDM 157
D.6 Structural Analysis 157
Appendix E—Involute Math (Gedeon Associates) 159
E.1 Involute Cutouts 160
E.2 Spreadsheet Calculations 161
Appendix F—Implications of Regenerator Figure of Merit in Actual Stirling Engines (Gedeon Associates) 163
F.1 Figure of Merit Reformulation 163
References 165
Appendix G—Random Fibers Correlations with Porosity Dependent Parameters—Updated with New 96% Porosity Data (Gedeon Associates) 167
G.1 Master Correlations 167
G.2 Figure of Merit 168
G.3 Correlating Porosity 168
G.4 Data Files 170

A Microfabricated Segmented-Involute-Foil Regenerator for Enhancing Reliability and Performance of Stirling Engines

Phase II Final Report for the Radioisotope Power Conversion Technology NRA Contract NAS3–03124

Mounir Ibrahim and Daniel Danila
Cleveland State University
Cleveland, Ohio 44115

Terrence Simon, Susan Mantell, and Liyong Sun
University of Minnesota
Minneapolis, Minnesota 55455

David Gedeon
Gedeon Associates
Athens, Ohio 45701

Songgang Qiu
Infinia Corporation
Kennewick, Washington 99336

Gary Wood
Sunpower Incorporated
Athens, Ohio 45701

Kevin Kelly and Jeffrey McLean
International Mezzo Technologies
Baton Rouge, Louisiana 70806

Abstract

Cleveland State University (CSU), the University of Minnesota (UMN), Gedeon Associates, Infinia Corp., Sunpower Inc. and International Mezzo Technologies (Mezzo) have completed Phase II of a Radioisotope-Power-Conversion Technology, NASA Research Award (NRA) contract. The project brought together experts in Stirling-cycle machine design, microfabrication processing, oscillatory-fluid-flow experimentation and Computational Fluid Dynamics (CFD) to design and fabricate an advanced regenerator matrix for use in Stirling-cycle space-power conversion technology. The main objectives were to significantly increase the overall thermal efficiency of the regenerator and the Stirling convertor and to improve the structural reliability and manufacturability of the regenerator.

Regenerators for the next generation of Stirling convertors should have microscale features that have been configured for improved reliability, heat transfer and fluid flow characteristics. These microscale features can be produced by batch-mode Electrical-Discharge Machining (EDM) and LiGA (X-Ray Lithography) processes. These processes utilize technologies that have been developed for MicroElectroMechanical Systems (MEMS).

During Phase II an actual-size microfabricated regenerator comprised of a stack of 42 disks, 19 mm diameter and 0.25 mm thick, with layers of microscopic, segmented, involute-shaped flow channels was fabricated and tested. The geometry resembles layers of uniformly-spaced segmented-parallel-plates, except the plates are curved. Each disk was made from electro-plated nickel using the LiGA process. For historical reasons the geometry is sometimes referred to as "involute-foil." This regenerator had feature

sizes close to those required for an actual Stirling engine but the overall regenerator dimensions were sized for the NASA/Sunpower oscillating-flow regenerator test rig. Examination by scanning electron microscope showed that the disks were an accurate rendition of the design specification except for a few flaws which were expected to be worked out of the manufacturing process. Testing in the oscillating-flow test rig showed the regenerator performed extremely well, producing the highest figures of merit ever recorded for any regenerator tested in that rig over its ~20 years of use.

Progress was also made in understanding the detailed fluid dynamics in the regenerator by CFD analysis at Cleveland State University and large-scale testing at the University of Minnesota. In general, the conclusions of CFD and large-scale testing reinforced the actual-size test results and revealed some important details about the microscopic flows and heat transfer responsible for the overall regenerator behavior.

The original batch-EDM regenerator fabrication process anticipated in Phase I did not appear to be fast or controlled enough to yield a high quality product in a reasonable time. Therefore, fabrication by a LiGA electro-plating process was chosen for the Phase II nickel prototype test regenerator; however higher-temperature lower-conductivity more-robust materials, than pure nickel, are required. Electroplating from low conductivity and corrosion-resistant materials (even alloys) is possible, but has not been explored under this effort.

In Phase III (now underway) the plan is to microfabricate and test an involute-foil regenerator in a Stirling engine. The two key elements of this work are to adapt a Sunpower space-power engine to use an involute-foil regenerator, and to fabricate and test the regenerator in the engine. This regenerator will also be an electroplated nickel structure.

For possible work beyond Phase III, see the conclusions and recommendations at the end of this report.

1.0 Introduction

The Stirling-engine regenerator has been called “the crucial component,” Organ (2000), in the Stirling-cycle engine. The regenerator, which obtains heat from the hot working fluid and releases heat to the cold working fluid, recycles energy internally, allowing the Stirling cycle to achieve high efficiency. The location of the regenerator within a Stirling convertor is shown in figure 1.1 .

Currently, regenerators are usually made of woven screens or random fibers. Woven-screen regenerators have relatively high flow friction. They also require long assembly times which tends to increase their cost. Random fiber regenerators also have high flow friction but are easy to fabricate and therefore are inexpensive. Figure 1.2 shows a typical random-fiber regenerator and figure 1.3 shows a close up of the fibers. Due to the method of fabrication, the fibers are random primarily in a plane perpendicular to the main flow path. Thus both woven screens and random fibers experience flow primarily across the wires (cylinders in cross flow). Cylinders in cross flow tend to cause flow separation resulting in high flow friction and considerable thermal dispersion, a thermal loss mechanism that causes an increase in apparent axial thermal conduction. For space engines, there must be assurance that no fibers of this matrix will eventually work loose and damage vital convertor parts during the mission. It is also important that local variations in porosity inherent to random fiber regenerators not result in local mismatches in flow channels which would contribute to axial thermal transport. Wire screens have some randomness associated with their stacking and thus may have locally non-uniform flow. The efforts thus far have shown that attractive features for effecting high fluid-to-matrix heat transfer with low pressure drop are a matrix in which: a) the heat transfer surface is smooth, b) the flow acceleration rates are controlled, c) flow separation is minimized and d) passages are provided to allow radial mass flow for a more uniform distribution when the inlet flow or the in-channel characteristics are not radially uniform. It is thought that properly designed microfabricated regular geometries could not only reduce pressure drop, maintain high heat transfer and allow some flow redistribution when needed, but could show improved regenerator durability for long missions.

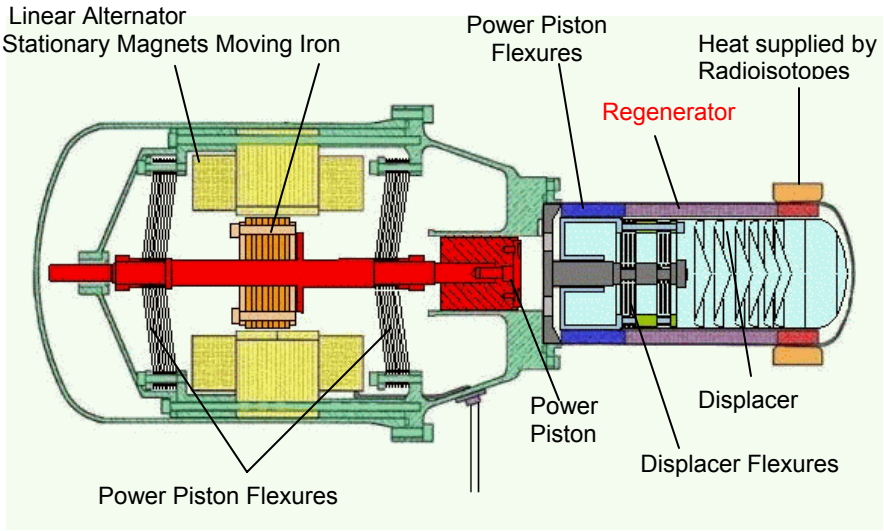

Figure 1.1.—Schematic of Stirling convertor showing the location of the regenerator.

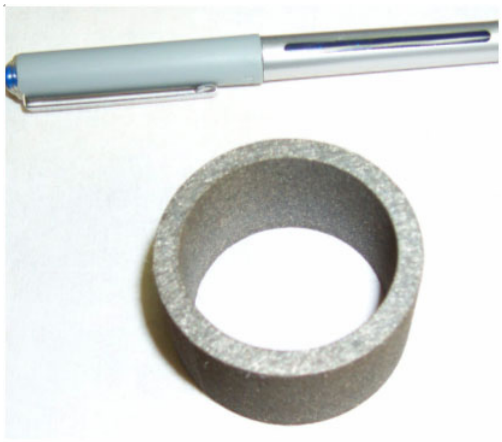

Figure 1.2.—Random Fiber Regenerator.

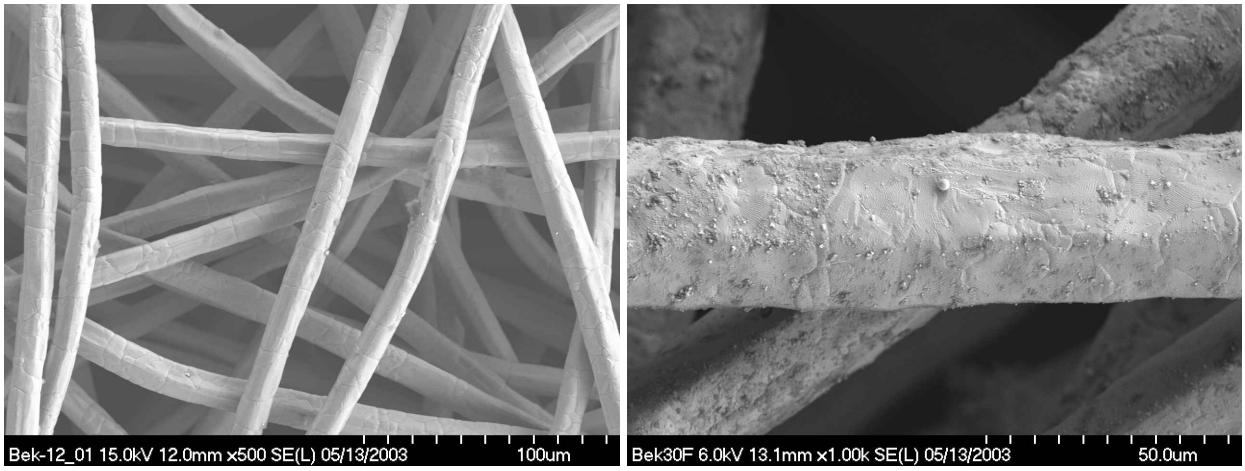

Figure 1.3.—Electron micrography of a random fiber regenerator matrix. Courtesy of NASA Glenn Research Center.

In Phase I of this project, a microscale regenerator design was developed based on state-of-the-art analytic and computational tools. For this design, a 6 to 9% engine-efficiency improvement was projected. A manufacturing process was identified and a vendor (International Mezzo Technologies) was selected to apply it. Mezzo completed EDM tools for fabricating layers of the chosen involute-foil microregenerator design, based on the team's specifications. They were ready to begin producing regenerator layers (annular portions of disks). Also, a Large-Scale-Mock-Up (LSMU) involute-foil regenerator was designed and fabrication had begun. Computational Fluid Dynamics (CFD) for different geometries was employed to model the fluid flow and heat transfer under both steady and oscillatory-flow conditions. The effects of surface roughness were included. Several geometries: lenticular, parallel plates (equally/non-equally spaced), staggered parallel plates (equally/non-equally spaced) and 3-D involute-foils were studied via CFD. The modeling was applied to both the microscale involute-foil regenerator and to the LSMU model of it.

A number of action items were addressed at the first-year review meeting held at NASA Glenn Research Center (GRC) on August 27, 2004. These items and their proposed resolutions were addressed in the final report for Phase I. One of these action items requested clarification of a plan for structural analysis of the microfabricated regenerator. Preliminary analysis showed that the involute-foil regenerator is of a sound design, structurally. Extremely high axial stiffness ensures that with an appropriate axial-compression force, the regenerator can be held firmly in place with negligible regenerator deformation. Special caution is needed for regenerator installation to prevent potential lateral deformation due to misalignment, as the radial stiffness is relatively low.

The goal of the current NASA project is to develop a new regenerator of high durability as well as high efficiency using emerging microfabrication technology. In addition to the benefit to Stirling convertor space-power technology, such regenerator development will also benefit Stirling cycle coolers and NASA's many cryocooler-enabled missions.

This report will show how the microscale involute-foil regenerator was fabricated and tested, and will review the test results. Also, the LSMU experimental model and the data obtained from it will be discussed. Moreover, the newly designed regenerator was analyzed via 1-D, 2-D and 3-D computational analyses . These computational tools enabled evaluating: 1) The figure of merit and 2) The effect of varying different parameters such as solid material used, thermal contact resistance, etc. for the new design.

2.0 Nomenclature

A, A_j	Area, m^2
b	Jet width, m
C	Specific heat, J/kg.K
CA	Crank Angle, degrees
C_f	Inertial coefficient
D_h, d_h	Matrix hydraulic diameter, m
D_p	Piston bore diameter, m
f	Oscillating frequency, Hz, or Darcy friction factor
F	Fraction of matrix not participating fully in thermal exchange with fluid, but equation (3.9) defines another usage of "F"
h	Convective heat transfer coefficient, $W/m^2 K$
K	Permeability, m^2
K, k_f	Thermal conductivity, W/m.K
L	Length, m
Nu	Nusselt number
Nu_m	Mean Nusselt number
Nu_x	Local Nusslet number
N_k	"conductivity ratio" defined as the effective axial conductivity divided by the molecular conductivity

Pe	Re * Pr = Peclet number
Pr	Prandtl number
Q_{in}	Heat into engine, W
$\dot{q}$	heat transfer rate, W/m^2
Δp	Pressure drop, Pa
r	Radial distance from the test section axis, m
R	Radius, m
Re	Reynolds number
Re_{max}	Maximum Reynolds number
S	Spacing between two cooler tubes, m
t	time, s
T	Temperature, °C
T_c	Cold end temperature, °C
T_h	Hot end temperature, °C
u_{max}	Maximum bulk mean velocity in regenerator, m/s
U	Darcy velocity in streamwise direction, m/s
V	Volume, m^3, or local velocity inside the channels, m/s
W_{PV}	PV, or indicated, power predicted for engine, W
$Wdis$	Displacer drive power, W
Va	Valensi number
x	Axial distance, m
x_p	The jet penetration depth, m
X_p	Amplitude of piston displacement, m
X_c	Amplitude of particle displacement within jet generator tubes, m
X_r	Amplitude of particle displacement within regenerator, m
X_{max}	Maximum particle displacement amplitude, m
β	Porosity
θ	Crank angle, degrees
μ	Dynamic viscosity, kg/m·sec
ν	Kinematic viscosity, m^2/sec
ρ	Density, kg/m^3
σ	Stefan-Boltzman Constant, W/m^2-K^4
ϕ	Dimensionless temperature or porosity of porous media
ω	Angular frequency, rad/sec

2.1 Abbreviations

ASC	Advanced Stirling Convertor (engine and linear alternator)
CAD	Computer Aided Design
CFD	Computational Fluid Dynamics
CSU	Cleveland State University
EDM	Electric Discharge Machining
FEA	Finite Element Analysis
FTB	Frequency Test Bed (convertor, or engine and linear alternator)
GRC	Glenn Research Center
LiGA	Lithographie, Galvanoformung and Abformung (the German words for lithography, electroplating and molding. X-ray lithography is used here)
LSMU	Large Scale Mock Up (of involute-foils)
MEMS	microelectromechanical systems
NASA	National Aeronautics and Space Administration
NRA	NASA Research Award

PMMA	polymethyl methacrylate (a clear plastic, also marketed as Acrylic, Plexiglas, Lucite, etc. Used as a photoresist in LiGA process for microfabrication of involute-foils)
SEM	Scanning Electron Microscope
SU-8	SU-8 is a negative, epoxy-type, near-ultraviolet photoresist used in microelectromechanical (MEMS) applications
TCR	Thermal Contact Resistance
UMN	University of Minnesota

3.0 Program Overview

3.1 Objectives

The main objective of this phase (II) was to build a prototype of the involute-foil regenerator and test it in a NASA/Sunpower oscillatory flow rig to determine how well it performs relative to currently used regenerator structures like random fiber and wire screen. This was accomplished using modern microfabrication techniques supported by large-scale involute-foil testing, theoretical analysis and computational-fluid-dynamics (CFD) modeling.

Forty-two layers of involute-foil disks (i.e., annular portions of disks) were microfabricated via a LiGA process; LiGA is derived from the german words for lithography, electroplating and molding. The large-scale testing was based on dimensions 30-times actual size, and test conditions dynamically similar to those expected in an engine. The CFD computations were based upon 2-D and 3-D simulations of representative elementary regenerator volumes, and 1-D simulations of regenerators and engines. For the Stirling-space-engine application, goals for the new regenerator were improved performance, reliability and manufacturability.

3.2 Approach

The approach included: 1) reviewing the literature, 2) identifying and computing performance figures of merit, 3) utilizing state-of-the-art CFD modeling and large-scale involute-foil testing, 4) applying state-of-the-art microfabrication techniques and 5) experimentally testing the fabricated microscale regenerator. A brief description of these items is given below.

First, a review of published theoretical and experimental regenerator performance literature was completed. Computational research was done in the area of microchannel fluid-dynamics and heat transfer to learn about the effect of roughness in small channels. In addition, a review of different manufacturing techniques for micro channels was carried out. Performance figures of merit were identified, and improved upon, based upon analytical solutions for simple channel geometries as well as from experimental test data available in the literature. State-of-the-art modeling was utilized via a 1-D Sage Stirling cycle simulation model and 2-D and 3-D CFD Navier-Stokes solvers for simulation of microscale regenerator geometry. In the microfabrication area, available methods were surveyed to provide the required matrix within the planned time and cost. Design, fabrication and experimental testing of a LSMU (Large Scale Mock Up) which was dynamically similar to an engine involute-foil matrix was carried out. Also, testing of a microscale involute-foil was done in an existing NASA/Sunpower-developed oscillating-flow test rig.

3.3 Technical Challenges

The technical challenges faced in this project are summarized below:

1) Microfabrication of Small-Feature Sizes: These features are sub-100 μm scale that must be built in an overall macro-scale regenerator of 100 mm scale. No more that a 10% passage-width nonuniformity tolerance (10 μm) in these channels was specified, based on computations made by Gedeon Associates. In addition, a high passage aspect ratio (length > 3 x width) for each element of the regenerator was specified, which required some research to achieve. If the originally planned EDM had been used, in

addition to LiGA, EDM tool wear and positioning would be limiting factors. Cost was also limiting, due to the limited funding.

2) CFD of Complex Geometries: There were computational challenges in dealing with the actual 3-D overall structures having interrupted passages. Examining the effects of surface roughness (on heat transfer) in micro channels required fine resolution of near-wall flow and heat transfer. These challenges are demonstrated by the resulting requirements of (a) the large number of computational grid points (for proper accuracy of the solution) and, (b) the long computation times, particularly for the oscillatory-flow simulations.

3.4 Phase II Work Plan Review

The following tasks were carried out during Phase II:

Task 1—Large Scale Mock Up (LSMU) final design, test plan and fabrication.
Task 2—Testing of LSMU.
Task 3—Continued computational modeling of LSMU and microscale involute-foils.
Task 4—Fabrication of electroplated nickel prototype regenerator matrix with actual-size features.
Task 5—Scanning Electron Microscope (SEM) inspection of microscale involute-foils.
Task 6—Actual-size oscillatory-flow testing in the NASA/Sunpower Test Rig.
Task 7—Documentation via technical and financial reporting, oral review presentations and a final report.

The following milestones were established to track Phase II progress:

MS1: Finalize design of the LSMU.
MS2: Complete fabrication of the LSMU and complete the LSMU test plan.
MS3: Complete fabrication of actual-size prototype regenerator and assessment of resulting matrix.
MS4: Complete initial testing of the LSMU.
MS5: Testing of the microfabricated nickel regenerator.

3.5 Description of Technology

3.5.1 Regenerator Concepts

In Phase I, different concepts were identified for the regenerator matrix that could be manufactured with existing technology and be expected to have better performance than existing matrices. These concepts included: 1) a “lenticular” array, 2) a honeycomb structure, 3) an involute-foil and 4) a modified involute-foil.

The modified involute-foil was selected. This design has multiple channels of uniform width with good flow and heat transfer characteristics. It is durable. In contrast to the foil (or wrapped-foil) regenerator, although the chosen regenerator concept does have some of the low-loss attributes of the foil regenerator, it has uniformly repeating geometric features with a robust structure that prevents the variability in channel size that has proven inherent in the wrapped-foil regenerator. In comparison to the random-wire regenerator or the screen regenerator, the chosen regenerator concept has the durability of the screen regenerator but with better flow-loss characteristics. This modified involute-foil regenerator can be fabricated with modern microfabrication techniques.

3.5.2 Selected Regenerator Concept

This regenerator consists of a stack of involute-foil disks (or annular portions of disks) that have been microfabricated by the LiGA or LiGA/EDM processes (the particular material determines whether EDM is required). It has a low resistance to flow because it has a reduced number of separation regions, compared to wire screen and random fiber. But it still has high heat transfer effectiveness approaching that of the other structures. The resulting figure of merit (~ the ratio of heat transfer to pressure drop) has proven superior to

the currently used random-fiber and wire-screen regenerator structures. It has known small features which are secured to the assembly so that it is not as susceptible to releasing small fragments of regenerator matrix material (as random-fiber and wire-screen, both of which have random features).

3.6 Summary of Phase II Accomplishments

3.6.1 Prototype Regenerator Fabrication (Mezzo)

The LiGA micromachining process was used to fabricate a nickel involute-foil regenerator that was tested and found to provide very good performance. The original manufacturing approach of using LiGA-fabricated EDM tools to fabricate stainless-steel regenerator parts seemed initially to offer little potential due to the extremely low material removal rate. In retrospect however, if higher-machine burn-rate settings and EDM tool dimensions are chosen such that greater overburn is allowable, then the EDM-LiGA approach will be more viable. It should also be noted that, in this effort, a new manufacturing technique was developed: namely using EDM to "skim cut" regenerator parts fabricated by LiGA. While the regenerator tested did provide excellent performance, LiGA and/or a LiGA-EDM process optimization could result in a better product. Potential improvements include:

i) Improve the lithography process to eliminate or greatly reduce "undercutting."
ii) Cease electroplating before overplating begins. This would eliminate the need to use the "skim cut" and would eliminate the source of burrs that are attributed to the EDM operation.
iii) To greatly reduce cost, explore the use of SU-8, a negative resist that requires substantially less exposure time than PMMA.
iv) For EDM, find acceptable combination of material removal rate, overburn, and geometry that gives a high quality part in a reasonable time and a reasonable cost.

3.6.2 Prototype Regenerator Testing (Gedeon Associates/Sunpower)

3.6.2.1 Physical Description

The regenerator sample tested consisted of a stack of 42 involute-foil disks (layers). The following CAD rendering (fig. 3.1) shows progressive magnifications of a typical disk viewed from the front.

The term "involute" refers to the curved shape of the channels. The centerline of each channel might be imagined as traced by a fixed point on a string unwinding from a circular cylinder (the generating circle) concentric with the disk. The diameter of that cylinder is equal to the diameter of the inner circular rib for the previous ring of flow channels.

The next CAD rendering (fig. 3.2) shows a typical single flow channel in the matrix. It is from an early solid model and does not correspond exactly to the final matrix geometry but it is useful to illustrate some of the important dimensions that define the geometry. L_c is the flow channel length (disk thickness), W is the channel width (arc length of web), g is the channel flow gap (normal distance across) and s is the basic involute element spacing (gap + web thickness).

From the CAD drawings it is possible to calculate the representative hydraulic diameter for the entire regenerator matrix like this: A unit cell of the matrix consists of one 7-ring disk and one 8-ring disk. The hydraulic diameter for such a 2-disk cell is a reasonable approximation for the entire matrix. There are 7 different basic channel shapes in the 7-ring disk and 8 in the 8-ring disk. For each basic channel shape we use available CAD tools to measure individual flow area and wetted perimeter. The total flow area A_T for the 2-disk cell is the sum of the areas of each individual channel elements multiplied by the number of occurrences per disk. The same is done to compute the total wetted perimeter W_T. The number of channel element occurrences per disk is just its involute generating circle diameter divided by the 100 μm involute spacing$s$ (see app. D). The final representative hydraulic diameter is $4A_T/W_T$ .The final hydraulic diameter calculated this way is:

$$D_h = 162.0\ \mu m$$

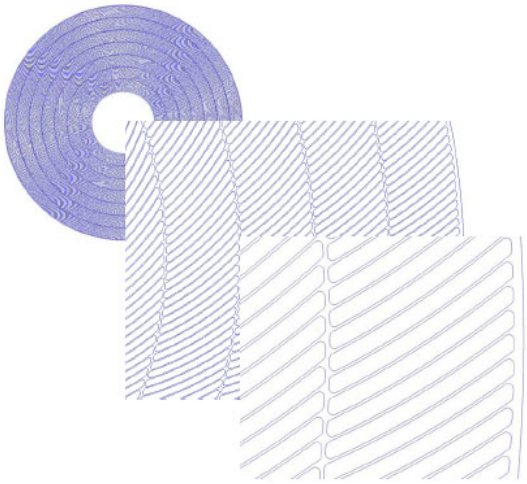

Figure 3.1.—Involute-foil geometry.

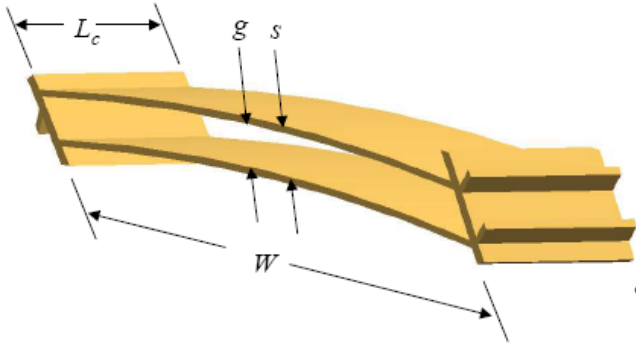

Figure 3.2.—Channel geometry.

The above value agrees within 0.2% of the value computed by UMN for the large-scale mock-up (4.872 mm) when scaled up by the scale factor 30. For parallel plates, the hydraulic diameter would be exactly twice the flow gap ($2g$) which is more like 170 μm.

For overall matrix porosity, the value reported by Mezzo was used:

$$\beta = 0.8384$$

This value was based on physical measurements of mass and the known material density for nickel. As reported by Mezzo, it agrees quite well with the theoretical average porosity for a 2-disk cell of 0.8299. There is only a 1% porosity discrepancy in the direction that suggests that the flow channel gaps are slightly wider than expected (by about 1%). From this observation, one might expect the actual hydraulic diameter to be larger by about the same amount, on average, which would bring it to about 163.7 μm (D_h scales with flow area if wetted perimeter remains about the same).

Another parameter of interest is the ratio of channel flow length L_c (disk thickness) to hydraulic diameter which CSU has been investigating with CFD modeling (see sec. 6.0). For the current batch of disks, the mean thickness is 238 μm (42 disks totaling 10.0 mm) so:

$$L_c / D_h = 1.47$$

Still another parameter of some importance is the channel aspect ratio, or ratio of channel width to hydraulic diameter. The weighted average flow channel width for the two types of disks is about 1200 μm so the average channel aspect ratio is:

$$W / D_h = 7.4$$

In addition to the above parameters, the way the disks are stacked on top of each other is important. The current scheme of alternating involute directional orientation and staggered ring walls is easy to describe but difficult to quantify in terms of any simple numerical ratio.

3.6.2.2 Test Canister Design

The regenerator disks are housed within the test canister depicted in figure 3.3 for testing in the NASA/Sunpower oscillating-flow rig:

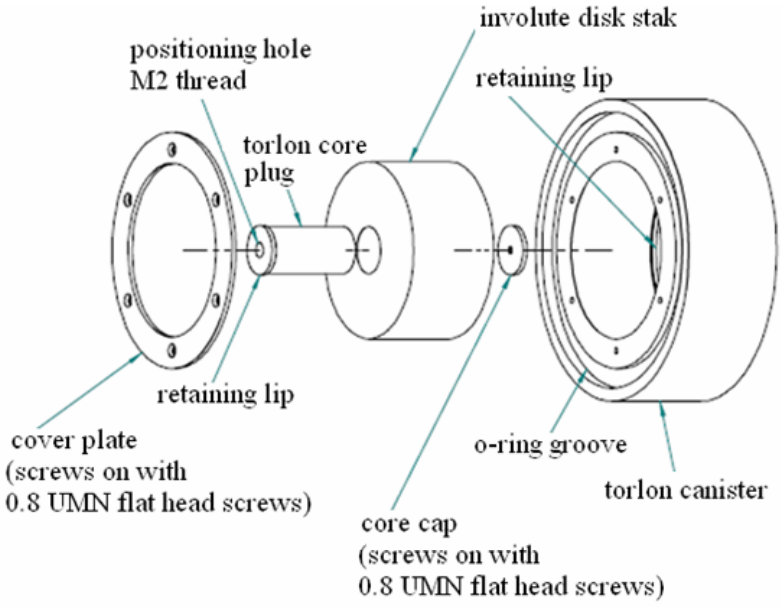

Figure 3.3.—Testing canister geometry.

3.6.2.3 Regenerator Verification from SEM Images

Scanning electron microscope (SEM) images of the involute-foil regenerator disks revealed excellent spacing uniformity of the flow channels and a generally smooth surface finish but also some defects. SEM micrographs were taken with the assistance of Randy Bowman at NASA GRC.

3.6.2.3.1 The Specimen

The sample photographed was the first one tested in the NASA/Sunpower oscillating-flow test rig. The matrix was not taken apart. The purpose was not to do an exhaustive survey of every one of the 42 disks inside but only to take a look at what was visible from the two ends of the assembled regenerator canister.

3.6.2.3.2 Spacing Uniformity

One objective was to assess the uniformity of spacing of the foil elements in the matrix. It was previously established that the spacing uniformity should be within ±10% to avoid significant adverse impact on the figure of merit (app. B). It was found that the Mezzo matrix is significantly better than this, as can be seen in the following images. The first image (fig. 3.4a) is a low-magnification view that gives one the qualitative impression that the spacing is uniform. The second image (fig. 3.4b) shows actual measurements with the Adobe Acrobat "measurement" tool used to conclude that the spacing uniformity is within ±2% in a small region of the matrix. The spacing may actually be more uniform than this because there was a significant error in the accuracy with which the estimate of the normal direction across the channel and the location of the channel edges was done with the measurement crosshairs.

The measurements are hard to read on the photograph but the values were saved in a "csv" (comma-delimited text) file (option in measurement dialog). Using Microsoft Excel's (Microsoft Corporation) statistical functions the standard deviation of foil spacing was computed to be 1.6% of the average spacing, for the 12 measurements.

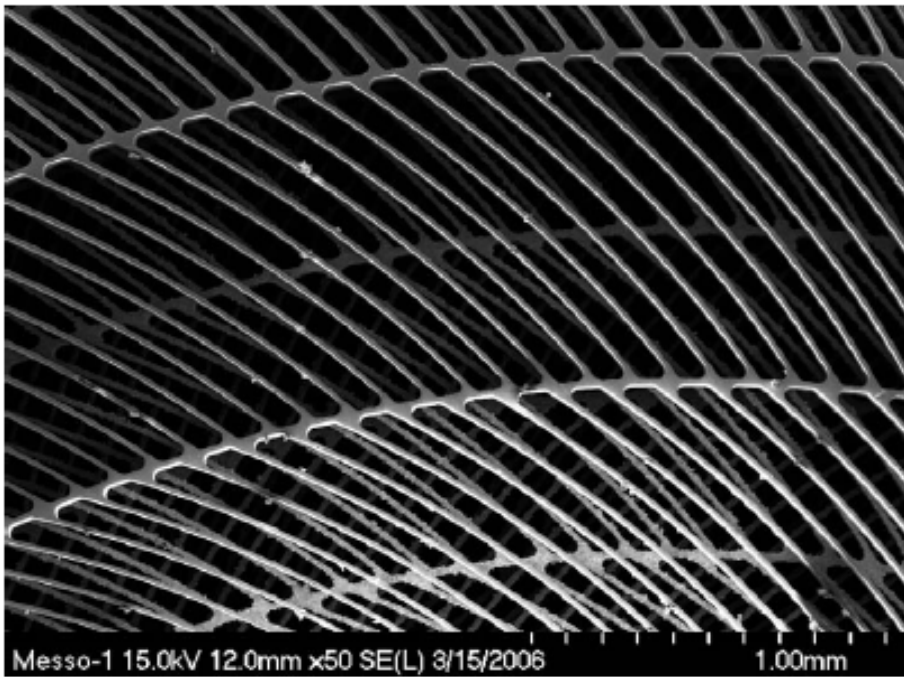

Figure 3.4.—(a) Face-on view at low magnification showing overall good foil spacing uniformity.

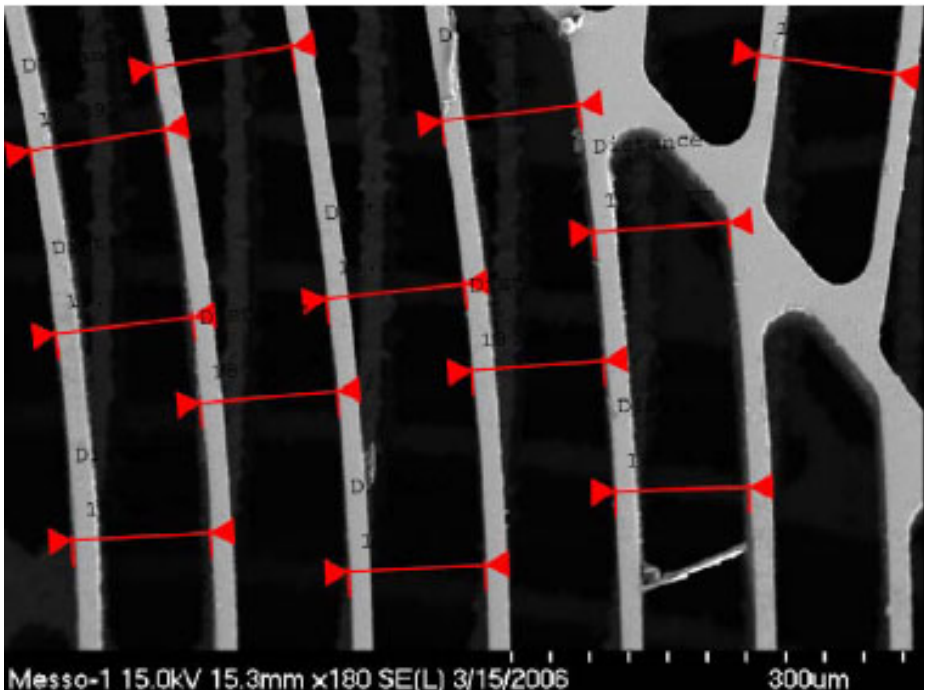

Figure 3.4.—(b) Adobe Acrobat measurement tool in action measuring localized foil spacing in a close-up image.

3.6.2.3.3 Perspective View

The images below were obtained by tilting the sample by 25°. The first one (fig. 3.5) gives a good idea of the 3-D matrix structure and also shows a very smooth surface finish on the walls of the flow channels. The second (fig. 3.6) shows a magnified view of a channel wall. We estimated the "roughness" height to be less than 1 μm, compared to an 85 μm channel gap. The roughness mainly consists of occasional pores and shallow grooves or steps, parallel to the flow direction.

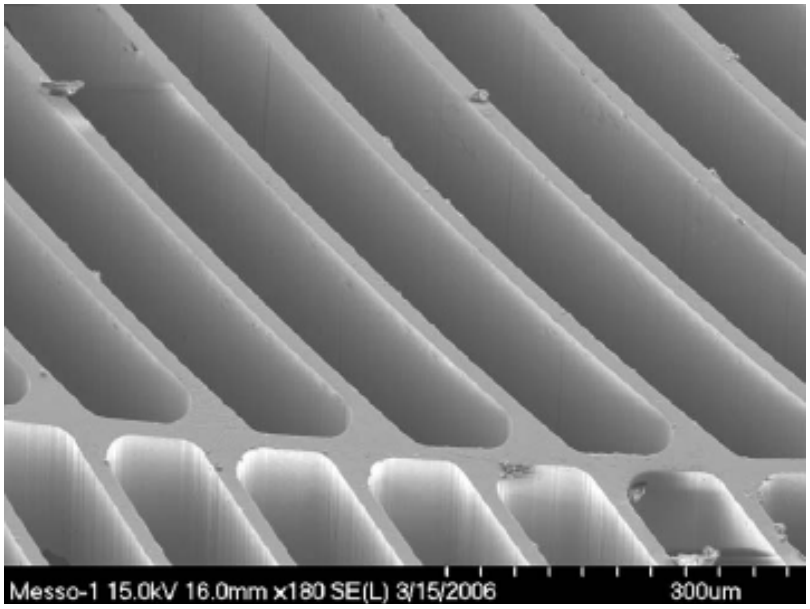

Figure 3.5.—A 25° tilted view showing 3-D structure near an annular ring with involute webs above and below. The dust visible on the surface is probably from testing or handling.

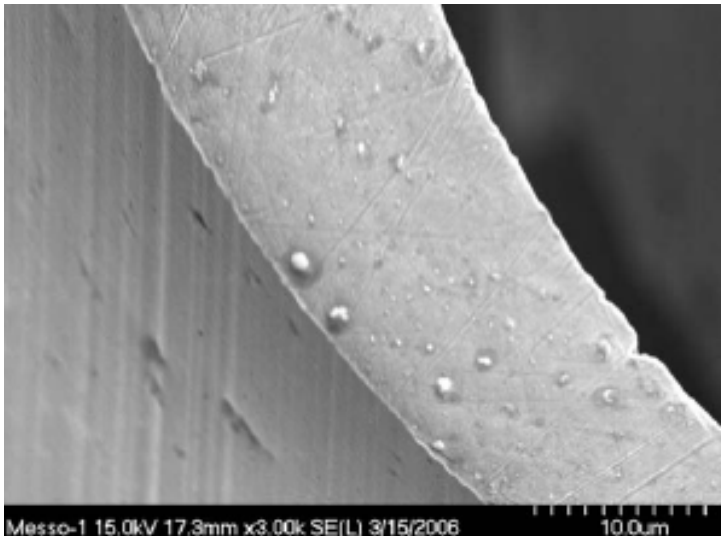

Figure 3.6.—Detail of flow channel surface roughness.

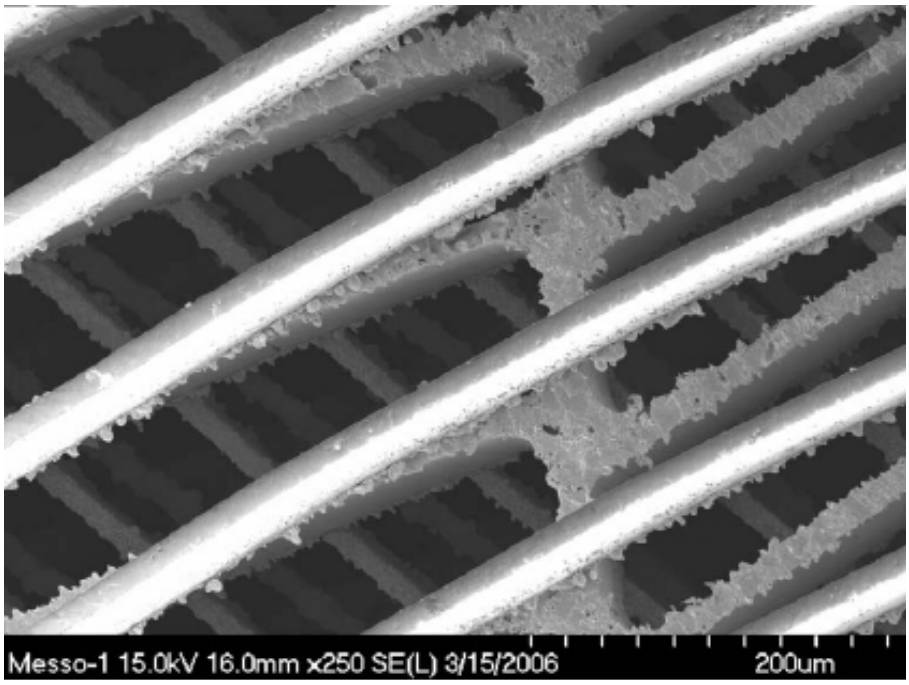

Figure 3.7.—Visible debris attached to the face of the second disk within the sample, visible below the top disk.

3.6.2.3.4 Defects

The matrix was not without its flaws. Figure 3.7 shows significant spatter-like debris on the face of the second disk below the surface of the regenerator—at one location (Microscope operators tend to focus on the defects). The debris comes from EDM removal of the disk from the plating substrate. The top disk also shows some evidence of this debris on its lower surface. Other images show similar debris comprised of small spherical particles of what appears to be nickel (preliminary SEM assay).

Eliminating the debris and edge roughness would be an important objective in further development. Roughness will have some effect (documented in the oscillatory flow tests) on the helium entering the flow channels and might pose a contamination problem if any of the material works loose.

Another "flaw" in this particular assembly is that the angular involute orientations are the same in the top two disks instead of opposite (crossed), as they are supposed to be. Subsequent inspection by Mezzo showed that there was a more-or-less random involute orientation throughout the matrix, although the two types of disks were correctly alternated. This stacking problem was corrected and the properly-stacked regenerator was also tested.

There is another sort of defect (see fig. 3.8) that appears to be associated with a flaw in the photo-lithographic mask used to expose the photo-resist material. Occasionally, one sees notches extending the full disk thickness. This particular notch extends a bit less than halfway through the web thickness. The presence of such defects might put an effective lower limit on the thinness of the webs before a significant number are cut completely through. In fact, it may explain why some webs were cut completely through in some cases.

3.6.2.3.5 Recommendations

In spite of the flaws, the test results for this matrix were very encouraging. However, some of the flaws are of concern for long-term reliability so work on quality control issues is needed for future matrices. Based on these photographs the two main concerns are spatter-like debris near the ends of the flow channels and notch defects extending completely through or mostly through channel walls.

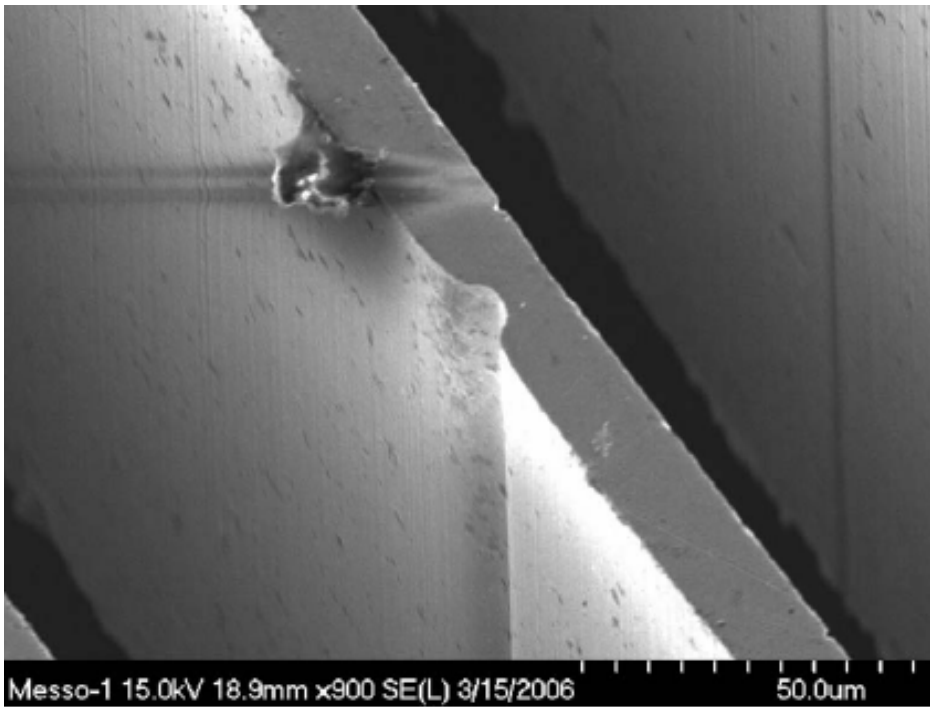

Figure 3.8.—Notch defect extending for the full length of an involute web.

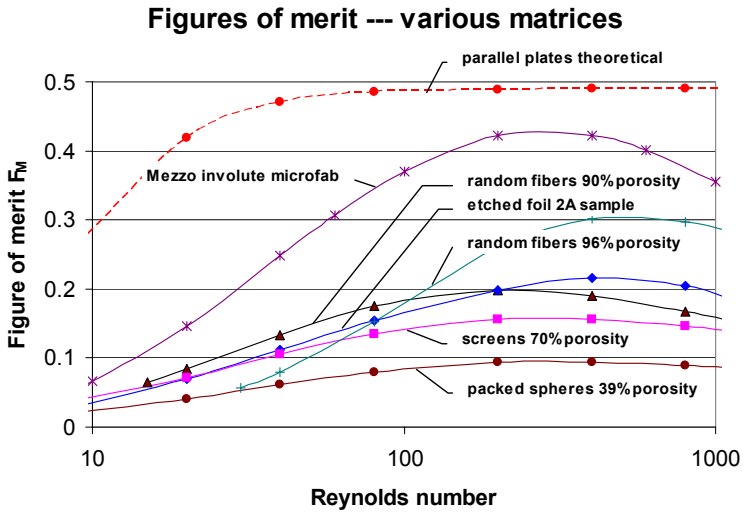

Figure 3.9.—Figures of merit for various matrices.

3.6.2.4 Test Results

The results of testing in the NASA/Sunpower oscillating flow test rig were very promising and are summarized along with results from several other regenerator types in figure 3.9.

The microfabricated regenerator has a figure of merit substantially higher than the other regenerator types—including the 90% random fiber regenerator which is roughly what is being used in the current generation of space-power Stirling engines. Figure of merit is defined as follows:

$$F_M = \frac{1}{f\left(\frac{R_e P_r}{4N_u} + \frac{N_k}{R_e P_r}\right)}$$

R_e	Reynolds number
P_r	Prandtl number
f	Friction factor
N_u	Nusselt number
N_k	Thermal dispersion conduction enhancement

The figure of merit is a first-cut measure of overall regenerator performance. It is inversely proportional to the product of regenerator pumping loss, W_p, thermal loss, Q_t, and the square of regenerator mean flow area, A_f, (see details in app. F, by Gedeon), as follows:.

$$F_M \propto \frac{1}{W_p Q_t A_f^2}$$

A_f tends to be constrained by power density (void volume) so when comparing regenerators in similar engines it may be ignored.

3.6.2.4.1 New 96% Porosity Random Fiber Data

In the plot (fig. 3.9) the figure of merit for 96% porosity random fibers is based on recent test data with improved accuracy compared to data previously reported. Based on the earlier data, it appeared that the figure of merit for 96% porosity random fibers was actually higher than that of the microfabricated regenerator at some Reynolds numbers. That is no longer the case and the microfabricated regenerator now has a figure of merit substantially higher than that for the 96% porosity random fibers. The microfabricated regenerator now ranks as the best regenerator ever tested in the NASA/Sunpower test rig.

3.6.2.4.2 Unexplored Dimensionless Ratios

The pressure-drop and heat transfer correlations discussed below (eqs. (3.1) through (3.4)) are for a particular regenerator matrix. Since the correlations are in terms of dimensionless quantities (like Reynolds number) they also apply to geometrically similar matrices. What does that mean?

Aside from the essential geometric property of the involute channels, namely that they consist of uniform-gap planar flow passages, and the chosen stacking geometry, the important dimensionless specifications are porosity β, the ratio of flow channel length to hydraulic diameter, L_c/D_h, and the aspect ratio, W/D_h.[1] Of these probably L_c/D_h is most important because it affects the degree to which flow is fully developed within any given flow channel at a given Reynolds number. Porosity is probably of lesser importance because it does not directly affect the nature of the flow channels. But it does affect the thickness of the webs between flow channels and therefore the way the flow enters the channels in distributing from one disk to the next. The aspect ratio is probably not too critical so long it is not significantly lower than the value mentioned above.

So one should beware of applying the correlations below to microfabricated involutes with significantly different porosity, L_c/D_h or W/D_h. But if one does, it is expected that the present correlations are conservative when applied to regenerators with higher porosity or higher L_c/D_h or higher W/D_h. In

[1]Since the porosity is a relatively good measure of the ratio of flow gap to element spacing, g/s, and the fill factor (1–β) is a relatively good measure of the ratio of web thickness to element spacing (1–g/s) there is no need to separately use g/s or (1–g/s) to characterize the matrix.

either of those cases the flow would then be closer to the ideal parallel plate flow and the figure of merit should increase somewhat.

3.6.2.4.3 Restacked Canister

Since the original test regenerator was found to have been incorrectly assembled (random spiral orientation) after it had been tested in the oscillating-flow test rig, it was decided that the spiral orientation was important enough to warrant re-testing the regenerator. Mezzo re-stacked the regenerator using the same disks but this time with disks both correctly sequenced and with the spiral direction reversed at each disk transition, according to the original plan. It was then tested in the oscillating-flow rig and found that the overall figure of merit changed slightly compared to the original testing, as shown in figure 3.10.

Figure 3.10 shows that the correct stacking produces a slightly better figure of merit at high Reynolds numbers and slightly worse values at low Reynolds numbers. As will be seen below, the friction factors for the two cases are almost identical so the main reasons for the differences are thermal losses, with the restacked regenerator producing more thermal loss at low Reynolds numbers and less at high Reynolds numbers. The increased thermal loss at low Reynolds numbers is probably a result of improved measurement accuracy as a result of new rig operating procedures, as explained below. The reduced thermal loss at high Reynolds numbers appears to be real.

To get a better feel for what is going on two data points near the peak of the figure of merit curve, at Reynolds numbers around 400 were taken, one data point for the original regenerator and one for the re-stacked canister. Both correspond to tests with 50 bar nitrogen.

As shown in table 3.1, the two data points are nearly identical in all respects except that the restacked canister has about 2.4% lower thermal loss (heat rejection to cooler) for a 2.0% larger regenerator temperature difference. Assuming thermal loss scales in proportion to temperature difference, this implies that the restacked regenerator would produce about 4.5% lower thermal loss for the same temperature difference. This is consistent with the figure of merit calculation which shows about a 5% improvement for the restacked regenerator over the originally-stacked regenerator at a Reynolds number of 400.

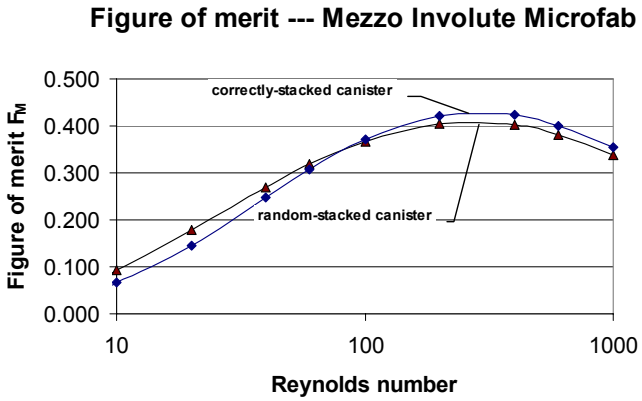

Figure 3.10.—Figure of merit values, random- and correctly-stacked canister.

TABLE 3.1—VALUES FOR THE ORIGINALLY- AND CORRECTLY-STACKED REGENERATORS

	Random stacking	Correct stacking
Mean pressure (bar)	50.0	50.0
Piston amplitude (mm)	4.001	4.000
Coolant flow rate (g/s)	6.161	5.712
Coolant ΔT (C)	2.149	2.264
Heat rejection (W)	**55.39**	**54.08**
T_{mean} regen hot end (C)	449.2	450.5
T_{mean} regen cold end (C)	340.1	339.2
ΔT regenerator (C)	**109.1**	**111.3**

At low Reynolds numbers, where heat rejection is smaller, the thermal differences between the two regenerators are likely due to changes in test-rig operating procedures. For the restacked regenerator a "single ramp-up" procedure designed to minimize difficulties with long-term thermal drift was adopted. Under this procedure, the operator increases the piston amplitude in 1 mm increments from 0 to 10 mm, waiting about 30 min for the rig to equilibrate after each change. Under the previous procedure, the operator ramped piston amplitude up and down twice over the range 0 to 10 mm, with only about 8 min equilibration time between changes. There was also a new procedure for measuring the baseline cooler heat rejection due to static thermal conduction. The rig was operated at 5 mm piston amplitude (mid range) for 2 hr then allowed to sit for 30 min at zero piston amplitude before logging the baseline static thermal conduction data points. Previously, static thermal conduction was averaged from zero-amplitude data points logged several times during the test without waiting as long for the rig to settle down to thermal equilibrium. The new procedure is considered to produce more accurate results at the low Reynolds number end of the experimental range.

3.6.2.4.4 Friction Factor Correlations

The Darcy friction factors for the original and re-stacked tests are:

$$f = \frac{120.9}{\mathrm{Re}} + 0.362\,\mathrm{Re}^{-0.056} \quad \text{(original stacking)} \tag{3.1}$$

and

$$f = \frac{117.3}{\mathrm{Re}} + 0.380\,\mathrm{Re}^{-0.053} \quad \text{(correct stacking)} \tag{3.2}$$

Plotted as functions of Reynolds number there is hardly any difference (correct stacking about 0.9% lower on average). The following plot (fig. 3.11) focuses in on a small range of Reynolds numbers to better resolve the two curves. If it is plotted over the full range from 10 to 1000, then the two curves become indistinguishable.

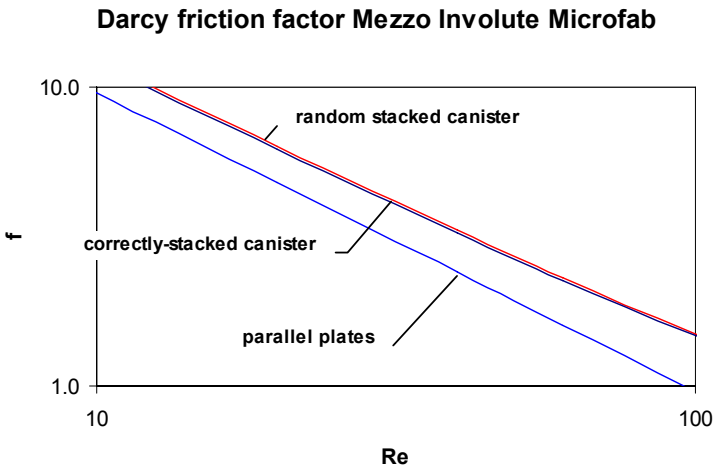

Figure 3.11.—Darcy friction factors, *f*, as functions of Reynolds number, Re, for the originally- and correctly-stacked regenerators.

The range of key dimensionless groups for these tests was:

TABLE 3.2.—DIMENSIONLESS GROUPS FOR THE PRESSURE DROP TESTS

Peak Re (Reynolds number) range	3.4 to 1190
Va range (Valensi number)	0.11 to 3.8
δ/L range (tidal amplitude ratio)	0.13 to 1.3

3.6.2.4.5 Heat Transfer Correlations: Simultaneous Nu and Nk

The correlations for simultaneous Nusselt number and enhanced conductivity (thermal dispersion) ratio derived for this matrix are:

$$\mathrm{Nu} = 1 + 1.99\mathrm{Pe}^{0.358} \quad N_k = 1 + 1.314\mathrm{Pe}^{0.358} \text{ (random stacking)} \tag{3.3}$$

and

$$\mathrm{Nu} = 1 + 1.97\mathrm{Pe}^{0.374} \quad N_k = 1 + 2.519\mathrm{Pe}^{0.374} \text{ (correct stacking)} \tag{3.4}$$

$\mathrm{Pe} = \mathrm{Re}\,\mathrm{Pr}$ is the Peclet number. Nu and N_k are plotted individually below for the case Pr = 0.7 (see figs. 3.12 and 3.13).

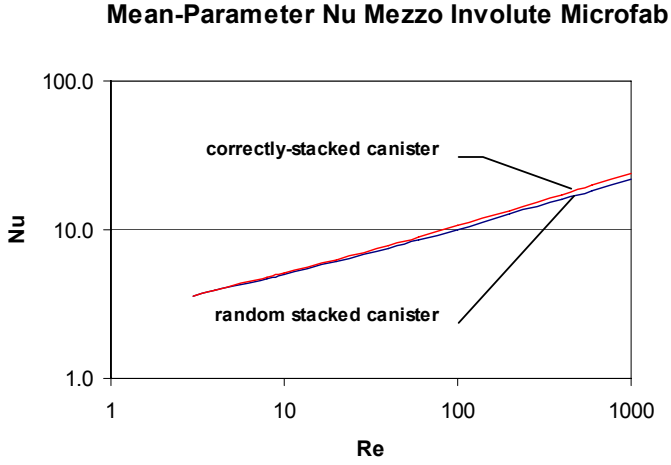

Figure 3.12.—Mean-Nusselt-number Nu values as functions of Reynolds number, Re, for the originally- and correctly stacked regenerators

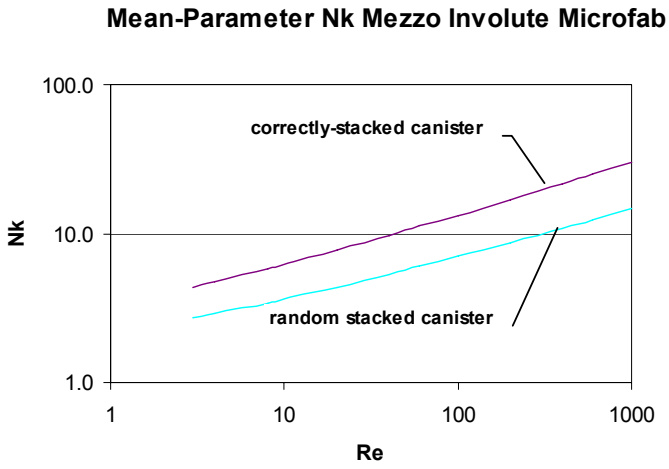

Figure 3.13.—Mean enhanced-thermal-conductivity (thermal-dispersion) ratio, N_k , values as functions of Reynolds number, Re, for the originally- and correctly stacked regenerators.

As a reminder, Nu and N_k are designed to be used together in a model like Sage where the Nusselt number may be understood as based on section-mean temperature rather than velocity-weighted (bulk) temperature. Under this assumption, N_k compensates for any discrepancy in enthalpy flow compared to using a bulk-temperature approach.

Comparing results for the two regenerators, in figure 3.12, shows that the Nu values are very close to one another except for a slight, but significant, increase at high Reynolds numbers for the correctly-stacked case. The N_k values in figure 3.13 are quite different, probably due to larger measured thermal losses at low Reynolds numbers attributed to lower baseline thermal losses measured under the new rig operating procedures. The combined effects of Nu and N_k together are best seen in the plot of figure of merit at the beginning of section 3.6.2.4 (fig. 3.9).

The range of key dimensionless groups for these tests is:

TABLE 3.3—TEST PARAMETER RANGES

Peak Re range (Reynolds number)	2.6 to 930
Va range (Valensi number)	0.064 to 2.4
δ/L range (tidal amplitude ratio)	0.17 to 1.8

3.6.2.4.6 Parallel Plate Nusselt Number Comparison

Figure 3.14 compares two Nusselt-number plots derived for the microfabricated involutes against the theoretical Nusselt number (Nu = 8.23) for fully-developed flow between parallel plates under the uniform heat flux boundary condition.

The curve labeled “Nu” is the Nu part of the simultaneous Nu, N_k correlation. The curve labeled “Nue” is an effective Nu_e correlation, derived under the assumption that $N_k = 1$. The two derived Nusselt numbers are close to each other but far from the theoretical Nusselt number. At high Reynolds numbers, the derived values are higher than the theoretical value, which makes sense because the flow in the microfabricated flow channels is more and more like developing flow with increasing Reynolds numbers and Nusselt numbers are known to be higher in developing flow (as documented by CSU see sec. 6.0). At low Reynolds numbers the derived values are lower than the theoretical value. This may be due to the effects of solid (nickel) thermal conduction within the individual regenerator disks which is of some significance at low Reynolds numbers. (see sec. 3.6.5).

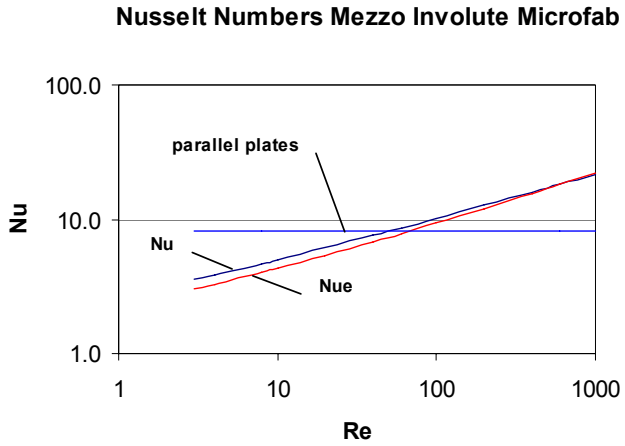

Figure 3.14.—Nusselt-number values as functions of Reynolds number, Re, compared to the fully-developed channel value

3.6.3 Large Scale Mockup (University of Minnesota, UMN)

The UMN contribution in the second year (Phase II) began with the design of a large-scale (30 X actual size), dynamically-similar mockup of the microfabricated regenerator for testing with higher spatial and temporal resolution than afforded by the actual size regenerator. The geometry, operating conditions and instrumentation used in testing with this model are discussed in sections 5.1 and 5.2. The use of dynamic similitude was verified by agreement of flow and heat transfer measurements from the Large-Scale MockUp (LSMU) with measurements from the NASA/Sunpower oscillatory flow rig. This facility was then used to measure frictional pressure drop, time and space-resolved heat transfer rates, and the unsteady matrix-flow thermal interaction associated with jets entering the matrix from passages of adjacent heat exchangers. Details are given in sections 5.3 through 5.5.

3.6.3.1 Darcy Friction Factor

A study of the momentum equation noted that for engine-representative Valensi and Reynolds numbers, the transient term is unimportant and pressure drop measurements can be taken in steady, unidirectional flow. Such measurements led to the following friction factor correlation for the LSMU:

$$f = \frac{153}{\mathrm{Re}} + 0.127\ \mathrm{Re}^{0.01} \tag{3.5}$$

Details are given in section 5.3.3. Figure 3.15 shows the comparison of this correlation to the correlation from the NASA/Sunpower oscillatory flow test rig (eq. (3.2)). These two correlations match very well at the low end of the Reynolds number range (~100 to 200), with the LSMU correlation no more than ~15% higher, and the NASA/Sunpower correlation is about 25% higher at the high end of the Reynolds number range (~1000). The LSMU correlation may be higher for lower Re values due to the shortness of the LSMU test section. The microfabricated test section friction factor may be higher for larger Re values due to the roughness associated with the EDM cutting process, shown earlier in figure 3.7.

3.6.3.2 Heat Transfer Coefficients

Unsteady heat transfer measurements were taken in an oscillatory flow with the LSMU experimental model. Details of this test are given in section 5.5. The following direct measurements were taken: 1) the heat flux between the fluid and the metal matrix was measured for several points interior to the matrix,

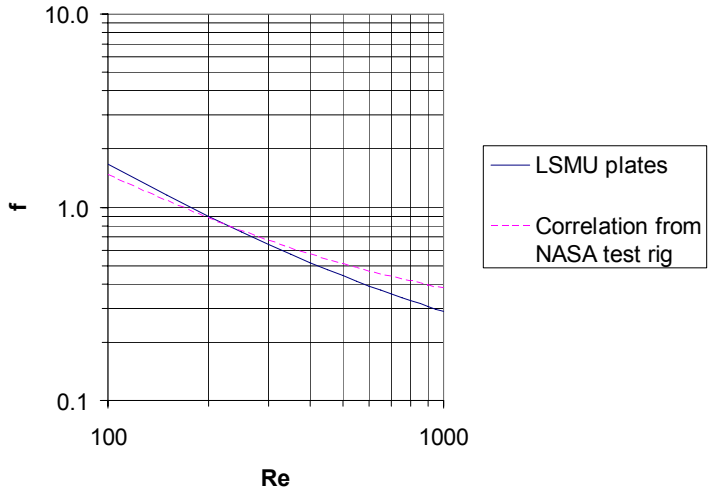

Figure 3.15.—Comparison of the Darcy friction-factor as functions of Reynolds number correlations for the LSMU and the microfabricated-actual-size involute-foil regenerators.

resolved in time within the cycle, and 2) temporally-resolved solid and fluid temperatures were taken at the location of the heat flux measurements. Thus, heat-transfer coefficient, $h = \dot{q}'' / (T_s - T_f)$ and Nusselt number, $\mathrm{Nu} = hd_h / k_f$ could be computed, resolved in space and location within the oscillation cycle. The Nusselt number relationship is complex, as discussed in section 5.5. However, when at and near the peak velocity and in the deceleration portion of the cycle, the instantaneous values compare well with values computed from a correlation developed from data taken in the NASA/Sunpower oscillatory flow experiments with the microfabricated actual-size regenerator (see NASA/Sunpower plot in fig. 5.58, from equation (3.4)). The adjusted values in table 5.6 when compared with the microfabricated-regenerator Nusselt numbers of figure 5.58, show that the actual-size regenerator values are about 20% higher than the adjusted LSMU values. It may be that the microfabricated regenerator values are higher because of the roughness shown in figure 3.7, resulting from the EDM skim cutting. Heat transfer rates between the gas and the matrix throughout the cycle agree well with values computed from the NASA/Sunpower rig correlation, as is shown and discussed in section 5.5 (see fig. 5.59).

3.6.3.3 Jet Penetration

One concern with integrating the microfabricated regenerator into the engine is the effectiveness of heat transfer on the regenerator ends where discrete jets, formed in the acceptor or rejector heat exchanger, penetrate and diffuse within the matrix while exchanging thermal energy with the matrix material. To address this, a slot jet and a round jet generator was mated to the LSMU and the thermal signatures of those jets were measured within the matrix as the jets (cold in this study) entered into and dispersed within the matrix. To supplement the thermal measurements and aid in understanding the processes, velocities were measured within the plenum between the LSMU and the jet generator, resolved in radial position and in location within the oscillation cycle. Details of this experiment are given in section 5.4. No jetting study was conducted in the NASA/Sunpower test rig but CFD computations of the LSMU experiments are under way. The computational results will be reported in the Phase III final report.

Two fundamental parameters were extracted from this study, both at the maximum-velocity location within the cycle when the jets are immerging into the matrix: 1) the depth into the matrix at which the thermal signature of an individual jet can no longer be distinguished (the “jet penetration depth”) and 2) a measure of the matrix volume fraction that resides outside of the jets over the matrix volume which

extends from the end of the matrix to the penetration depth (the "fraction of inactive material," F). Since the jets diffuse while they penetrate, F is not to be taken too literally. In fact, considerable heat transfer between the matrix and the jets occurs beyond the "edge" of the immerging jets. These two values are given in table 3.4.

TABLE 3.4—RESULTS OF THE JET PENETRATION STUDY - LSMU

Jet geometry	Penetration depth, x_p/d_h (multiples of the matrix hydraulic diameter)	"Inactive" fraction of the matrix volume, F (between the edge of the matrix and the penetration depth)	Dimensionless total volume of "inactive" matrix, $F\ x_p/d_h$ (normalized by the volume $A_j d_h$)
Round jet	13	0.47	6.1
Slot jet	10	0.69	6.9

A total volume of "inactive" matrix scaled on the volume $A_j d_h$ can be computed as: $F\ x_p/d_h$, where A_j is the cross-sectional area of the matrix attributable to each jet of the adjoining heat exchanger and d_h is the matrix hydraulic diameter. This total volume value is shown also in table 3.4.

3.6.4 Analysis Tools and CFD Results (CSU)

The microfabricated involute-foil regenerator was numerically simulated utilizing commercial CFD software (Fluent) under both steady-state and oscillatory-flow conditions. The geometry consists of a stack of disks with each disk containing involute-shaped micron-range channels, with channel flow direction perpendicular to the plane of the disk. The lateral orientation of the channels alternates from disk to disk in the flow direction. Simulations were done for both 2-D and 3-D computational domains. Steady-state simulations were performed for Reynolds numbers from 50 up to 2000 based on the channel hydraulic diameter and the mean flow velocity. Oscillatory flow simulations were conducted for maximum Reynolds number, Re_{max}, of 50 and a Valensi number, Re_{ω}, of 0.229. More details of this study are given in section 6.0.

The results of this CFD research have been validated by comparing the CFD data with the literature and recent experimental correlations obtained at UMN (LSMU, large scale, friction-factor equation 3.5) and at Sunpower (actual-scale geometry, friction-factor equation 3.2 and Nusselt number equation 3.4). The agreement between these experimental correlations and the CFD data was good.

For the steady-state 3-D simulation, both the local friction factor and the local-mean Nusselt numbers (i.e., mean value from the channel entrance to the local flow direction position) depart from the 2-D simulation values upon entering the second layer. That is where the 3-D effects become obvious and they persist as the axial coordinate advances. At the entrance of every layer, the forced reorientation of the flow results in small rises of both the friction factor and the mean Nusselt number with subsequent decrease as the flow settles into the new layer. Overall the plots of the friction factor and the mean Nusselt number tend to flatten out as the flow reaches a fully developed condition.

As for the oscillatory flow simulations in 2-D and 3-D (with 6 layers), a base case was chosen using helium as a working fluid, stainless steel for the solid material, 310 K at the hot end, 293 K at the cold end, a maximum Reynolds number, Re_{max}, of 50 and a Valensi number, Re_{ω}, of 0.229. Different parameters were examined (utilizing the 2-D model) to study the effects of changing: 1) the oscillation amplitude and frequency, 2) the Thermal Contact Resistance (TCR) between layers, and 3) the solid material. The effects of these parameters on the total regenerator heat loss (convection and conduction) were documented and are expected to be a useful tool for further development of Stirling engine regenerators. The baseline case with zero TCR, i.e., perfect thermal contact between layers, showed total losses of 2.896 W which was split between enthalpy losses (1.722 W) and conduction losses (1.174 W). As the TCR changed to infinity (perfect insulation between layers) the total losses decreased by 14%. This came about as a result of an increase in the enthalpy losses of 13.8% and a decrease in the

conduction losses by 54.7%. As we changed the solid material from stainless steel to nickel (while keeping an infinite TCR) we obtained an increase in the total loss by 3.8% due to a decrease in the enthalpy loss by 5.1% and an increase in the conduction loss by 36.3%.

CFD simulations for the experimental jet penetration study done by UMN have been postponed to Phase III. This study will include a slot jet and a round jet to examine the jet spread angle and penetration depth.

3.6.5 Analytic Support (Gedeon Associates)

3.6.5.1 Adapting the Sunpower FTB for a Microfab Regenerator

During Phase II the eventual goal of installing a microfabricated regenerator into the Sunpower FTB (frequency test bed) Stirling engine for testing was considered. Various options of increasing difficulty and cost required to adapt the engine to an involute-foil microfabricated regenerator with expected increasing levels of performance were identified.

3.6.5.1.1 Background

The Sunpower FTB Stirling convertor (engine plus linear alternator) sits in a test cell as a prototype for an Advanced Stirling Convertor (ASC) under development for NASA funded from a companion NRA program to the CSU microfab regenerator program. The FTB is a good choice for trying out a microfabricated regenerator because it is available and operates at a relatively low temperature (650 °C) compared to the ASC (850 °C). Parts are easier to make and operation does not require special high-temperature considerations. The goal is to adapt the FTB to use a microfabricated regenerator with minimal changes.

During Phase I of the CSU-NRA contract some estimates were made of the performance advantage for a space power engine using a microfabricated regenerator (see app. C). During those studies there was the luxury of completely optimizing the engine to take advantage of the new regenerator. With the FTB, that freedom was not available. A mostly-fixed engine was available, allowing a swap-out of the random-fiber regenerator for a microfabricated regenerator and maybe a few other changes.

Here are the things Sunpower was willing to change, listed in order of increasing difficulty and cost:

1. Use either of two available heater heads, allowing two different regenerator lengths.
2. Make a new heater head allowing for an increased regenerator length, with the same outer diameter and a *new* acceptor heat-exchanger insert with increased flow resistance (to increase pressure drop for displacer tuning reasons).
3. Make a new heater head as above, but also with a different outer diameter to accommodate a "thinner" regenerator.

Sunpower requested adherence to the following constraints:

1. Keep the current displacer rod diameter so as to be able to use the existing piston/cylinder assembly for the new regenerator and thereby eliminate that experimental uncertainty.
2. Restrict the regenerator length to no more than 60 mm to avoid displacer cantilever support problems.

3.6.5.1.2 Sage 1-D Code Model

This Sage code modeling was done prior to any actual testing of the involute-foil test regenerator, so the regenerator is modeled as a simple foil-type regenerator. The material was stainless steel and foil element thickness was fixed at 15 μm. The flow gap (between involute elements) was allowed to float as an optimized variable. The solid conduction empirical multiplier *Kmult* was set to 1.0 as a conservative estimate pending a better understanding of the advantages of interrupting the solid conduction path.

In order to maintain the displacer phase angle with a fixed rod, the overall flow resistance of the rejector + regenerator + acceptor must be maintained. So the lower flow resistance of the microfabricated

regenerator compared to the random fiber regenerator it replaces could not be used to full advantage. The model maintained flow resistance indirectly by imposing the constraint that the excess displacer drive power (*Wdis*) be zero. The displacer was constrained by a "displacer driver" component and *Wdis* is the power it requires to move the displacer at the desired amplitude and phase. To satisfy this constraint the model optimized the regenerator flow gap and, sometimes, the acceptor flow passage dimension. When the acceptor flow passage dimension was optimized there was enough slack to also maximize efficiency. Otherwise the regenerator flow gap was used only to meet the tuning constraint without regard to efficiency.

3.6.5.1.3 Performance Estimates

The simulated performances for the microfabricated regenerator with the above progressive FTB accommodations are given in table 3.5, compared to the baseline random fiber performance (via the ratio of the improved microfab efficiency to that of the baseline).

TABLE 3.5—SIMULATED PERFORMANCE RESULTS

	W_{pv}, W	Q_{in}, W	PV efficiency	Efficiency/ baseline
Baseline random-fiber regenerator	128.0	303.7	0.422	—
Microfab—existing head, L_{regen} = short*	123.8	292.1	0.424	**1.005**
Microfab—existing head, L_{regen} = long*	113.2	260.8	0.434	**1.028**
Microfab—new head, same OD, L_{regen} = 60 mm, smaller acceptor passages	101.7	227.5	0.447	**1.059**
Microfab—new head, smaller OD, L_{regen} = 60 mm, smaller acceptor passages	110.7	247.2	0.448	**1.062**

*Short and long regenerators refer to two different dimensions allowed for design and not available for publication at this stage of the work.

The final efficiency value falls in the range of the 6 to 9% efficiency gain projected earlier (see app. C). Most of the efficiency gain is achieved by making a new heater head, slightly longer but of the same diameter. The added bother of reducing heater head diameter hardly increases efficiency at all, though it does increase power level somewhat.

The higher efficiency values of the last two microfabrication cases (table 3.5) are a result of the acceptor taking the burden of providing the additional pumping dissipation to maintain the displacer phase angle, freeing the regenerator gap to optimize for efficiency. The acceptor is the best place to put the added dissipation because at the hot temperature it should, in theory, be partially recoverable. The extra dissipation subtracts from the available PV power, at-least somewhat, and it would be better to reduce the displacer rod diameter instead. But that is not allowed in the current FTB and will have to wait until the future when a space-power convertor might be designed from the ground up to employ a microfabricated regenerator.

3.6.5.1.4 Regenerator Dimensions

The regenerator flow gaps for the microfab cases of table 3.5 are given in table 3.6.

TABLE 3.6—FLOW-GAP VALUES

	Flow gap, μm
Microfab—existing head, L_{regen} = short*	52.3
Microfab—existing head, L_{regen} = long*	58.0
Microfab—new head, same OD, L_{regen} = 60 mm, smaller acceptor passages	92.7
Microfab—new head, smaller OD, L_{regen} = 60 mm, smaller acceptor passages	91.6

*Short and long regenerators refer to two different dimensions allowed for design and not available for publication at this stage of the work.

The last two have much larger gaps (presumably much easier to make) as a result of the acceptor providing the additional damping to maintain the displacer phase angle. The overall regenerator dimensions are not included in the table to avoid revealing any proprietary FTB dimensions.

3.6.5.1.5 Recommendations

Converting a FTB to use a microfabricated regenerator is feasible and it appears that the best option is the next to the last—a new longer heater head with the same OD and a re-designed acceptor insert. It remains to be worked out exactly how to hold the new regenerator in place and what measures will be required at either end to distribute the flow from the acceptor and rejector.

3.6.5.2 Radiation-Loss Theoretical Analysis

During the Phase I final review an evaluation of the effects of radiation through the regenerator was requested. This was done by a simplified theoretical analysis of radiation down a long thin tube (the results were later confirmed by a CSU CFD analysis). A long thin tube overestimates radiation through a stack of involute-foil disks because there is a clear sight path down the whole length of the tube. In the actual involute-foil stack it is impossible to see any light passing through it when held up to a bright light source.

Looking down a long thin tube—eye focused to the far end—one sees mostly wall. So, too, radiation emitted at the hot end of such a tube sees mostly wall, where it is absorbed before it gets too far, provided those walls are diffuse gray absorbing surfaces (not highly reflecting). Emitted radiation gets about 3.5 tube diameters before 99% of it hits the tube wall (easy to work out by comparing the surface area of a hemisphere with radius 3.5 tube diameters with that of the tube cross-section area). Some fraction of that radiation is reflected but it too cannot get very far before multiple reflections eventually absorb practically all of it. The walls of a long thin diffuse-gray tube act like a sort of distributed radiation shield.

To the extent that the microfabricated regenerator (stack of involute-foil disks) looks like a bundle of long thin tubes it will also block radiation transmission. The analogy is not too far fetched. A view at the hot end of the regenerator looking toward the cold shows mostly foil surfaces, except for a tiny view angle where the cold end is visible. So, a quantitative estimate of radiation loss down a long thin tube can serve as a basis for estimating the radiation loss in a microfab regenerator. Perhaps it is not too unreasonable to substitute passage hydraulic diameter for tube diameter.

The remainder of this section considers the limiting case of diffuse *black* regenerator walls, which is arguably a reasonable approximation for long narrow passages. The results are summarized in table 3.7 which shows that radiation loss under these assumptions is negligible compared to other regenerator losses:

TABLE 3.7—RELATIVE LOSS ESTIMATES FOR A 100 W CLASS SPACE-POWER STIRLING REGENERATOR

Hot temperature	850 °C (1120 K)
Cold temperature	100 °C (370 K)
Passage aspect ratio L/d	300
Passage wall emissivity ε	0.5
Radiation flow at cold end	10 mW
Radiation flow at hot end	200 mW
Time-average enthalpy flow	13,000 mW
Solid conduction	7,000 mW

3.6.5.2.1 Radiation in Long Thin Tube

A tube of radius a (diameter d) and length L, as shown in figure 3.16, was used in this study. Coordinate $\xi = x/d$ is the dimensionless axial coordinate. The tube has open ends at $\xi = 0$ and $\xi_L = L/d$. The tube wall is presumed to be a diffuse black surface (emissivity $\varepsilon = 1$) with a fixed wall temperature $T(\xi)$ that varies linearly with ξ between T_0 and T_L. The tube terminates in black cavities at the two ends at temperatures T_0 and T_L. Of interest is the radiation heat flux $q(\xi)$ through the tube section $A(\xi)$.

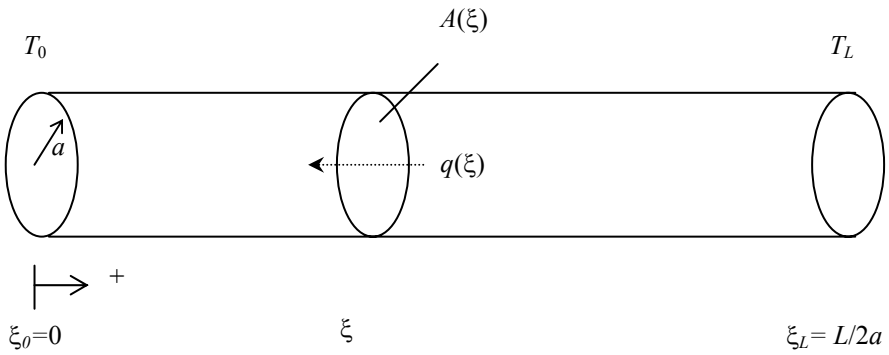

Figure 3.16.—Schematic of the tube used to study radiation heat transfer in the regenerator.

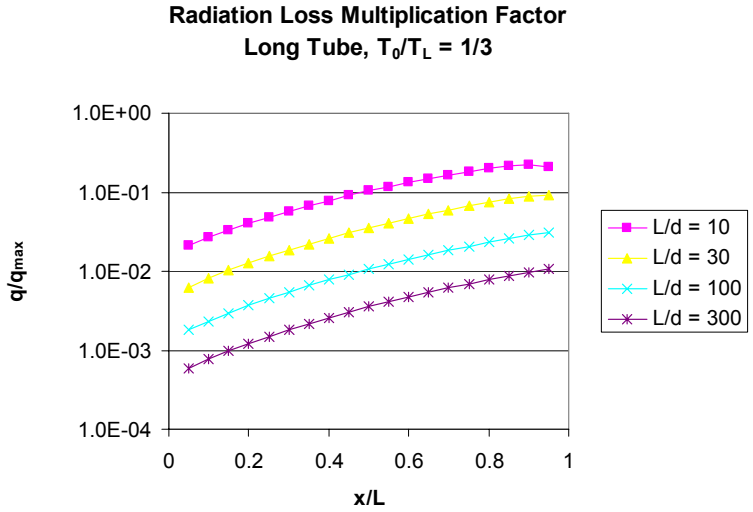

Figure 3.17—Radiation loss estimates.

If radiation flux $q(\xi)$ is small compared to the helium time-average enthalpy flux and solid thermal conduction flux down the regenerator (when installed in a running engine) then it will have a small effect on the usual regenerator temperature distribution and the assumption of a linear temperature distribution is valid.

The radiation flux depends on position and can be represented as a fraction R of the worst-case radiation flux:

$$q(\xi) = R\, q_{\max} \tag{3.6}$$

Where $q_{\max}$ is the black-body radiation exchange between two parallel planes at temperatures T_0 and T_L (flux limit as tube length approaches zero):

$$q_{\max} = -\sigma\left(T_L^4 - T_0^4\right) \tag{3.7}$$

Constant σ is the Stefan-Boltzmann constant 5.729E-8 W/(m^2 K^4).

In general, multiplication factor R depends on the position ξ, temperature ratio T_0/T_L and tube aspect ratio L/d. Numerical calculation in a custom-written Delphi Pascal program for the representative case T_0/T_L = 1/3 (typical for Stirling engine) and various values of L/d gave the results shown in figure 3.17. L/d_f for the involute-foil regenerator is ~350 for a total regenerator length of 60 mm. In figure 3.17, the cold end is at x/L = 0.0 .

3.6.5.2.2 Justifying the Black-Wall Assumption

Even though the actual wall emissivity for a metallic regenerator material is probably closer to $\varepsilon = 0.5$ than $\varepsilon = 1$, multiple reflections in a long thin tube render the apparent tube-wall emissivity near one at any location. The apparent emissivity is the value ε_a for which the total outgoing radiation (emitted + reflected) is $\varepsilon_a \sigma T^4(\xi)$. Figure 8.9 on p. 257 of (Siegel and Howell, 1981) shows that the apparent wall emissivity for an isothermal tube approaches 1 within a few diameters of the tube entrance, regardless of actual emissivity. In particular, for actual emissivity $\varepsilon = 0.5$ the apparent emissivity is nearly 1 at a distance of only 2 tube diameters from the entrance. For the present analysis this means that it is not unreasonable to consider the tube walls to be black surfaces, which greatly simplifies the analysis because reflected radiation need not be considered. This black-wall assumption is arguably valid so long as the wall temperature does not change much over a distance of several diameters, which implies that the local radiation environment is similar to that of an isothermal tube.

3.6.5.2.3 Applied to a Regenerator

For the temperatures of a space-power engine, T_L might be on the order of 1120 K and T_0 might be on the order of 370 K ($T_L/3$) so the worst-case parallel-plate radiation heat flux $q_{\max}$ works out to 8.9 W/cm^2. A regenerator void frontal area (corresponding to the tube interior of the above analysis) for a 100 W class Stirling engine is on the order of 2 cm^2 (see app. C). So the total worst-case radiation flow would be about 18 W. The actual radiation flow down the regenerator would be reduced by a fraction correspond to the curve $R(\xi)$ in the above plot for $L/d = 300$. The aspect ratio for our current microfab regenerator design (based on length to hydraulic-diameter ratio) is about 350 for a total regenerator length of 60 mm.

The conclusion is that the radiation heat flow down the regenerator would be very small. Near the cold end about 6×10^{-4} of 18 W, or about 10 mW. Near the hot end about 1×10^{-2} of 18 W, or about 200 mW. In terms of the time average enthalpy flux (13 W) and the solid thermal conduction (7 W) the radiation loss is smaller by two orders of magnitude. For detailed derivation of the radiation heat transfer loss see appendix A.

3.6.5.3 Solid Thermal Conduction in Segmented Foil Regenerators

One of the selling points for our stacked-disk design was that it interrupts the solid thermal conduction path from one end to the other. This section explores this statement in detail and finds that the truth is more complicated and depends on disk thickness, solid thermal conductivity and also the properties and Reynolds number of the gas flowing through it.

An analysis of segmented foil regenerators shows a complicated reality. In one extreme, coupling between the regenerator gas and solid bridges the contact resistance between segments, producing solid conduction in individual segments approaching that of a continuous foil regenerator. In the other extreme, high thermal conduction within each segment produces a stair-step solid temperature distribution with distinct temperature gaps between segments, increasing the net enthalpy flow down the regenerator. In either case solid conduction shows up as a regenerator thermal loss. The Mezzo regenerator lies closer to the second extreme, which is likely the cause of the reduced figure of merit at low Reynolds numbers in recent testing. This raises concerns about using high-conductivity materials, such as the pure metals (Nickel, Gold and Platinum) favored by the current electroplating fabrication process (LiGA). If such materials are used, the optimal regenerator disks need to be shorter and have thinner walls than disks made of lower conductivity materials

3.6.5.3.1 Average Solid Conduction

Equation (3.8) is a simple approximation for the average solid conduction in a segmented foil regenerator (Symbol definitions for this section are shown in table 3.8)

$$\frac{\overline{Q}_s}{Q_{s0}} \approx \frac{1}{1+2\dfrac{(1-\beta)}{\beta}\dfrac{k_s}{k}\dfrac{1}{F}} \tag{3.8}$$

where F is the not-quite so simple factor:

$$F = \langle \mathrm{Re\ Pr} \rangle \frac{L_c}{D_h}\left(1 - e^{-\frac{2\mathrm{Nu}}{\langle \mathrm{Re\ Pr} \rangle}\frac{L_c}{D_h}}\right)^2 \tag{3.9}$$

TABLE 3.8—SYMBOL DEFINITIONS FOR THIS SECTION (3.6.5.3)

$\overline{Q}_s$	Spatial average solid conduction for segmented foil regenerator
Q_{s0}	Conduction for continuous foil regenerator with same solid area
β	Regenerator porosity (void fraction)
D_h	Hydraulic diameter (twice flow gap)
L_c	Foil segment length (disk thickness of Mezzo design)
k_s	Solid thermal conductivity
K	Gas thermal conductivity
< Re Pr >	Time averaged Re Pr product
Re	Reynolds number based on hydraulic diameter
Pr	Prandtl number
Nu	Nusselt number (hD_h / k)

The physics behind this approximation is that heat-transfer coupling between the gas and solid tends to short-circuit the contact resistance between solid segments, reducing the temperature gap between segment endpoints. This imposes temperature gradients within the segments and therefore thermal conduction. The thermal conduction varies along the segment length but the average value is of interest. The details are derived in the following subsections of this section 3.6.5.3.

The point in looking at average solid conduction is that when it is high—approaching that of a continuous-foil matrix—then any contact resistance between segments is doing no good. Is that the case for the Mezzo regenerator? Table 3.9 shows some key values for that regenerator:

TABLE 3.9—KEY VALUES FOR MEZZO INVOLUTE-FOIL REGENERATOR

β	0.84
L_c/D_h	250/2(85) = 1.5
k_s/k	86/0.18 = 480

For these values the average solid conduction ratio of equation (3.8) reduces to equation (3.10).

$$\frac{\overline{Q}_s}{Q_{s0}} \approx \frac{1}{1+\dfrac{180}{F}} \tag{3.10}$$

The factor F depends mainly on Reynolds number and relative segment length L_c/D_h and is plotted in figure 3.18 for the case of Prandtl number, Pr = 0.7 and Nusselt number, Nu = 8.23 (developed flow between parallel plates, constant heat flux boundary condition).

As relative segment length L_c/D_h increases, F grows quickly so that solid conduction approaches that of a continuous-foil regenerator. For the Mezzo regenerator with L_c/D_h = 1.5, the F factor peaks at about 15, at a Reynolds number of about 30, which means that solid conduction is never more than about 8% of continuous foil conduction, according to equation (3.9). In other words the Mezzo regenerator segments

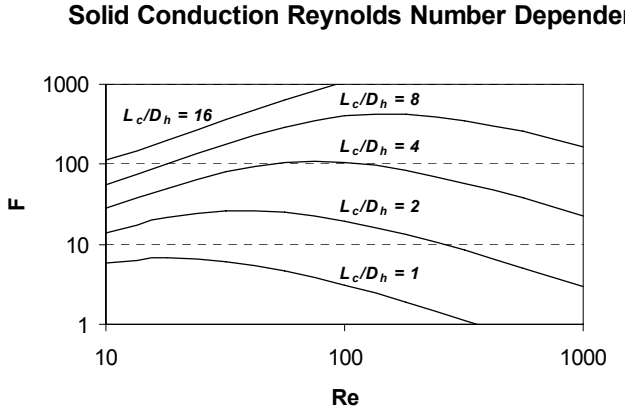

Figure 3.18.—Factor *F* of equation (3.9) as a function of Reynolds number at various segment lengths L_c/D_h, for Pr = 0.7 and Nu = 8.23.

never have more than about 8% the regenerator-average temperature gradient. Each segment is relatively isothermal. The high contact resistance does indeed block most of the solid thermal conduction.

3.6.5.3.2 Price of Localized Solid Conduction

But isothermal regenerator segments are not without their cost. A stair-step solid temperature profile (piecewise constant) results in a minimum enthalpy flow per unit flow area of

$$h_{\min} = -c_p \rho \langle u \rangle \Delta T_g \tag{3.11}$$

where $<u>$ is the time-averaged flow velocity (section-mean, absolute value) and ΔT_g is the solid temperature difference between successive regenerator segments (see fig. 3.19). This is easy to understand by considering a regenerator cross-section between segments (disks) where the overall regenerator temperature is increasing in the positive direction. For positive flow the gas temperature is always lower than the solid temperature of the negative segment because it is heating up overall. For negative flow the gas temperature is always higher than the solid temperature of the positive segment. So the time-average difference in gas temperatures passing through the gap must be at least ΔT_g. The minimum enthalpy flow can be put in dimensionless form by dividing by molecular gas conduction $-k\,dT/dx$. A key observation is that the overall regenerator temperature gradient dT/dx is just $\Delta T_g/L_c$ for a stair-step temperature distribution. After a bit of simplification the minimum enthalpy flow for a stair-step temperature distribution reduces to

$$h_{\min} = -k \frac{dT}{dx} \langle \mathrm{Re}\,\mathrm{Pr} \rangle \frac{L_c}{D_h} \tag{3.12}$$

Compare this to the following continuous-regenerator enthalpy flow, of equation (3.12), p. 52 of the 1996 regenerator test-rig contractors report (Gedeon and Wood, 1996):

$$h = -k \frac{dT}{dx} \left\langle \frac{(\mathrm{Re}\,\mathrm{Pr})^2}{4\mathrm{Nu}} \right\rangle \tag{3.13}$$

At low Reynolds numbers the minimum enthalpy flow $h_{\min}$ dominates h while the reverse is the case at high Reynolds numbers. The Reynolds number at which the two are the same is found by equating $h_{\min}$ to h and solving. That critical Reynolds number, assuming constant Nusselt and Prandtl numbers, is

$$\langle \mathrm{Re} \rangle_c = \frac{4\mathrm{Nu}}{\mathrm{Pr}} \frac{L_c}{D_h} \tag{3.14}$$

Whenever Reynolds number is higher than this, the effect of the stair-step temperature distribution will be of diminishing significance. For the Mezzo regenerator $<\mathrm{Re}>_c$ is about 50, where the value of $h_{\min}$ from equation (3.12) is about 50 times higher than the helium static conduction loss. If the regenerator were continuous foil the solid conduction loss would be a factor k_s/k $(1-\beta)/\beta$ higher than helium static conduction (conductivity ratio times area ratio) or about 91 times higher. So the segment-localized solid conduction produces an adverse helium enthalpy flow that is nearly as bad as if the solid conduction passed unimpeded by contact resistance through the entire regenerator.

This coupling of localized solid conduction to helium enthalpy flow likely explains why the experimental test results for the Mezzo regenerator showed a suspiciously low Nusselt number below Re = 100 (as in fig. 3.14). The derived Nusselt number was forced to account for the $h_{\min}$ enthalpy flow based on a regenerator model that did not assume a stair-step temperature distribution. High solid conduction was at the root of the problem, in spite of the high contact resistance between regenerator disks. Had the solid conduction been lower, then the temperature gaps would have been smaller and $h_{\min}$ would have been smaller.

What might be done about this problem? The obvious solution is to make the regenerator disks from lower conductivity material. The ratio of solid to gas conductivity k_s/k is rather high for a nickel regenerator, or about 5 times that for a stainless-steel regenerator. As a rule of thumb, alloys have lower thermal conductivity than pure metals. The following table (table 3.10) gives some idea of the solid conduction losses of pure-metal regenerators compared to a stainless-steel regenerator.

TABLE 3.10—SOLID CONDUCTION

Material	Thermal conductivity near room temperature* (W/m C)	Ratio relative to 316 stainless steel
316 stainless steel	16	1
platinum	73	4.6
nickel	86	5.4
gold	300	19

* Source: 1985 Material Selector Handbook, Materials Engineering

Let's not be too pessimistic here. The good figure-of-merit measured for the nickel regenerator includes the effects of solid conduction loss. But the involute-foil would do even better in the future with a lower conductivity material or thinner walls, especially at lower Reynolds numbers where the temperature-gap effect dominates. The Mezzo regenerator figure of merit peaked at a Reynolds number of about 200 whereas most Stirling engine optimizations performed in the past prefer Reynolds number amplitudes on the order of 100 or lower.

3.6.5.3.3 Solid Conduction Derivation

The solid temperature in a segmented-foil regenerator lies somewhere between the two extremes illustrated in figure 3.19—between a piecewise constant stair-step distribution and a continuous distribution. The first case corresponds to static-conduction in vacuum with very high contact resistance between segments. There is a temperature gap ΔT_g between segments. In the second case the gas is in very good thermal contact with the solid and has sufficient heat capacity to dump any required amount of heat in the segment entry regions so as to eliminate the temperature discontinuities.

The reality is somewhere between the two. That reality looks something like the illustrations in figure 3.20 which shows the gas and solid temperature distributions (time averages) for the middle two segments of a 6 segment (shorter) segmented regenerator. The solutions were generated by a 1-D Sage-code simulation, as discussed in detail later. Gas temperatures are averaged over the positive and negative flow half-cycles individually. Without time averaging, the temporal temperature variations (due to finite solid heat capacity) would appear significant at this scale, but they occur roughly 90° out of

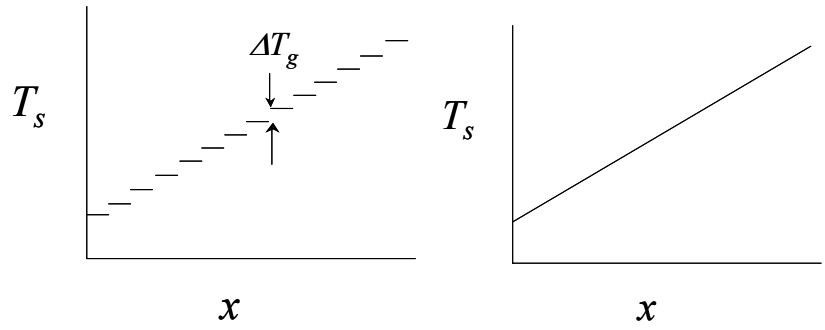

Figure 3.19.—Extreme limiting cases for solid temperature distribution in a segmented foil regenerator.

phase with the mass flow rate; so they do not affect the net enthalpy flow. The upper illustration shows a solution for a segmented regenerator with the same properties as the involute-foil regenerator (250 μm thick), except with stainless-steel solid material in order to better show the solid temperature variation. The lower illustration is for a stainless-steel regenerator with 3x longer segments, corresponding to 750 μm thick disks, and a higher Reynolds number, where the solid temperature gradient increases to about 60% of the regenerator average.

In any case the average solid conduction within a segment is proportional to the average solid temperature gradient, which may be written $(\Delta T_m - \Delta T_g)/L_c$, where ΔT_m is the temperature difference between neighboring segment centers, ΔT_g is the temperature gap between neighboring segment endpoints and L_c is the segment length. The average solid conduction is then the product of solid conductivity k_s, solid cross-section area A_s and the average temperature gradient:

$$\overline{Q_s} = -k_s A_s \frac{\Delta T_m - \Delta T_g}{L_c} \tag{3.15}$$

The solid temperature gap ΔT_g depends on the overall energy balance which can be roughly formulated in terms of a control volume between the beginning of a regenerator segment (left) and its middle (right), as shown in figure 3.21.

The energy balance is formulated in terms of the time-average enthalpy flow H carried by the gas and the axial solid conduction Q_s. At the left boundary (segment endpoint) these values are H_e and zero, respectively (zero solid conduction because of presumed high contact resistance between segments). At the right boundary (mid segment) the values are H_c and Q_{sc}. The half-segment energy balance may therefore be written as in the following equation (3.16):

$$H_e = H_c + Q_{sc} \tag{3.16}$$

The heat transfer q between gas and solid, shown in figure 3.21, is not part of the energy balance because both gas and solid are included together and what leaves one enters the other.

The essential idea is that the inter-segment temperature gap ΔT_g results in an increased net enthalpy flow at the segment entrance compared to the equilibrium value deep within the segment after the gas has had time to drop its extra heat to the solid. For a long segment the increased enthalpy flow is $-cp < \dot{m} > \Delta T_g$, where $< \dot{m} >$ is the time-averaged absolute mass flow rate. For a short segment the increase is not as much. In a section of any length the difference in net gas enthalpy flow between the segment end and its midpoint is approximately:

$$H_e - H_c \approx -c_p \langle \dot{m} \rangle \Delta T_g \left(1 - e^{-A/2}\right)^2 \tag{3.17}$$

where the extra factor $(1 - e^{-A/2})$ is derived later under the sub-title, "Steady Heat Transfer Solution," with A given by equation (3.23).

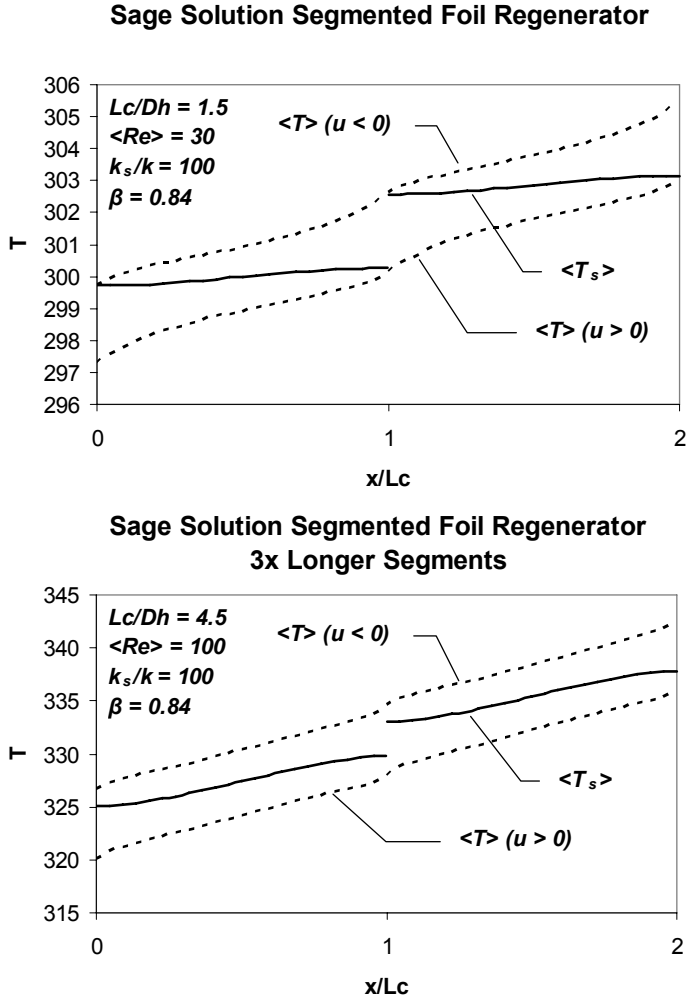

Figure 3.20.—Time-average solid- and gas-temperature distributions for the middle-two segments of a 6-segment foil regenerator. Top: 250 μm long (shorter) segments, Bottom: 750 μm long (longer) segments.

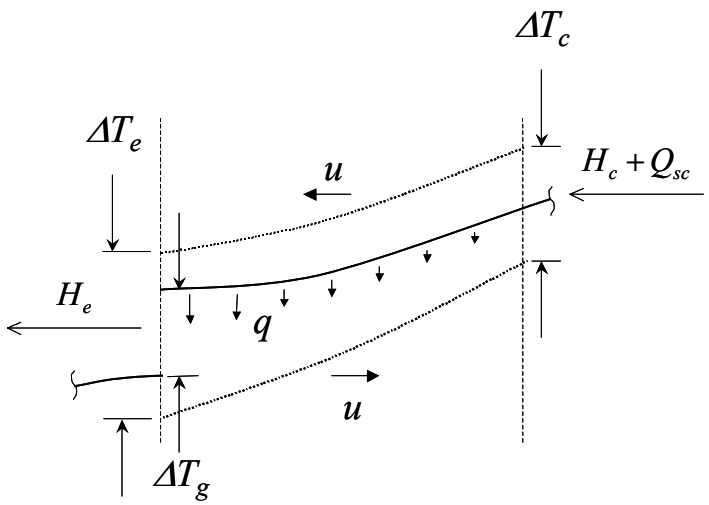

Figure 3.21.—Energy balance between segment end (left) and center (right), bounded by vertical dotted lines. The solid curve represents time-average solid temperature. The dotted curves above and below represent gas temperatures time-averaged separately for positive and negative flow directions.

The dumping of heat from the gas to the solid results in solid conduction that varies smoothly from zero at the segment endpoint to a maximum at the midpoint. If the segment is not too long then it is reasonable to assume that the average solid conduction is halfway between the endpoint and midpoint values. In other words:

$$Q_{sc} = 2\overline{Q}_s \tag{3.18}$$

In terms of the above simplifications the energy balance can be written as in equation (3.19):

$$-c_p \langle \dot{m} \rangle \Delta T_g \left(1 - e^{-A/2}\right)^2 \approx 2\overline{Q}_s \tag{3.19}$$

Solving for ΔT_g and substituting into equation (3.15) gives the average solid heat flux in the form

$$\overline{Q}_s \approx k_s A_s \frac{\Delta T_m}{L_c} - 2\frac{k_s A_s}{L_c} \frac{1}{c_p \langle \dot{m} \rangle \left(1 - e^{-A/2}\right)^2} \overline{Q}_s \tag{3. 20}$$

The first term on the right is just the conduction Q_{s0} for a continuous foil with the same solid cross section and boundary temperatures. The second term contains several factors that can be arranged into more standard dimensionless groups. Solving for $\overline{Q}_s$ the result is equation (3.8), given near the beginning of this section.

The average segmented regenerator conduction approaches the continuous foil conduction as the term $2\frac{(1-\beta)}{\beta}\frac{k_s}{k}\frac{1}{F}$ of equation (3.8) approaches zero, which can happen for a number of reasons. For example, high porosity β (thin foil), low solid conductivity k_s, long segment length L_c, or low Reynolds

number. On the other hand the average segmented regenerator conduction approaches zero as that same term approaches infinity, which happens for the opposite reasons.

3.6.5.3.4 Sage Models

The illustrations in figure 3.20 were the result of modeling individual segments of a foil regenerator using the Sage code. It would be very awkward and time consuming to model a total regenerator this way (consisting of hundreds of segments) but it is not too difficult to model, say, a 6-segment regenerator in order to get an idea of what is going on. The Sage model illustrated in the following figure 3.22 does just that.

This Sage model is equivalent to the NASA/Sunpower regenerator test-rig containing a rather short, 6-disk, involute-foil regenerator. Each canister of the model contains a simulation of a single involute-foil regenerator disk, identical to one fabricated by Mezzo except made of stainless steel instead of nickel. The reason for stainless steel is because its lower thermal conductivity results in a higher solid temperature variation which shows up better on plots. The regenerator segments are inter-connected by gas-flows (including gas thermal conduction continuity) but the solid domains are not connected, corresponding to high contact resistance between disks.

Middle segments A and B, in figure 3.22, are the segments of main interest (whose solutions are plotted in fig. 3.20) with the "buffer" segments on each side included to give some opportunity for the temperature solutions to develop to their equilibrium (spatially periodic) values.

3.6.5.3.5 Baseline Sage Model

The working gas is helium at 25 bar charge pressure and the driving piston motion is sinusoidal with amplitude adjusted to produce an average Reynolds number of 30 in the regenerator segments. This Reynolds number gives the largest *F* factor according to figure 3.18. The endpoint boundary temperatures are adjusted so the temperature difference between segments is about 2.5° corresponding to about what it would be in a realistic Stirling-engine regenerator (e.g., 800 °C temperature difference over 320 disks). The segment temperatures range from about 293 to 308 K, so the model corresponds to a short section near the cold end of the regenerator.

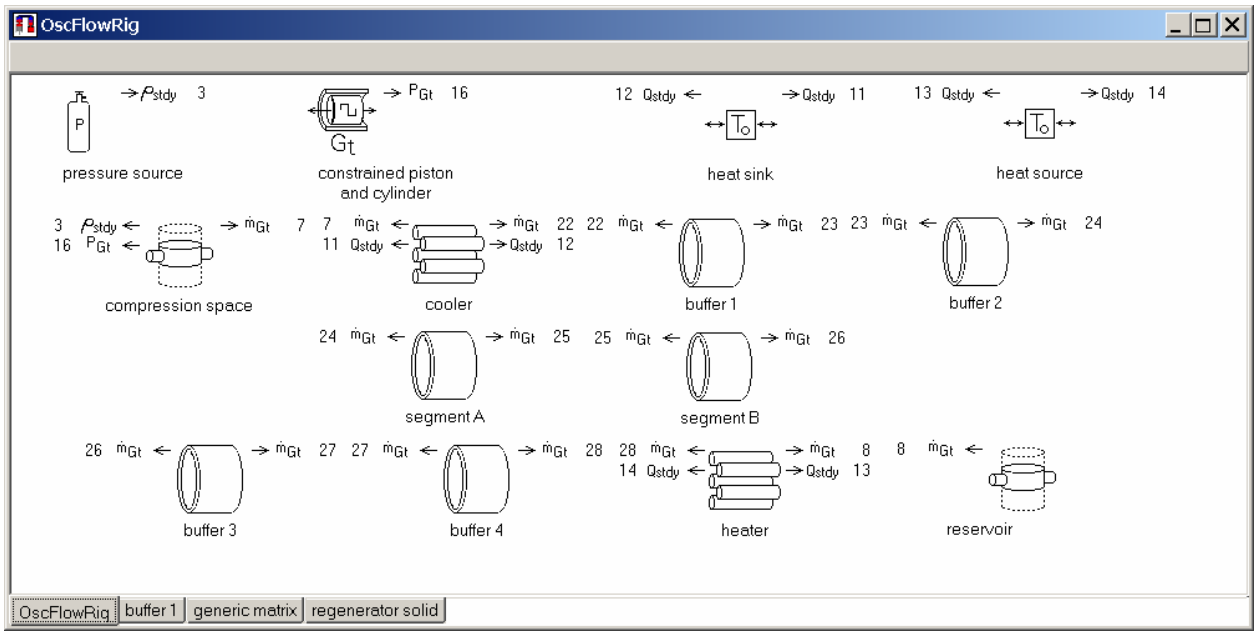

Figure 3.22.—Sage model diagram for 6-segment regenerator.

The Nusselt number in each segment is set to the constant value 8.23, corresponding to developed laminar flow between parallel plates (constant heat-flux boundary condition). This is the most unrealistic part of the model since it neglects the increased Nusselt number in the developing-flow region, which is arguably the entire section. But the intent of the model is only to get a rough idea of what is going on for purposes of validating the simplified theory derived in this memo. It does not make sense to use the Nusselt number derived from recent testing of the Mezzo regenerator because that Nusselt number applies to the regenerator as a whole and not to individual segments of the detailed model.

3.6.5.3.6 Longer Segments

The baseline model is not very satisfying from an academic viewpoint because there is not much solid temperature variation within segments. This can be remedied by increasing the segment length by a factor of 3, producing a ratio $L_c/D_h = 4.5$. To keep the same overall temperature gradient the temperature difference between segments is also increased by a factor of 3. By increasing the average Reynolds number to 100 (increasing charge pressure and stroke) the F factor of figure 3.18 is roughly at its maximum value of about 100 and the average temperature of the solid should be about 70% of the regenerator average according to equation (3.8). That is not too far off from the 60% of the Sage solution shown in the lower illustration of figure 3.20.

3.6.5.3.7 Steady Heat Transfer Solution

At the heart of the preceding solid conduction derivation is the energy balance in a single segment of the regenerator. That energy balance is the result of a simplified steady-state solution for heat transfer between a solid segment of length L_c with a time-invariant linear temperature distribution $T_s(x) = mx$ and two steady gas streams of mass-velocities $\pm\rho u$, as illustrated in figure 3.23.

The governing equation, equation (3.21), is a simplified energy equation for incompressible, steady flow, considering only heat transfer to the solid:

$$\frac{dT}{dx} = -\frac{hs}{c_p \rho u}\left(T - T_x\right) \tag{3.21}$$

In figure 3.23, the gas temperature solution for positive directed flow is denoted T_+ and the solution for negative flow T_-. The boundary condition is that there is a temperature difference ΔT_0 between the gas and solid at the negative end for T_+ and the positive end for T_-.

Of interest is the temperature difference $T_- - T_+$ at either entrance, denoted ΔT_e, compared to the temperature difference at the segment midpoint, denoted ΔT_c. That temperature difference determines the amount of heat transfer to or from the solid between the segment end and midpoint. Skipping all the details, the final result is:

$$\Delta T_e - \Delta T_c = \left(\Delta T_0 + \frac{mL_c}{A}\right)\left(1 - e^{-A/2}\right)^2 \tag{3.22}$$

where A is:

$$A = \frac{4\mathrm{Nu}}{\mathrm{Re}\,\mathrm{Pr}}\frac{L_c}{D_h} \tag{3.23}$$

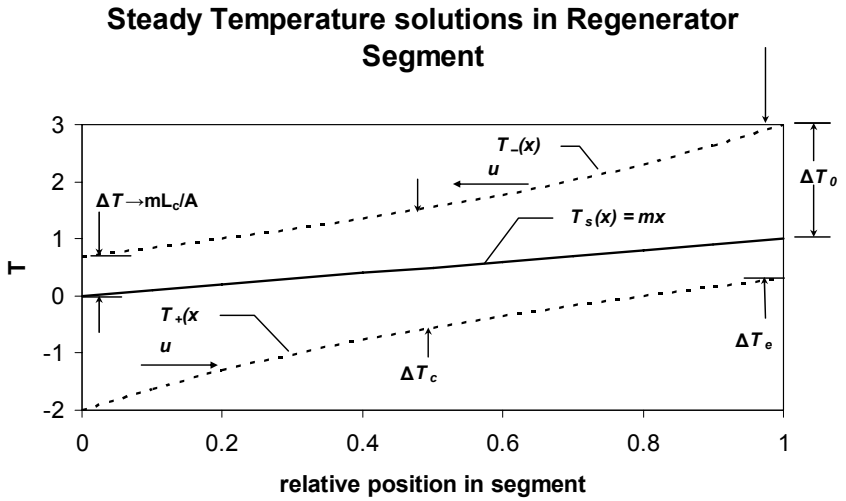

Figure 3.23.—Steady-flow gas-temperature solutions for regenerator solid segment with linear temperature distribution.

The asymptotic temperature difference $T–T_s$ for a long section is just $\pm mL_c/A$, depending on the flow direction. In that case the first factor on the right in equation (3.22) is the total gas temperature change from section entrance to exit, which is the same as the solid temperature difference ΔT_g between regenerator segments. Making this approximation regardless of segment length results in the following approximation, equation (3.24), for the change in net gas enthalpy flux (per unit flow area) between the ends and middle of a regenerator segment:

$$h_e - h_c \approx -c_p \rho |u| \Delta T_g \left(1 - e^{-A/2}\right)^2 \tag{3.24}$$

This is essentially the approximation used in energy balance equation (3.17). In making the leap from steady flow to sinusoidal flow the factor $|u|$ appears in equation (3.17) in the form of the time-average absolute mass flow rate, the time variation of the factor $(1–e^{-A/2})$ is ignored and A is evaluated at the mean Reynolds number.

3.6.6 Structural Analysis of Microfabricated Involute-Foil Regenerators (Infinia)

Finite element analysis of the microfabricated involute-foil regenerator showed that the regenerator has very high average axial direction stiffness 6.5×10^9 N/m (3.75×10^7 lb/in.). Without any radial side disturbance, the stress level was much lower than the material yielding strength. If a radial side disturbance such as misalignment is localized in a small area, the Von Mises stress is beyond the material yielding strength and permanent deformation could occur in that area, which may decrease the Stirling efficiency. In order to prevent local permanent deformation, the radial side load must be small, or the disturbance area must be large.

In summary, the proposed microfabricated involute-foil regenerator has high axial stiffness. The stress level is sensitive to the radial side disturbance, which therefore requires special cautions and an appropriate process for installation to prevent lateral permanent deformation.

The structural analysis is more thoroughly discussed in section 7.0.

3.7 Summary of Expected Benefits of Segmented-Involute-Foil Regenerators

The power conversion efficiency obtained with this new regenerator is estimated to show a 6 to 9% overall improvement based on calculations for the Sunpower ASC engine. The specific power (We/kg) will be directly proportional to the efficiency. As for lifetime and reliability, the microfabricated regenerator has the potential to remove any concerns about stray fibers, as may result from use of random-fiber or wire-screen matrices. An estimate of development risk is "medium" since the manufacturing viability has been established but the concept has not yet been tested in an engine. However, an involute-foil-layered regenerator has been very successfully tested in the NASA/Sunpower oscillating-flow test rig (with results shown in fig. 3.9). And involute-foil regenerator microfabrication is currently underway for testing in an engine during the Phase III effort.

4.0 Mezzo Microfabrication Process

4.1 Background

This section of the report focuses on the contributions of International Mezzo Technologies. One important reason Mezzo was selected as the subcontractor for this project was its expertise with the LiGA micromachining process and its investment and commitment towards combining the advantages of LiGA with Electric Discharge Machining (EDM). The combination of LiGA-EDM theoretically provides a means to fabricate high aspect ratio micro features normally associated with the LiGA process, out of any conducting material.

The initial research plan involved Mezzo using the LiGA process to fabricate well-defined, high-aspect-ratio EDM tools. These LiGA-fabricated EDM tools would then be used to make the micromachined regenerator parts from materials with the desired high temperature properties and low thermal conductivity (stainless steel, Inconel, etc.). EDM tools were fabricated via LiGA and efforts to EDM parts from stainless steel showed initial promise in terms of being able to produce the correct geometry, at least at shallow depths. But the process was very slow, tool wear rate was high, and it became apparent that the probability of fabricating the desired stainless-steel regenerator using LiGA-EDM with the available funding was low.

To fabricate the regenerator on schedule, Mezzo changed its manufacturing approach. The standard LiGA process was used to directly produce individual nickel regenerator components which were then assembled, sent to Cleveland State University, and subsequently tested at Sunpower. By changing its fabrication strategy, Mezzo was able to provide the regenerator for the project and Sunpower was able to experimentally verify that the involute-foil-layered regenerator geometry provided high performance. This change in plans also supported the desire to move the oscillating-flow rig testing from Phase III (year 3) to Phase II (year 2)—since available Phase III funding for this and other NRA contracts was in jeopardy. This section provides a summary of the successful effort that resulted in the manufacture via the LiGA process of the electroplated nickel regenerator that was tested by Sunpower in the oscillating-flow test rig.

4.2 LiGA-EDM

The need to change from a LiGA-EDM approach to a pure LiGA approach was initially supported by test results at Mezzo that focused on limiting overburn to what was believed to be an acceptably low 10 μm. The ramifications of this assumption will be revisited in this section of this report. Mezzo used a Mitsubishi Model EA8 die-sinker EDM machine to define features. It was found that the combination providing the lowest power and highest frequency (setting E1013) provided the best definition of micro features with a low overburn (approximately 10 μm of overburn). At this setting, a feature on the EDM LiGA tool with width 60 μm would produce a corresponding feature width of 80 μm in the material being machined. Using that setting, material removal rates have been quantified. Table 4.1 provides the material removal rate of a flat LiGA tool having electrode area 72.77 mm^2. The material removal rate of a variety

of materials was quantified. In these experiments, no piezoelectric stack was used to provide enhanced flushing. For reference it has been found that the use of the piezoelectric stack increased the allowable burn rate of erbium by a factor of three, so similar improvement might be expected with other workpiece material selections. Electrode wear, burn depth, volume removed, burn time, and removal rate were all measured and are provided in table 4.1.

TABLE 4.1—EDM RESULTS USING LiGA TOOL (AREA = 72.8 mm^2, PIEZOELECTRIC STACK OFF)

Electrode material	Workpiece material	Machine burn setting	Electrode wear, μm	Burn depth, μm	Volume removed, mm^3	Burn time, hr	Removal rate, mm^3/hr
LiGA Ni	420 SS	E1013	15	12.7	0.92	18	0.05
LiGA Ni	Titanium	E1013	38	38	2.77	24	0.115
LiGA Ni	Aluminum	E1013	5	33	2.4	18	0.133

It can be seen that the removal rate of 420 SS (stainless steel) is 0.05 mm^3/hr. To put this removal rate in perspective, the nickel involute-foil regenerator consisted of approximately 45 disks, each around 25.4 mm in diameter, each 0.25 mm thick. The total volume of the regenerator would then be 5700 mm^3. Of that volume, if the assumption is made that the overall porosity is 80%, then the volume of material to be removed is 4560 mm^3. To fabricate a similar regenerator from stainless steel, based on the material removal rate provided in table 4.1, would require 91,207 hr (10.4 years), not counting the time to change tools, etc. It is reasonable to assume that the use of the piezoelectric stack might reduce this time by a factor of two. Also, Mezzo does not use a micro EDM which allows combinations of higher frequency and lower power than does the more traditional die sinker EDM used at Mezzo. However, conversations with users of micro EDM equipment indicated that the material removal rates achieved at Mezzo were roughly comparable with typical micro EDM results. In summary, no reasonable scenario currently exists whereby, *if the overburn is to be limited to a value on the order of 10 μm*, the time to produce the CSU regenerator would be less than 1 to 2 years.

For reference, it is also worthwhile to compare the material removal rates achieved in this project with the potential material removal rates that *can* be achieved by the Mitsubishi machine at higher power. The maximum removal rate of stainless steel is approximately 2.5 in^3/hr. This corresponds to a removal rate of approximately 41,000 mm^3/hr. The material removal rate at the highest setting therefore exceeds by a factor greater than 800,000 the material removal rates associated with the Cleveland State project. However, the overburn associated with such high material removal rates is about 400 μm—far in excess of the allowable limit for the CSU involute-foil regenerator.

The reasonable question needs to be asked: Is there an intermediate acceptable balance between overburn, LiGA feature width, and material removal rate. Recently, a preliminary set of tests was performed where the power settings were increased and the material removal rate was measured as a function of overburn. The goal of the tests was to plot for a given tool geometry the overburn versus the material removal rate. The result of one test is shown in table 4.2. The LiGA tool consisted of a 500 μm-wide LiGA nickel rib. Material removal rates and overburn are shown as a function of power setting.

TABLE 4.2—MATERIAL REMOVAL RATES/ OVERBURN FOR 500 μm-WIDE LiGA FEATURE

Power setting	Electrode surface area, mm^2	Workpiece material	Volume removed, mm^3	Burn time, hr	Removal rate, mm^3/hr	Over-burn, μm	Removal rate ratio	CSU regen. burn time, yr
E1013	72.77	420 SS	0.9242	18	0.05	9	1	10
E1014	2.806	420 SS	0.2707	1.9	0.14	11.5	2.8	3.6
E1015	2.954	420 SS	0.3013	0.2	1.5	18	29.4	0.34
E1018	2.9654	420 SS	0.6026	0.09	6.7	32.5	130.5	0.07
E1019	2.9654	420 SS	0.5272	0.08	6.5		127	0.08

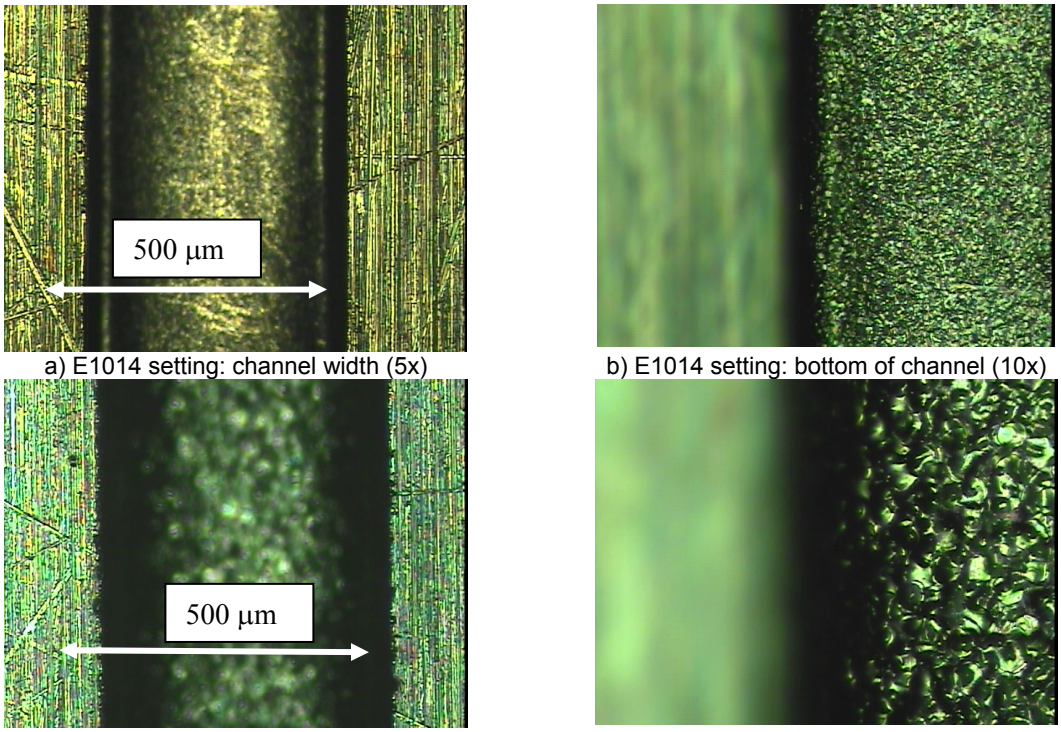

a) E1014 setting: channel width (5x)

b) E1014 setting: bottom of channel (10x)

c) E1018 setting: channel width (5x)

d) E118 setting: bottom of channel (10x)

Figure 4.1.—Comparison between power setting and surface finish of bottom (sides not seen).

Comparing settings E1013 and E1018, it is possible to deduce that if the acceptable overburn is increased from 9 to 32 μm, the removal rate increases by 100 fold. In retrospect, Mezzo probably concentrated excessively on extremely low power settings that were mandated by another LiGA-EDM project. In that project, LiGA nickel posts of diameter approximately 30 μm were used to produce features (holes) of diameter 50 μm. No more than 10 μm of overburn could be tolerated. The same assumption seems to have been made in accessing the potential of using LiGA-EDM to fabricate the CSU regenerator. In retrospect, a tool width of 40 μm, at high power setting, might produce a 100 μm-wide channel at a material removal rate that would be acceptable. Figure 4.1 shows EDM results for some of the EDM settings shown above. E1018 has a material removal rate that is 130.5/2.8 = 46.6 times faster than E1014. The recast region on the sidewall does not look bad. The RMS roughness of the bottom of the channel is yet unquantified, but higher for the E1018 setting

The conclusion of the recent EDM effort is that if extremely small overburn is necessitated, then EDM may be unacceptably slow. However, if the relationship between EDM material removal rate, overburn, and acceptable regenerator geometries is known, there may be a design space where the combination of EDM and LiGA is a useful manufacturing option that should be explored.

4.3 LiGA-Fabricated Regenerator

4.3.1 Manufacturing Process

Two closely related LiGA processes are described below. One is referred to as the “optimal” process that was originally envisioned, the other describes the process that was actually followed. The difference between the two processes is associated with unanticipated problems in the development component of the lithographic patterning of the polymethyl methacrylatete (PMMA, or Plexiglass type plastic) templates.

In an optimum LiGA exposure-development sequence, the sidewalls of the lithographically- patterned PMMA template are straight, as shown in figure 4.2a. In this project, unexpected difficulties developing the PMMA resulted in excess material removal, or “undercutting,” at the PMMA-substrate interface as

shown in figure 4.2b. This undercutting leads to a more complicated two-step electroplating process and an extra step involving EDM. Because of "undercutting" during the development process, the following process (described in fig. 4.3) was used to fabricate the regenerator components:

1. An x-ray mask was fabricated. The mask consisted of a tightly packed array of nineteen regenerator disks patterns.
2. A 250 μm-thick sheet of PMMA was bonded to a 400-series (magnetic) stainless steel substrate.
3. An x-ray lithography-electroplating process sequence was used to produce the nickel regenerator disk parts. It was found that development of the exposed PMMA caused some unexpected, undesired "undercutting" at the PMMA-substrate interface. Undercutting is associated with excess PMMA being dissolved during the development process. This fact motivated a two-part electroforming process. A copper electrodeposition step was used to fill the bottom of the features with copper to a depth equal to the height of the "undercutting" region. Beyond this point, nickel was deposited. To ensure that all these voids were completely filled with metal, the electroplating process was continued after all the features were filled, resulting in an "overplated" deposit.
4. Initially, polishing was tried to remove the overplated layer. The polishing was found to destroy parts, so an alternative process was used and found to be successful. This successful process involved attaching the conductive substrate to a magnetic chuck, orienting the substrate in the vertical plane (fig. 4.3a and b). Then a wire EDM was used to take a "skim pass" just above the non-conductive PMMA layer (fig. 4.3b). This step removed the overplated nickel. The substrate was then released from the chuck.
5. At this point, the nickel and copper electrodeposited features and the remaining PMMA was debonded from the substrate (fig. 4.3c) and the unexposed PMMA was dissolved in acetone (fig. 4.3d). The remaining nickel-copper features were again attached to the magnetic chuck with the nickel features in contact with the chuck (fig. 4.3e and f). A second EDM process was used to remove the copper and nickel in the "undercut" region. It should be noted that if the copper had completely filled the "undercut" region, the copper could have been removed with an etch, leaving only nickel parts with the desired geometry. However, it was found that insufficient copper was deposited to fill the "undercut" region. As a result, some nickel was also deposited into the "undercut" region, making it necessary to use a second EDM "skim cut" to remove both the nickel and copper within the "undercut" region. Following the second EDM "skim cut" the parts were released from the chuck (fig. 4.3g) and inspected.

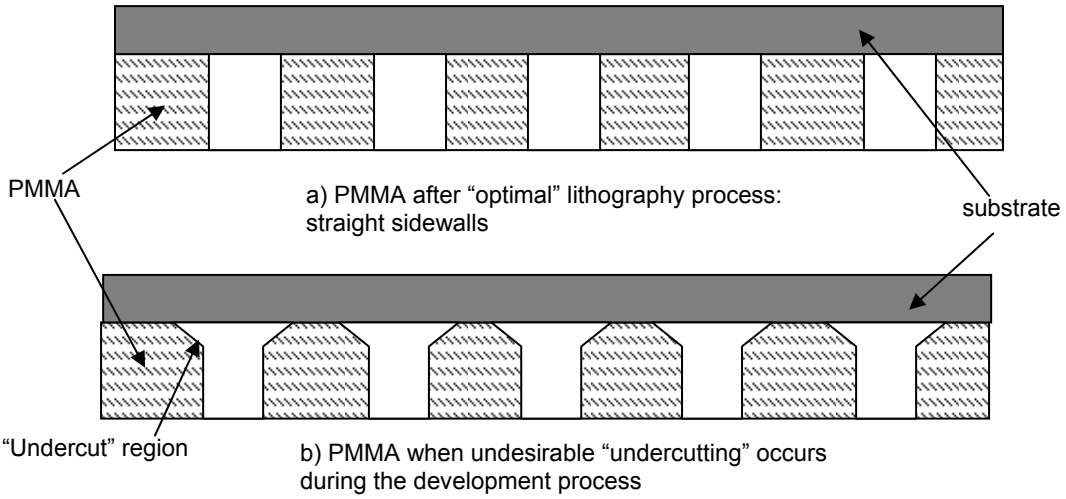

Figure 4.2—Comparison of desired and actual lithographic patterning of PMMA.

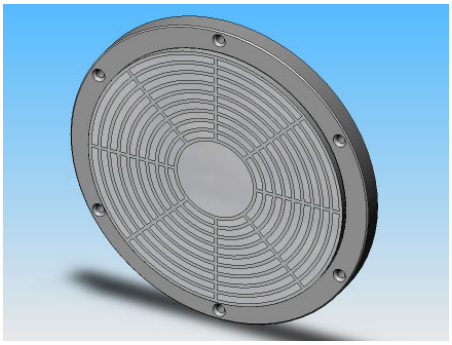

a) Plated sample as removed from the plating bath. The polymer resist is still intact.

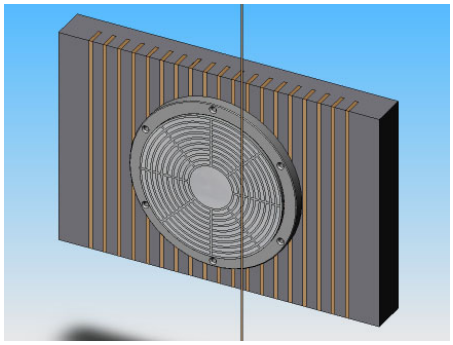

b) Same sample mounted on a magnetic chuck in wire EDM machine. The wire EDM machine skims any over plated nickel to the same surface as the polymer resist.

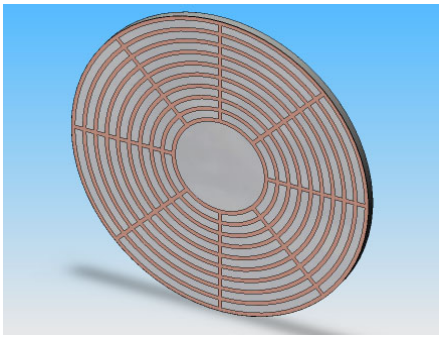

c) Sample removed from substrate.

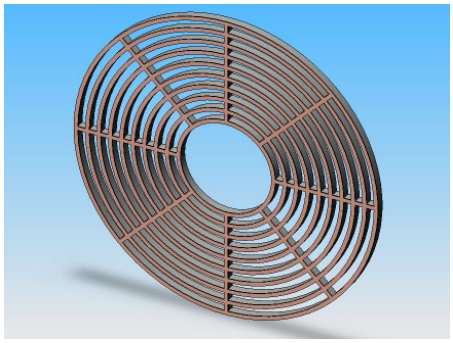

d) PMMA dissolved.

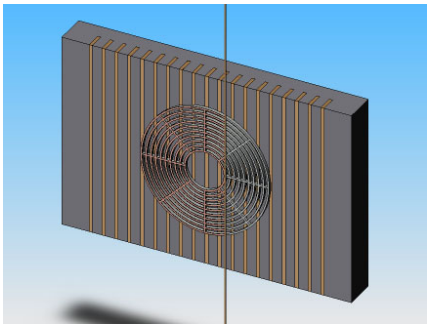

e) Sample mounted to magnetic chuck with copper plating exposed.

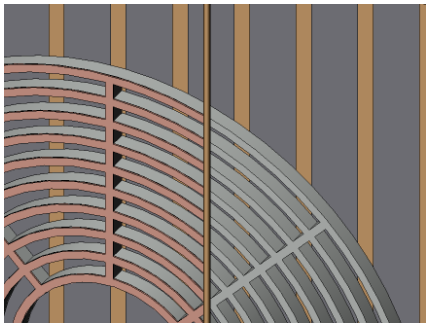

f) Second EDM pass removes copper and nickel associated with “undercut” region.

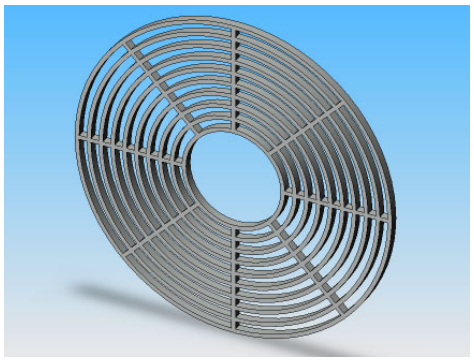

g) Part separated from chuck, ready for inspection.

Figure 4.3—Actual process used to fabricate regenerator disks.

4.3.2 Fabricated Regenerator

The previously described process was used to fabricate the regenerator tested in this project. Micrographs of typical parts are shown in figure 4.4a to d. The nickel webs are approximately 15 μm in width, and arranged in an involute pattern (fig. 4.4a and b). The thickness of each disk is approximately 250 μm. Figure 4.4c shows a single involute-foil slipped onto the stacking fixture. Figure 4.4d shows a single disk leaning against the outer housing of the regenerator. Figure 4.5 shows the final regenerator that was tested.

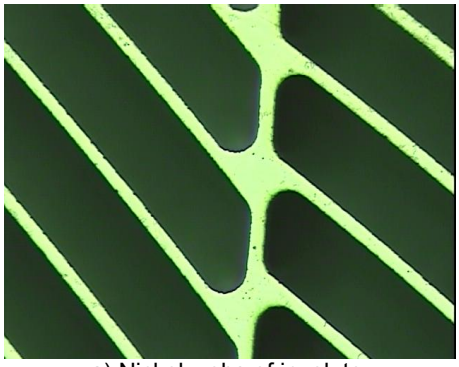

a) Nickel webs of involute.

b) Lower magnified view of involute pattern.

c) Disk stacked onto fixture.

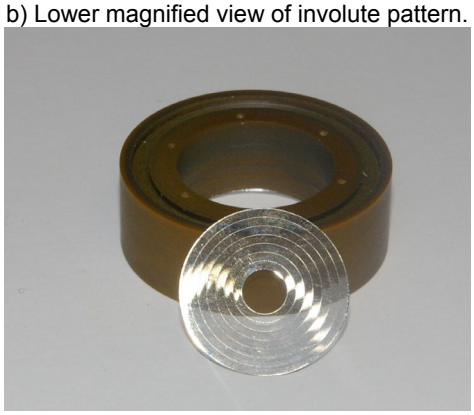

d) Disk leaning against outer housing.

Figure 4.4.—Different magnified views of regenerator disks.

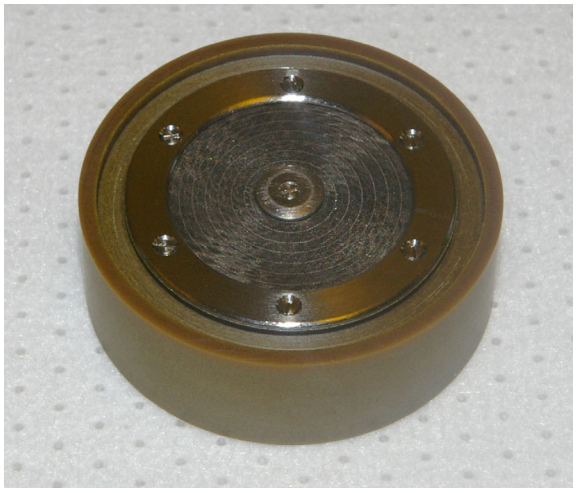

Figure 4.5.—Assembled regenerator (stack of 42 disks).

4.4 Microfabrication Process Conclusions

In this project, the LiGA micromachining process was used to fabricate a regenerator that was tested and found to provide very good performance (see sec. 3.6.2.4 for test results). Also, the manufacturing approach of using LiGA-fabricated EDM tools to fabricate regenerator parts seemed initially to offer little potential due to the extremely low material removal rate. In retrospect, however, if dimensions are chosen such that greater overburn is allowable, then the EDM-LiGA approach will be more viable. It should also be noted that in this effort, a new manufacturing technique was developed: namely using EDM to "skim cut" regenerator parts. While the regenerator tested did provide good performance, LiGA and/or LiGA-EDM process optimization could result in a better product. Potential improvements include:

i) Improve the lithography process to eliminate or greatly reduce "undercutting."
ii) Cease electroplating before overplating begins. This would eliminate the need to use the "skim cut" and would eliminate the source of burrs that was attributed to the EDM operation.
iv) To greatly reduce cost, explore the use of SU-8, a negative resist that requires substantially less exposure time than PMMA.
iv) For EDM, find acceptable combination of material removal rate, overburn, and geometry that gives a high quality part in a reasonable time and cost.

5.0 Large Scale Mockup (University of Minnesota, UMN)

5.1 Large Scale Mockup (LSMU) Design

The microfabricated regenerator is of an annular design that cannot be scaled up in its entirety by a factor of 30 and still be operational in our oscillatory flow facility. Thus, only a 30° sector of it was chosen for modeling. Two geometries are shown in figure 5.1a and b. The second pattern geometry is achieved by shifting and flipping the first geometry. Figure 5.2 shows the dimensions of typical LSMU channels. The channel width is 2.58 mm and the fin thickness is 0.42 mm. The channel length changes from 54.56 to 32.72 mm as one passes from the inner radius to the outer radius of the first pattern layer. For the channels of the inner and outer edge of the second pattern layer, the lengths are 22.43 and 14.32 mm, respectively. For the channels of the center area, the lengths change from 49.73 to 34.65 mm. The layers were stacked to make the LSMU assembly. Figure 5.3 shows the mesh of the first pattern layer stacked on top of the second pattern layer.

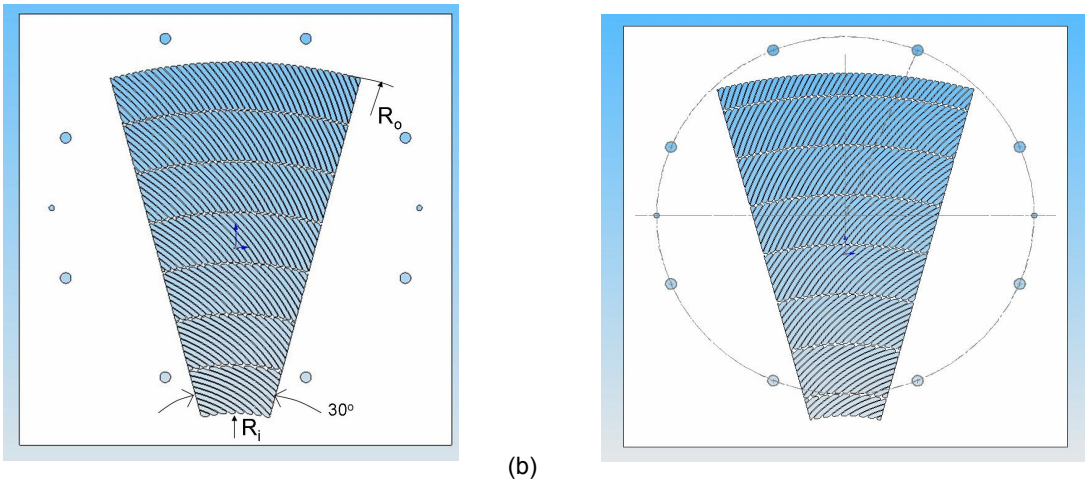

(a) (b)

Figure 5.1(a)—First pattern geometry (6 ribs). (b) Second pattern geometry (7 ribs).

The LSMU regenerator layers were fabricated by wire EDM. Figure 5.4 shows a photo of a LSMU layer, which is a 30° sector of the first pattern design. The choice of aluminum was influenced by the EDM manufacturing choice for more rapid cutting compared to stainless steel, another reasonable choice. By inspection, the surface appears smooth with a matte finish. Literature indicates the roughness obtained by wire EDM is 0.05 μm.

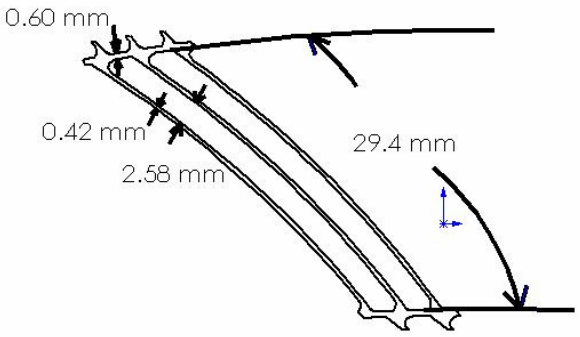

Figure 5.2—Geometry of typical channels.

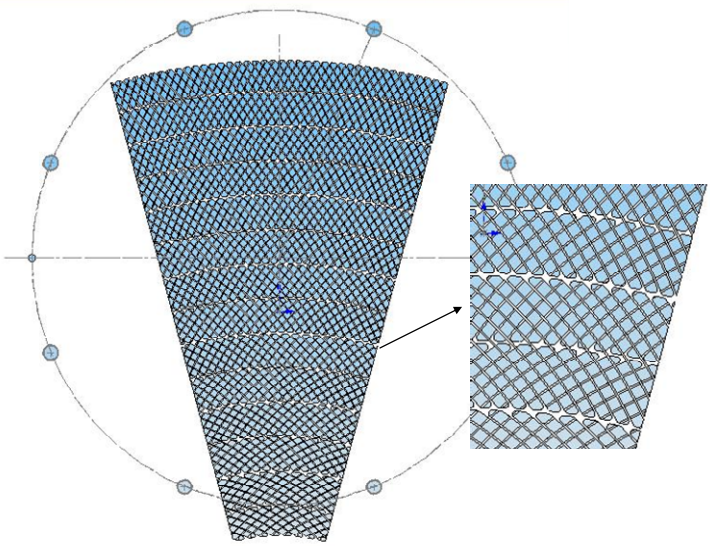

Figure 5.3.—The mesh of the first pattern layer stacked on top of the second pattern layer.

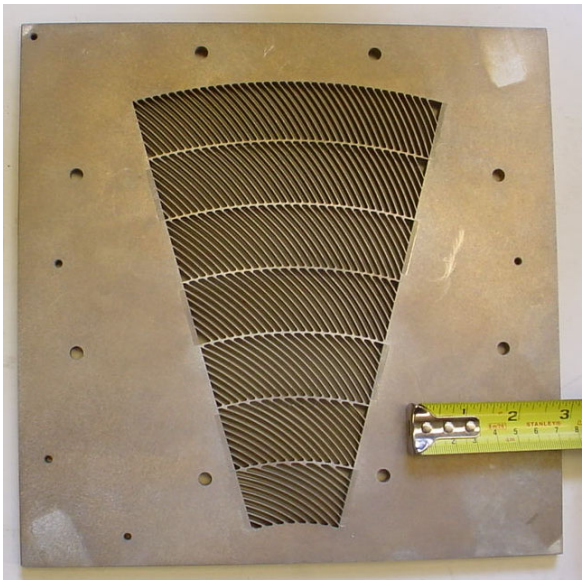

Figure 5.4.—The LSMU layer fabricated by wire EDM.

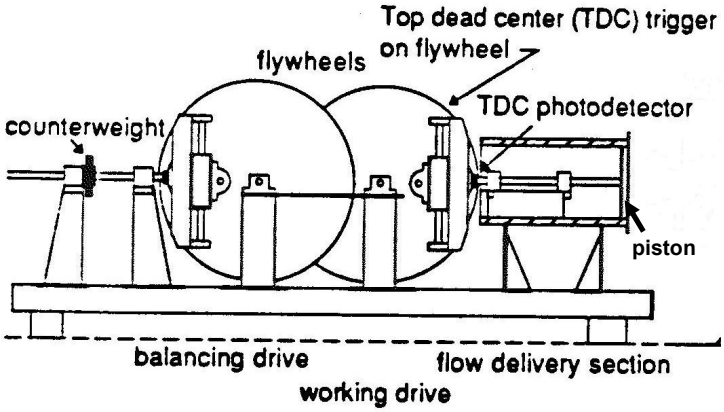

Figure 5.5.—Schematic of the oscillatory-flow generator (Seume et al. 1992).

5.2 The Operating Conditions

For engine operational data on which to base the LSMU design, a "pattern engine" was selected. It is representative of modern Stirling engines being developed for NASA space power applications. The pattern engine was designed for operation with a random wire regenerator. Operational data for this pattern engine and the hydraulic diameter of the microfabricated regenerator were used to calculate the Reynolds number and Valensi number for our pattern engine with a microfabricated regenerator installed. The computed Reynolds numbers varied from 19.7 to 75.7 for the hot end to the cold end of the regenerator while the Valensi number varied from 0.12 to 0.6. Then the stroke, piston diameter and frequency of the oscillatory-flow test facility were selected for use in the large-scale experiment that matched these dimensionless numbers. A Scotch-yoke mechanism is employed to produce precise sinusoidal movement of the piston with a zero-mean velocity in the oscillatory-flow test facility. Figure 5.5 shows a schematic of the oscillatory-flow generator, the details of which were given in a NASA report (Seume et al. 1992). Figure 5.6 shows a picture of the oscillatory-flow generator.

Figure 5.1a shows the geometry of the first pattern regenerator layer (with 6 ribs), where the outer radius, R_o, is 284.25 mm and the inner radius, R_i, is 77.25 mm. The second pattern regenerator layer

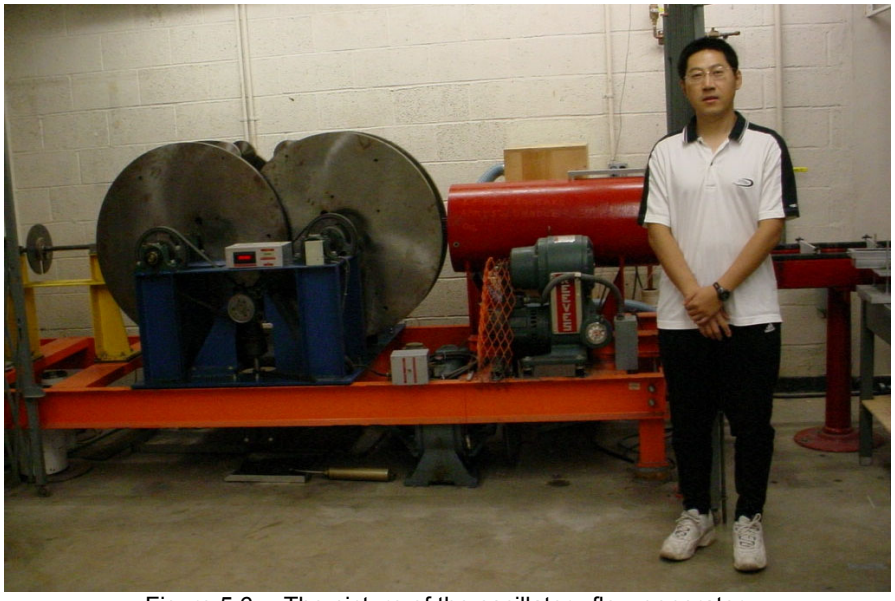

Figure 5.6.—The picture of the oscillatory-flow generator.

(7 ribs) has the same outer and inner radii as the first pattern. The scale factor is 30 times the actual size. For the first pattern regenerator layer, scaled-up channel lengths change from 54.56 mm for the slots near the inner radius to 32.72 mm for the slots near the outer radius. Scaled-up channel width is 2.58 mm (101 mils). The hydraulic diameter of the channel, d_h, is 4.87 mm (192 mils). The wall thickness is 0.42 mm (17 mils). The plate thickness is 7.95 mm (312 mils or 5/16 in.). The porosity is 86%. The area of the 30° sector of an annulus is $\pi \times (Ro^2 - Ri^2) \times 30/360 = 0.01959$ m^2.

The stroke, piston diameter and operating frequency are selected to match the Valensi number and Reynolds number of the pattern engine. For air, at ambient pressure and temperature, viscosity, $\nu = 15.9\times10^{-6}$ m^2/s. The stroke and piston diameter are set to the most suitable values of the options available in the present rig:

Stroke = 178 mm (7 in.); piston diameter, D_p = 216 mm (8.5 in.).

Assuming incompressible fluid and balancing the volumetric flows in the regenerator and the driving piston/cylinder zone:

$$2X_{\max} \times A \times \phi = \frac{\pi D_p^2}{4} \times \text{Stroke} \tag{5.1}$$

The amplitude of fluid displacement based on the LSMU regenerator flow area is

$$X_{\max} = \frac{\pi D_p^2 \times \text{Stroke}}{8 \times A \times \phi} = \frac{\pi 0.216^2 \times 0.178}{8 \times 0.01959 \times 0.86} = 0.1936 \text{ m} \quad (7.6 \text{ in.}) \tag{5.2}$$

Operational frequency is 0.2 Hz. Thus,

$$\text{Re}_{\max} = \frac{U_{\max} \times d_h}{\nu} = \frac{X_{\max} \times \omega \times d_h}{\nu} = \frac{0.1936 \times 2 \times \pi \times 0.2 \times 4.87 \times 10^{-3}}{15.9 \times 10^{-6}} = 74.5 \tag{5.3}$$

$$\mathrm{Va} = \frac{d_h^2 \omega}{4\nu} = \frac{d_h^2 2\pi f}{4\nu} = \frac{2 \times 3.14 \times 0.2 \times (4.87 \times 10^{-3})^2}{4 \times 15.9 \times 10^{-6}} = 0.47 \tag{5.4}$$

The microfabricated regenerator (in the operating engine) Reynolds number varies from 19.7 to 75.7 from the hot end to the cold end of the regenerator, while the Valensi number varies from 0.12 to 0.6. In our large-scale experiment, the Reynolds number is 74.5 and the Valensi number is 0.47, a reasonable match to the dimensionless numbers for the pattern engine. The local maximum velocity, U_{max}, is 0.24 m/s. Adolfson (2003) found that quasi-steady velocity measurements with hot-wire anemometry could be made with less than 10% uncertainty when the velocity exceeds 0.12 m/sec.

Thus, in the large scale experiment, the stroke is 178 mm, the piston diameter is 216 mm and the frequency is 0.2 Hz, selected to match the Reynolds number and the Valensi number of the microfab regenerator in the pattern engine. Table 5.1 shows a comparison of microfabricated regenerator and LSMU regenerator geometry and working conditions.

5.3 The LSMU Experiments Under Unidirectional Flow

The Darcy friction factor, the permeability and the inertial coefficient of the LSMU layers were measured under unidirectional flow.

TABLE 5.1—COMPARISON OF MICROFABRICATED AND LSMU INVOLUTE-FOIL REGENERATORS

	Microfabricated regenerator	LSMU regenerator
Geometry		
Channel width (mm)	0.086	2.58
Channel wall thickness (mm)	0.014	0.42
Regenerator layer thickness (mm)	0.25	7.9
Hydraulic diameter, d_h (mm)	0.162	4.87
Working conditions		
Working medium	Helium	Air
Operating frequency (Hz)	83	0.2
Pressure (MPa)	2.59	0.101
Temperature of the hot end (K)	923	313
Temperature of the cold end (K)	353	303
U_{max} of the hot end (m/s)	3.7	0.24
U_{max} of the cold end (m/s)	2.85	0.24
Kinematic viscosity of the hot end (m^2/s)	32.3×10^{-6}	15.9×10^{-6}
Kinematic viscosity of the cold end (m^2/s)	6.48×10^{-6}	15.9×10^{-6}
Reynolds number, Re_{max}, of the hot end	19.7	74.5
Reynolds number, Re_{max}, of the cold end	75.7	74.5
Valensi number, Va, of the hot end	0.12	0.47
Valensi number, Va, of the cold end	0.6	0.47

5.3.1 The LSMU Experimental Setup

Figure 5.7 shows the set up of the experiments under unidirectional flow. At one side of the LSMU slices, the transition piece is connected with a fan by a 11.08 m (12 ft) long flexible tube and a 0.54 m (21 in.) long acrylic tube. At the other side, the transition piece connects the LSMU plates with a sector-of-an-annulus shaped opening. The transition piece is for transitioning from a round to a sector-of-annulus cross section. It consists of 9 layers with the sector-of-annulus shaped opening and one layer with the round opening, which are shown in figure 5.8. The thickness of one layer is 12.7 mm (0.5 in.). Screen material (not shown in fig. 5.8) is sandwiched between every two layers to help with the flow diffusion. The pressure drop across the LSMU layers is measured by a micro manometer. The hot-wire anemometer is used to measure the velocity of the outlet flow. The voltage readings of the anemometer are input to the multimeter and then collected by the computer.

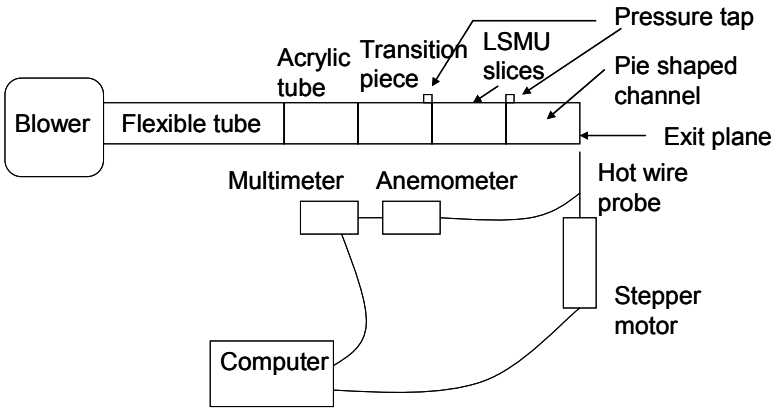

Figure 5.7.—The schematic of the experimental setup of unidirectional flow test.

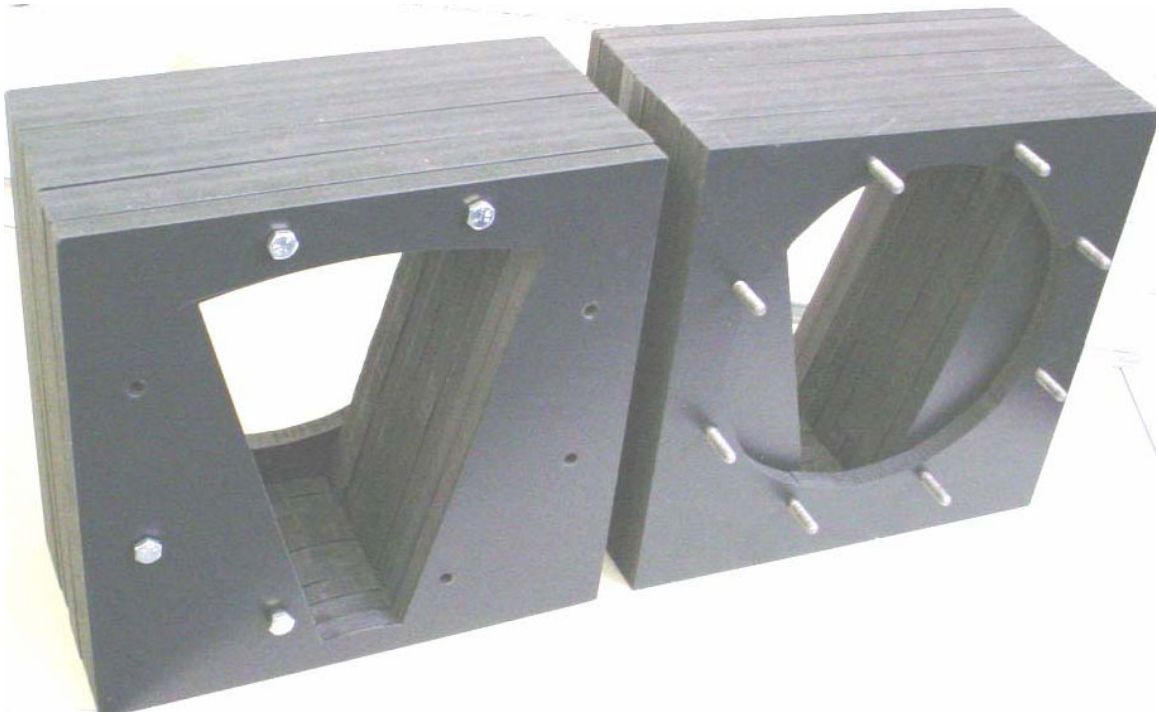
Figure 5.8.—Two transition sections (without screens).

5.3.2 Traverse of the Hot Wire Probe Over the Area of a Sector of an Annulus

A program was written in the c programming language to traverse the hot-wire probe over the area of a sector of an annulus. The measurement grid is shown in figure 5.9. Dots show the locations at which velocity measurements were taken. In the radial direction, the increment is 9 mm. In the upper area, including areas 1a, 1b, 2a and 2b, the angular increment is $\pi/60$. In the lower area, the angular increment is $\pi/120$. There are 348 grid points in total. The order in which the probe visited the various areas is 1a, 2a, 2b, 1b, 3 to 10. The probe visited the centroid, shown by a cross in figure 5.9, before and after each area was visited. This allowed a check for time variations.

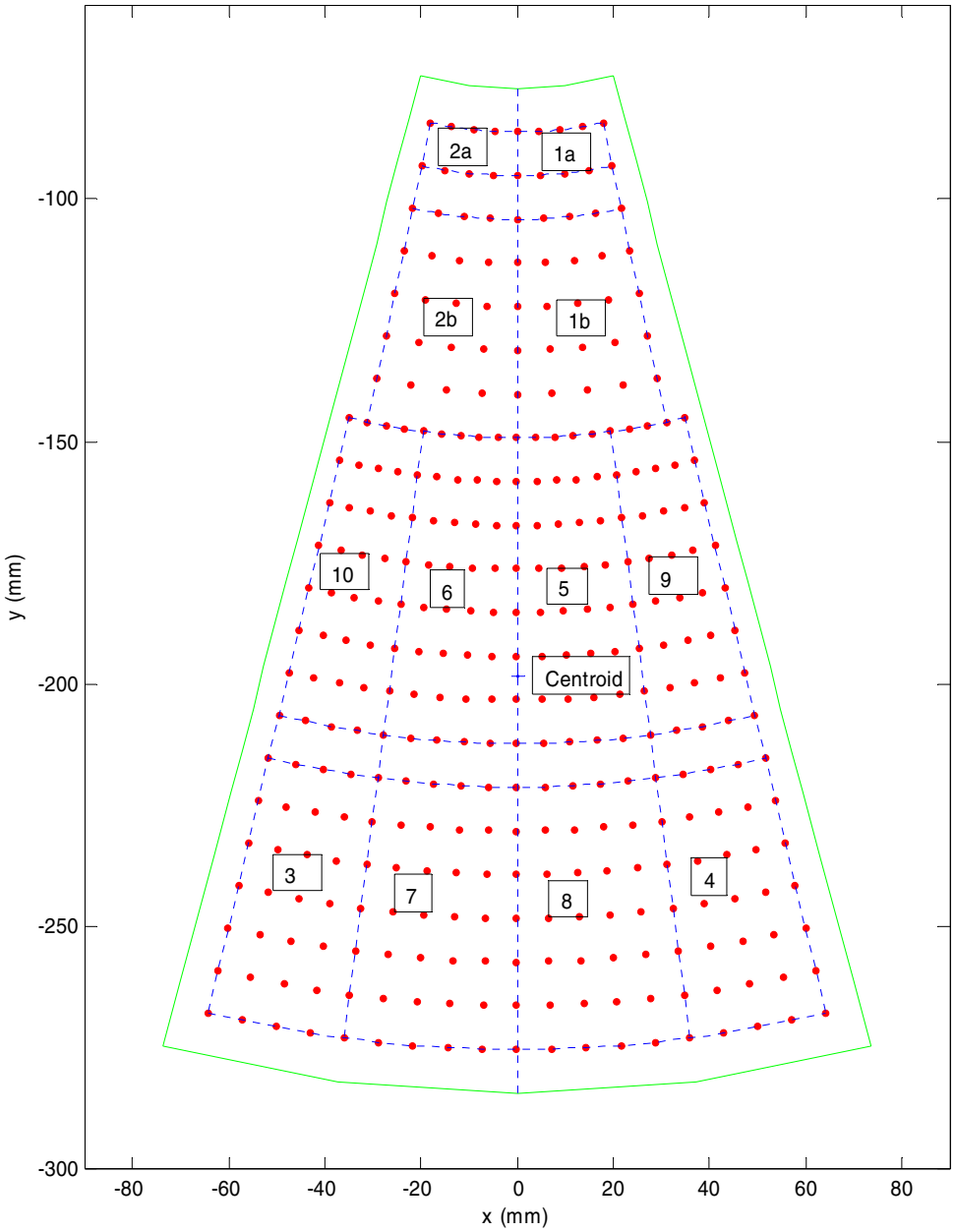

Figure 5.9.—The measurement grid.

5.3.3 Friction Factor

LSMU layers: The Darcy velocity in the LSMU layers (i.e., the approach velocity to the LSMU), was measured, with 8 plates or layers in the LSMU for this friction-factor measurement. The local velocity inside the channels, V, of the LSMU test section is calculated by dividing the Darcy velocity by the porosity. The Reynolds number is based on local velocity inside the channels and the hydraulic diameter of the channels, which is 4.87 mm. Also, the pressure drop, Δp , across the LSMU test section was measured. The friction factor is obtained from:

$$f = \frac{\Delta p \times (D_h / L)}{\frac{1}{2}\rho V^2} \tag{5.5}$$

where L is the length, or sum of the LSMU layer thicknesses. The result will be compared with the friction factors of continuous and staggered channels of parallel plates, a random fiber matrix and a woven screen matrix in figures 5.11 and 5.12 (and later against CFD computational results; see sec. 6.0). The following paragraphs describe the origins of the friction-factor data to be compared with the measured LSMU friction factor.

Continuous channels: First, the equivalent continuous channel geometry to the LSMU regenerator is described. The LSMU channel length varies from 54.5 to 32.7 mm for the 6 rib plate. The average length of 43.6 mm is chosen to calculate the aspect ratio for the continuous channel comparison case. Thus, the aspect ratio is 43.6/2.58 = 17. The hydraulic diameter of the equivalent continuous channels is 4.87 mm. For fully developed flow in a continuous channel, f*Re = 89.9 when the aspect ratio is 20; f*Re = 96 for an infinite aspect ratio (Munson et al. 1994). The friction factor of fully developed flow of a 43.6 mm long by 2.58 mm wide continuous channel is calculated by interpolation as f = 89.9/Re. This is the continuous channel equation plotted in figures 5.11 and 5.12.

Staggered fins or plates: The curve for the Fanning friction factor for a strip fin configuration from Kays and London (1964) is used to describe staggered fin channels. These "staggered plates" curves of figure 5.11 and 5.12 are taken from figure 5.10 which is copied from Kays and London (1964). The Darcy (or Darcy-Weisbach) friction factor is computed from the Fanning friction factor by multiplying by 4.0.

Random fiber: From the Sage code manuals (Gedeon, 1999), the friction factor for a random fiber matrix is:

$$f = 192/\mathrm{Re} + 4.53\,\mathrm{Re}^{-0.067} \tag{5.6}$$

The local bulk mean velocity (not the Darcy velocity) is used to calculate the Reynolds number.

Woven screens: From Sage (Gedeon, 1999), the friction factor for a woven screen matrix is:

$$f = 129/\mathrm{Re} + 2.91\,\mathrm{Re}^{-0.103} \tag{5.7}$$

Again, the local velocity (not the Darcy velocity) is used to calculate the Reynolds number.

A comparison of friction-factor as a function of Reynolds number, or f versus Re, for the different geometries is shown in table 5.2. Figure 5.11 shows the Darcy-Weisbach friction factor versus Reynolds number for the different geometries. The Reynolds numbers are based upon the local, in-channel velocity and the hydraulic diameter is computed as $\frac{4V_{\text{fluid}}}{A_{\text{wetted}}}$. The curve for the continuous channel is based on laminar flow. Figure 5.12 shows the same data but in a log plot.

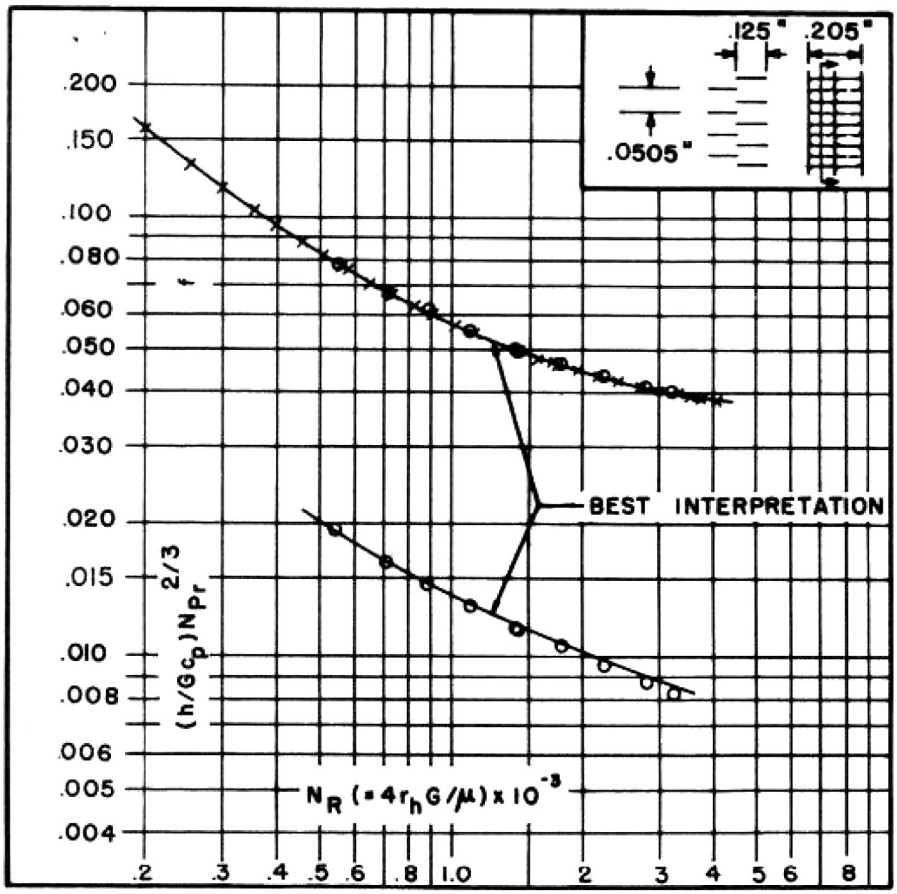

Fin pitch = 19.82 per in.

Plate spacing, $b = 0.205$ in.

Splitter symmetrically located

Fin length flow direction = 0.125 in.

Flow passage hydraulic diameter, $4r_h = 0.005049$ ft

Fin metal thickness = 0.004 in., nickel

Splitter metal thickness = 0.006 in.

Total heat transfer area/volume between plates, $\beta = 680$ ft^2/ft^3

Fin area (including splitter)/total area = 0.841

Figure 5.10.—*f* versus Re for staggered strip-fin. (Figure used with permission from Kays and London (1964).)

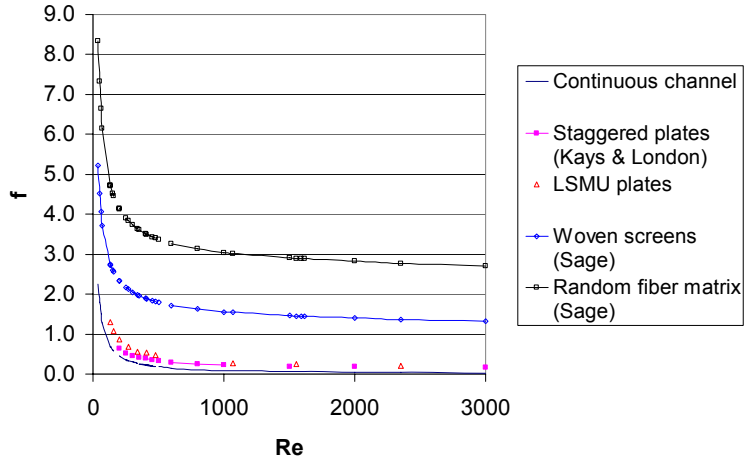

Figure 5.11.—Darcy-Weisbach friction factor versus Reynolds number for different geometries. The Reynolds number is based on the local velocity and hydraulic diameter.

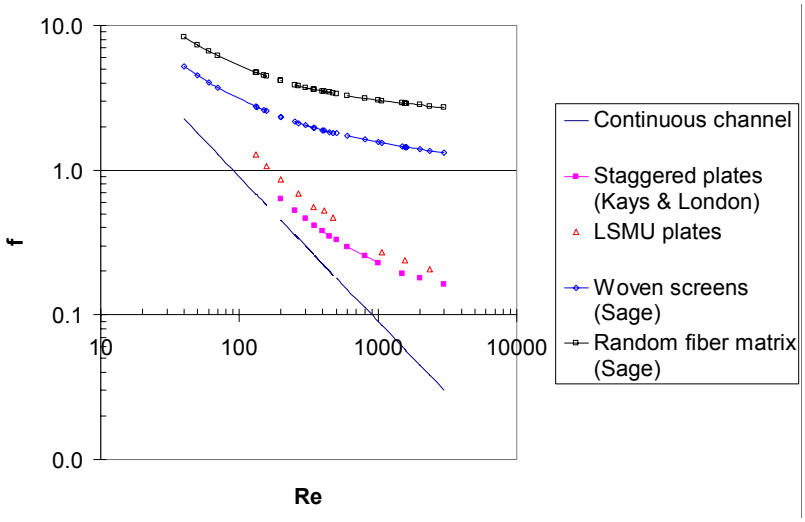

Figure 5.12.—Darcy-Weisbach friction factor versus Reynolds number for different geometries in log scale. The Reynolds number is based on the local velocity and hydraulic diameter.

TABLE 5.2—COMPARISON OF FRICTION-FACTOR, *f* VERSUS REYNOLDS NUMBER, Re, FOR DIFFERENT GEOMETRIES

Re	*f* continuous channel	*f* staggered plates	*f* LSMU layers	*f* random fiber	*f* woven screens
40.00	2.25			8.34	5.22
50.00	1.80			7.33	4.52
60.00	1.50			6.64	4.06
70.00	1.28			6.15	3.72
131.55	0.68		1.29	4.73	2.74
156.61	0.57		1.08	4.45	2.55
150.00	0.60			4.52	2.60
199.13	0.45		0.86	4.14	2.33
200.00	0.45	0.630		4.14	2.33
268.30	0.34		0.69	3.83	2.12
250.00	0.36	0.525		3.90	2.16
340.68	0.26		0.56	3.63	1.97
300.00	0.30	0.464		3.73	2.05
408.97	0.22		0.53	3.50	1.88
350.00	0.26	0.414		3.61	1.96
477.13	0.19		0.48	3.40	1.81
400.00	0.22	0.382		3.51	1.89
450.00	0.20	0.349		3.44	1.84
500.00	0.18	0.330		3.37	1.79
600.00	0.15	0.294		3.27	1.72
800.00	0.11	0.254		3.13	1.62
1000.00	0.09	0.227		3.04	1.56
1067.26	0.08		0.27	3.02	1.54
1500.00	0.06	0.194		2.90	1.46
1556.17	0.06		0.24	2.89	1.45
2000.00	0.04	0.179		2.82	1.39
2350.71	0.04		0.21	2.77	1.36
3000.00	0.03	0.163		2.71	1.32

5.3.4 Permeability and Inertial Coefficient

The Darcy-Forchheimer equation (a steady-flow form of the 1-D momentum equation) can be written in terms of the empirical coefficients permeability, K, and inertial coefficient, C_f, as

$$\frac{\Delta p}{L} = \frac{\mu}{K} U + \frac{C_f}{\sqrt{K}} \rho U^2 \tag{5.8}$$

Equation (5.8) could be rewritten as

$$\frac{\Delta p}{LU} = \frac{\mu}{K} + \frac{C_f}{\sqrt{K}} \rho U \tag{5.9}$$

The Darcy velocity U can be calculated by

$$U = \varphi \cdot V \tag{5.10}$$

where φ is the porosity. The porosity is 0.86 for the LSMU layers and is 0.9 for staggered plates (Kays and London, 1964). The porosity values for the woven screens and random fibers were both chosen to be 0.9. The porosity dependence parts of equations (5.6) and (5.7) are given in Gedeon's Sage manuals (Gedeon, 1999). The porosity of the continuous channels is chosen to be the same as that for the LSMU plates (0.86).

From the plot of $\Delta p / L \cdot U$ versus U, the intercept is taken to be μ / K. Permeability is calculated by dividing the dynamic viscosity by the intercept value. Figures 5.13 through 5.17 show the $\Delta p / L \cdot U$ versus U plots for continuous channels, staggered plates, LSMU layers, woven screens and random fibers, respectively. For continuous channels, there is no inertial effect (since the flow path contains no "obstacles"). The plot is a horizontal line and μ / K is taken to be 40.7. For staggered plates, μ / K is taken to be 434, found by extrapolation to zero velocity since no Darcy behavior was seen in the plot (no flat section in fig. 5.14). For the LSMU layers, μ / K is taken to be 77. Woven screens and random fiber matrices have a similar pattern to one another, an almost constant slope over the velocity range available. A fitting equation is generated for the lower-velocity region and is extrapolated to the $U = 0$ m/s intercept for evaluation of K, as discussed above. The intercept is obtained from the fitting curve. For the woven screen and random fibers, μ / K is taken to be 36439 and 53201, respectively. Table 5.3 shows permeability for different geometries.

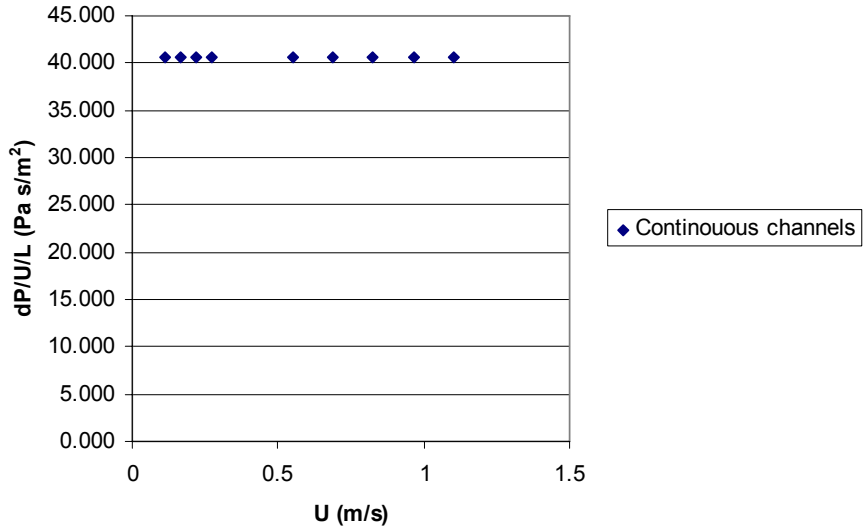

Figure 5.13.—$\Delta p/L/U$ versus U for continuous channels.

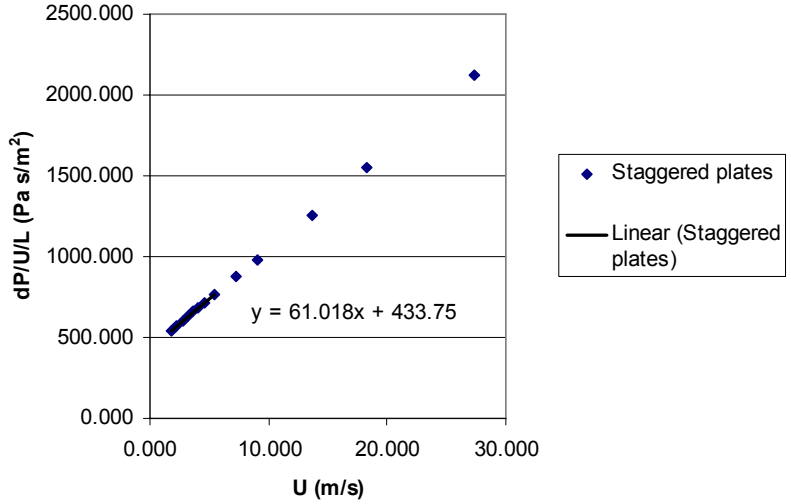

Figure 5.14.—$\Delta p/L/U$ versus U for staggered plates.

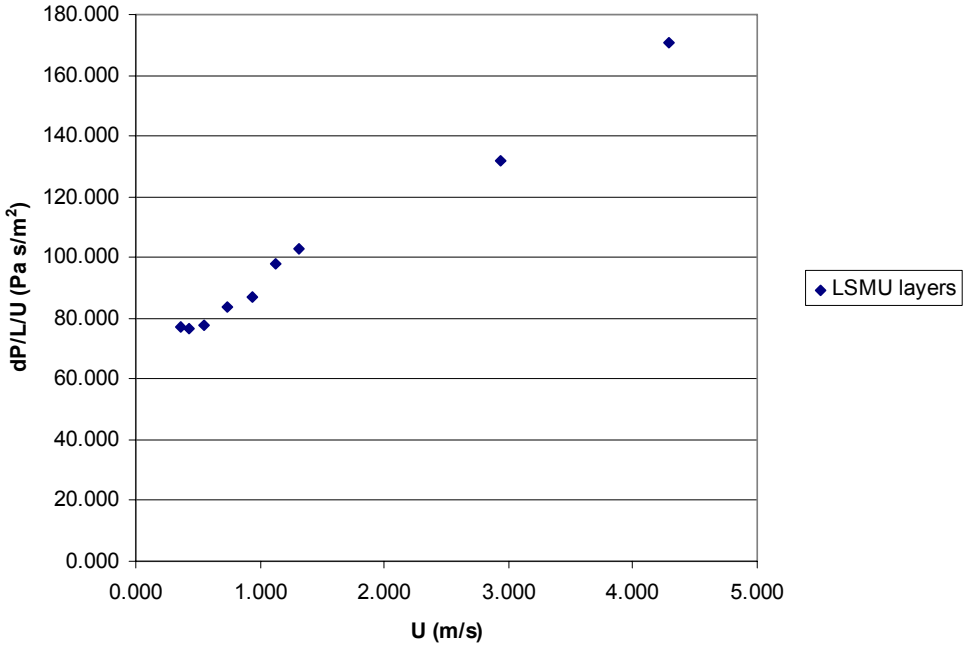

Figure 5.15.—Δ*p*/*L*/*U* versus *U* for LSMU layers.

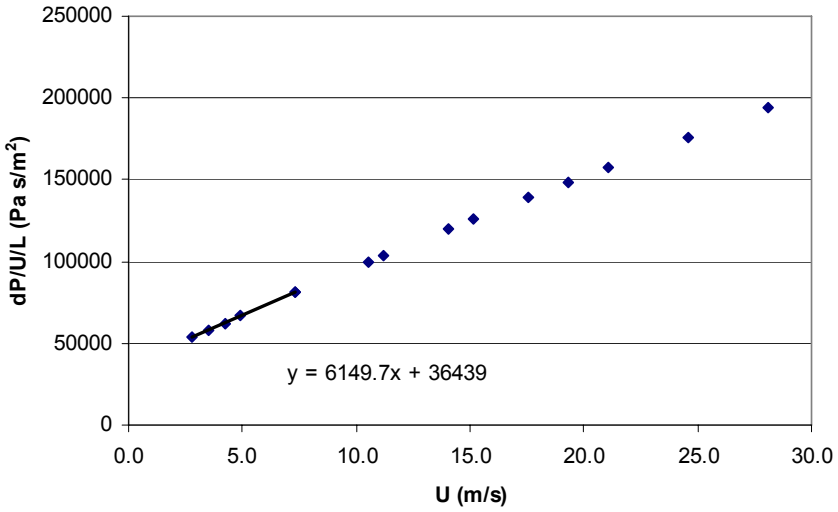

Figure 5.16.—Δ*p*/*L*/*U* versus *U* for a woven screen matrix.

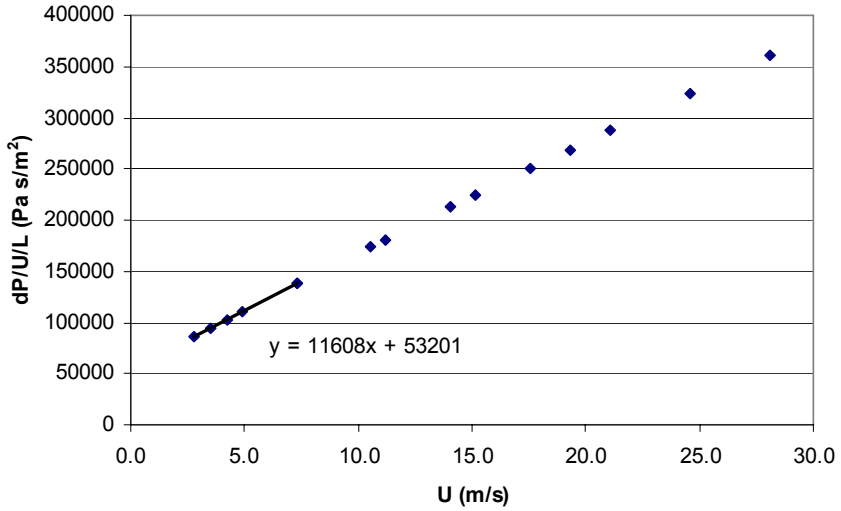

Figure 5.17.—Δ*p*/*L*/*U* versus *U* for random fibers.

TABLE 5.3—COMPARISON OF PERMEABILITY FOR DIFFERENT GEOMETRIES

	Dh, mm	K, m^2	K/Dh^2
Continuous channels	4.872	4.54E-07	1/52.3
Staggered plates*	1.539	4.26E-08	1/55.6
LSMU layers	4.872	2.40E-07	1/98.98
Woven screen matrix*	0.2	5.07E-10	1/78.9
Random fibers*	0.2	3.47E-10	1/115.2

* Extrapolated into Darcy region.

The choice of the hydraulic diameter of the woven screen matrix and random fibers will not affect the value of K/Dh^2, which is proven by the following.

Equation (5.5) can be rewritten as

$$\frac{\Delta p}{V \cdot L} = \frac{f \cdot \rho \cdot V}{2D_h} \tag{5.11}$$

Since $\mathrm{Re} = VD_h/\upsilon$ and $U = V\varphi$,

Equation (5.11) can be written as

$$\frac{\Delta p}{U \cdot L} = \frac{f \cdot \rho \cdot \mathrm{Re} \cdot \upsilon}{2\varphi \cdot {D_h}^2} \tag{5.12}$$

As shown by equation (5.9), when the flow velocity is small, $\Delta p / L \cdot U$ is dominated by the viscous term, μ / K. Thus,

$$\frac{\Delta p}{U \cdot L} = \frac{f \cdot \rho \cdot \mathrm{Re} \cdot \upsilon}{2\varphi \cdot {D_h}^2} = \frac{\mu}{K} \tag{5.13}$$

$$\frac{K}{D_h{}^2} = \frac{2\varphi}{f \cdot \mathrm{Re}} \tag{5.14}$$

For random fiber matrix, from equation (5.6),

$$f\,\mathrm{Re} = 192 + 4.53\,\mathrm{Re}^{0.933} \tag{5.15}$$

For a woven screen matrix, from equation (5.7),

$$f\,\mathrm{Re} = 129 + 2.91\,\mathrm{Re}^{0.897} \tag{5.16}$$

Therefore, for small Reynolds numbers, the value of $f\,\mathrm{Re}$ is a constant, 192 and 129 for random fiber and woven screen matrix, respectively. Thus, K/Dh^2 does not change with the selection of the hydraulic diameter of the matrix, provided that the porosity remains fixed.

Equation (5.9) could be rewritten as

$$\frac{\Delta p}{LU^2} = \frac{\mu}{KU} + \frac{C_f}{\sqrt{K}}\rho \tag{5.17}$$

The inertial coefficient, C_f, can be evaluated accurately as the velocity goes toward infinity. However, due to the limitation of the equipment available, 6.5 m/s is the maximum mean velocity that was reached. Figures 5.18 and 5.19 show the $\Delta p / L \cdot U^2$ versus U plot for LSMU plates and staggered plates, respectively. For LSMU plates, $\frac{\mu}{K 6.473} + \frac{C_f}{\sqrt{K}}\rho$ is taken to be 34.6. For staggered plates, $\frac{\mu}{K 27.37} + \frac{C_f}{\sqrt{K}}\rho$ is taken to be 77.5. The inertial coefficient values are 0.00939 for LSMU plates and 0.01075 for staggered plates.

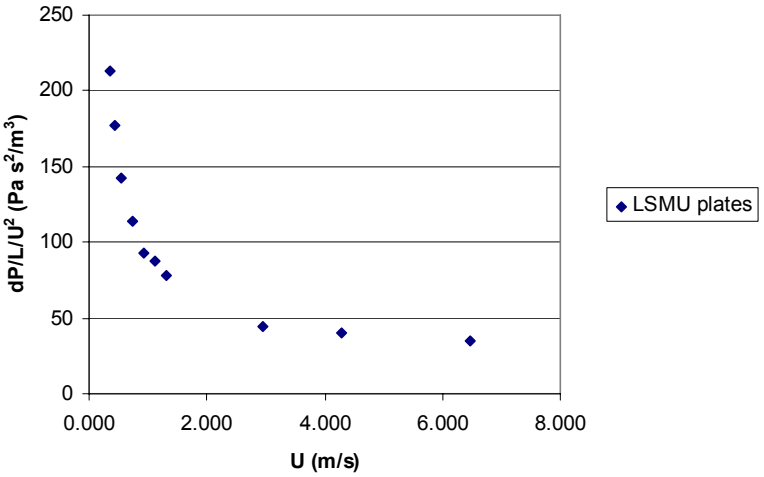

Figure 5.18.—$\Delta p/L/U^2$ versus U for LSMU plates.

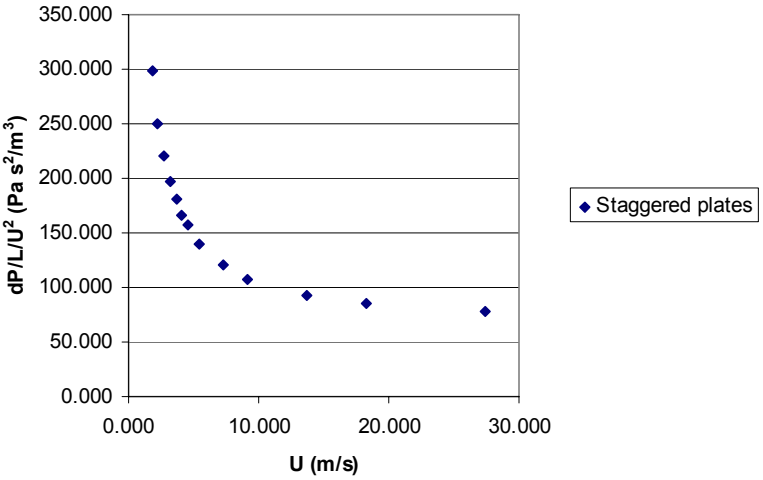

Figure 5.19.—$\Delta p/L/U^2$ versus U for staggered plates.

5.3.5 Friction Factor of Various LSMU-Plate Configurations

Figure 5.21 shows the comparison of Darcy friction factor of various LSMU plate configurations, including 8 LSMU plates, 10 LSMU plates, 5 aligned LSMU plates, and 8 LSMU plates (double thickness). For the "aligned" test, five 6-rib LSMU plates are stacked together and tested under the unidirectional flow. Figure 5.20 shows a picture of 5 aligned LSMU plates. The fins are aligned throughout the entire area. One must take the view toward the bottom of figure 5.20 to see this. The total thickness of the 5 plates is 39.7 mm. The hydraulic diameter, d_h, of the flow channel is 4.87 mm. The ratio of the length to the hydraulic diameter is 8.15. For laminar flow in a continuous channel, the ratio of the entrance length to the hydraulic diameter is 0.06∗Re. Under current test conditions, the Reynolds number varied from 207 to 1618. Thus, the entrance length changes from $12.4d_h$ to $97.1d_h$ and the flow of the 5 aligned plates is in the developing regime. Figure 5.21 shows the aligned plates have lower friction factor values than those for the standard LSMU plate arrangement. This is because the flow through the aligned plates is continuous and has minimal flow separation whereas the LSMU plates under the standard arrangement would have wakes from trailing edges and separation on leading edges.

A comparison can be made between the case where 10 LSMU plates are stacked under the standard configuration and the case where 8 LSMU plates are stacked similarly. The two cases compare very closely. The shorter assembly has only slightly larger friction factor values. This is an indication that the flow develops rapidly within the assembly, perhaps in the first 3 or 4 plates. The fitting equation for friction factor versus Reynolds number for the 8 LSMU plates is:

$$f = \frac{153.1}{\mathrm{Re}} + 0.127\,\mathrm{Re}^{0.01} \tag{5.18}$$

This equation fits the 10 LSMU plate data also.

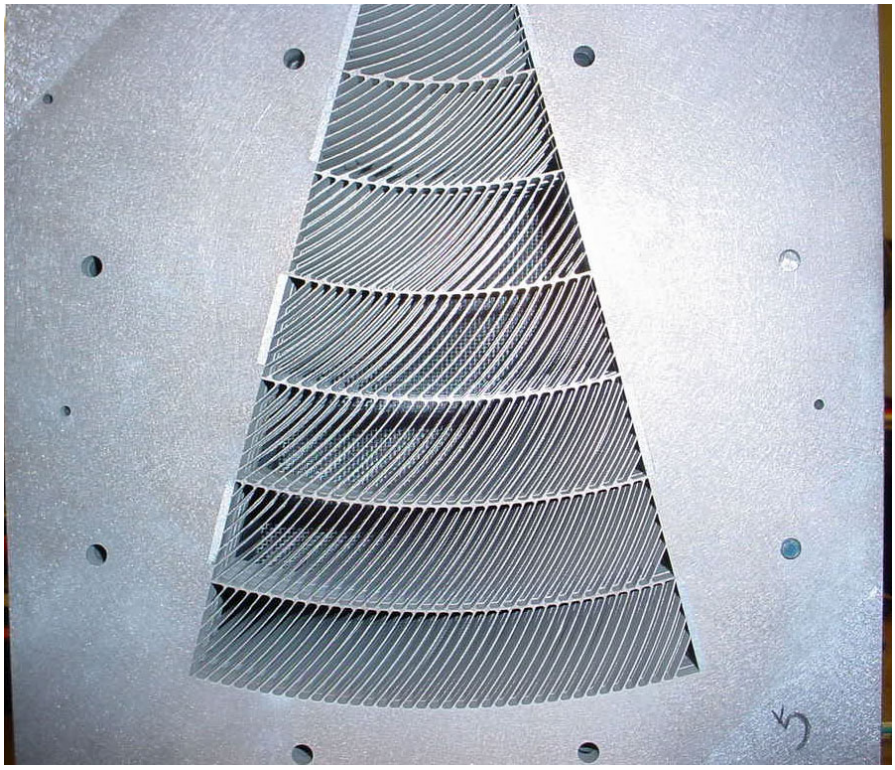

Figure 5.20.—A picture of 5 aligned LSMU plates.

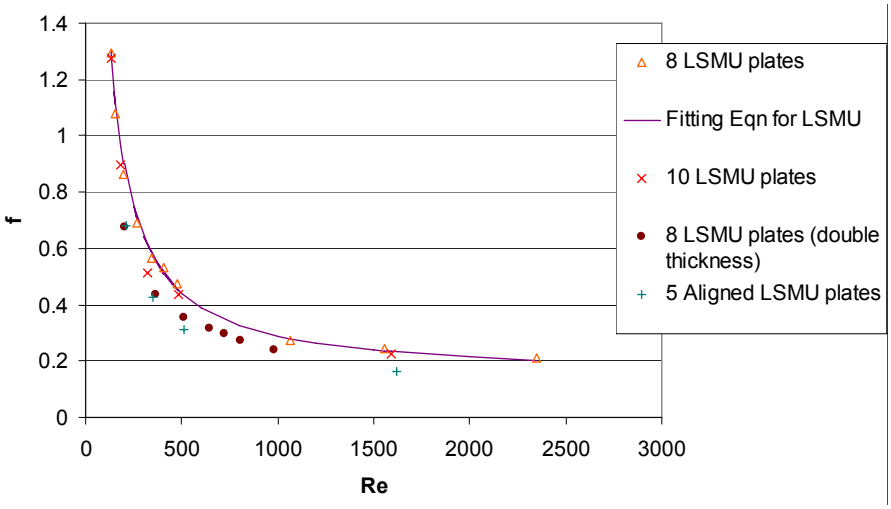

Figure 5.21.—Comparison of Darcy friction factors of various LSMU-plate configurations.

To determine what the friction factor would be with the LSMU geometry but with plates that are twice as thick, we stacked two, 6-rib plates together and two 7-rib plates together, and then repeated, giving 4 groups with the eight LSMU plates (or the equivalent of 4 double-thickness plates). Figure 5.21 shows that the friction factor is reduced from that with normal stacking with this new stacking order. The reason is that there are fewer flow redistributions from 6-rib geometry to 7-rib geometry, or the reverse, with this stacking order.

5.4 The Jet Penetration Study

5.4.1 The Jet Penetration Study for the Round Jet Generator

The geometry of the round jet generator is shown in figure 5.22. The fabricated round jet generator is shown in figure 5.23. Round holes are arranged in an equilateral triangle pattern. The hole diameter is 20 mm and the center-to-center spacing is 40 mm. The jet generator is 30.5 cm (12 in.) long giving a hole L/D ratio of 15.2.

5.4.1.1 The Experimental Setup

Since the diameter of the hot wire support tube is 4.57 mm, a spacer for hot wire insertion was fabricated that is thicker than 4.57 mm, smaller than, but comparable in size to, the thickness of an LSMU plate (7.95 mm or 5/16 in.). Insertion of the hot-wire probe is thus limited to the plenum between the jet generator and the matrix and velocity data are not taken between LSMU layers. Temperature data are used to document the thermal field in the matrix, as affected by the penetrating jet. For this measurement, a thermocouple wire, which is much thinner than the velocity probe, is passed through a much thinner spacer inserted between two adjacent LSMU layers in the test. The thermal effect of the jet flow within the regenerator is documented by temperature profiles from the thermocouple traversed in the radial direction (of the test section which is a sector of an annulus, see fig. 5.22) across the primary jet of the test section and its two neighboring jets on that radius (also shown in fig. 5.22). Traverses are taken at several axial locations to document the widening thermal effects of the jets as one moves away from the jet generator. The thermal field is due to the low temperature of the jet being dispersed within the matrix, hydrodynamically and thermally and, possibly, being turned radially away from its center by the matrix material.

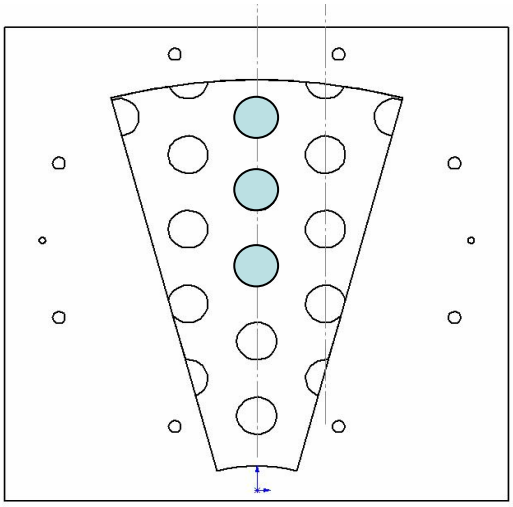

Figure 5.22.—The round jet generator and the plenum shape, a sector of an annulus. The center colored jet is the primary jet.

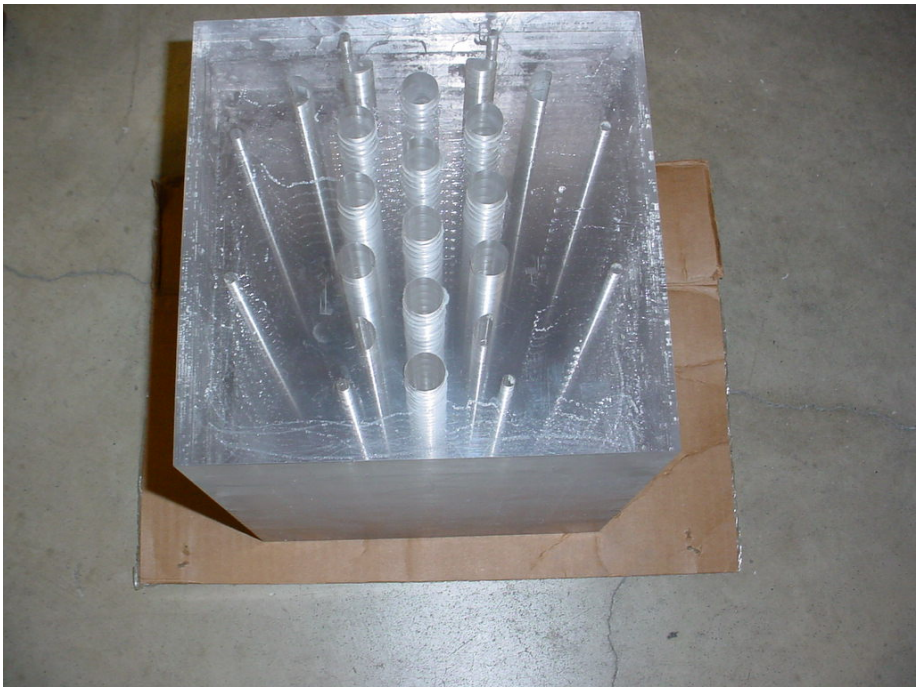

Figure 5.23.—The round jet generator.

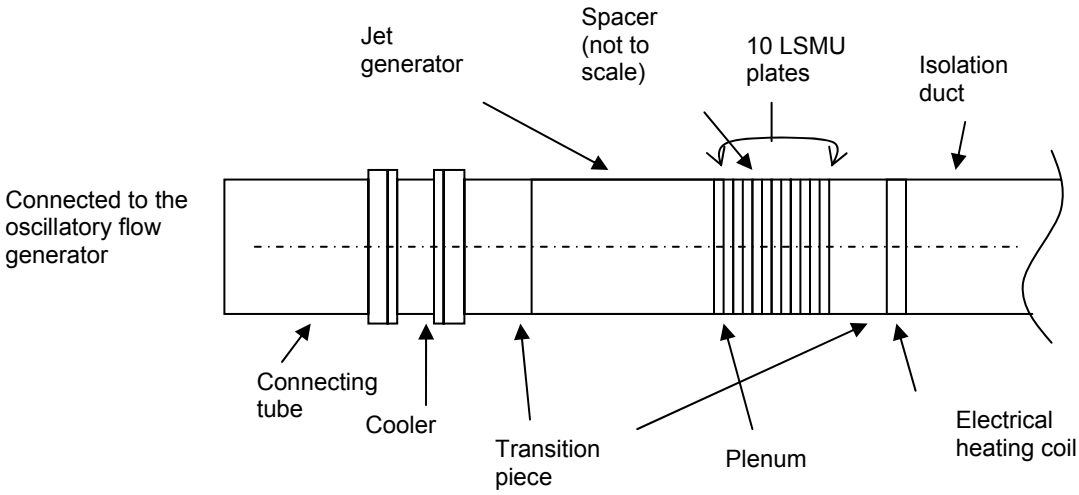

Figure 5.24.—The schematic of the test facility.

Figure 5.24 shows a schematic of the test facility. The main components of the facility are the oscillatory-flow generator, a cooler, two transition pieces (one on each end of the regenerator), a jet generator, ten LSMU plates, an electrical heating coil and an isolation duct. The cooler is a compact heat exchanger used to heat the passenger compartment of a car (called a heater core). One transition piece is put between the regenerator and the heating coil; the other transition piece is located between the jet generator and the cooler. The isolation duct is a long, open tube. It has active mixing to isolate the experiment from the room conditions. For the oscillatory flow generator, the stroke is 178 mm, the piston diameter is 216 mm and the frequency is 0.2 Hz, selected to match the Reynolds number and the Valensi number of the microfabricated regenerator in the pattern engine (79 and 0.53, respectively). There is a plenum between the jet generator and the LSMU plates which allows the hot-wire traverse for

documenting the periodicity of the jets along a radius through the centerlines of the holes highlighted in figure 5.22. The nominal thickness of the plenum, δ, is determined such that the axial-flow area, $\pi d_c^2 / 4$, equates to the radial-flow area, $\pi d_c \delta$. The diameter of the jet channel, d_c, is 20 mm; thus, the nominal thickness for the spacer, δ, is 5 mm. This plenum allows a single hot-wire probe, with a support tube diameter of 4.57 mm, to be inserted into the plenum for taking velocity measurements.

A spacer consisting of two 0.76 mm (0.030 in.) thick stainless-steel sheets (right and left of fig. 5.25) was inserted between two adjacent LSMU plates to allow the thermocouple wire used to take temperature profiles to pass through the test matrix. The opening of the spacer, which is the gap between two stainless steel sheets, is 0.51 mm (0.020 in.).

Thermocouples of type E with a diameter of 76 μm (3 mils) are used for unsteady temperature measurements within the LSMU plate test section. The time constant of the thermocouple is 0.05 sec, which means the thermocouple can sufficiently quickly respond to changes in flow temperature. The thermocouple measuring the temperature within the LSMU matrix is mounted on a stepper motor driven rail so that it can be traversed inside the spacer and between two LSMU plates. The spacer can be moved to other axial locations within the LSMU matrix, allowing temperature documentation at various axial locations. The temperatures within the LSMU matrix, $T(x, r, \mathrm{CA})$, are presented as functions of x, the distance in the axial direction; r, the distance along the centerline radius; and CA, the crank angle. One stationary thermocouple is located at one end of the jet generator and adjacent to the plenum. It is for measuring the cold end temperature, $T_c(\mathrm{CA})$. Another stationary thermocouple is located at the end of the

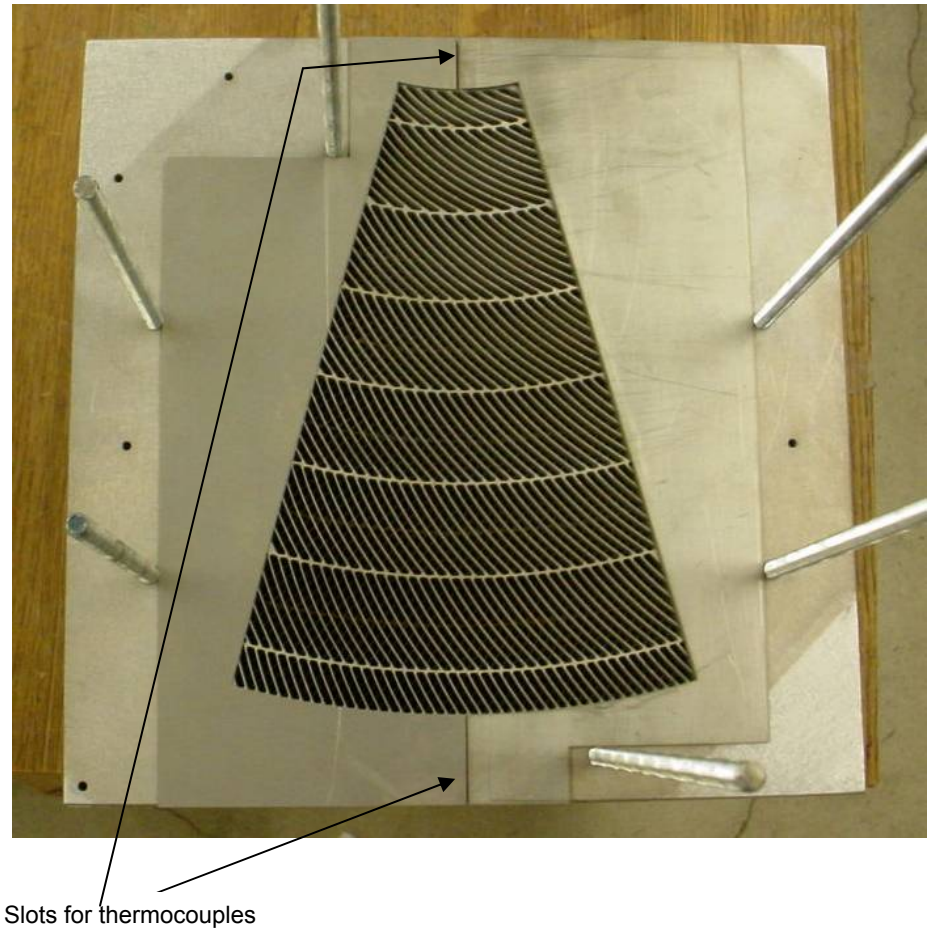

Figure 5.25.—The spacer on the LSMU plates.

transition piece which is adjacent to the LSMU plates. It is for measuring the hot end temperature, T_h(CA). At each location, these three temperatures are taken at a sampling frequency of 500 Hz for 50 cycles. To eliminate temperature drift, a dimensionless temperature is calculated as:

$$\phi(x,r,\mathrm{CA}) = \frac{T(x,r,\mathrm{CA}) - T_c}{T_h - T_c} \tag{5.19}$$

The cold end temperature, T_c(CA), is averaged over the portion of one cycle when the flow is passing from the jet generator to the LSMU regenerator plates. This gives an average temperature, T_c, for each cycle. The hot end temperature, T_h(CA), is averaged over the portion of one cycle when the flow is passing from the heater to the LSMU regenerator plates. This gives an average temperature, T_h, for one cycle. The dimensionless temperature $\phi(x,r,\mathrm{CA})$ is calculated for each reading of the cycle. Averages of $\phi(x,r,\mathrm{CA})$ are taken over an ensemble of 50 cycles.

5.4.1.2 Jet-to-Jet Uniformity for the Round Jet Array

To verify that the flow was uniformly distributed in the round jet generator under oscillatory flow conditions, the velocities within the plenum between the jet generator and the LSMU regenerator plates were measured. Results are given versus time within a oscillation cycle based upon an ensemble average of 50 cycles. Figure 5.22 shows the round jet generator and the plenum which is a sector of an annulus in shape. The hot-wire probe is driven by the stepper motor to move horizontally along a line which passes through the centerlines of the three holes highlighted in figure 5.22. Each velocity measurement is taken at a sampling frequency of 500 Hz for 50 cycles. Velocity profiles taken during the blowing half of the cycle, when the flow is passing from the jet generator to the LSMU plates, are shown in figure 5.26. The origin of the horizontal axis is the center of the center jet. Velocity profiles during the drawing half of the cycle, when the flow is passing from the LSMU plates back to the jet generator are shown in figure 5.27. Velocity profiles show that the jets from the three round channels shown are very similar to one another. This confirms that when the center jet is interrogated, the data are representative of data for flow from all interior jets.

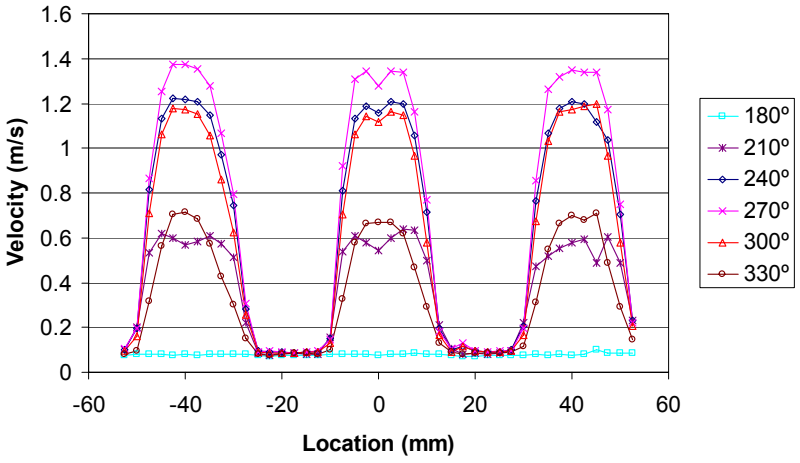

Figure 5.26.—Velocity profiles during the blowing half of the cycle, when the flow is passing from the jet generator to the LSMU plates. The origin of the horizontal axis is the center of the center jet.

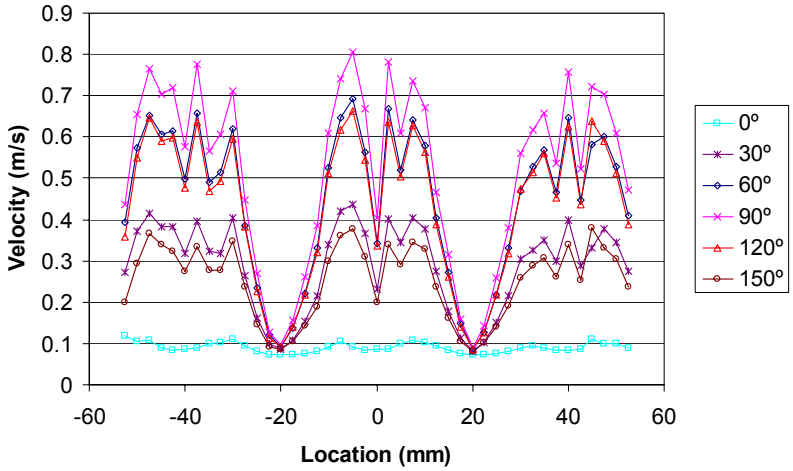

Figure 5.27.—Velocity profiles during the drawing half of the cycle, when the flow is passing from the LSMU plates back to the jet generator. The origin of the horizontal axis is the center of the center jet.

When the crank angle is 270°, the average velocity of the jet is 0.988 m/s. From the mass conservation equation for incompressible flow, the area-mean flow velocity within the round jet can be calculated:

$$U_c A_c = \frac{\pi D_p^2}{4} U_p \tag{5.20}$$

where A_c is the open area of the jet generator, U_c is the average velocity over the round jet generator, D_p is piston diameter, and U_p is the piston velocity. In the oscillatory flow generator, the piston moves in a sinusoidal fashion. The displacement, X_p, can be calculated from the stroke and the frequency,

$$X_p = \frac{\text{Stroke}}{2} \cos(2\pi f t) \tag{5.21}$$

The piston velocity can be obtained by taking the first derivative of the piston displacement,

$$U_p = \dot{X}_p = \pi f \,\text{Stroke}\, \sin(2\pi f t) \tag{5.22}$$

The opening area of the jet generator is 4308 mm^2. The piston velocity is

$$U_p = 0.112 \sin(2\pi f t) \quad \text{m/s}$$

The average velocity over the round jet generator is

$$U_c = 0.95 \sin(2\pi f t) \quad \text{m/s}$$

which matches very well with 0.988 m/s, which is the average velocity measured by the hot wire when the crank angle is 270°.

5.4.1.3 Some Important Parameters in the Round Jet Generator and the LSMU Plates

The displacement of the fluid particle within the round jet also can be calculated from the mass conservation equation for incompressible flow,

$$X_c A_c = \frac{\pi D_p^2}{4} X_p \tag{5.23}$$

so,

$$X_c = 757 \cos\left(2\pi f t\right) \quad \text{mm}$$

The amplitude ratio, A_R, is the fluid displacement during half a cycle divided by the tube length. For the round jet generator, which is 305 mm (12 in.) long, the amplitude ratio is 2.48.

The maximum Reynolds number in the round jet generator is,

$$\mathrm{Re}_{\max} = \frac{Uc_{\max}\, d}{\nu} = \frac{0.95 \times 0.02}{15.9 \times 10^{-6}} = 1195$$

The Valensi number in the round jet generator is,

$$\mathrm{Va} = \frac{d^2 \varpi}{4\nu} = \frac{0.02^2 \times 2\pi \times 0.2}{4 \times 15.9 \times 10^{-6}} = 7.9$$

The flow velocity within the LSMU plates can be calculated from:

$$U_r A_r = \frac{\pi D_p^2}{4} U_p \tag{5.24}$$

where A_r is the open area of the LSMU plates. The flow velocity within the LSMU plates is:

$$U_r = 0.243 \sin(2\pi f t) \quad \text{m/s}$$

The displacement of the fluid particle within the LSMU plates can be calculated as,

$$X_r A_r = \frac{\pi D_p^2}{4} X_p$$

where

$$X_r = 194 \cos(2\pi f t) \quad \text{mm}$$

For the LSMU of 10 plates, which is 79.4 mm long, the amplitude ratio is 2.44.

5.4.1.4 Jet Penetration of the Round Jet Generator

Dimensionless temperatures at six axial locations have been measured. The six locations are: between the plenum on the jet generator side and the first LSMU plate, between plates 2 and 3, between plates 3 and 4, between plates 5 and 6, between plates 8 and 9, and after plate 10. The dimensionless temperature profiles are shown in figures 5.28 through 5.33.

During the blowing half of the cycle, when the flow is passing from the jet generator to the LSMU plates, the crank angle changes from 180° to 360°. Three cold jets, which are distinguished from the rest of the region, can be seen in figure 5.28. Figure 5.32 shows that the jet edges are nearly imperceptible. The jet penetration depth is about the thickness of 8 LSMU plates, which is 63.5 mm. The hydraulic diameter of the LSMU plates is 4.872 mm so the jet penetration depth is about 13 times the hydraulic diameter. A movie of the jet penetration was generated and can be obtained from the authors (contact tsimon@me.umn.edu.) In figures 5.32 and 5.33, one can see an effect of the boundary of the test section at the larger radius of figure 5.22 beginning to influence the temperature data for $r > 35$ mm.

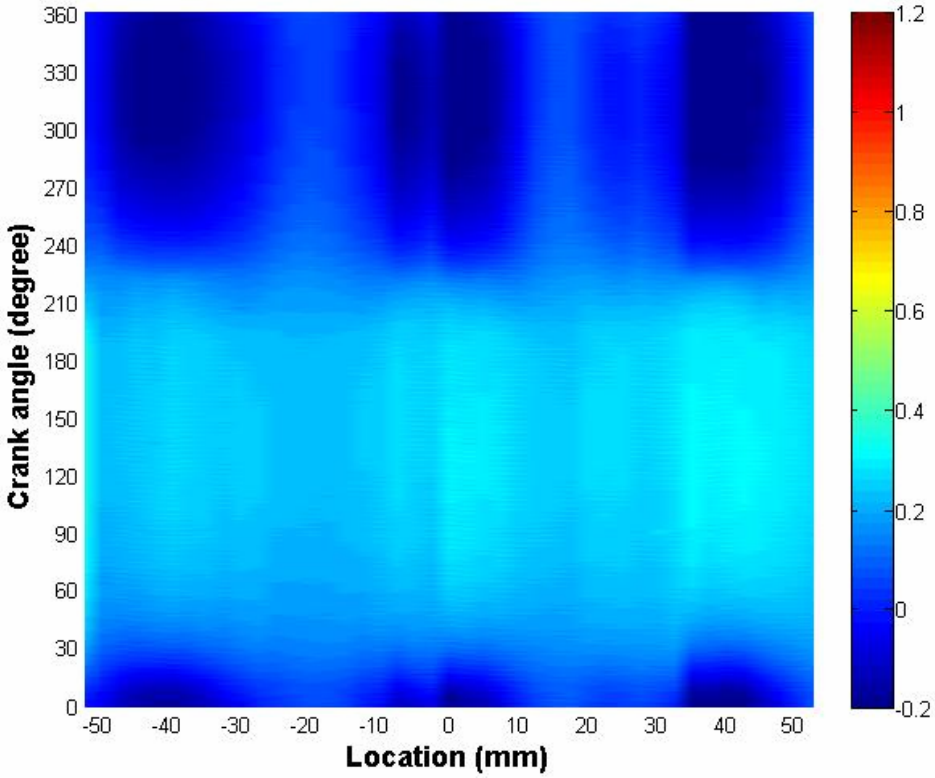

Figure 5.28.—Dimensionless temperature profiles between the plenum and the first LSMU plate. The origin of the horizontal axis is the center of the center jet. Neighboring jets are centered at -40 mm (the one at the larger radius of fig. 5.20) and 40 mm.

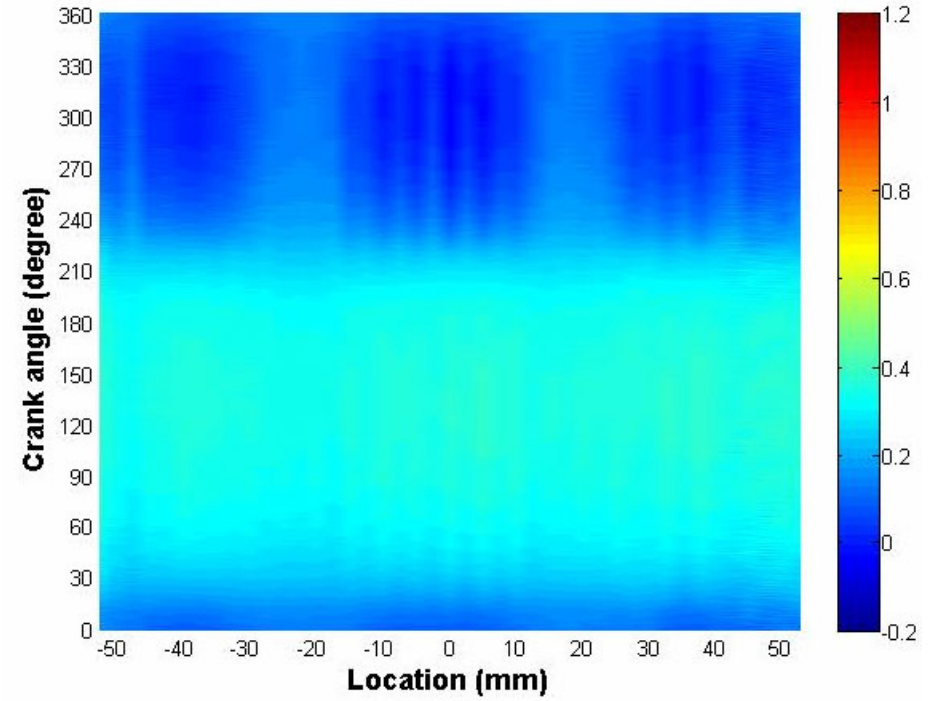

Figure 5.29.—Dimensionless temperature profiles in the middle of the LSMU plates, between plate 2 and 3. The origin of the horizontal axis is the center of the center jet.

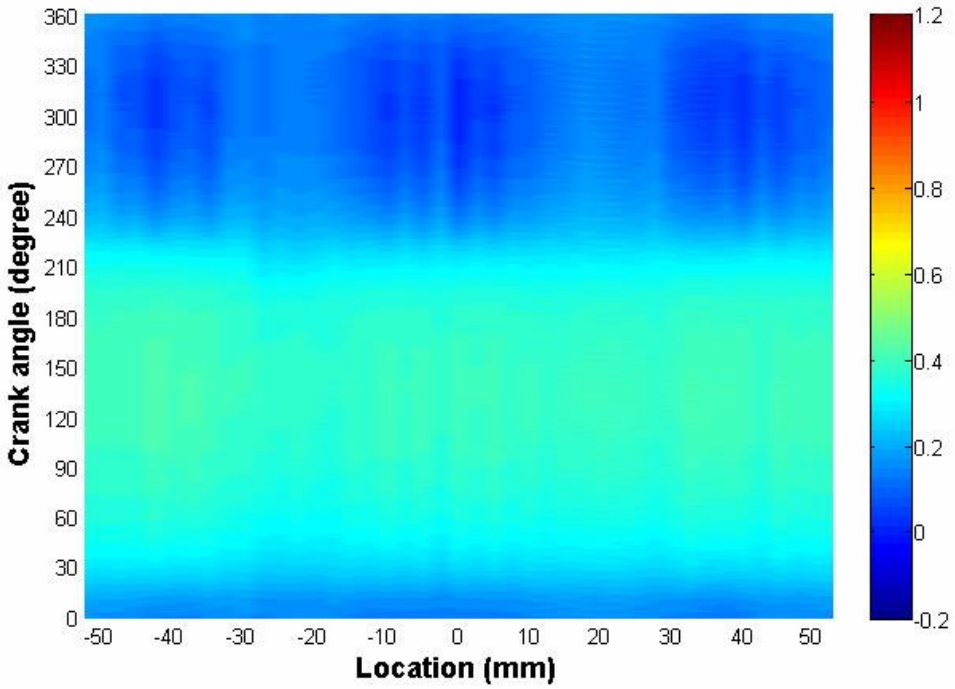

Figure 5.30.—Dimensionless temperature profiles in the middle of the LSMU plates, between plate 3 and 4. The origin of the horizontal axis is the center of the center jet.

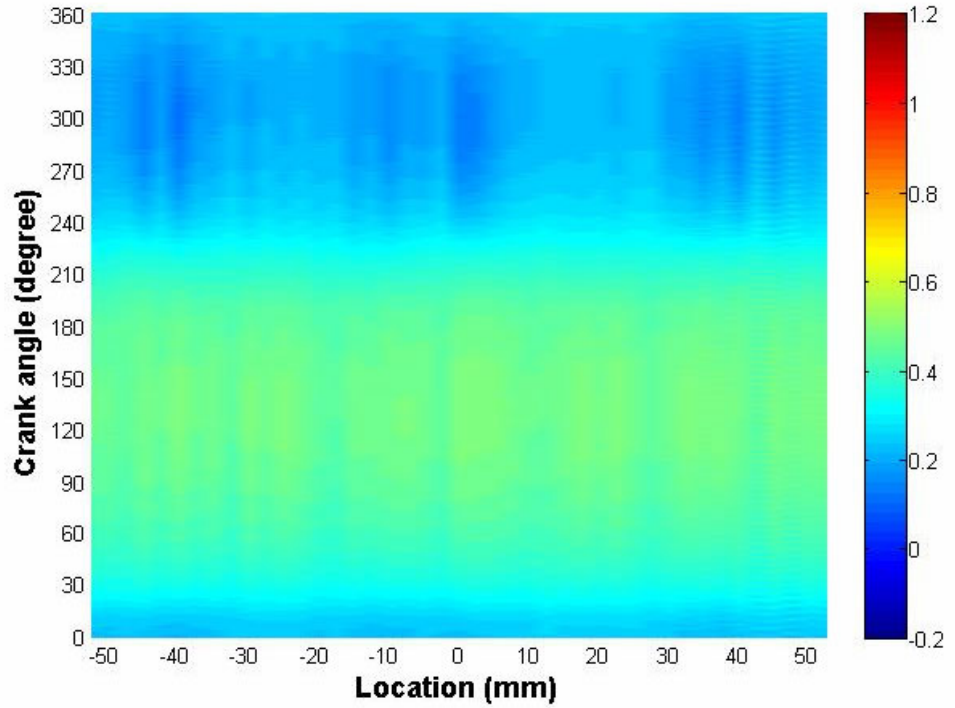

Figure 5.31.—Dimensionless temperature profiles in the middle of the LSMU plates, between plate 5 and 6. The origin of the horizontal axis is the center of the center jet.

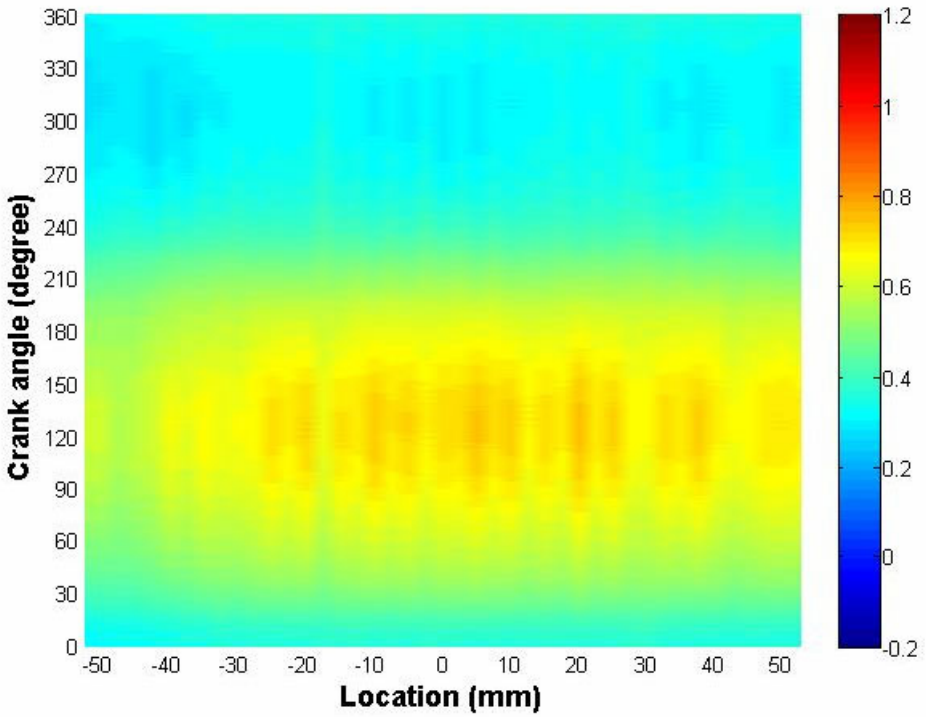

Figure 5.32.—Dimensionless temperature profiles in the middle of the LSMU plates, between plate 8 and 9. The origin of the horizontal axis is the center of the center jet.

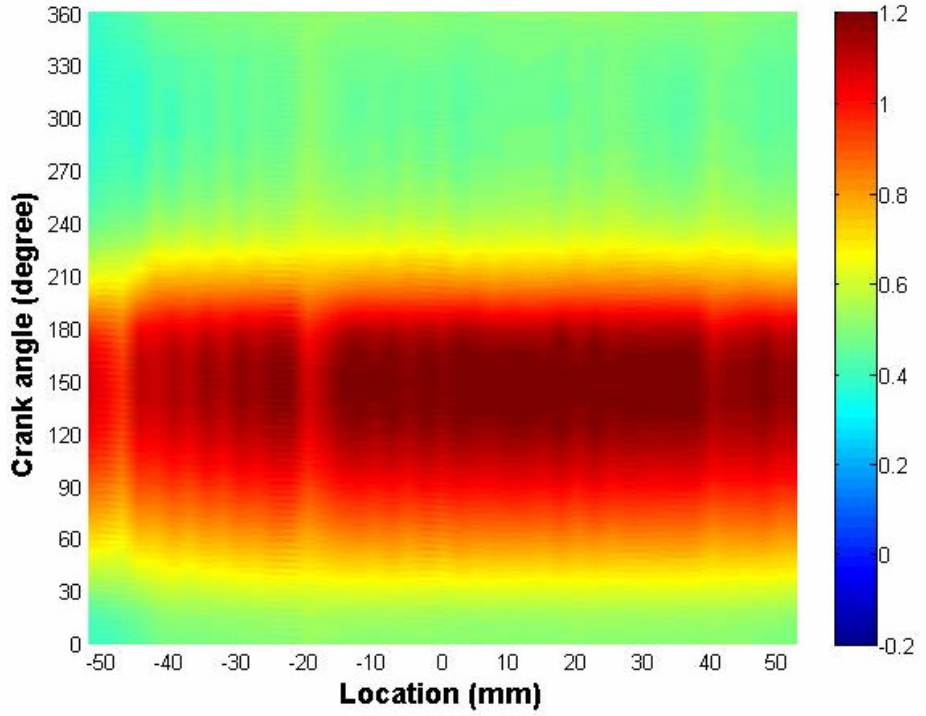

Figure 5.33.—Dimensionless temperature profiles after 10 LSMU plates. The origin of the horizontal axis is the center of the center jet.

5.4.1.5 Jet Growth and the Fraction of Inactive Matrix Material

The center jet's edge, as the jet expands along the axial flow direction, is defined by assuming the edge occurs at that point at which the dimensionless temperature is the average of the maximum and the minimum dimensionless temperatures found in traversing across the jet--at a certain axial location and a certain crank angle. One way of representing this assumption about the jet width, b, is via the temperature expression:

$$\phi(x, b/2, \mathrm{CA}) = \frac{1}{2}(\phi_{\max}(x, \mathrm{CA}) + \phi_{\min}(x, \mathrm{CA})) \tag{5.25}$$

where ± $b/2$ represent the two edges of the jet along the radial direction, with the center of the jet at the origin. Throughout the blowing half cycle, this jet diameter remains almost invariant with crank angle. The dimensionless temperature at 270° crank angle is chosen to evaluate the jet growth. Figure 5.34 shows the jet growth along the axial direction (Note that the jet edges are difficult to identify between plates 5 and 6 and the jet width there is extrapolated).

Figure 5.35 shows the jet penetration in the matrix and the jet penetration depth x_p. The fraction of inactive matrix material is the fraction of matrix material that is not participating fully in thermal exchange with the working medium over the jet penetration depth, x_p. The fitting equation of figure 5.34 can be used to get jet diameter, $b(x)$, over $0<x/d_h<13$ for the LSMU plates. For one jet, the corresponding matrix area is a hexagon with side length of 23.1 mm, which is shown in figure 5.36. The area of the hexagon is A_j. The fraction of inactive matrix material is calculated by

$$F = \frac{1}{x_p}\int_0^{x_p} \frac{\left[A_j - \frac{\pi b(x)^2}{4}\right]}{A_j} dx \tag{5.26}$$

A value of 47% is found for the LSMU plates with the round jet generator.

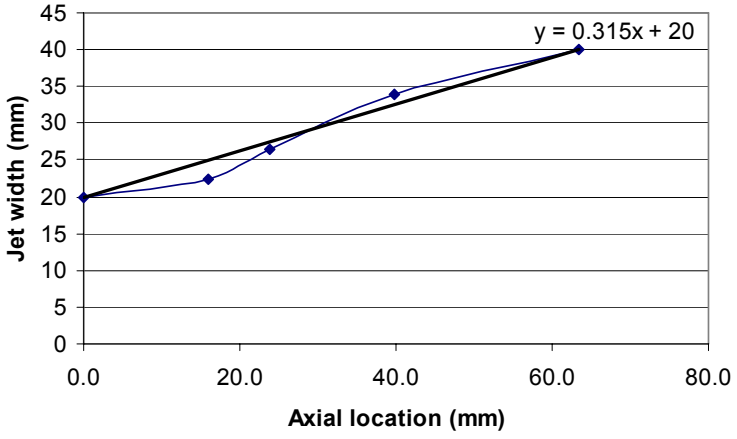

Figure 5.34.—Jet width of the center jet at crank angle 270°.

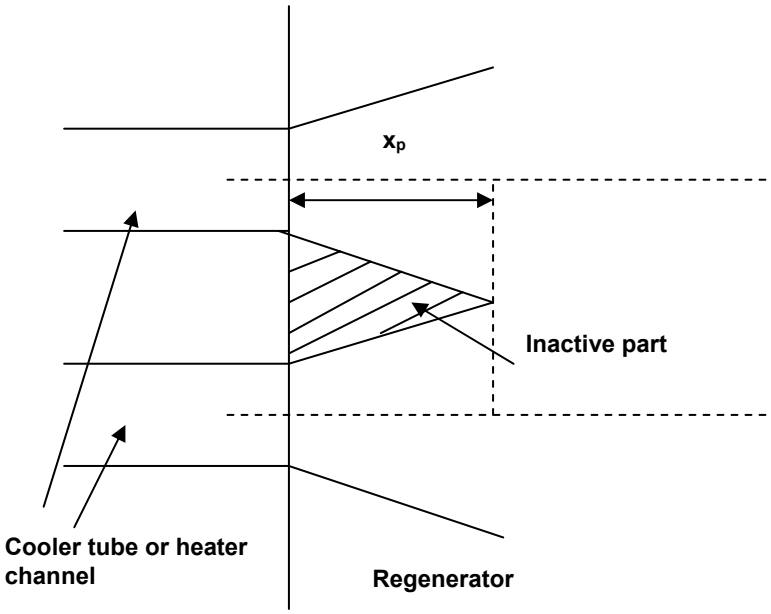

Figure 5.35.—Jet penetration.

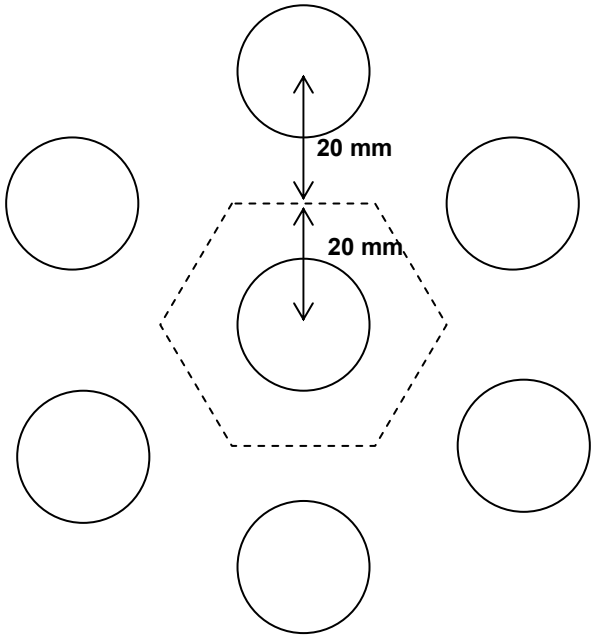

Figure 5.36.—Area assigned to each jet.

5.4.2 The Jet Penetration Study for the Slot Jet Generator

Figure 5.37 shows the slot jet generator and the plenum which is a sector of an annulus in shape. The fabricated slot jet generator is shown in figure 5.38. The slot channels are separated by the fins in the slot jet generator. The channel width is 8.5 mm and the fin thickness is 23 mm. The jet generator is 30.5 cm (12 in.) long. The experimental setup is shown in figure 5.24.

5.4.2.1 Jet-to-Jet Uniformity of the Slot Jet Array

To verify that the flow is uniformly distributed in the slot jet generator under oscillatory flow conditions, the velocities within the plenum between the jet generator and the LSMU regenerator plates are measured. Results are given versus time within an oscillation cycle based upon an ensemble average of 50 cycles. The hot-wire probe is driven by the stepper motor to move horizontally along a line which passes through the center of the jet generator, normal to the slots (as indicated in fig. 5.37).

The velocity measurement is taken at a sampling frequency of 500 Hz for 50 cycles. Velocity profiles taken during the blowing half of the cycle, when the flow is passing from the jet generator to the LSMU plates, are shown in figure 5.39. The origin of the horizontal axis is the center of the center jet. Velocity profiles show that the jets from the three slot channels shown are very similar to one another. Velocity profiles during the drawing half of the cycle, when the flow is passing from the LSMU plates back to the jet generator, are shown in figure 5.40. These velocity profiles show that the velocities in the center are slightly lower than the velocities which are distant from the center. Figure 5.41 shows the geometry of the 6-rib LSMU plate and the traversing route of the hot-wire probe. The flow in the center is very close to the rib of the 6-rib LSMU plate, which decreases the flow velocity. Figure 5.42 shows the geometry of the 7-rib LSMU plate and the traversing route of the hot wire probe.

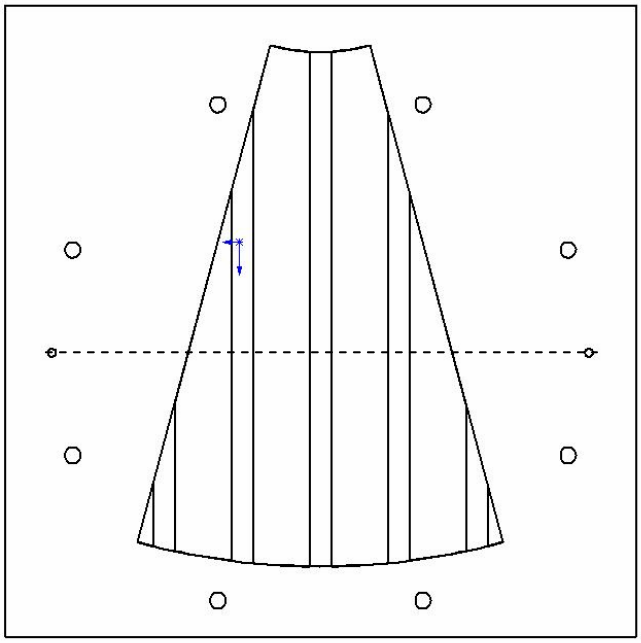

Figure 5.37.—The slot jet generator and the plenum shape, a sector of an annulus.

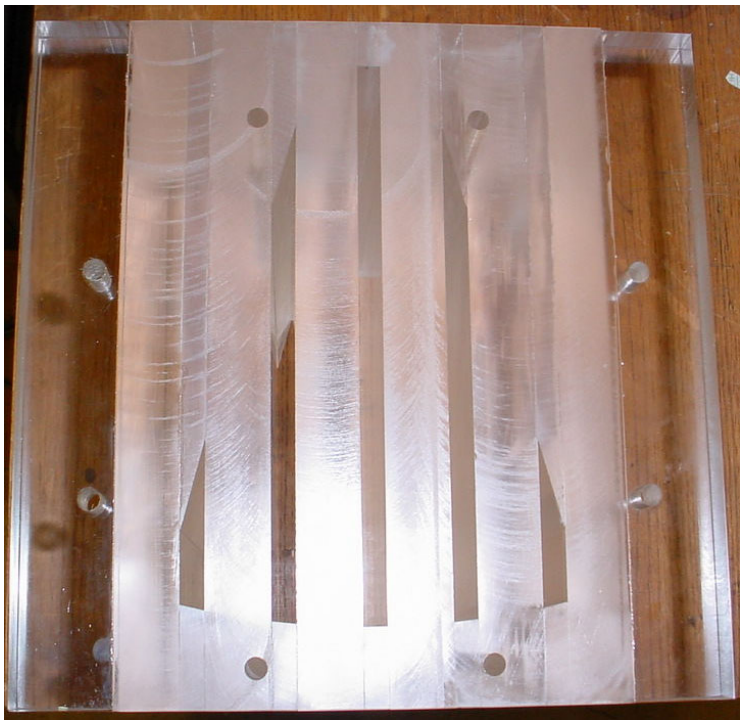

Figure 5.38.—The slot jet generator.

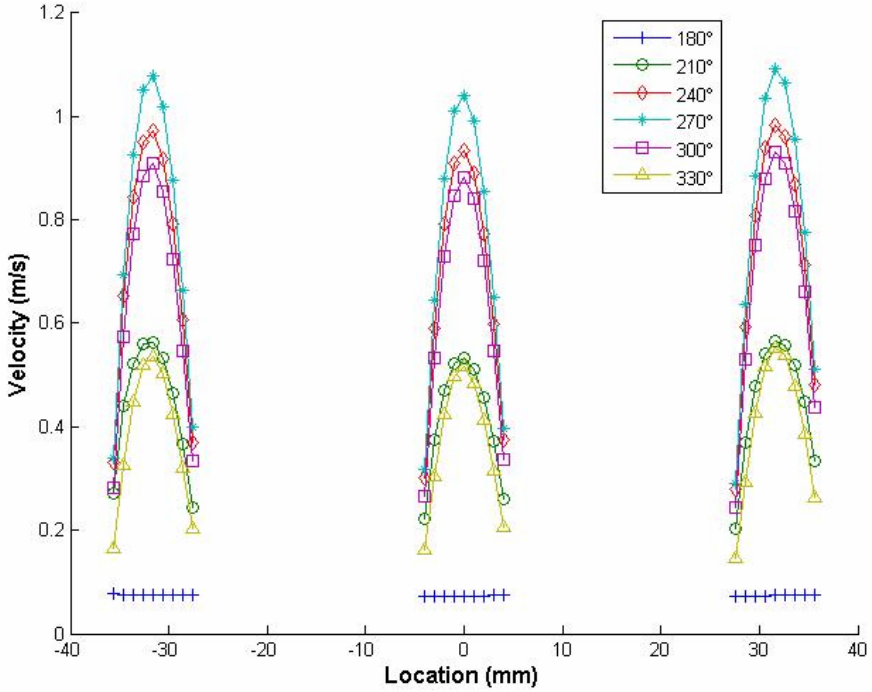

Figure 5.39.—Velocity profiles during the blowing half of the cycle, when the flow is passing from the jet generator to the LSMU plates. The origin of the horizontal axis is the center of the center jet.

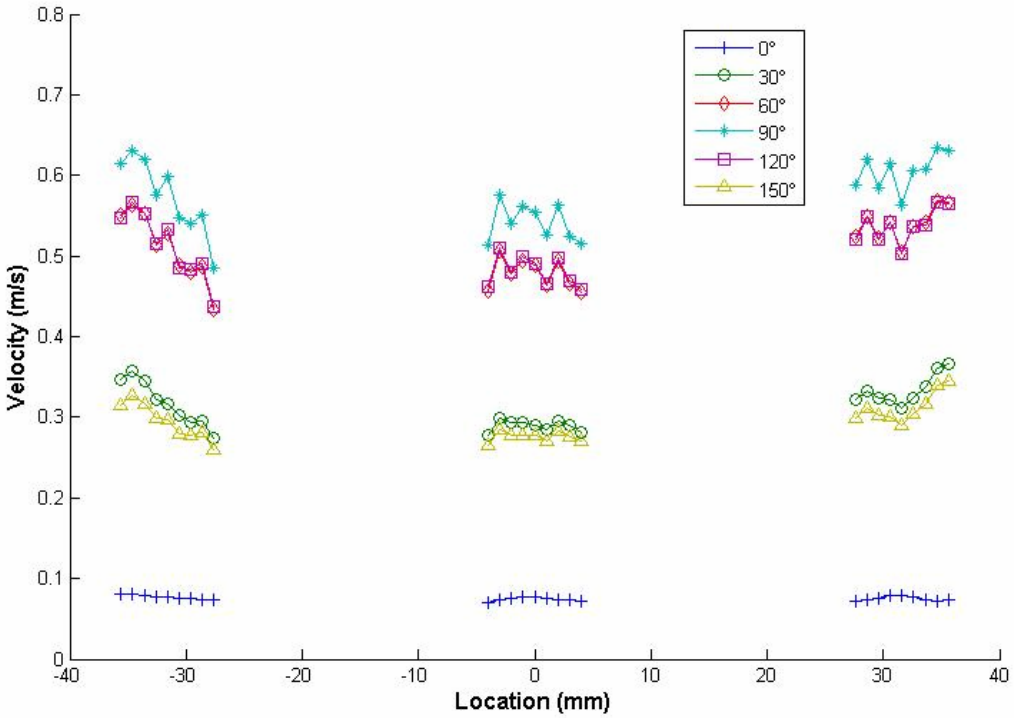

Figure 5.40.—Velocity profiles during the drawing half of the cycle, when the flow is passing from the LSMU plates back to the jet generator. The origin of the horizontal axis is the center of the center jet.

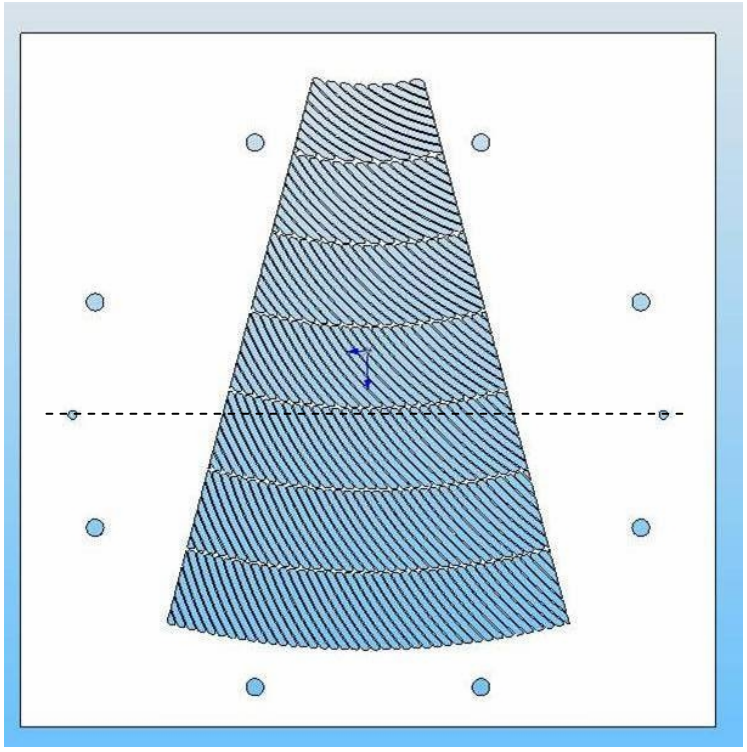

Figure 5.41.—Geometry of the 6-rib LSMU plate.

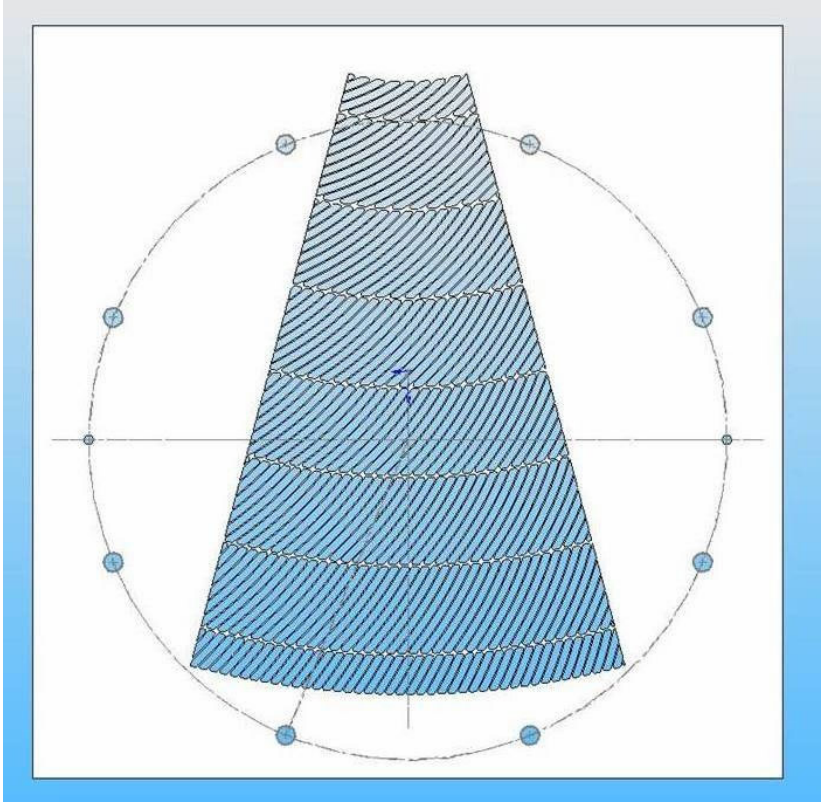

Figure 5.42.—Geometry of the 7-rib LSMU plate.

When the crank angle is 270°, the average velocity of the jet is 0.783 m/s. From the mass conservation equation for incompressible flow, the flow velocity within the slot jet can be calculated:

$$U_h A_h = \frac{\pi D_p^2}{4} U_p \tag{5.27}$$

where A_h is the open area of the slot jet generator, U_h is the average velocity over the slot jet generator, D_p, is piston diameter and U_p is the piston velocity.

In the oscillatory-flow generator, the piston moves in a sinusoidal fashion. The displacement, X_p, can be calculated from the stroke and the frequency,

$$X_p = \frac{\text{Stroke}}{2} \cos(2\pi f t) \tag{5.28}$$

The piston velocity can be obtained by taking the first derivative of the piston displacement,

$$U_p = \dot{X}_p = \pi f \,\text{Stroke}\left[\sin\left(2\pi f t\right)\right] \tag{5.29}$$

The open area of the slot jet generator is 5278 mm^2. The piston velocity is

$$U_p = 0.112 \sin\left(2\pi f t\right) \quad \text{m/s}$$

The average velocity over the slot jet generator is

$$U_c = 0.776\sin(2\pi ft) \quad \text{m/s}$$

which matches very well with 0.783 m/s, which is the average velocity measured by hot wire when the crank angle is 270°.

5.4.2.2 Some Important Parameters in the Slot Jet Generator

The displacement of the fluid particle within the slot jet also can be calculated from the mass conservation equation for incompressible flow,

$$X_h A_h = \frac{\pi D_p^2}{4} X_p \tag{5.30}$$

so,

$$X_h = 618\cos(2\pi ft) \quad \text{mm}.$$

The amplitude ratio, A_R, is the fluid displacement during half a cycle divided by the tube length. For the slot jet generator, which is 304.8 mm (12 in.) long, the amplitude ratio is 2.03.

The maximum Reynolds number in the slot jet generator is,

$$\mathrm{Re}_{\max} = \frac{U_{h,\max}\, d}{\nu} = \frac{0.776 \times 0.017}{15.9 \times 10^{-6}} = 830$$

The Valensi number in the slot jet generator is,

$$\mathrm{Va} = \frac{d^2\omega}{4\nu} = \frac{0.017^2 \times 2\pi \times 0.2}{4 \times 15.9 \times 10^{-6}} = 5.7$$

5.4.2.3 Jet Penetration of the Slot Jet Generator

Dimensionless temperatures at five axial locations were measured. The five locations were: between the plenum on the jet generator side and the first LSMU plate, between plates 3 and 4, between plates 5 and 6, between plates 6 and 7, and between plates 8 and 9. The dimensionless temperature profiles are shown in figures 5.43 through 5.47. A movie of the jet penetration was generated and can be obtained from the authors (contact tsimon@me.umn.edu.)

During the blowing half of the cycle, when the flow is passing from the jet generator to the LSMU plates, the crank angle changes from 180° to 360°. Three cold jets, which are distinguished from the rest of the region, can be seen in figure 5.43 (between the plenum and the first LSMU plate). Figure 5.46 shows that the jet edges are nearly imperceptible between plates 6 and 7. The jet penetration depth is about the thickness of 6 LSMU plates, which is 47.6 mm. The hydraulic diameter of the LSMU plates is 4.872 mm so the jet penetration depth is about 10 times the hydraulic diameter. In figures 5.44 and 5.45, one can see the effect of the rib of the 6-rib LSMU plate, which causes the center jet to have slightly higher temperatures during the blowing half cycle.

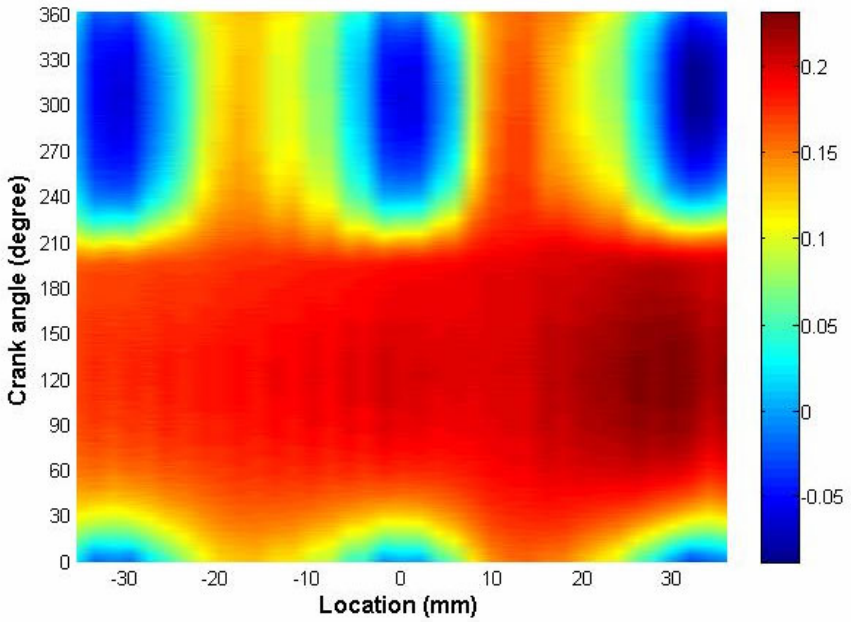

Figure 5.43.—Dimensionless temperature profiles between the plenum and the first LSMU plate. The origin of the horizontal axis is the center of the center jet. Neighboring jets are centered at -31.5 mm (left side of fig. 5.37) and 31.5 mm.

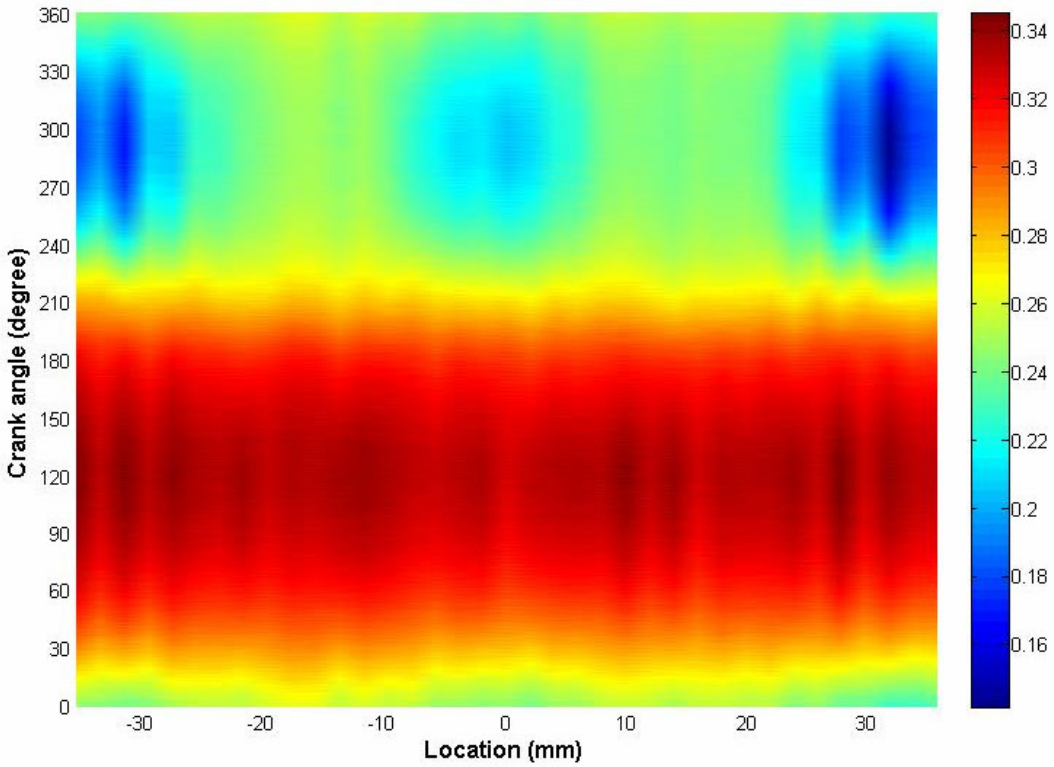

Figure 5.44.—Dimensionless temperature profiles in the middle of the LSMU plates, between plates 3 and 4. The origin of the horizontal axis is the center of the center jet.

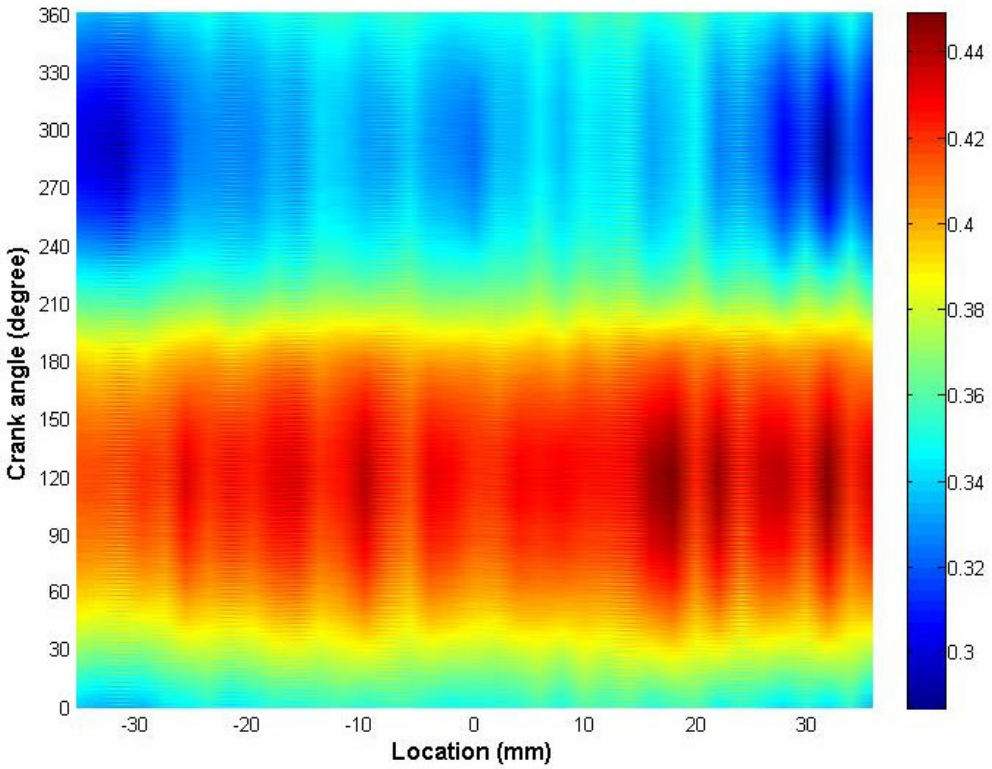

Figure 5.45.—Dimensionless temperature profiles in the middle of the LSMU plates, between plates 5 and 6. The origin of the horizontal axis is the center of the center jet.

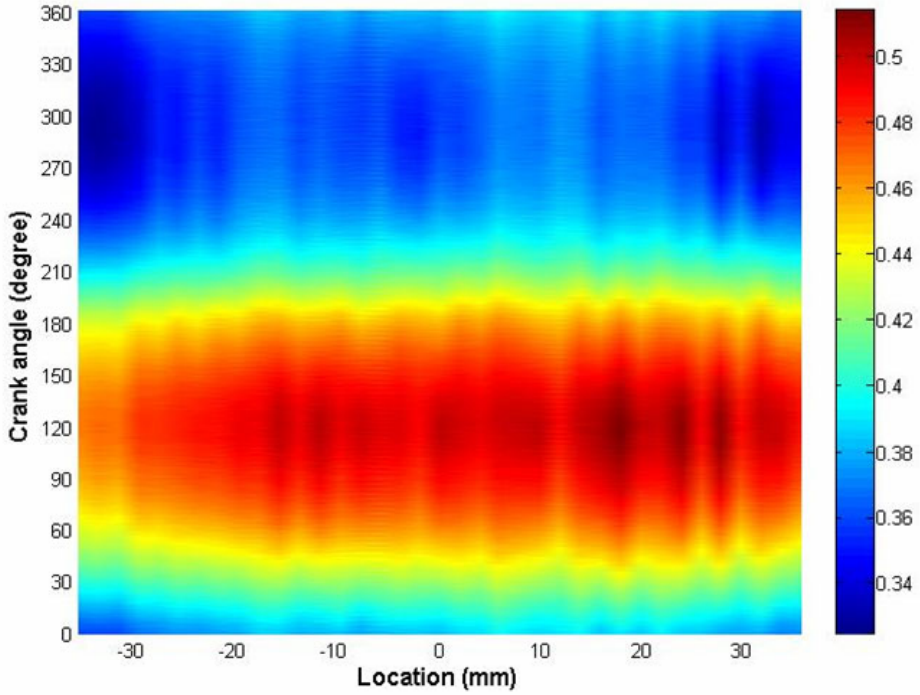

Figure 5.46.—Dimensionless temperature profiles in the middle of the LSMU plates, between plates 6 and 7. The origin of the horizontal axis is the center of the center jet.

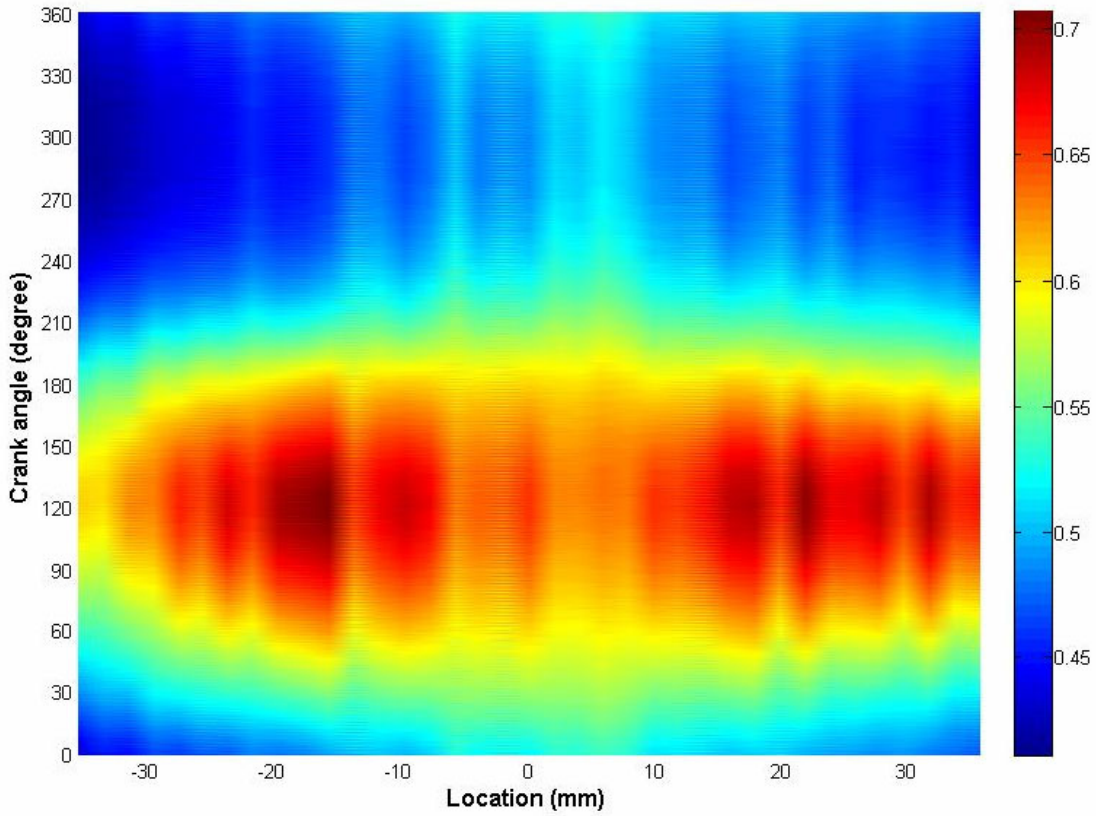

Figure 5.47.—Dimensionless temperature profiles in the middle of the LSMU plates, between plates 8 and 9. The origin of the horizontal axis is the center of the center jet.

5.4.2.4 Jet Growth and the Fraction of Inactive Matrix Material

Throughout the blowing half cycle, the slot jet width remains almost invariant with crank angle. The dimensionless temperature at 270° crank angle is chosen to evaluate the jet growth. Figure 5.48 shows the jet growth. The jet edges are difficult to identify between plates 6 and 7 and the jet width there is found by extrapolation.

The fraction of inactive matrix material is calculated by

$$F = \frac{1}{x_p} \int_0^{x_p} \frac{[S - b(x)]L}{SL} dx \tag{5.31}$$

where $b(x)$ is the jet width, x_p is the jet penetration depth, S is the jet center-to-center spacing (31.5 mm), and L is the jet length. A value of 69% is found for the LSMU plates with the slot jet generator. This compares to 47% for the round jets entering the LSMU regenerator and 55% for the round jets entering the 90% porous screen regenerator studied by Niu et al. 2003.

5.5 Unsteady Heat Transfer Measurements

Unsteady heat transfer with the LSMU plates was investigated. The LSMU dynamically simulates the microfabricated regenerator plates of the segmented-involute-foil regenerator.

5.5.1 Embedded Thermocouple

Figure 5.49 shows a sketch of one embedded thermocouple. The drilled hole is 0.30 mm (0.012 in.) in diameter and 2 mm (0.080 in.) deep. Figure 5.50 shows a picture of one of the embedded thermocouple installations.

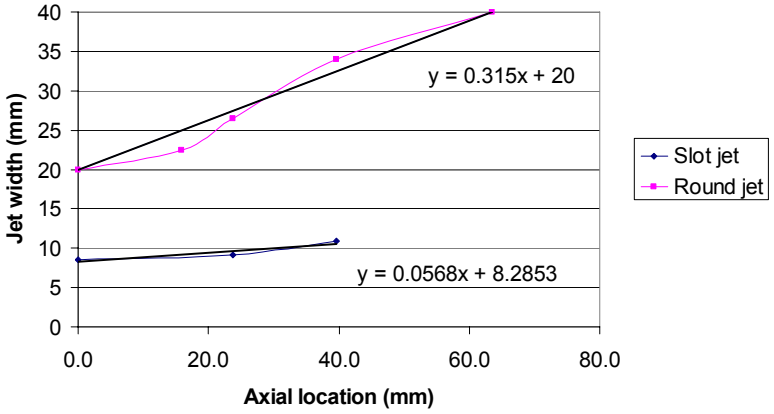

Figure 5.48.—Jet width of slot jet and round jet at crank angle 270°.

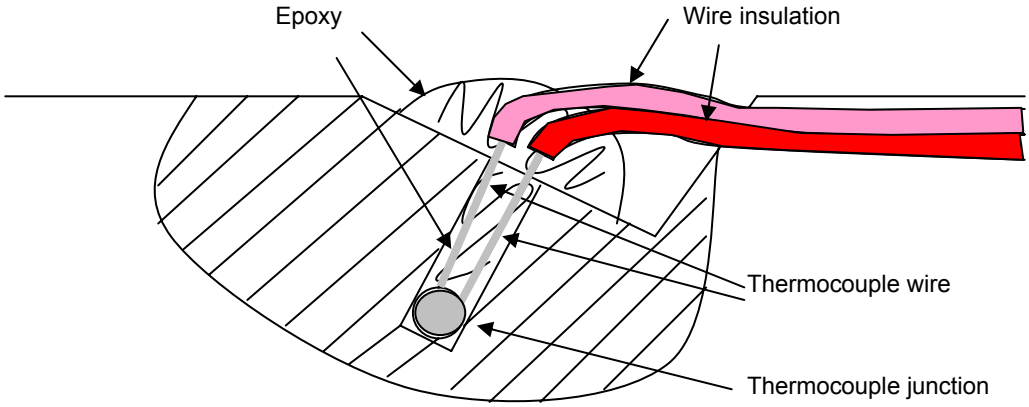

Figure 5.49.—Sketch of embedded thermocouple.

Figure 5.50.—Picture of one embedded thermocouple.

5.5.2 Experimental Procedure

There are three thermocouples mounted in the 6-rib plate and three thermocouples mounted in the 7-rib plate. The three thermocouple locations are labeled 1 to 3 along the radial direction pointing to the center of the arc, as shown in figure 5.51. For the case presented in this report, ten plates are stacked in the design order. The 6-rib plate with thermocouples is plate 5 and the 7-rib plate with thermocouples is plate 6. One thermocouple is traversed between plates 5 and 6 to measure the air temperature, as shown in figure 5.52. The thermocouple junctions in plate 5 are near the traversing thermocouple, while the thermocouple junctions in plate 6 are more distant from the traversing thermocouple. For every embedded thermocouple location, air temperatures are measured at 5 locations on the same radial line as that on which the embedded thermocouples reside: -2 mm, -1 mm, 0, 1 mm, and 2 mm away from the embedded thermocouple radial location, labeled "1" through "5," respectively. Two runs with different warm-up times, both sufficiently large, were conducted. Table 5.4 shows the case names of the two runs. Case B13 is chosen to show the data processing.

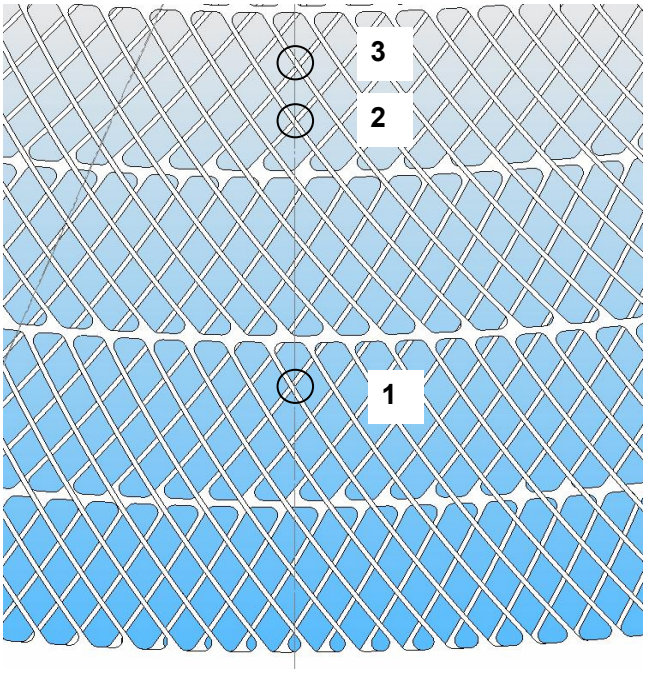

Figure 5.51.—Locations of the embedded thermocouples.

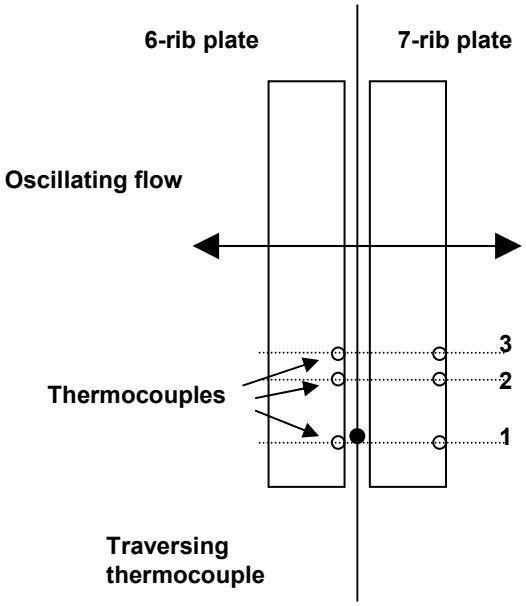

Figure 5.52.—Temperature measurement locations for the case presented.

TABLE 5.4.—CASE NAMES OF THE TWO RUNS

	Case	Date	Number of plates	Tra. t.c. between plate	Embedded t.c. loc.	Tra. t.c. loc.
1	A11	8/11	10	5 and 6	1	1
2	A12	8/11	10	5 and 6	1	2
3	A13	8/11	10	5 and 6	1	3
4	A14	8/11	10	5 and 6	1	4
5	A15	8/11	10	5 and 6	1	5
6	A21	8/11	10	5 and 6	2	1
7	A22	8/11	10	5 and 6	2	2
8	A23	8/11	10	5 and 6	2	3
9	A24	8/11	10	5 and 6	2	4
10	A25	8/11	10	5 and 6	2	5
11	A31	8/11	10	5 and 6	3	1
12	A32	8/11	10	5 and 6	3	2
13	A33	8/11	10	5 and 6	3	3
14	A34	8/11	10	5 and 6	3	4
15	A35	8/11	10	5 and 6	3	5
16	B11	8/16	10	5 and 6	1	1
17	B12	8/16	10	5 and 6	1	2
18	B13	8/16	10	5 and 6	1	3
19	B14	8/16	10	5 and 6	1	4
20	B15	8/16	10	5 and 6	1	5
21	B21	8/16	10	5 and 6	2	1
22	B22	8/16	10	5 and 6	2	2
23	B23	8/16	10	5 and 6	2	3
24	B24	8/16	10	5 and 6	2	4
25	B25	8/16	10	5 and 6	2	5
26	B31	8/16	10	5 and 6	3	1
27	B32	8/16	10	5 and 6	3	2
28	B33	8/16	10	5 and 6	3	3
29	B34	8/16	10	5 and 6	3	4
30	B35	8/16	10	5 and 6	3	5

After at least 5 hr of warm up time, data collection begins:

Step 1: Hot end and cold end plenum temperatures of the LSMU test setup are collected for 20 cycles.
Step 2: Solid temperatures at location 1 in the 6-rib plate and the 7-rib plate, and air temperature around location 1 are collected simultaneously. Data are measured over 50 cycles.
Step 3: Hot end and cold end plenum temperatures of the LSMU test setup are collected for 20 cycles.
Step 4: Solid temperatures at location 2 in the 6-rib plate and the7-rib plate, and air temperature around location 2 are collected simultaneously. Data are measured over 50 cycles.
Step 5: Hot end and cold end plenum temperatures of the LSMU test setup are collected for 20 cycles.
Step 6: Solid temperatures at location 3 in the 6-rib plate and the 7-rib plate, and air temperature around location 3 are collected simultaneously. Data are measured over 50 cycles.
Step 7: Hot end and cold end plenum temperatures of the LSMU test setup are collected for 20 cycles.

5.5.3 LSMU Unsteady-Heat-Transfer-Measurement Results

Assuming the axial temperature distribution of the fin is linear, one can perform an energy balance of the plate fin in the vicinity of the embedded thermocouple:

$$h(x,r,t)A_s(T_f(x,r,t)-T_s(x,r,t))=mC\frac{\partial T_s(x,r,t)}{\partial t} \tag{5.31}$$

where h is the convective heat transfer coefficient, A_s is the surface area of the plate, T_f is the air temperature, T_s is the temperature of the plate, m is the mass of the plate, and C is the specific heat of the plate material. Equation (5.31) becomes:

$$h(x,r,t)(T_f(x,r,t)-T_s(x,r,t))=\rho C\frac{s}{2}\frac{\partial T_s(x,r,t)}{\partial t} \tag{5.32}$$

where s is the plate thickness and ρ is the density of plate material. The convective heat transfer coefficient can be calculated from the measured temperature differences between the air and the plate and temporal gradients of the plate temperature. The Nusselt number can be obtained from:

$$\mathrm{Nu}=\frac{hd_h}{k} \tag{5.33}$$

where d_h is the hydraulic diameter of the channel (4.87 mm) and k is the thermal conductivity of the air.

Figure 5.53 shows the air temperature at location 3 and the solid temperatures of the 6-rib plate and the 7-rib plate at location 1 in case B13. Consider the axial difference between the traversing thermocouple junction and the embedded thermocouple junction in the nearest plate (the 6-rib plate). Because there is an axial gradient in the system, the air temperature at the location of the air thermocouple is not the air temperature at the axial location of the plate thermocouple junction. A small correction is made. It is assumed that the axial temperature gradient of the air can be obtained from the temperature difference between the 6-rib and 7-rib plates. This temperature gradient is used to shift the air temperature from the air thermocouple location 1.3 mm (0.05 in.) to the embedded thermocouple location (6-rib plate). Figure 5.54 shows the temperature difference between the air and solid after the shift. This temperature difference profile is not balanced, which means the value of the peak does not match the valley. Figure 5.55 shows the comparison of the Nusselt number of current experiment with the correlation from the NASA/Sunpower oscillating-flow test rig. Recall that similar measurements by Niu et al. (2003), but in a wire-screen matrix, showed a similar plot of Nusselt number versus cycle position. The following features were noted: The heat flux computed from the solid temporal gradient is zero when the temperature difference is not, creating a zero Nusselt number. The temperature difference becomes zero when the heat flux is not, creating an infinite Nusselt number. When Niu et al. (2003) compared the measured results to correlation results computed by assuming quasi-steady behavior, the comparison was close only when the fluid velocity was near the peak value or during the deceleration part of the cycle. We expected similar behavior here.

Figure 5.56 shows the comparison of the heat flux from this LSMU experiment with the correlation from the NASA/Sunpower oscillating-flow test rig. The lack of symmetry of Nusselt number and heat flux of the current experiment results from the lack of symmetry of the temperature difference profile. A balanced temperature difference profile can be generated by a small shift, moving the curve of figure 5.54 vertically 0.04 °C. This is within the uncertainty in measuring a temperature within this system. This gives the symmetric curve we expect (since the measurement is in the axial center of the LSMU plates). Figure 5.57 shows the temperature difference between the air and solid based after this shift. Figures 5.58 and 5.59 show the Nusselt number comparison and heat flux comparison after this shift is made.

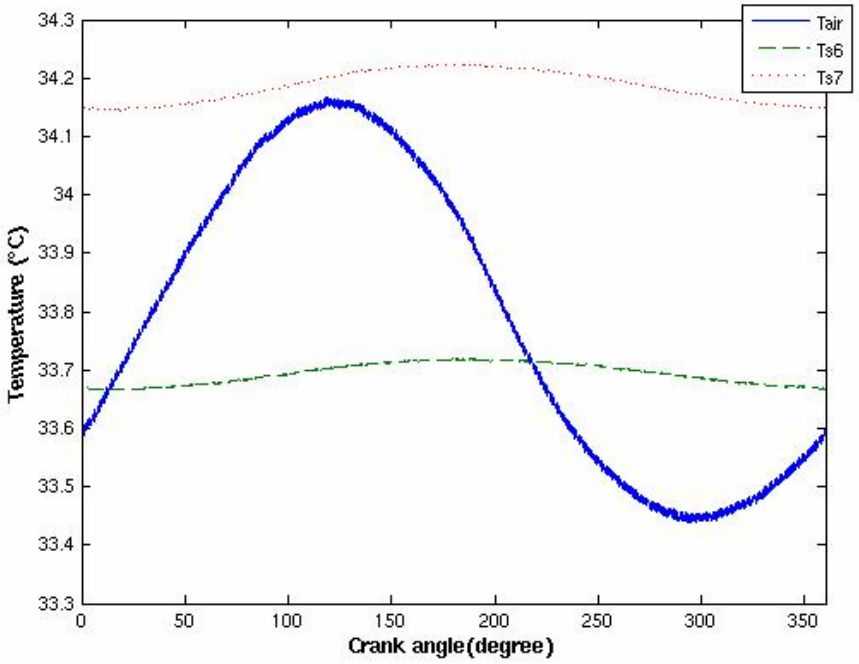

Figure 5.53.—Air temperature at location 3 (T_{air}), solid temperatures of the 6-rib plate (T_{s6}), and the 7-rib plate (T_{s7}), at location 1 in case B13.

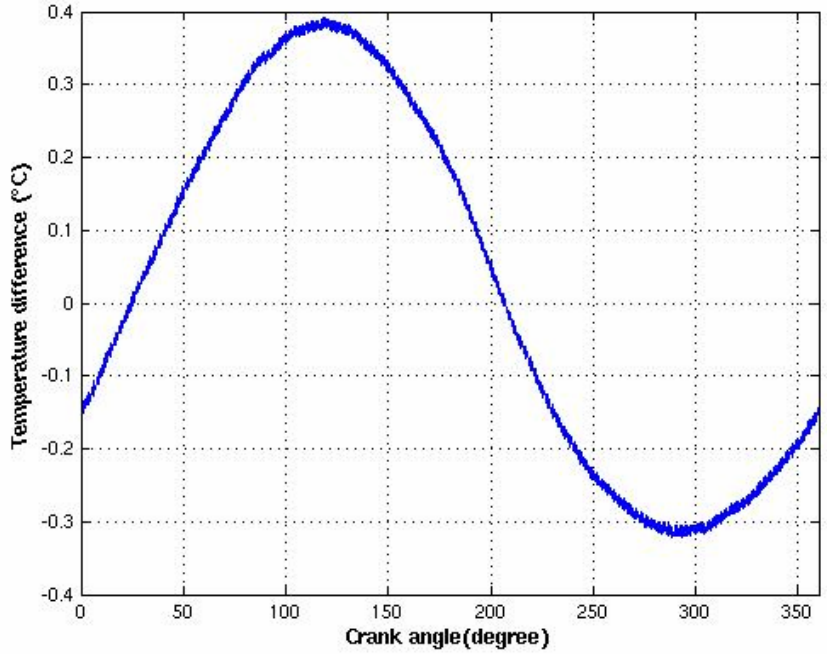

Figure 5.54.—The temperature difference between the air and solid.

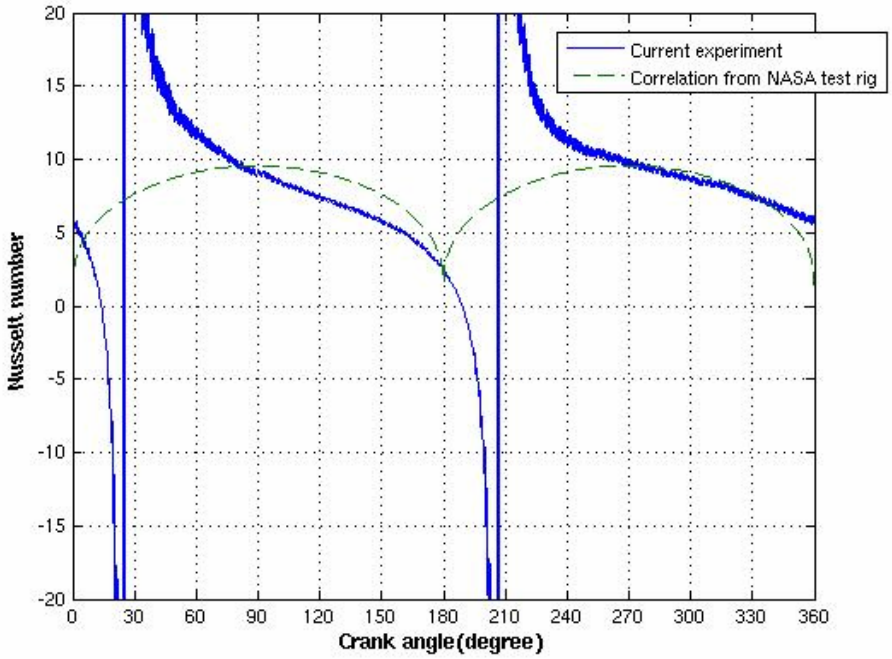

Figure 5.55.—Comparison of the Nusselt number of the current LSMU experiment with the correlation from the NASA/Sunpower oscillating-flow test rig.

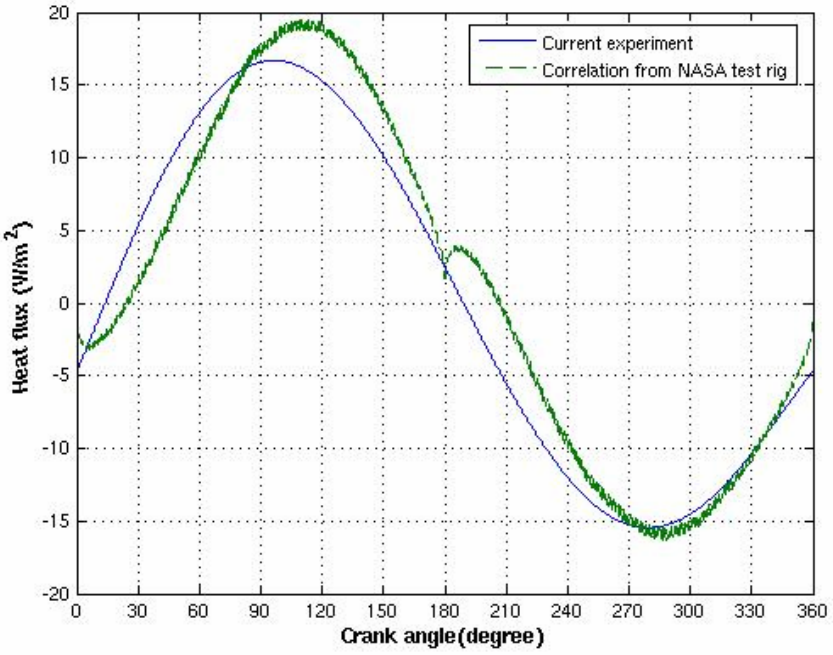

Figure 5.56.—Comparison of the heat flux of the current LSMU experiment with that given by the correlation from NASA/Sunpower test rig and the measured temperature difference.

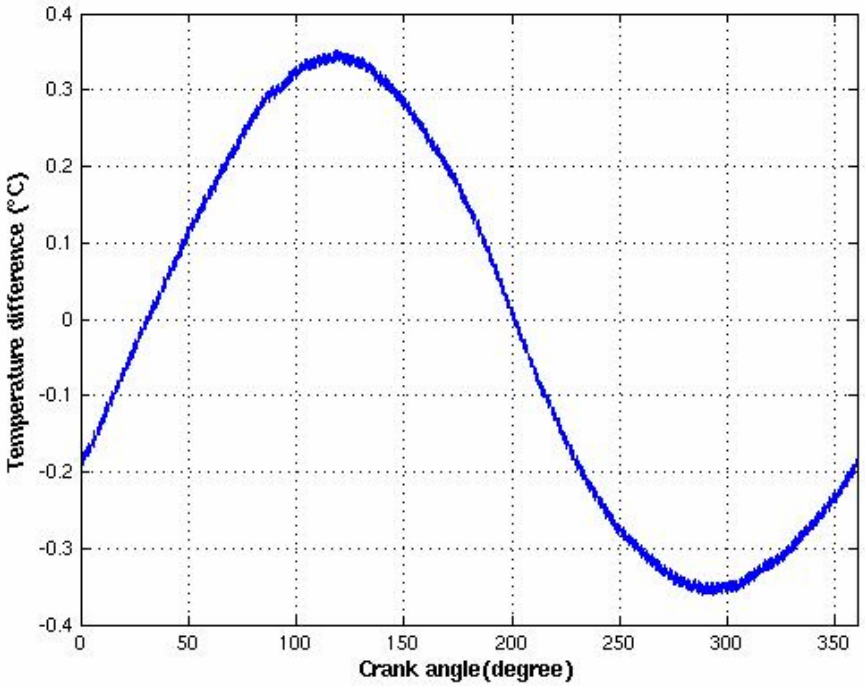

Figure 5.57.—The temperature difference between the air and solid, with the shifted air temperature.

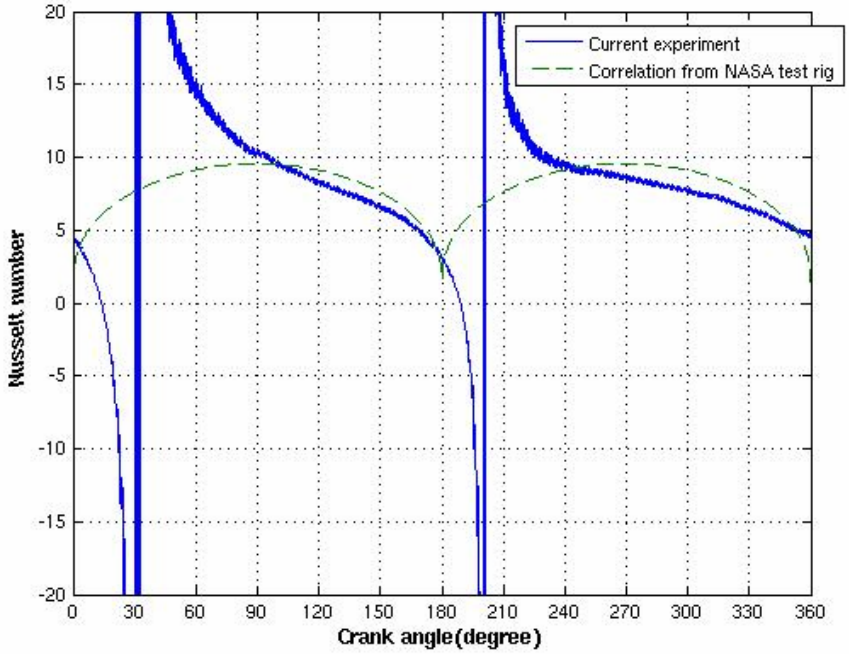

Figure 5.58.—Comparison of the Nusselt number of current LSMU experiment (with the shifted air temperature) with the correlation from NASA/Sunpower oscillating-flow test rig, equation (3.4).

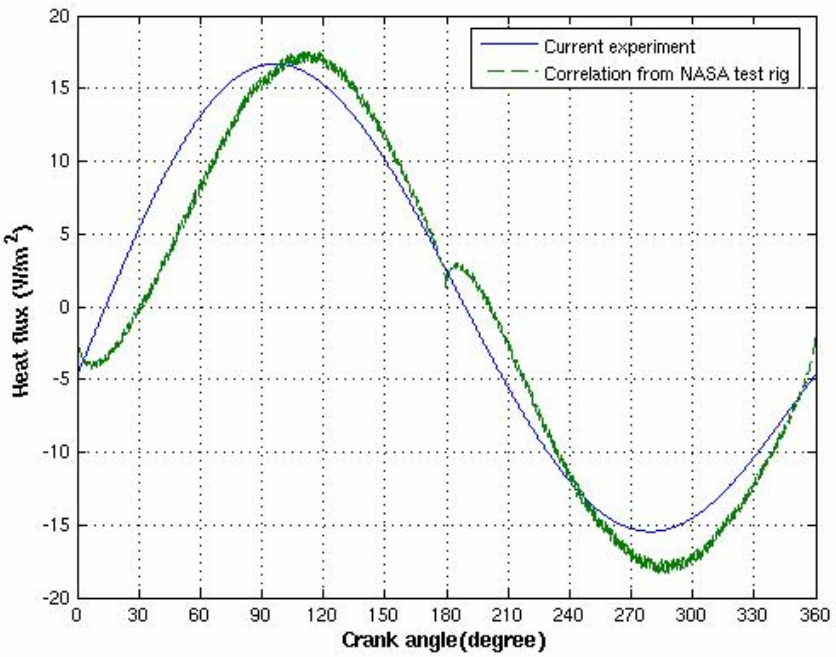

Figure 5.59.—Comparison of the heat flux of the current LSMU experiment with the correlation from the NASA/Sunpower oscillating-flow test rig and the measured temperature difference with the shifted air temperature.

In the following, only the original temperature shift is applied (to effectively move the air thermocouple to the axial location of the metal thermocouple). The Nusselt numbers of the 6 cases for which the traversing thermocouple is at location 3 (closest to the embedded thermocouple) are calculated for cycle positions 120° and 300°. The results are shown in table 5.5. The average value is 7.14 and the RMS is 1.07.

TABLE 5.5—NUSSELT NUMBER FOR DIFFERENT CASES

Case	Crank angle 120°	Crank angle 300°
A13	7.7302	7.5696
A23	8.2965	6.545
A33	6.5366	5.3525
B13	7.3799	8.6731
B23	7.2222	7.9134
B33	5.1717	7.2729

For the following, the second temperature shift is applied (to make the temperature difference plot symmetric, essentially to get the mean air temperature and the mean metal temperature equal to one another). The Nusselt numbers of the 6 cases for which the traversing thermocouple is at location 3 (closest to the embedded thermocouple), are calculated at cycle positions 120° and 300°. The results are shown in table 5.6. The average value is 7.07 and the RMS is 0.86. We note that at a cycle position of 300° the local velocity in our test is 0.21 m/sec. With this, the correlation of Gedeon (eq. (3.4)) gives a Nusselt number of 9.1. The average value in table 5.6 is 7.07, which is about 22% lower than the Gedeon value. The difference is 2.4 standard deviations so we expect it to be significant. We note that the microfabricated regenerator had roughness at the entrance of each channel due to EDM debris whereas our LSMU did not. Roughness would tend to enhance heat transfer.

TABLE 5.6.—NUSSELT NUMBER FOR DIFFERENT CASES BASED ON THE NEW SHIFT

Case	Crank angle 120°	Crank angle 300°
A13	7.7302	7.5696
A23	7.3766	7.2917
A33	6.0522	5.7459
B13	8.2363	7.6841
B23	7.7836	7.3048
B33	6.1025	5.9403

6.0 Analysis Tools and CFD Results (Cleveland State University (CSU))

6.1 Computational Fluid Dynamics (CFD) Summary

The microfabricated, segmented-involute-foil regenerator was numerically investigated utilizing commercial CFD software under both steady-state and oscillatory-flow conditions. The geometry consists of a stack of disks (segments) with each disk containing involute-shaped, micron-range channels, with channel flow direction perpendicular to the plane of the disk. The lateral orientation of the channels alternates from disk to disk in the flow direction. Two-dimensional (2-D) and three-dimensional (3-D) simulations were carried out. Steady-state simulations were performed for Reynolds numbers from 50 up to 2000 based on the channel hydraulic diameter and the mean flow-field velocity.

The results of this CFD research have been validated by comparing the CFD data with the literature and experimental correlations obtained at UMN (LSMU, large-scale geometry) and at Sunpower (actual-scale geometry). For the oscillatory-flow simulations in 2-D and 3-D a base case was chosen using helium as a working fluid, stainless steel for the solid material, 310 K at the hot end, 293 K at the cold end, a maximum Reynolds number, $Re_{max,}$ of 50 and a Valensi number, $Re_{\omega,}$ of 0.229. The effects of changing: 1) the oscillation amplitude and frequency, 2) the thermal contact resistance between layers, and 3) the solid material, on the total-regenerator heat loss (convection and conduction) were documented. These results are expected to be useful for further development of involute-foil regenerators for Stirling engines.

6.2 CFD Introduction

The Fluent CFD commercial code was used for 2-D and 3-D, steady and unsteady, fluid flow and heat transfer simulations of a microfabricated involute-foil regenerator for a Stirling engine. The knowledge gained enabled fundamental understanding of how fluid flow and heat transfer takes place inside the segmented-involute-foil flow paths. It also helped provide support for physical testing (large-scale and actual-size); comparison of the microscale CFD results with the test results and Sage 1-D code simulations, provided additional insight for making decisions about the involute-foil design details.

In a Stirling engine the regenerator is one of the most important parts. In search of an improved regenerator, a novel segmented-involute-foil design was proposed. It consists of two types of alternately stacked disks with microfabricated channels. Figure 6.1 (similar to fig. 3.1 shown earlier) shows a progressively exploded flow direction view of one of the involute-foil regenerator disks. On the second zoom the channels can be seen more clearly. The disk portrayed in figure 6.1 has six ribs. There is a second type of disk that has seven ribs. This enables the staggering of the ribs in the stack, to reduce axial conduction and improve axial channeling of the flow.

Figure 6.2 shows a two-layer view down the flow path while figure 6.3 shows a 3-D view in which one can distinguish the alternate orientations of four layers of the involute-foil flow channels. Both figures show the alternating-layer ribs and indicate how each layer of ribs was offset from its two adjacent layers. Figure 6.4 (similar to fig. 3.2 shown earlier) shows a 3-D view of only one channel of one layer with dimension labels. It can be seen in this figure that the walls of the channel are curved with an

involute-foil profile. Table 6.1 shows involute-foil channel dimensions and the segment or layer length (thickness, in the table). Note that the channel "width," *W*, given in table 6.1 is a nominal value; as can be seen in the middle view of figure 6.1, *W* varies somewhat from the inner to the outer ring of each layer of the actual-size involute-foil segments (this variation of "*W"* is also true for the large-scale segmented-involute-foils of the LSMU—as can be seen in figs. 5.41 and 5.42).

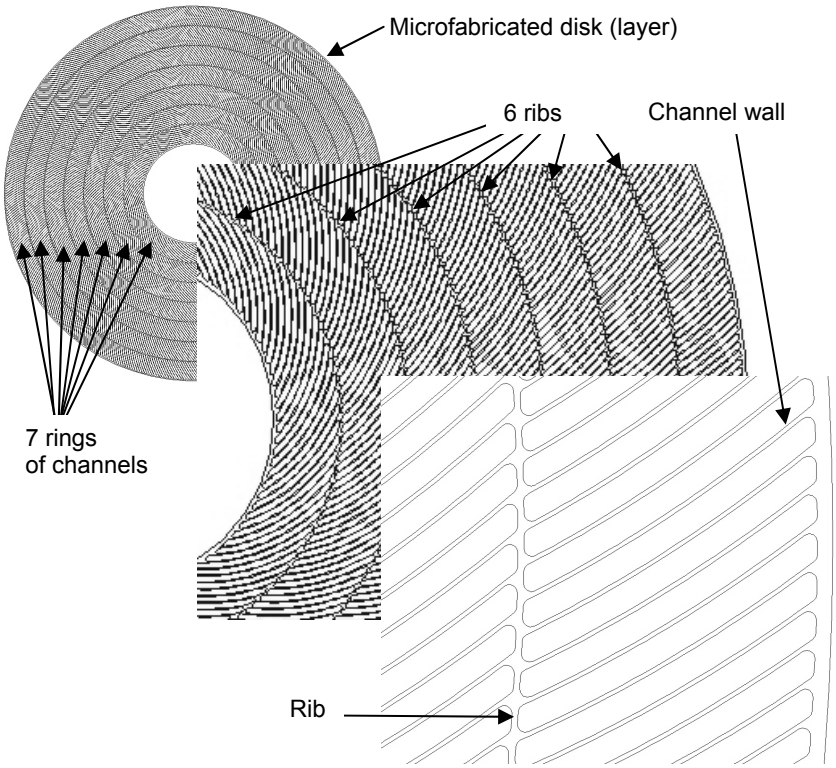

Figure 6.1.—Exploded view of the microfabricated disk.

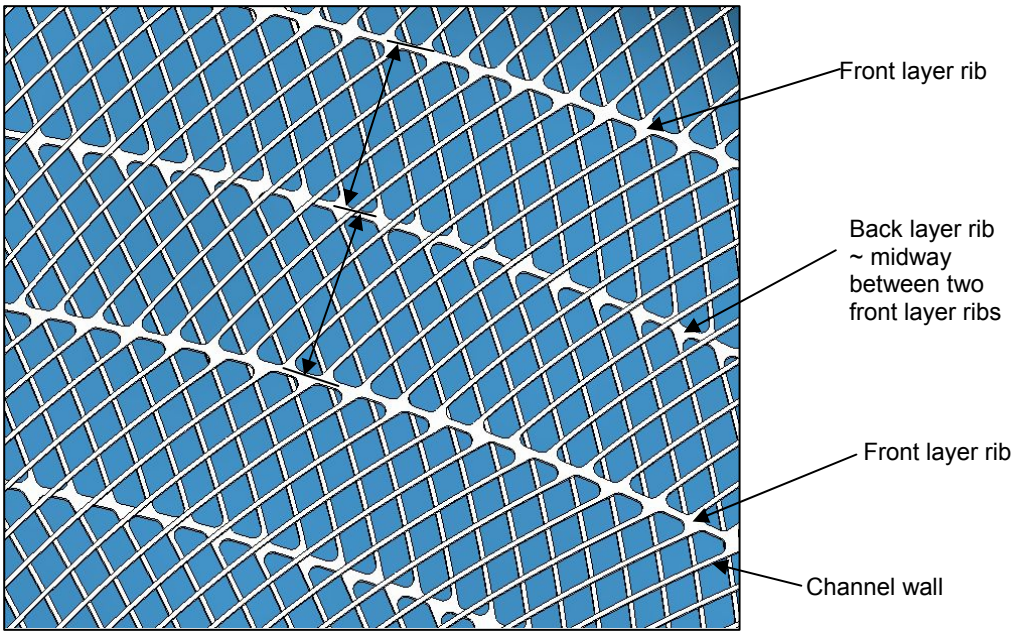

Figure 6.2.—Frontal view of two layers of microfabricated segmented-involute-foil channels.

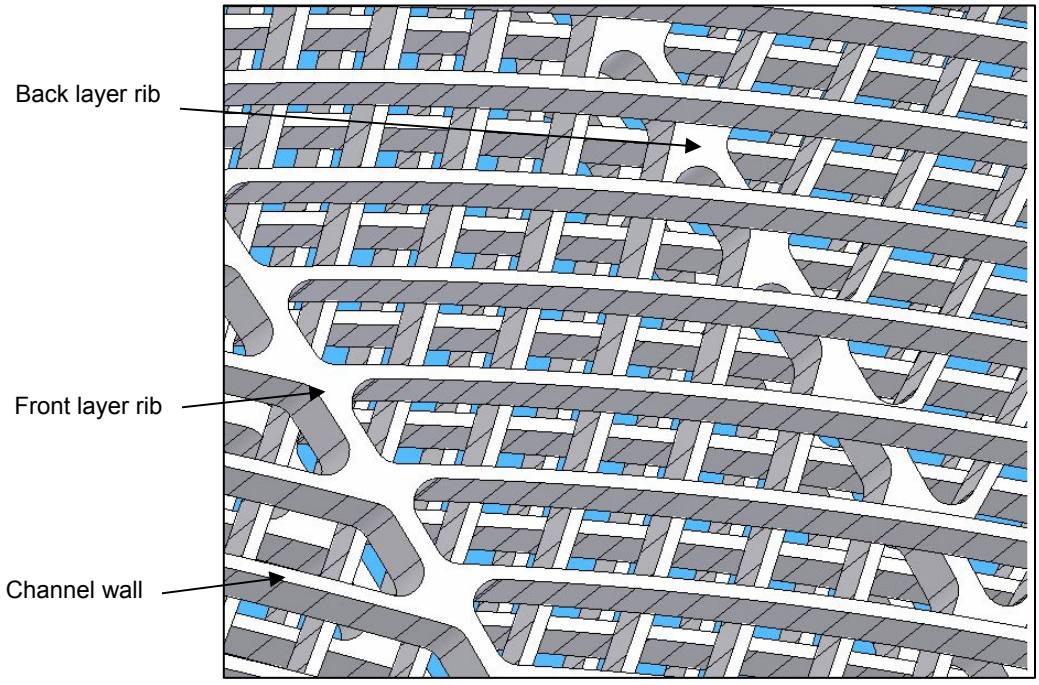

Figure 6.3.—3-D view of four layers of microfabricated segmented-involute-foil channels.

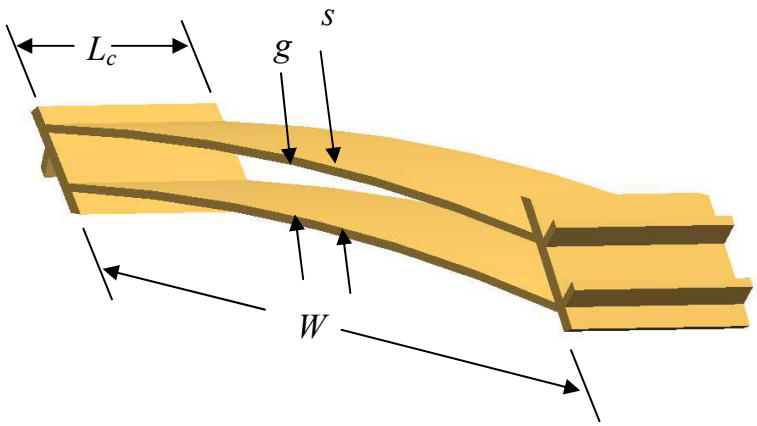

Figure 6.4.—Segmented-involute-foil channel, of one layer.

TABLE 6.1—INVOLUTE-FOIL CHANNEL DIMENSIONS

Dimension	Unit	Value
Gap, g	μm, 10^{-6} m	86
Gap+wall, s	μm	100
Wall thickness, s-g	μm	14
Channel width, W	μm	1000
Disk (layer, segment) thickness, *Lc*	μm	265
Porosity		0.838
Hydraulic diameter, Dh, 4A/P	μm	162

This design has several potential advantages compared to existing designs (such as random-fiber and wire-screen matrices) as demonstrated by Sage and Finite Element Analysis (FEA) analyses done in the Phase I part of this contractual effort—and the actual microfabricated hardware and test results from Phase II :

1) Improved ratio of heat transfer to pressure drop, i.e., high Figure of Merit,
2) Low axial conduction due to minimal contact area between disks,
3) Better reproducibility and control over geometric parameters,
4) High structural integrity and durability.

It was a challenge to analyze this geometry for fluid flow and heat transfer via CFD so as to facilitate the comparison between this geometry and other regenerator geometries. The first difficulty is the complex 3-D geometry, as depicted in figure 6.2. The second is the oscillatory nature of the flow as it occurs in the Stirling engine.

In this section a description will be given for the modeling set-up used to analyze the problem. This includes the grid generation for the computational domain and the matrix under investigation. Results of the numerical investigation for the different parameters of the proposed problem will be presented followed by the conclusions.

6.3 Establishing the Computational Domain

It was decided early on that it would not be feasible from a microscopic computational point of view to model the whole regenerator. Therefore it was necessary to look for simplifications, which usually come in the form of symmetries and boundary-condition approximations.

6.3.1 Radial Direction Periodicity

One simplification comes from recognizing the periodicity in the radial direction that comes from the concentric arrangement of several rings of channels. The flow through the whole disk can be approximated by the flow through just one ring of channels situated halfway between the OD and the ID of the annulus (of the disk). A seven-fold reduction of the computational domain can be achieved with large savings of computational resources. In fact, without this reduction of the domain, the modeling of the geometry is not feasible. Furthermore, this simplification enables the next simplification.

6.3.2 Angular Direction Periodicity

This simplification comes from recognizing that there exists a sector of the ring of channels that, when repeated in the angular direction, reassembles the full ring. This is sometimes called circular symmetry. For the case studied the sector is about 8.87° and it reduces the domain by about 40 times (about 40 sectors make a full ring). The following figures show how these two periodicities are employed. Figure 6.5 shows a ring of channels selected from the middle of the microfabricated disk.

By inspecting the ring of channels one can select for modeling only one sector and employ periodic boundary conditions as shown in figure 6.6.

Figure 6.7 shows an enlarged area from the middle of the sector of figure 6.6. In figure 6.7, one can see the channel walls, the angle formed between channel walls (81° in this middle ring) in two successive layers and how the involute-foil profile of the wall deviates from a flat wall (by about 2°). This figure suggests possible further simplification of the geometry by approximating the involute-foil profile with a straight line and the angle between successive layer walls with a right angle (this will be discussed later).

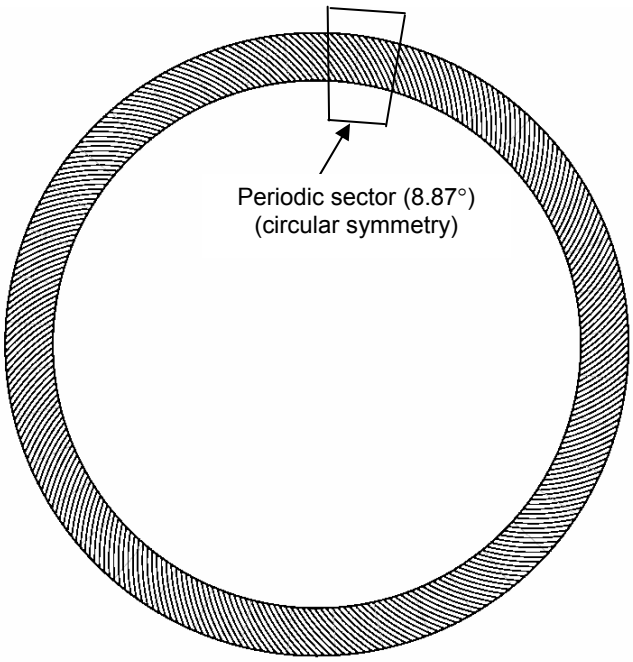

Figure 6.5.—Ring of channels in the “radial middle” of the microfabricated disk-annulus, and a sector of that ring.

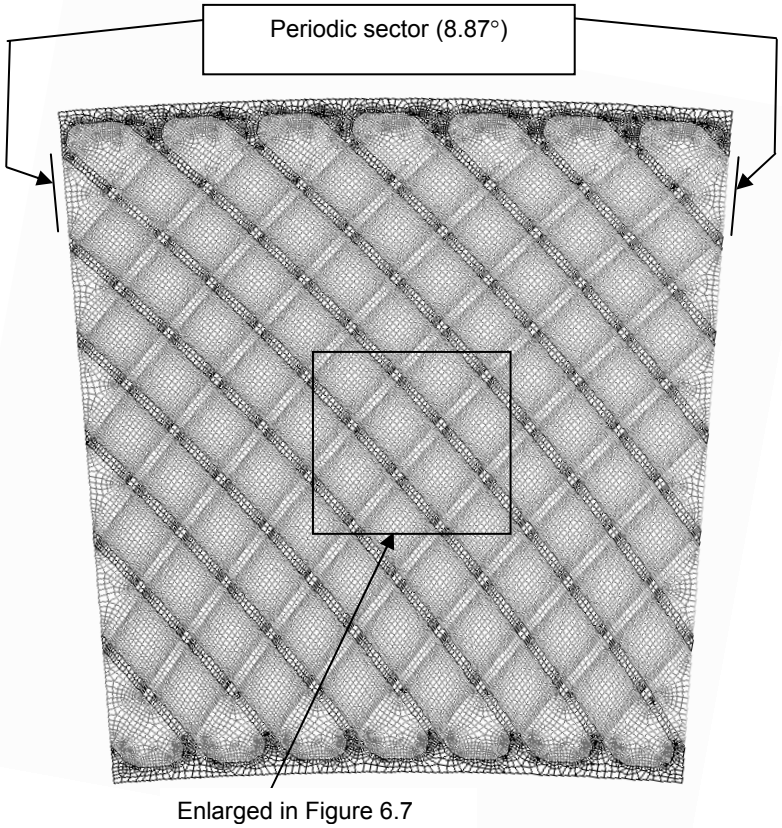

Figure 6.6.—Periodic sector from figure 6.5, showing two layers, with computational grids.

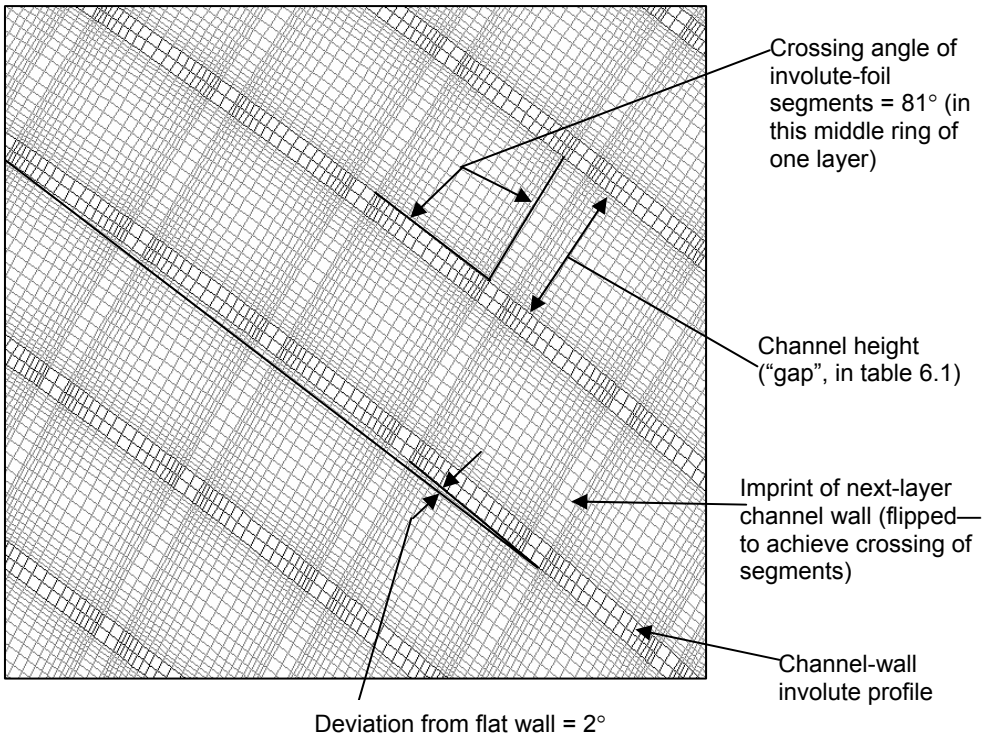

Figure 6.7.—Enlarged area in the middle of the periodic sector.

6.3.3 Flow Direction Periodicity

This simplification comes from recognizing that the regenerator is a stack of just two types of alternating layers. Thus, the repeating unit is comprised of two layers. One can use the flow output of one repeating unit as the input to the next one, and so on. Figure 6.8 shows an isometric view of three successive layers (or more precisely, four boundaries of these three layers). Because the frontal area occupied by the circular ribs is very small in comparison to the rest of the frontal area, a simplification was made to line up the ribs from disk to disk. In the real geometry (see figs. 6.2 and 6.3), the ribs are staggered from disk to disk. The orientation (crossing angle) of the channel walls was not significantly altered by the alignment of the ribs. As shown in figure 6.8, the ribs of two successive layers are aligned but the channel walls are still approximately perpendicular from layer to layer. Aligning the ribs enables a bounded domain in the radial direction for both layers that forms a repeating unit.

As mentioned above, the minimum thickness of the repeating unit has to be the thickness of two layers. However, the interface between two layers is a geometric discontinuity. The exit (velocities and temperatures profiles) of one repeating unit would be used as a boundary inlet to next one. It is better to have no geometric discontinuities at boundary inlets and outlets. Therefore the selected repeating unit consisted of half the thickness of one layer, followed by a full-thickness layer, and ending in another half thickness of the next layer. So a half-layer thickness was used at the entry and exit. Figure 6.9 shows this arrangement.

6.3.4 Computational Domains for Oscillatory-Flow Simulations

Flow direction periodicity works only for steady-state modeling. The transient simulation for the case studied requires oscillatory (alternating-direction, zero-mean) flow, requiring a stack of several layers to be included in the domain. A minimum of six layers was determined to be adequate to capture the oscillatory-flow phenomena. However even if radial and angular periodicities are employed, the grid size would still be too large for the available computation capability. Further simplifications, as indicated in figure 6.10, must be used. If the foil-crossing angle from one layer to the next is approximated to 90°

(instead of 81), the involute-foil profile is approximated as straight and the round ends of the channels are neglected, then one can build a manageable grid. This is expected to capture most of the 3-D oscillatory-flow phenomena of the microfabricated design. Figure 6.10 shows such a computational domain.

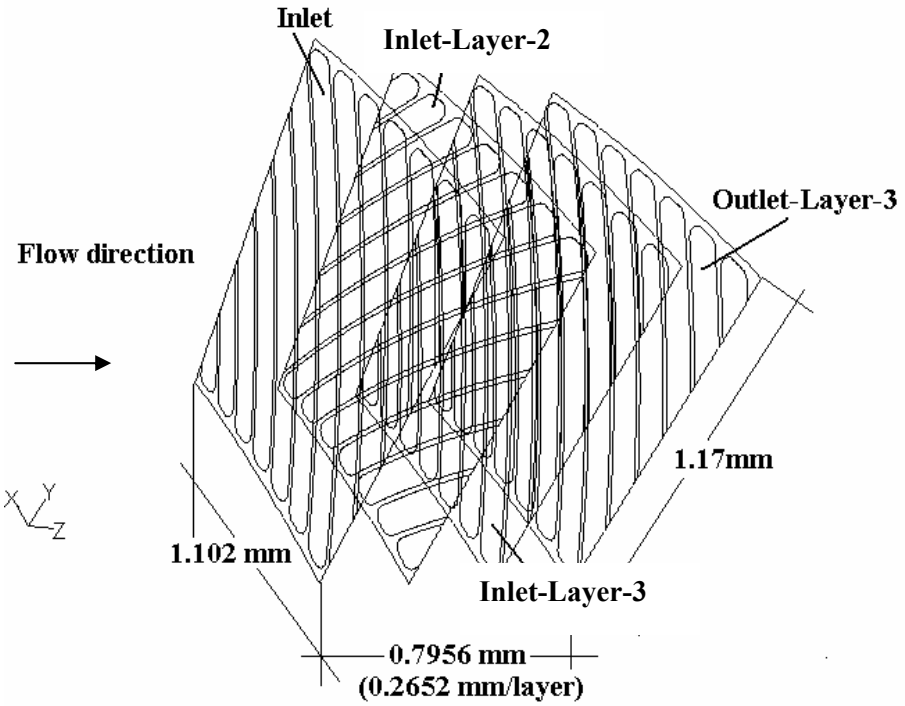

Figure 6.8.—Isometric view of four of the boundaries of three successive layers.

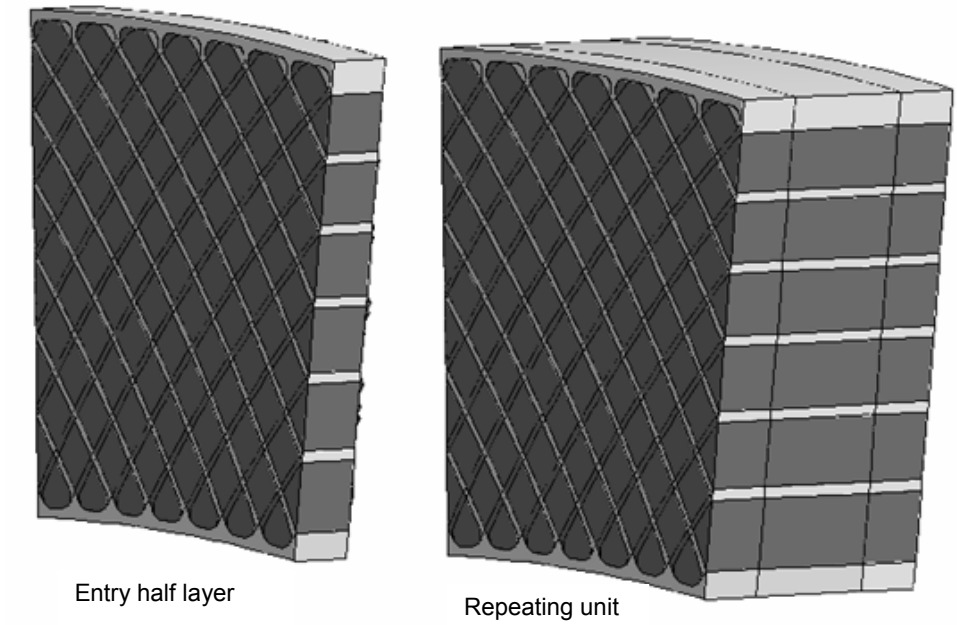

Figure 6.9.—3-D involute-foil-layers computational domain, entry unit and repeating unit. The half-full-half computational domain unit can be repeated periodically until the required stack height is achieved.

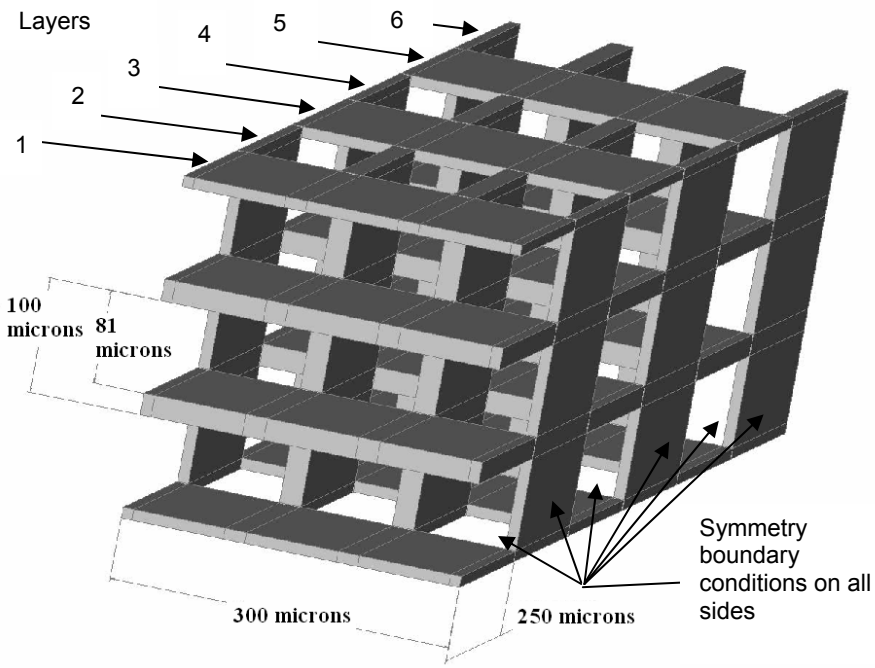

Figure 6.10.—3-D straight-channel-layers computational domain, for 6 layers.

Table 6.2 shows dimensions of the computational domain shown in figure 6.10. In order to maintain the same hydraulic diameter as the actual involute-foil geometry, the gap was adjusted to 81 μm, from 84 (see section 3.6.2.1). In order to maintain the same spacing, the wall thickness was adjusted to 19 μm, from 16. Another adjustment was made to, the layer thickness which was decreased from 265 to 250 μm. This was done to better match the actual disks that were fabricated for experimental testing, since the original design called for 265 μm thick disks, but the manufacturer (Mezzo) fabricated 250 μm thick disks. The resulting porosity, as shown in table 6.2, was 0.81 instead of the actual regenerator's 0.84.

TABLE 6.2—3-D STRAIGHT CHANNEL
COMPUTATIONAL DOMAIN DIMENSIONS

Dimension	Unit	Value
Gap, g	μm, 10^6 m	81
Gap+wall, s	μm	100
Wall thickness, s-g	μm	19
Channel width, W	μm	300, symmetry
Disk (layer) thickness, Lc	μm	250
Porosity		0.81
hydraulic diameter, Dh, 2g	μm	162

6.3.5 Two-Dimensional Computational Domains

Further simplifications were also made, for part of the CFD study, by using a 2-D computational domain. For the cases studied the 2-D domain consisted of a single parallel-plate channel with 6 successive sections. There was no variation in flow geometry upon exiting one section and entering the next. However, by changing the solid-interface settings one could set various values for the thermal contact resistance (TCR) between sections. This was expected to capture the interruption in the wall thermal conduction that is obtained by alternating the orientation of the channel walls (from one layer to the next) in the 3-D domain. Figure 6.11 shows such a 2-D computational domain. This 2-D domain allowed for quick parametric studies and finding trends that could be later confirmed in 3-D with fewer runs.

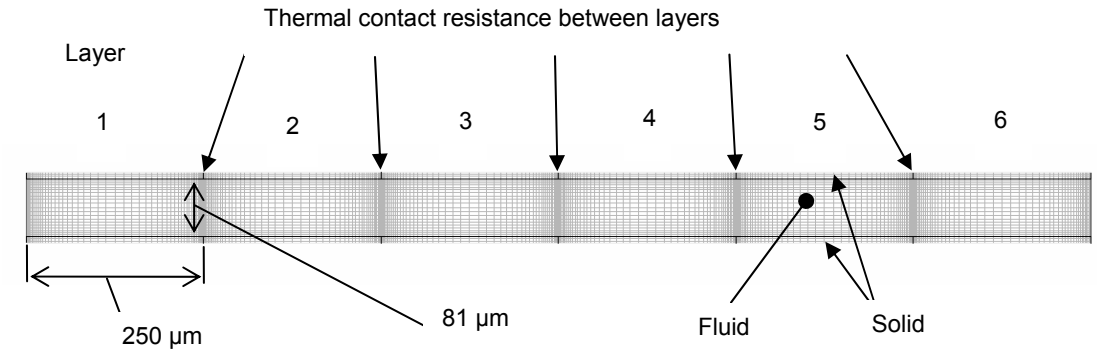

Figure 6.11.—2-D computational domain.

As presented above, three computational domains, two 3-D and one 2-D, were identified for dealing with the geometry to be studied. They represent different levels of compromise between the actual problem and the resources required to model the problem. They are at the first level of a study matrix. The next levels are formed by considering different boundary conditions to be imposed on these computational domains.

6.4 Material Properties and Boundary Conditions

6.4.1 Material Properties

For the fluid, helium gas was used at an operating pressure of 2,500,000 Pa. Table 6.3 shows the properties used for helium.

As for the solid, two materials were used: stainless steel and pure nickel with properties as shown in tables 6.4 and 6.5, respectively.

TABLE 6.3—HELIUM PROPERTIES USED IN THIS STUDY

Property	Units	Method	Values			
Density	kg/m^3	incompressible ideal-gas				
Cp	J/kg-K	constant	5193			
			T^0 coef.	T^1 coef.	T^2 coef.	T^3 coef.
Thermal conductivity	W/m-K	polynomial	0.01998	0.000509	-2.61E-07	8.53E-11
			C1	C2		
Viscosity	kg/m-s	Sutherland Law	1.46E-06	79.96		
Molecular weight	kg/kg-mol	constant	4.0026			

TABLE 6.4—STAINLESS-STEEL PROPERTIES

Property	Units	Method	Values			
Density	kg/m^3	constant	8030			
			T^0 coef.	T^1 coef.	T^2 coef.	T^3 coef.
Cp	J/kg-K	polynomial	148.86	1.5139	-0.0018	7.35E-07
Thermal conductivity	W/m-K	polynomial	6.182	0.03505	-2.63E-05	1.02E-08

TABLE 6.5—NICKEL PROPERTIES

Property	Units	Method	Values
Density	kg/m^3	constant	8900
Cp	J/kg-k	constant	460.6
Thermal conductivity	W/m-k	constant	91.74

6.4.2 Dimensionless Quantities, Correlations and Boundary Conditions

The following dimensionless quantities and correlations were used in this CFD study.

6.4.2.1 Dimensionless Quantities

$$\mathrm{Re}_{\omega} = \frac{\omega D_h^{\,2}}{4\nu} \text{ (Valensi number)} \tag{6.1}$$

$$\mathrm{Re}_{\max} = \frac{u_{m,\max} D_h}{\nu} \text{ (maximum Reynolds number)} \tag{6.2}$$

$$x^+ = \frac{x}{D_h \mathrm{Re}} \text{ (dimensionless length used for friction-factor plots)} \tag{6.3}$$

$$x^* = \frac{x}{D_h \mathrm{Re}\,\mathrm{Pr}} \text{ (dimensionless length used for Nusselt number plots)} \tag{6.4}$$

$$f_D = \frac{\Delta p\, D_h}{\rho \frac{u_m^{\,2}}{2} \Delta x} \text{ (Darcy friction factor)} \tag{6.5}$$

$$f_F = \frac{f_D}{4} \text{ (Fanning friction factor)}$$

$$\mathrm{Nu\_m} = \frac{h_m D_h}{k} \text{ (mean Nusselt number)} \tag{6.6}$$

$$\mathrm{Nu_x} = \frac{h_x D_h}{k} \text{ (local Nusselt number)} \tag{6.7}$$

6.4.2.2 Friction Factor and Heat Transfer Correlations

In order to compare the steady-flow CFD results to the literature, the following correlations were selected from Shah and London (1978). The Fanning friction-factor correlation of equation (6.8) is attributed to Shah (1978) and applies to laminar, hydrodynamically developing flow, the flow regime for the case studied.

$$f_F = \frac{1}{\mathrm{Re}}\left(\frac{3.44}{\left(x^+\right)^{1/2}} + \frac{24 + \frac{0.674}{4x^+} - \frac{3.44}{\left(x^+\right)^{1/2}}}{1 + 0.000029\left(x^+\right)^{-2}} \right) \tag{6.8}$$

For steady heat transfer, the correlation of equation (6.9) was selected from Shah and London (1978) and is attributed to Stephan (1959). This correlation applies to laminar simultaneously (thermally and hydro-dynamically) developing flow which is the flow and thermal regime for the case studied. This correlation is valid for a constant wall temperature and Prandtl numbers between 0.1 and 1000. These conditions are also true for the cases studied under these CFD steady-state simulations:

$$\mathrm{Nu\_m} = 7.55 + \frac{0.024\left(x^*\right)^{-1.14}}{1 + 0.0358\left(x^*\right)^{-0.64}\,\mathrm{Pr}^{0.17}} \tag{6.9}$$

This correlation will be referred to in the results section as the "Stephan Nu" or "Stephan (1959)" correlation.

As for the oscillatory-flow cases, the following correlations, of equations (6.10) and (6.11), for involute-foil friction factor and heat transfer are attributed to Gedeon (see eqs. (3.2) and (3.4) and discussion). These correlations were obtained from involute-foil experimental data. The experiments were done at Sunpower, Inc., on a NASA/Sunpower oscillating-flow test rig equipped with a microfabricated involute-foil regenerator. This regenerator had 42 disks in its stack. The material used for the disks was nickel.

$$f_D = \frac{117.3}{\mathrm{Re}} + 0.38\,\mathrm{Re}^{-0.053} \tag{6.10}$$

This correlation will be referred in the results section as the "Gedeon f_Darcy correlation." Heat transfer under oscillatory flow conditions is given by:

$$\mathrm{Nu\_m} = 1 + 1.97\,\mathrm{Pe}^{0.374} \tag{6.11}$$

This correlation will be referred in the results section as the "Gedeon Nu_m correlation"

6.4.2.3 Boundary Conditions

Steady-state runs: For steady-state runs, the solid temperature was kept constant at 673 K while the fluid enters the channel at 660 K.

Oscillatory-flow runs: The running conditions for the base case examined in the oscillatory-flow study are shown in table 6.6.

TABLE 6.6—BASE CASE FOR OSCILLATORY-FLOW CONDITIONS

Valensi number, Re_ω	0.22885
Maximum Reynolds number, Re_{max}	49.78
Frequency, Hz	27.98
Hydraulic diameter, m	0.000162
Max mass flux, kg/m^2-s	6.17215
Cold end solid B.C.	Adiabatic
Hot end solid B.C	Adiabatic
Inlet fluid temperature, cold end, K	293.1
Inlet fluid temperature, hot end, K	310.2
Mean pressure, Pa	2500000
Mean, max velocity, m/s	1.5488

6.5 Summary of All Cases Studied

Tables 6.7 and 6.8 summarize the steady-state and oscillatory-flow conditions, respectively, attempted in this study.

TABLE 6.7—SUMMARY (STUDY MATRIX) OF STEADY-STATE RUNS

Geometry	Material	Transient or steady	Re
3-D	SS	steady	50
			94
			183
			449
			1005
			2213

TABLE 6.8—SUMMARY (STUDY MATRIX) OF OSCILLATORY FLOW RUNS

Case Examined	Geometry	Material	Transient or steady	Layer thermal contact resistance	Re_{max}	Re_{ω}
Comparison with literature, parallel plates	2-D	Stainless steel	steady	zero	Re = 50	
Base case 2-D			oscillatory flow	zero	50	0.229
Effect of thermal contact				infinite	50	0.229
Effect of oscillation amplitude				zero	150 (3x)	0.229
Effect of frequency				zero	150	0.687 (3x)
Effect of material change		Nickel		infinite	50	0.229
Comparison with literature	3-D	SS	steady	zero	Re = 50	
Base case 3-D			oscillatory flow	zero	50	0.229
Effect of thermal contact				infinite	50	0.229

6.6 CFD Grid-Independence Test and Code Validation

Three computational domains were identified as good candidates for modeling the problem at hand. One was a 2-D domain and the other two were 3-D domains. The questions were: What is a proper grid? Will the number of grid locations required to get good results be prohibitively large? From the examination of the geometry, one can see that the real involute-foil flow in one channel of one layer (fig. 6.4) should approximate that of a parallel-plate geometry. And from the above section we assume that the flow is laminar. For this geometry under laminar flow there are theoretical correlations available in 2-D. The 2-D computational domain presented above has geometric parameters equivalent to the 3-D geometry (same hydraulic diameter, length). It was then natural to select the 2-D domain for studying grid independence and code validation

6.6.1 2-D CFD Grid-Independence-Study Results

2-D computational domains with four different grid sizes were chosen. The grid sizes (in-the-*x*-direction X in-the-*y*-direction, per layer) are: 20X10, 30X20, 50X20 and 100X40. These are shown in figures 6.12 to 6.15 respectively and are summarized in table 6.9. In some cases, the sizes of the grid cells in a certain direction are not uniform. A ratio between two successive cell widths is imposed (ratios imposed are indicated in the figure labels and in table 6.9), and that allows for denser grids where the velocity and temperature gradients are expected to be higher. For channel flow, it is appropriate to have a denser grid in the neighborhood of channel walls, and at interfaces between axial-segments where discontinuies in wall thermal boundary conditions (or flow areas) occur, since velocity and temperature gradients are usually the largest in such regions.

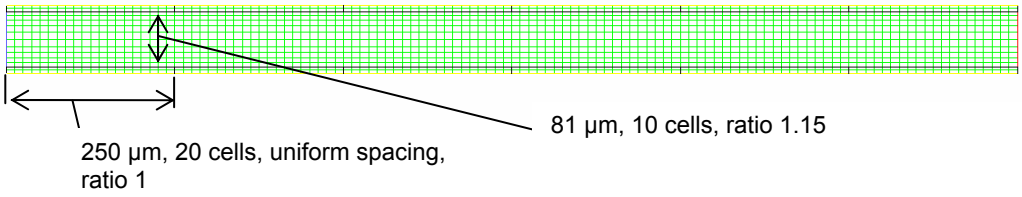

Figure 6.12.—The 20X10 2-D grid.

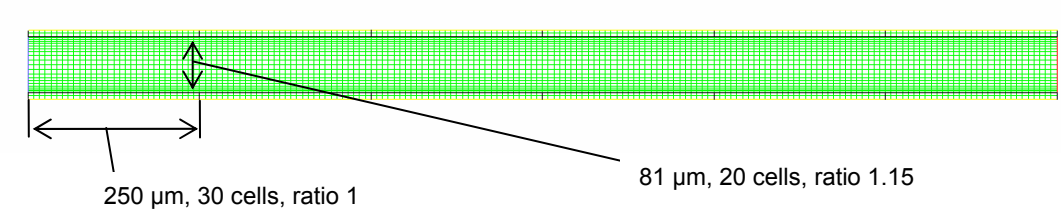

Figure 6.13.—The 30X20 2-D grid.

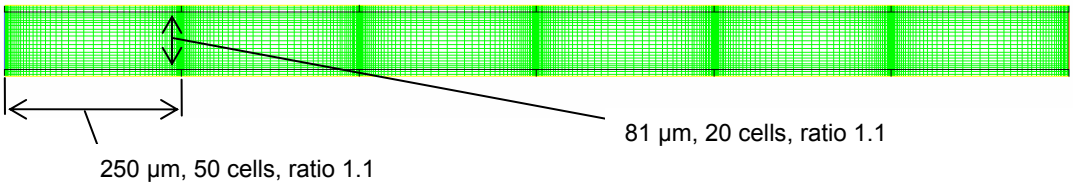

Figure 6.14.—The 50X20 2-D grid.

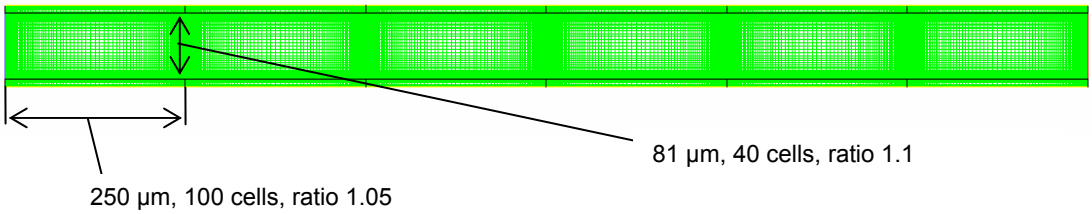

Figure 6.15.—The 100X40 2-D grid.

TABLE 6.9—SUMMARY OF GRIDS TESTED IN GRID-INDEPENDENCE STUDY

Grids/axial-segment	Number cells between plates	Vertical grid-spacing ratio	Number cells along axial segment (layer)	Horizontal or axial (segment) spacing ratio
20X10	10	1.15	20	1, uniform
30X20	20	1.15	30	1
50X20	20	1.1	50	1.1
100X40	40	1.1	100	1.05

The above four grid sizes were tested and the results were plotted for friction factor as a function of dimensionless length, x^+, for Reynolds number, Re = 150 (see fig. 6.16). Similarly, the results were plotted for mean Nusselt number, Nu_m as a function of the different dimensionless length, x^*—also for Reynolds number, Re = 150 (see fig. 6.17) and for Re = 1000 (see fig. 6.18). The results show poor results obtained from the smallest grid (20X10) while little gain in accuracy is achieved by moving from a grid size of 50X20 to 100X40 (The 50X20 grid size was eventually selected as the best compromise between accuracy and computing resources, to be used following the completion of the grid-independence study).

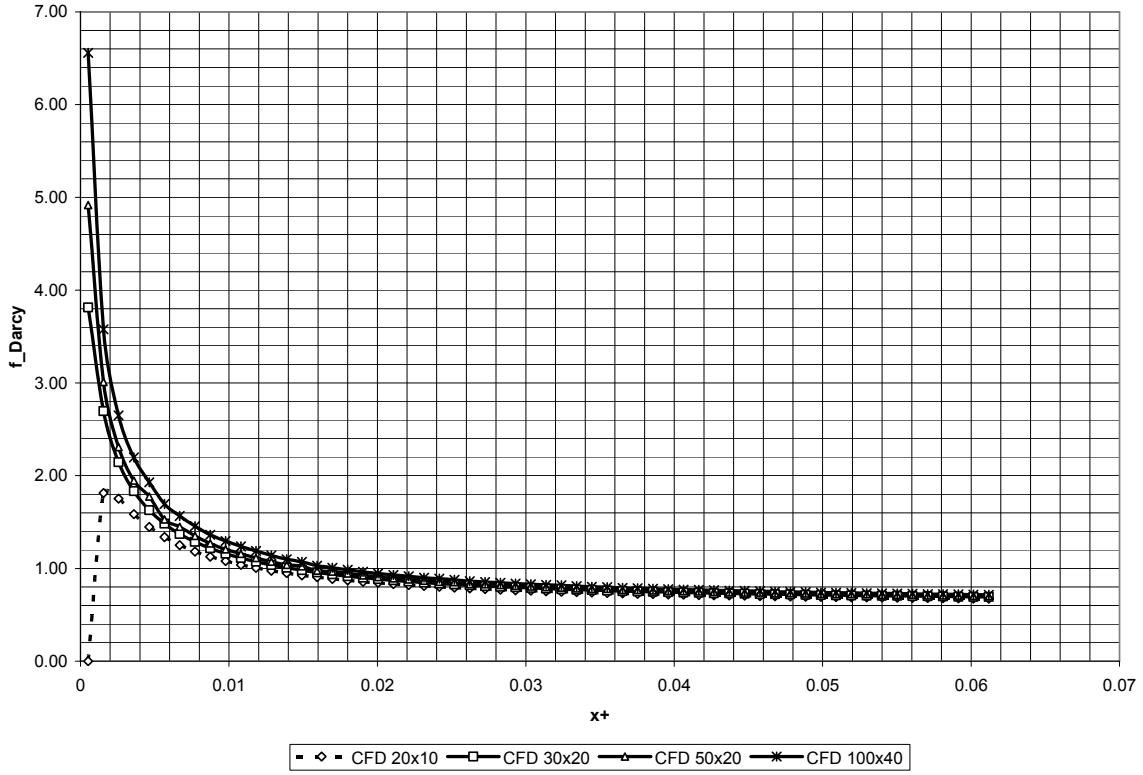

Figure 6.16.—Grid independence study: Darcy friction-factors, *f_Darcy*, as functions of dimensionless length, x^+, at Reynolds number, Re = 150 {for grids/segment of 20X10, 30X20, 50X20 and 100X40 (horizontal X vertical)}.

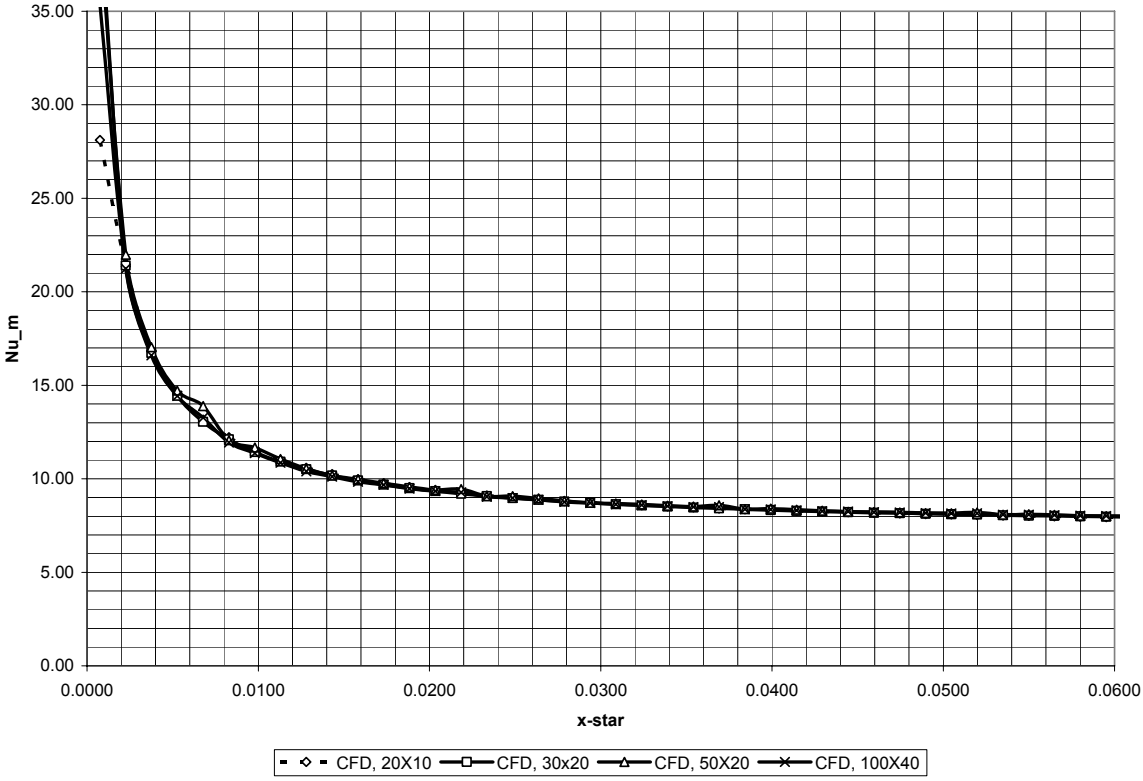

Figure 6.17.—Grid independence study: Mean Nusselt numbers, Nu_m, as a functions of dimensionless length, x^*, at Reynolds number, Re = 150 {for grids/segment of 20X10, 30X20, 50X20 and 100X40 (horizontal X vertical)}.

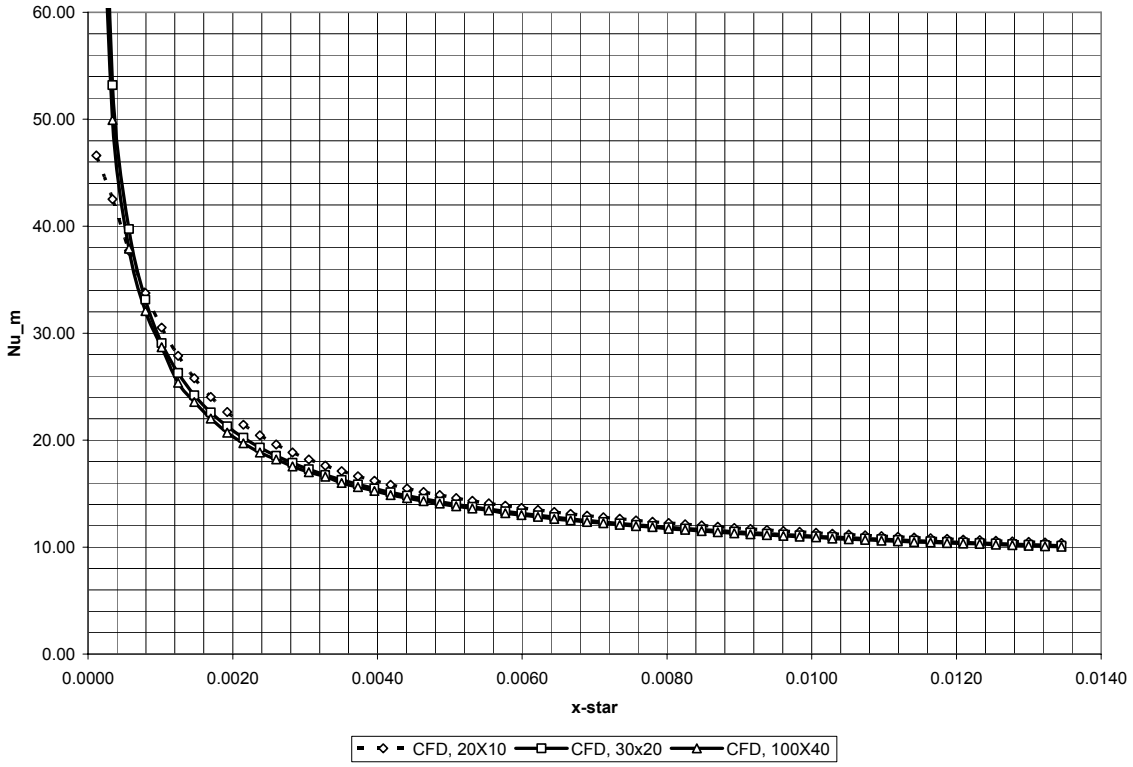

Figure 6.18.—Grid independence study: Mean Nusselt numbers, Nu_m, as a functions of dimensionless length, x^*, at Reynolds number, Re = 1000 {for grids/segment of 20X10, 30X20 and 100X40 (horizontal X vertical)}.

6.6.2 CFD Code Validation

It is best if the CFD solution can be checked, and validated, against experimental data or an exact analytical solution of the same problem. However, sometimes it is necessary to do an approximate validation if data and analytical solutions are not available. In the case studied, the solution for an approximate 2-D grid was chosen as representative of the 3-D channel flow and compared to existing theoretical correlations.

Figures 6.19 and 6.20 show the comparison between the CFD-calculated friction factor and the Shah (1978) correlation for Reynolds numbers, Re = 150 and 1000, respectively. At Reynolds number of 150 the 30X20 and 50X20 friction factors agree well with the correlation. At Reynolds number of 1000 the 30X20 CFD results seem to be lower than the theoretical correlation at the entrance of the channel but agree well downstream where the flow is closer to being fully-developed. Figures 6.21 and 6.22 show the comparison between the CFD calculated Nusselt numbers and the Stephan correlation, as reported by Shah and London (1978), for Reynolds numbers of 150 and 1000, respectively. Again the agreement is generally good except for the entrance region. The entrance region seems to be a difficult area for both measurements and computations. Overall there is good agreement with the correlation for both the friction factor and the mean Nusselt number and one can expect meaningful results from both the fluid flow and the heat transfer analysis from these grids.

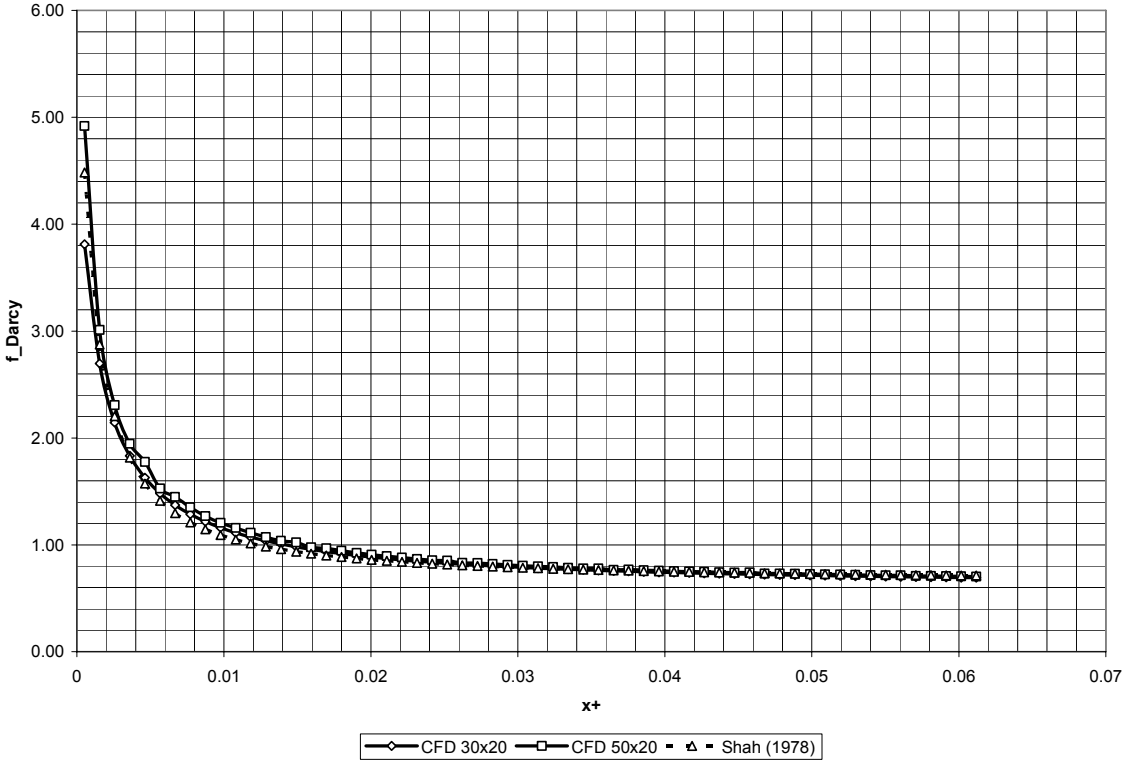

Figure 6.19,—Code validation: Darcy friction-factors, *f_Darcy*, as functions of dimensionless length, x^+, at Reynolds number, Re = 150; comparisons of CFD computations for grids/segment of 30X20 and 50X20 with Shah (1978) correlation.

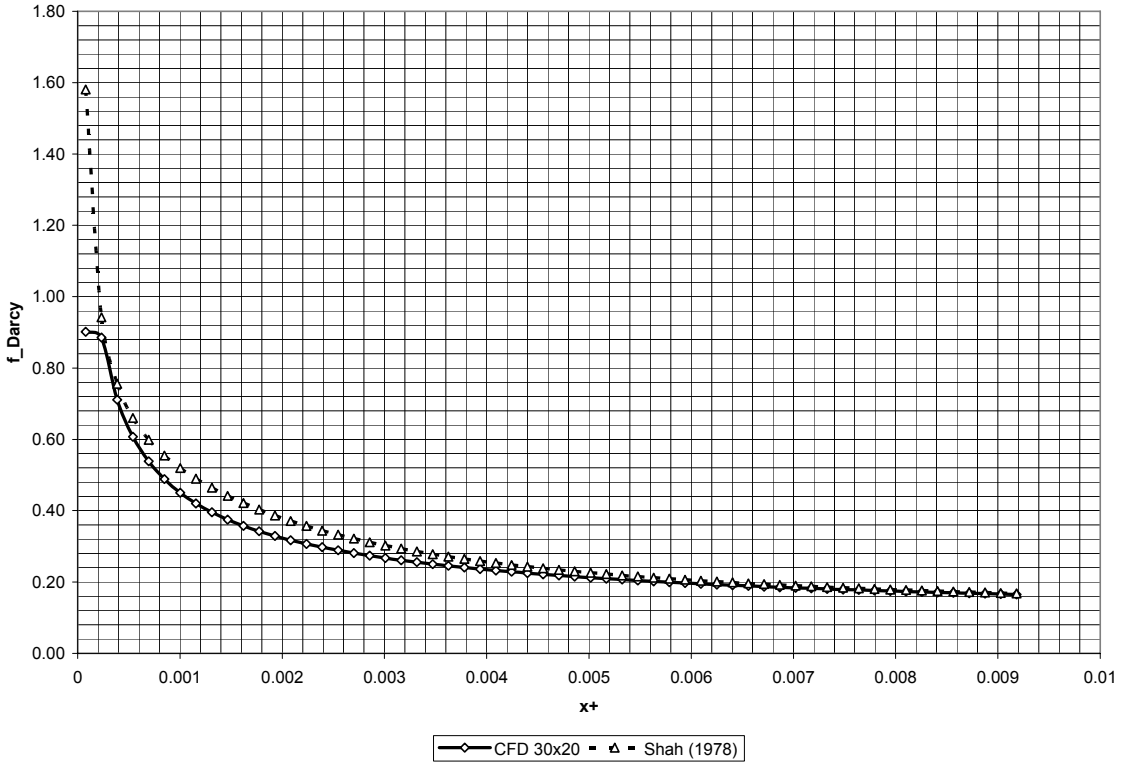

Figure 6.20.—Code validation: Darcy friction-factors, *f_Darcy*, as functions of dimensionless length, x^+, at Reynolds number, Re = 1000; comparison of CFD computations for grids/segment of 30X20 with Shah (1978) correlation.

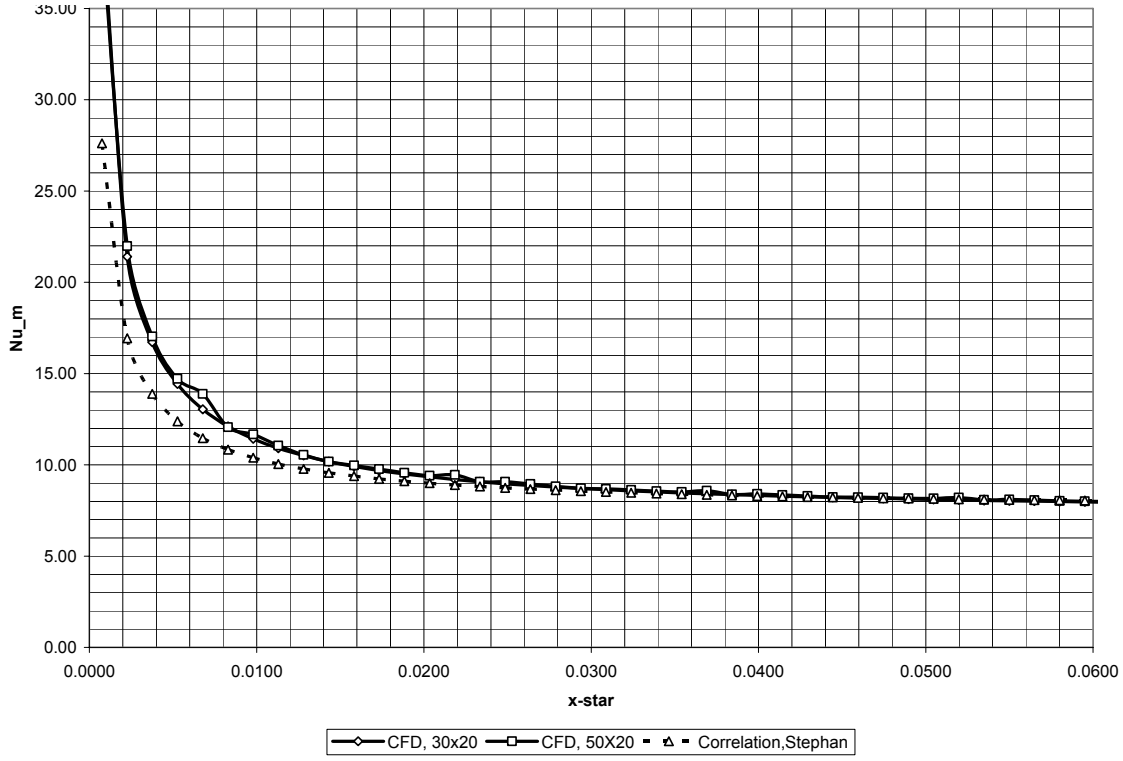

Figure 6.21.—Code validation: Mean Nusselt numbers, Nu_m, as functions of dimensionless length, x^*, at Reynolds number, Re = 150; comparisons of CFD computations for grids/segment of 30X20 and 50X20 with Stephan (1959) correlation.

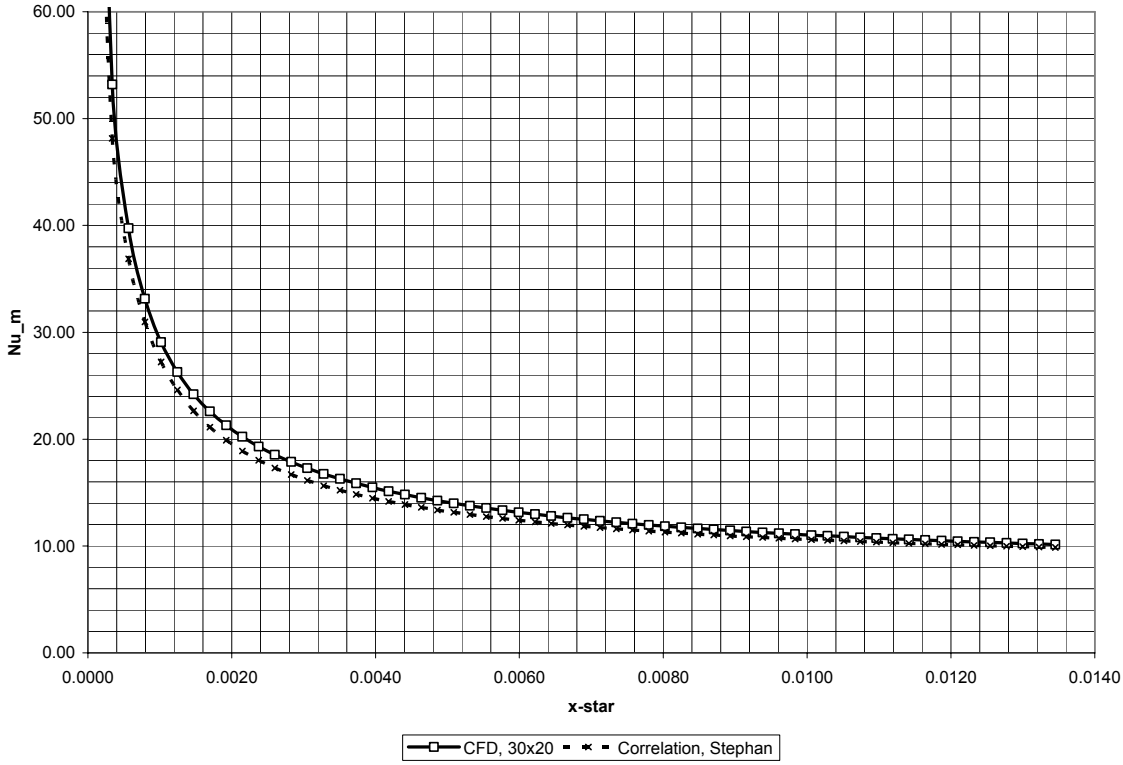

Figure 6.22.—Code validation: Mean Nusselt numbers, Nu_m, as functions of dimensionless length, x^*, at Reynolds number, Re = 1000; comparisons of CFD computations for grids/segment of 30X20 with Stephan (1959) correlation.

6.6.3 Summary: Number and Types of Cells used for Various 2- and 3-D CFD Cases

Table 6.10 shows the number and type of cells used in the following study for all 2-D and 3-D cases.

TABLE 6.10—DESCRIPTION OF THE NUMBER AND TYPE OF CELLS USED.

Case description	Zone	Cell count	Type of cell	
2-D 6 Layer Grid, see figure 6.11	fluid	6000	Quadrilateral	
	solid	1800	Quadrilateral	
	total	7800		
	Mesh file size, Mb	0.67		
Case Description	Zone	Cell count	Type of cell	
3-D straight channel grid, see figure 6.10	fluid	1404000	Hexahedral	
	solid	421200	Hexahedral	
	total	1825200		
	Mesh file size, Mb	372		
Case description	Zone	Entry layer cell count	Repeating unit cell count	Type of cells
3-D involute-foil channel grid, see figure 6.9	fluid	582480	2329920	Hexahedral
	solid	93600	374400	Hexahedral
	total	676080	2704320	
	Mesh file size, Mb	135	523	

6.7 Results of Two-Dimensional (2-D) CFD Simulations of Involute-Foil Layers

Table 6.11 shows a summary (study matrix) of all 2-D cases, steady and oscillatory flow, made following the grid-independence studies. Steady state was examined first at Reynolds number, Re = 50 in order to compare with available correlations. Then oscillatory-flow cases were conducted to examine the effects (on friction-factor and Nusselt number) of changing: 1) the thermal contact resistance between the 6 layers, 2) the oscillation amplitude, 3) the oscillation frequency, and 4) the solid material.

TABLE 6.11—SUMMARY (STUDY MATRIX) OF 2-D CFD SIMULATIONS

Case examined	Material	Transient or steady	Layer thermal-contact resistance	Re_{max}	Re_{ω}
Comparison with literature, parallel plate	Stainless Steel	Steady	zero	Re = 50	NA
Base case		Oscillatory flow	zero	50	0.229
Effect of thermal contact resistance			infinite	50	0.229
Effect of oscillation amplitude			zero	150 (3x)	0.229
Effect of frequency			zero	150	0.687 (3x)
Effect of material change	Nickel		infinite	50	0.229

6.7.1 2-D Steady-State Simulations

Figures 6.23 and 6.24 show friction factor and Nusselt number comparisons (respectively) for Reynolds number, Re = 50. This is also the maximum Reynolds number for the base-case oscillatory-flow run. Except for a small region at the entrance, the simulation results agree well with the correlations from Shah and London (1978).

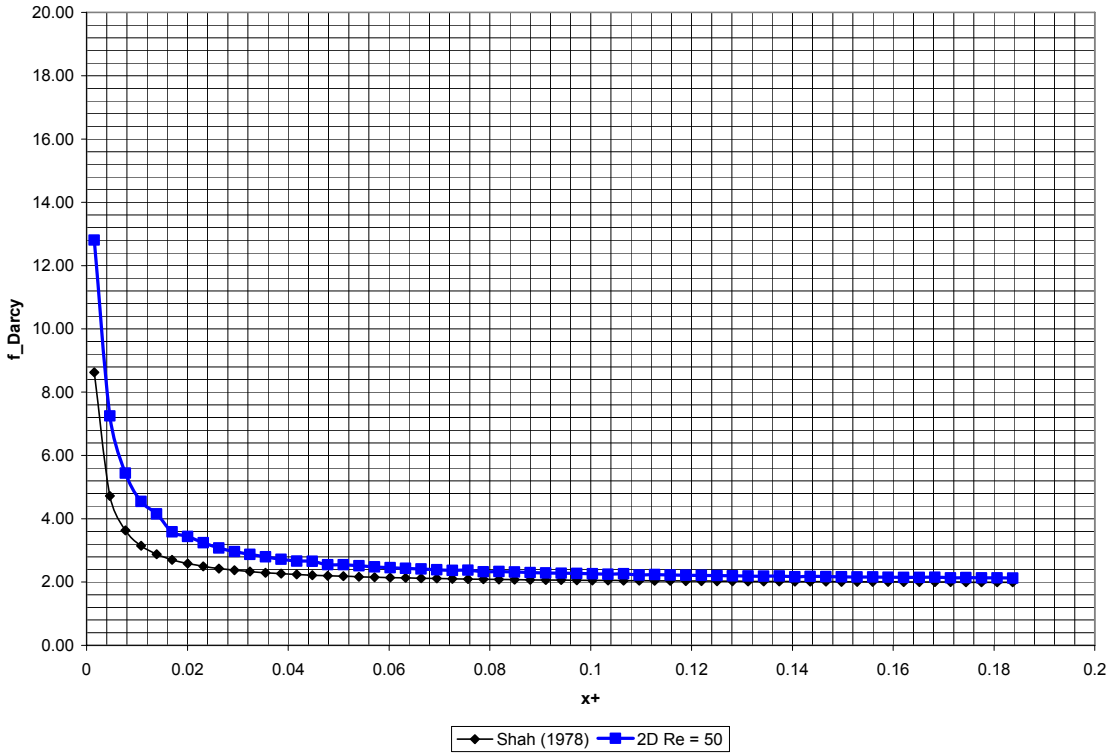

Figure 6.23.—Darcy friction factor, *f_Darcy*, as functions of dimensionless length, x^+: Comparison of values computed from 2-D CFD simulations (50X20 grids/segment) with Shah (1978) correlation, at Reynolds number, Re = 50.

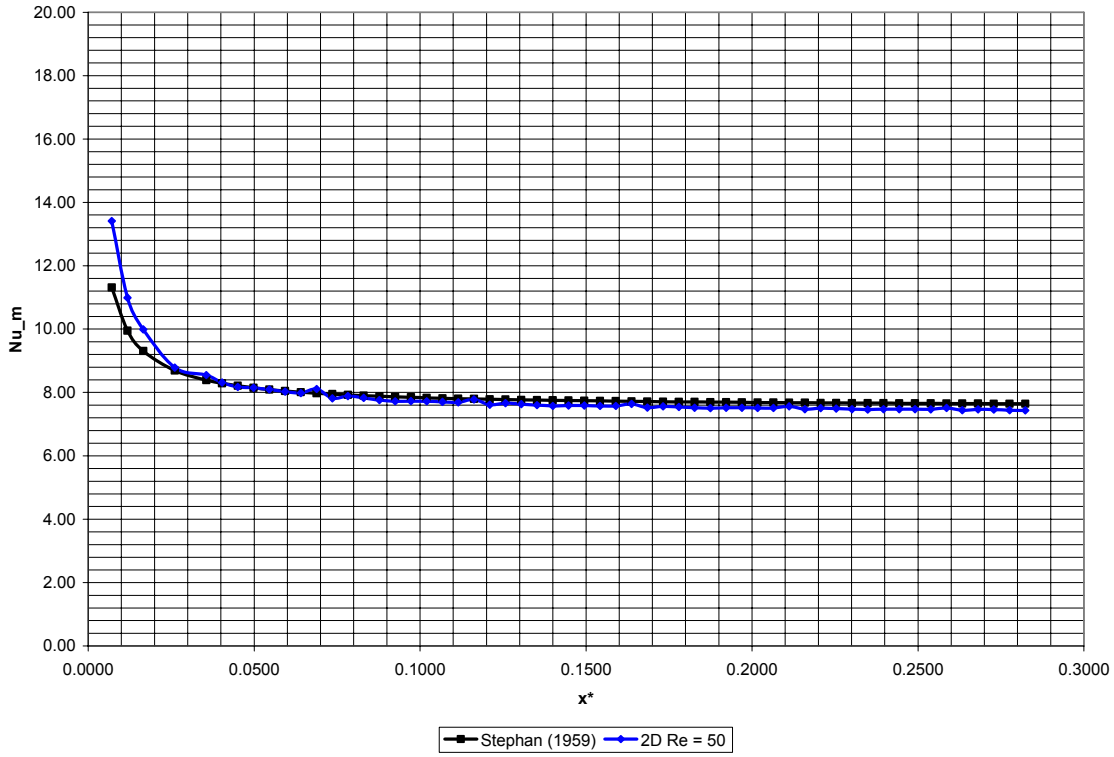

Figure 6.24.—Mean Nusselt numbers, Nu_m, as functions of dimensionless length, x^*: Comparison of values computed from 2-D CFD simulations (50X20 grids/segment) with Stephan (1959) correlation, at Reynolds number, Re = 50

6.7.2 2-D Oscillatory-Flow Simulation

6.7.2.1 Base-Case 2-D Oscillatory Flow

For the oscillatory-flow simulations the base-case forcing-function, at 27.98 Hz, is:

$$\text{Mass flux} = 6.17215*\cos(2*\pi*27.98*t + 1.56556)\ (\text{kg/m}^2\text{-s}) \tag{6.12}$$

This function is applied at the west (left) fluid boundary. Figure 6.25 shows the variation of the mass flux with the crank angle. By monitoring an oscillatory flow variable through several cycles, one notices that it takes several cycles until the monitored variable starts varying between the same minimum and maximum values. The final condition is called cycle-to-cycle convergence, or is said to have converged to a steady-periodic cycle. All the following 2-D oscillatory-flow cases were run until cycle-to-cycle convergence was obtained and only after that were the data extracted. Figure 6.26 shows that for the base case it took approximately 10 cycles to obtain cycle-to-cycle convergence. The variable monitored in this case is the mean fluid temperature in the middle of layer three.

For characterizing the oscillatory flow, the friction factor is compared with the experimental correlation obtained by Gedeon (eq. (6.10) or (3.2)) for the involute-foil. The friction factor plotted versus the crank angle is shown in figure 6.27. The values obtained by the present simulation fall below the correlation. This was expected since the correlation was obtained from experimental results on an actual involute-foil regenerator while the present 2-D simulation represents an idealized case, with flow through a foil-channel that doesn't flow around foils in adjacent layers (i.e., there are no obstacles in the flow path).

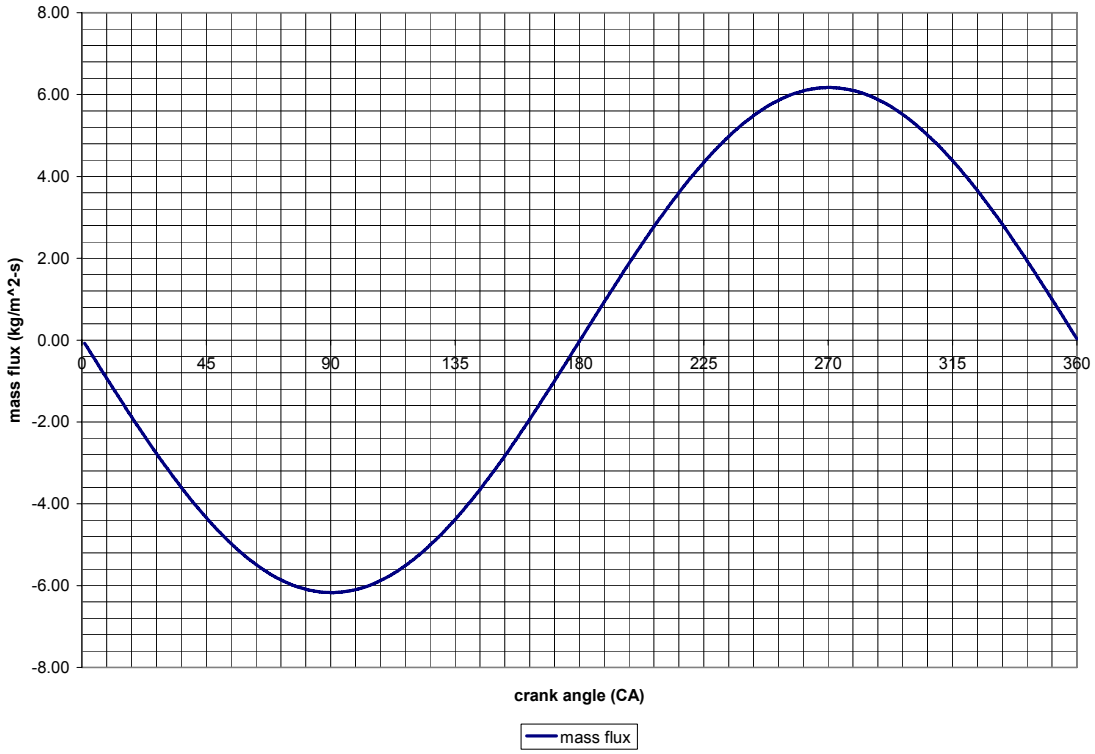

Figure 6.25.—Mass-flux forcing-function as a function of crank angle, *CA*, degrees, for the base-oscillatory-flow case.

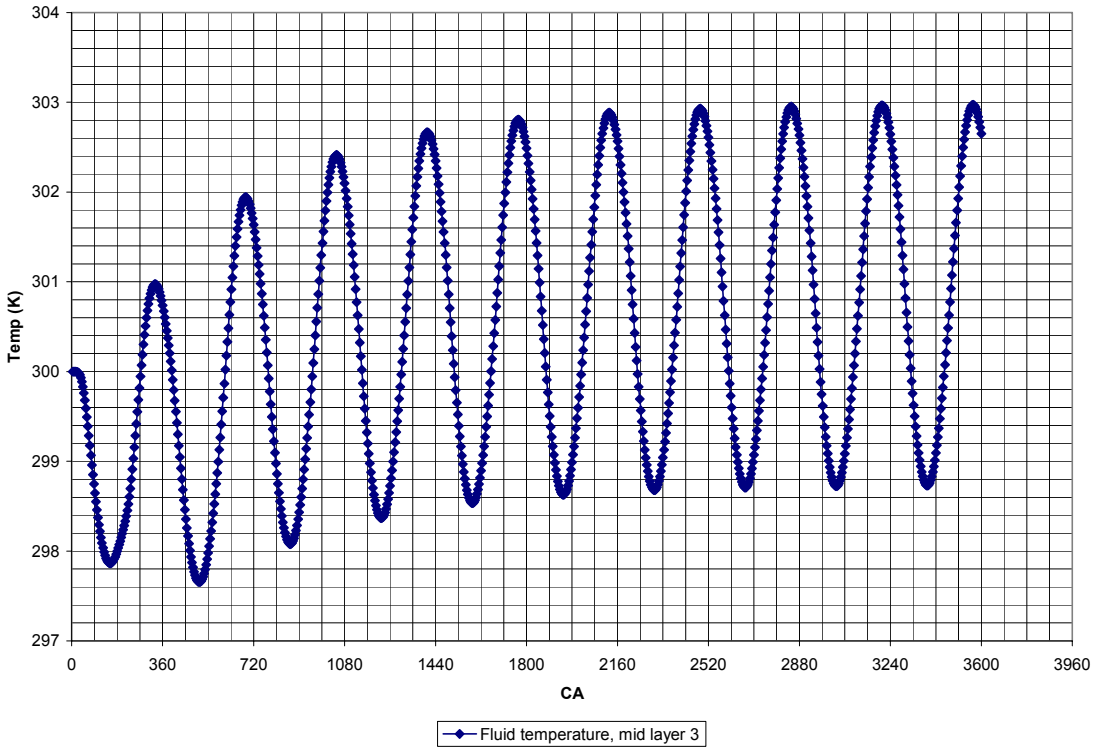

Figure 6.26.—Temperature in the middle of layer three as a function of crank angle, *CA*; degrees, shows progress toward cycle-to-cycle convergence for 2-D base oscillatory-flow case.

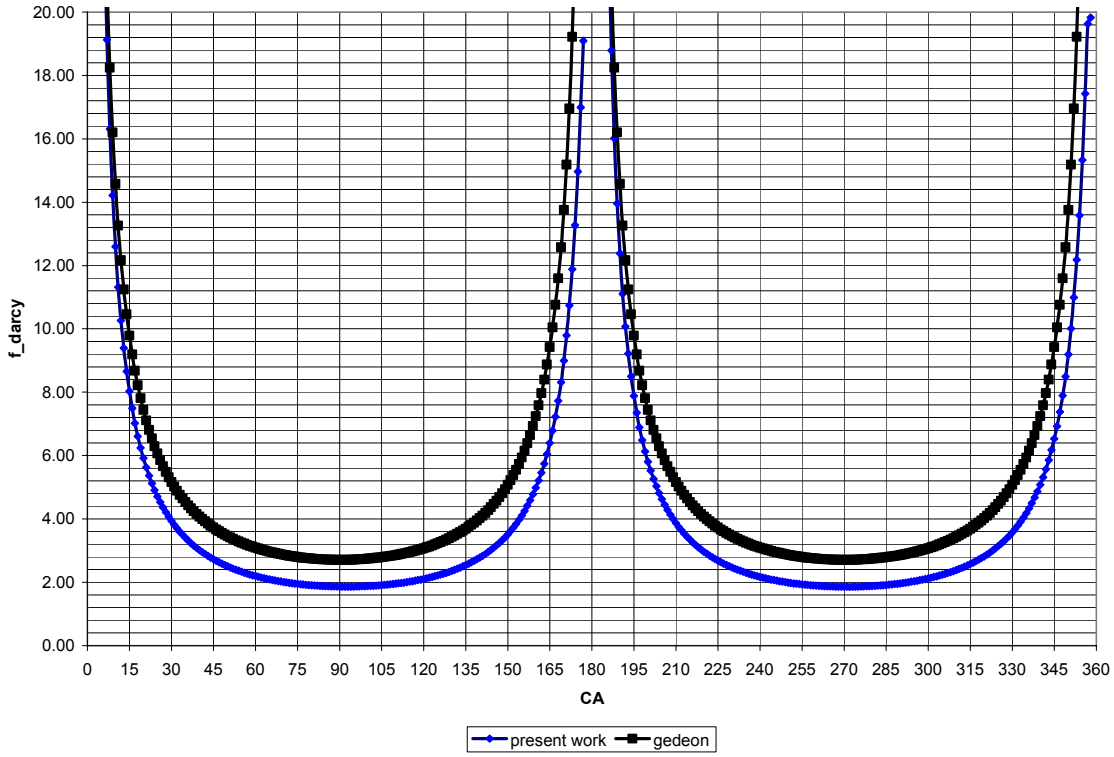

Figure 6.27.—Darcy friction factors, *f_Darcy*, as functions of crank angle, *CA*, degrees; comparisons of values calculated from 2-D CFD base-oscillatory-flow case (50X20 grids/segment) with Gedeon involute-foil correlation of equation (6.10) and (3.2).

In order to characterize the heat transfer that takes place during an oscillatory-flow run, the mean Nusselt number is plotted with respect to the crank angle, in figure 6.28. For comparison the experimental correlation, also obtained by Gedeon (eq. (6.11) or (3.4)), for the mean Nusselt number is used. However the correlation obtained by Gedeon represents a mean over the length of a stack of 42 layers tested at Sunpower Inc. The present work focuses only on the region from the middle of layer 3 to the middle of layer 4. So the length over which the Nusselt number is averaged in the present work is equal to the thickness of one layer only. That is done in order to stay away from the ends where entrance effects can distort the results. On the other hand, calculating a mean Nusselt number over the length of 6 layers would not have been representative of the actual geometry. Furthermore, experimental testing done at the University of Minnesota looked at the mean Nusselt number calculated between two layers similar to what has been done in the present work. The shape of the mean-Nusselt-number, or Nu_m, plot versus the crank angle is different from the Gedeon correlation and this difference arises from how the Nusselt number is averaged. The experiments done at the University of Minnesota (UMN) show a Nusselt number curve similar to the present work. However the comparison with Gedeon correlation is useful for the maximum Reynolds number regions that are located around 90° and 270° crank angle, where flow rates are maximum in the two directions. At these locations the 2-D analysis lies slightly below the correlation.

By integrating the fluid enthalpy crossing a plane section in the middle of layer three over the whole cycle, one can calculate the net enthalpy loss over the cycle. If one integrates the solid-conduction heat transfer at the middle of layer three over the whole cycle, a net-conduction loss over the cycle can be obtained. Since both losses are crossing the plane at the middle of layer three they can be added together to obtain a total axial heat loss over the cycle. For the base-oscillatory-flow case, table 6.12 shows these 2-D CFD heat-loss results.

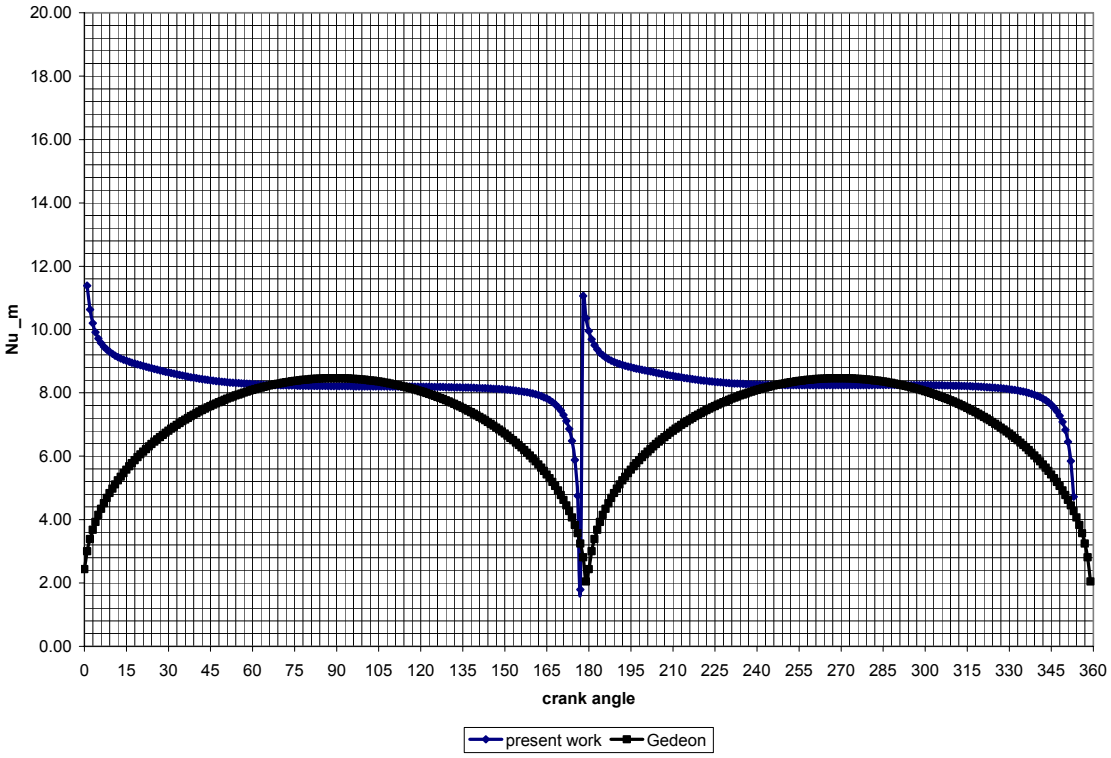

Figure 6.28.—Mean Nusselt numbers, Nu_m, as functions of crank angle, *CA*, degrees; comparison of values calculated from 2-D CFD base-oscillatory-flow case (50X20 grids/segment) with Gedeon involute-foil correlation of equation (6.11) or (3.4) {CFD assumes perfect thermal contact between layers, or zero thermal contact resistance (TCR)}

TABLE 6.12—2-D CFD BASE-OSCILLATORY-FLOW-CASE ENTHALPY, CONDUCTION AND TOTAL-AXIAL HEAT LOSSES

	Enthalpy loss, W	Conduction loss, W	Total loss, W
Base case	1.722	1.174	2.896

6.7.2.2 Effect of Changing the Thermal Contact Resistance

In order to study the effect of thermal contact resistance (TCR) between the layers a change was made from the zero TCR of the base case to an infinite TCR condition at the interfaces between the layers (or from perfect thermal contact to perfect thermal insulation, between solid layers). The effect of thermal contact resistance is important because in reality the contact between the layers is not perfect. This added contact resistance impedes the solid conduction from layer to layer. This contact resistance between the layers causes discontinuities in the solid-wall temperature profile between the hot and cold sides of the interface. The changed wall-temperature profile should affect the heat transfer between the wall and the fluid which, in turn, should change the plot of the Nusselt number. However the friction factor is not affected (as expected). Figure 6.29 shows a comparison of the Nusselt number behavior between the base-case, zero-TCR and the infinite-TCR cases.

The infinite TCR (adiabatic contact) has caused the Nusselt number to rise, especially in the regions of low Reynolds numbers close to where the flow reverses (near 180° and 360° crank angle). This was expected. When no TCR is present, the solid wall temperature on each side of the contact between the solid layers is the same. When the infinite TCR is introduced, a temperature difference in the solid wall between the two sides of the contact results. The fluid flowing in the channel past the contact between the two solid layers sees the discontinuity in the wall temperature profile. The increased delta-T between the wall and the fluid causes an increase in the heat transfer and that is reflected in the higher Nusselt number. At lower Reynolds numbers, the fluid has more time to absorb the heat and the effect of the infinite thermal contact resistance is more pronounced. However, when the flow stops, as it does when it switches direction, the temperature between the fluid and the solid equalizes and delta-T becomes very small, tending to zero. That introduces a discontinuity in the calculation of the Nusselt number and figure 6.29 shows that discontinuity at 180° and 360° of crank angle. The other change that has happened is related to the difference between the cooling and the heating parts of the cycle. The cooling half happens from zero to 180° of crank angle when the flow goes from the cold side to the hot side, and the heating half happens from 180° to 360°. When zero thermal contact resistance was present (base-case) the mean-Nusselt-number curves for the two halves looked the same. However with infinite thermal contact introduced, the heating half of the cycle shows a higher mean Nusselt number.

In terms of heat loss, table 6.13 shows the results of integrating the enthalpy loss and the conduction loss over the whole cycle. In the case of the solid conduction, increasing the TCR from zero (base case) to infinite has resulted in a reduction of 54.7%. The enthalpy loss has increased by 13.8%. However the total loss has decreased by 14.0%. This suggests that is a good idea to increase the thermal contact resistance in order to reduce the heat loss.

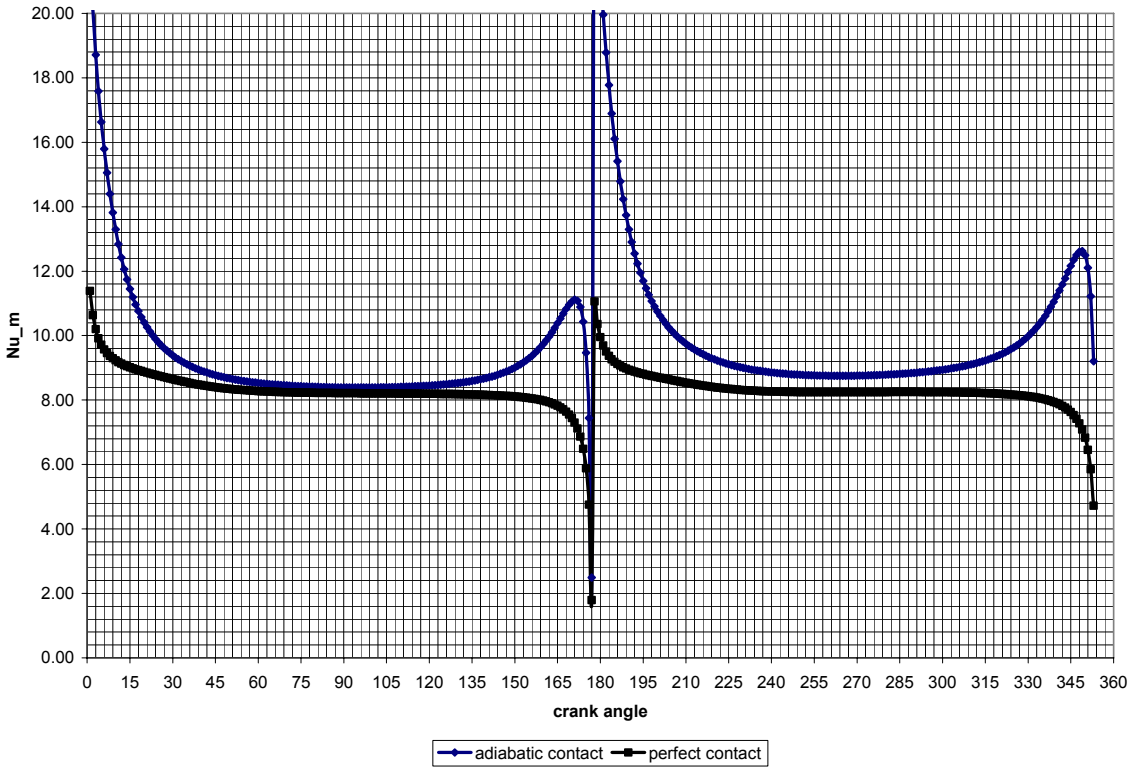

Figure 6.29.—Mean Nusselt numbers, Nu_m, as functions of crank angle, *CA*, degrees; comparison of values calculated from 2-D CFD oscillatory-flow cases (50X20 grids/segment) for (1) zero TCR (perfect thermal contact, base case) and (2) infinite TCR (adiabatic contact or perfect insulation).

TABLE 6.13—HEAT-LOSS COMPARISON OF ZERO-TCR BASE CASE TO INFINITE-TCR CASE

	Enthalpy loss, W	Change	Conduction loss, W	Change	Total loss, W	Change
Base Case	1.722		1.174		2.896	
Infinite TCR	1.960	13.8%	0.531	-54.7%	2.491	-14.0%

6.7.2.3 Effect of Changing the Oscillation Amplitude

The increase of the oscillation amplitude results in an increase of the maximum Reynolds numbers at 90° and 270° CA. Figure 6.30 shows how the behavior of the friction factor has changed due to an increase in oscillation amplitude by a factor of three. The friction factor has dropped and that is consistent with the steady-state simulations. When the Reynolds number is increased, the friction factor becomes smaller. Figure 6.31 shows how the mean Nusselt number changes when the oscillation amplitude (and, consequently, the maximum Reynolds number) are increased by a factor of three. The figure shows that Nusselt number stays much the same. When the hot or the cold fluid is pushed deeper into the stack the temperature difference between the wall and the fluid should increase. That represents the driving potential for the heat transfer. The figure tells us that the heat flux has also increased in such a way that the heat transfer coefficient has stayed about the same. The increased flow due to the increase in amplitude of the mass-flow would be responsible for sustaining the increased wall heat flux.

In terms of heat loss, table 6.14 shows the results of integrating the enthalpy loss and the conduction loss over the whole cycle, for the base case and the increased-oscillation-amplitude case.

TABLE 6.14—HEAT LOSS COMPARISON OF BASE CASE (Re_{max} = 50) AND INCREASED-OSCILLATION-AMPLITUDE CASE (Re_{max} = 150)

	Enthalpy loss, W	Change	Conduction loss, W	Change	Total loss, W	Change
Base Case	1.722		1.174		2.896	
Re_{max} = 150	18.249	10.6x	0.956	-18.6%	19.204	6.6x

A reduction in conduction loss occurred after the oscillation amplitude was increased by a factor of three. However, due to the higher flow, the enthalpy loss increased by a factor of 10.6. The effect on the total heat loss is an increase by a factor of 6.6. The reduction in the axial conduction is attributed to the higher heat flow from gas to metal due to the higher instantaneous gas mass flow. This resulted in heating the solid faster in the axial direction and thus lower (instantaneous) axial heat conduction resulted.

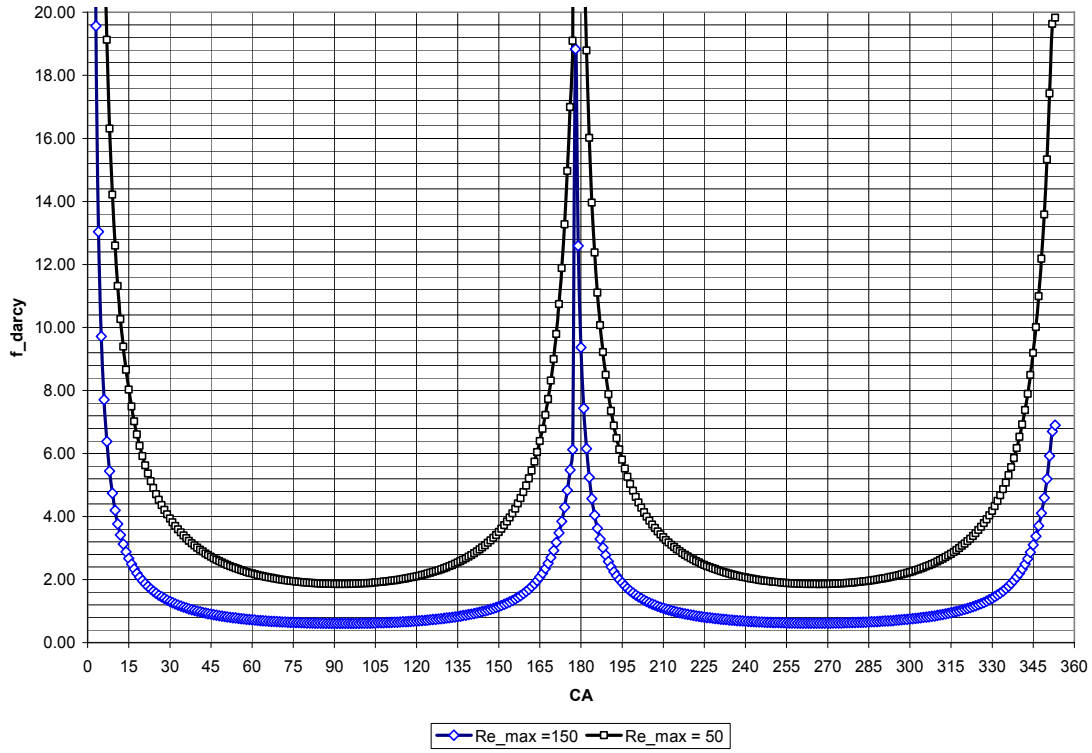

Figure 6.30.—Darcy friction factors, *f_Darcy*, as functions of crank angle, *CA,* degrees; comparisons between 2-D CFD oscillatory-flow cases (50X20 grids/segment): base-case (Re_{max} = 50) and increased-oscillation-amplitude case (Re_{max} = 150).

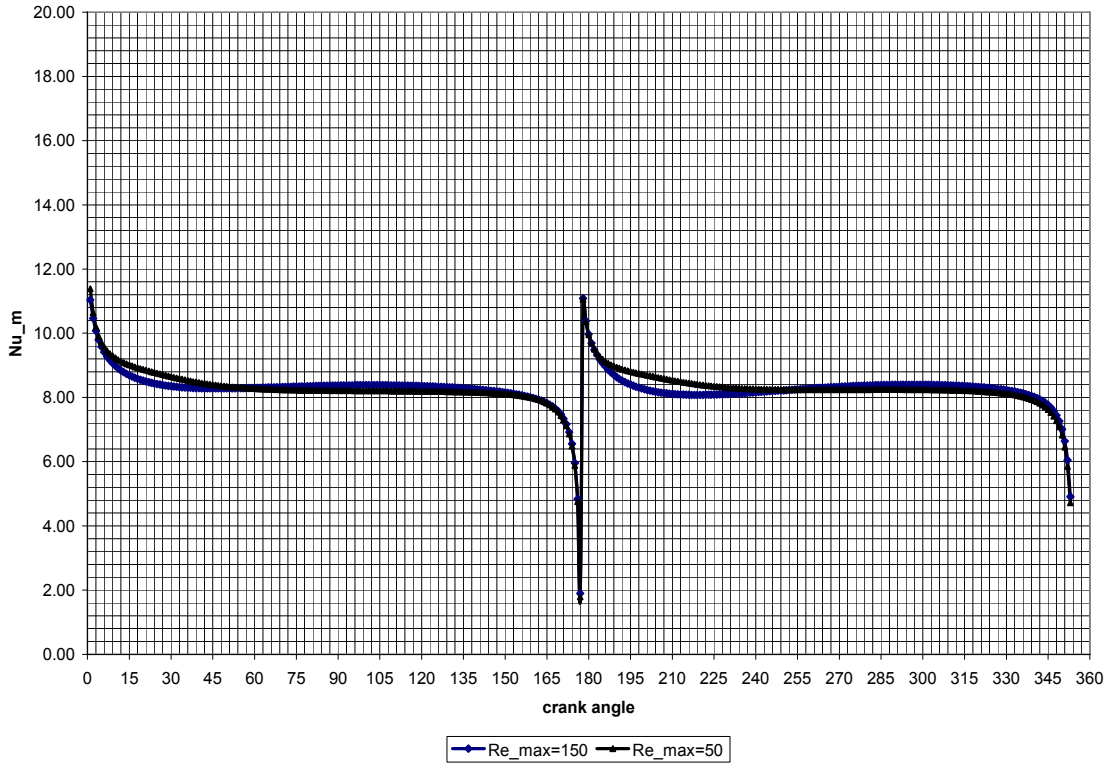

Figure 6.31.—Mean Nusselt numbers, Nu_m, as functions of crank angle, *CA,* degrees; comparisons between 2-D CFD oscillatory-flow cases (50X20 grids/segment): base case (Re_{max} = 50) and increased-oscillation-amplitude case (Re_{max} = 150).

6.7.2.4 Effect of Changing the Oscillation Frequency

The effect of increasing the oscillation frequency was also studied. As shown in the CFD oscillatory-flow test matrix (table 6.8, summary of oscillatory-flow runs), a frequency that is three times the base-case frequency was chosen for testing this effect. Therefore, frequency increased from 27.98 to 84Hz while the Valensi number, Re_ω or Va, increased from 0.229 to 0.687. A change in frequency would alter both the fluid flow and the heat transfer behavior. Figure 6.32 shows the behavior of the friction factor when the oscillation frequency is increased three times. It can be seen that at low Reynolds numbers, in the vicinity of where the flow reversal takes place (~180° and 360°), the friction factor deviates from the one at the base-case frequency. When the fluid is decelerating prior to 180°, the friction factor becomes smaller. At crank angles immediately after flow reversal, the friction factor becomes larger. Similarly, the shape of the Nusselt number curve in figure 6.33 changes when the frequency is increased. To summarize, when the fluid is accelerating, the Nusselt number is higher than the base-case number and when the fluid is decelerating, the Nusselt number becomes lower than the base-case number.

In terms of heat loss, table 6.15 shows the results of integrating the enthalpy loss and the conduction loss over the whole cycle for the base-case (Re_{max} = 50, Re_ω = 0.229), the increased-oscillation-amplitude case (Re_{max} = 150, Re_ω = 0.229), and the increased-oscillation-frequency case (Re_{max} = 150, Re_ω = 0.687).

TABLE 6.15—HEAT LOSS COMPARISON OF BASE CASE, (Re_{max} = 50, Re_{ω} = 0.229), THE INCREASED-OSCILLATION-AMPLITUDE CASE (Re_{max} = 150, Re_{ω} = 0.229) AND THE INCREASED-OSCILLATION-FREQUENCY CASE (Re_{max} = 150, Re_{ω} = 0.687)

	Enthalpy loss, W	Change	Conduction loss, W	Change	Total loss, W	Change
Base case Re_{max} = 50, Re_{ω} = 0.229	1.722		1.174		2.896	
Inc. osc. amplitude Re_{max} = 150, Re_{ω} = 0.229	18.249	10.6x	0.956	-18.6%	19.204	6.6x
Inc. osc. frequency Re_{max} = 150, Re_{ω} = 0.687	13.466	7.8x	1.009	-14.1%	14.474	5.0x

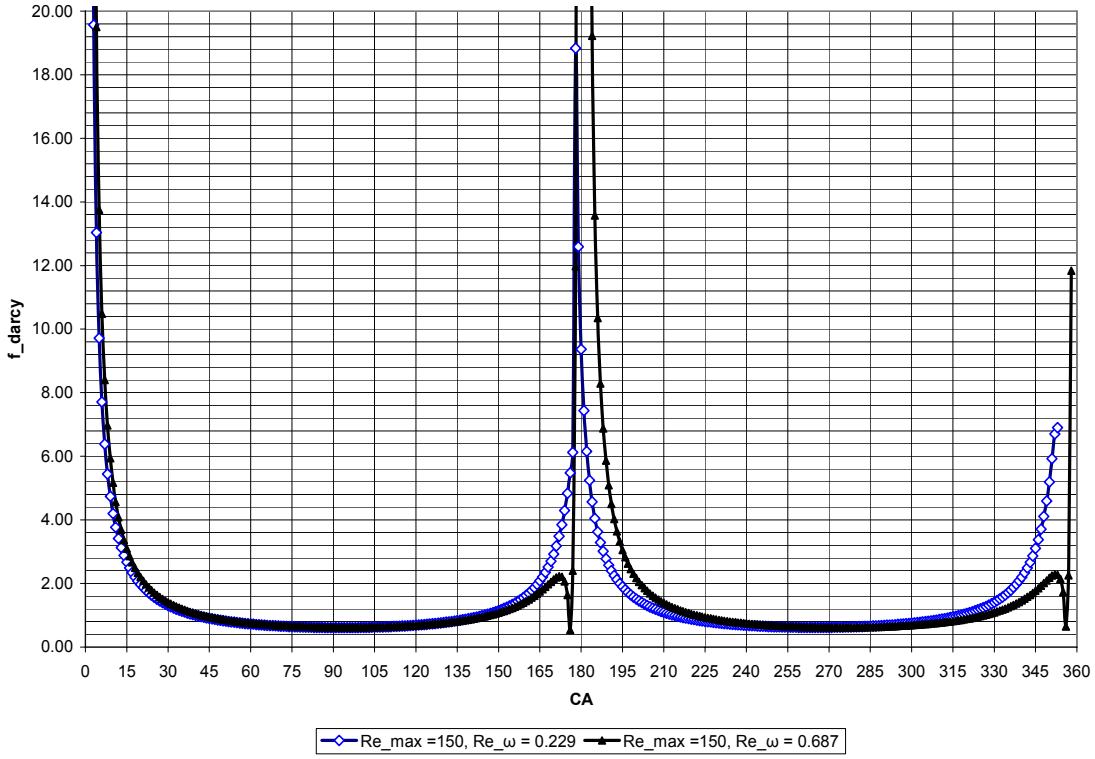

Figure 6.32.—Friction-factor comparison between the base case (Re_{max} = 50, Re_{ω} = 0.229) and the increased-oscillation-frequency case (Re_{max} = 150, Re_{ω} = 0.687).

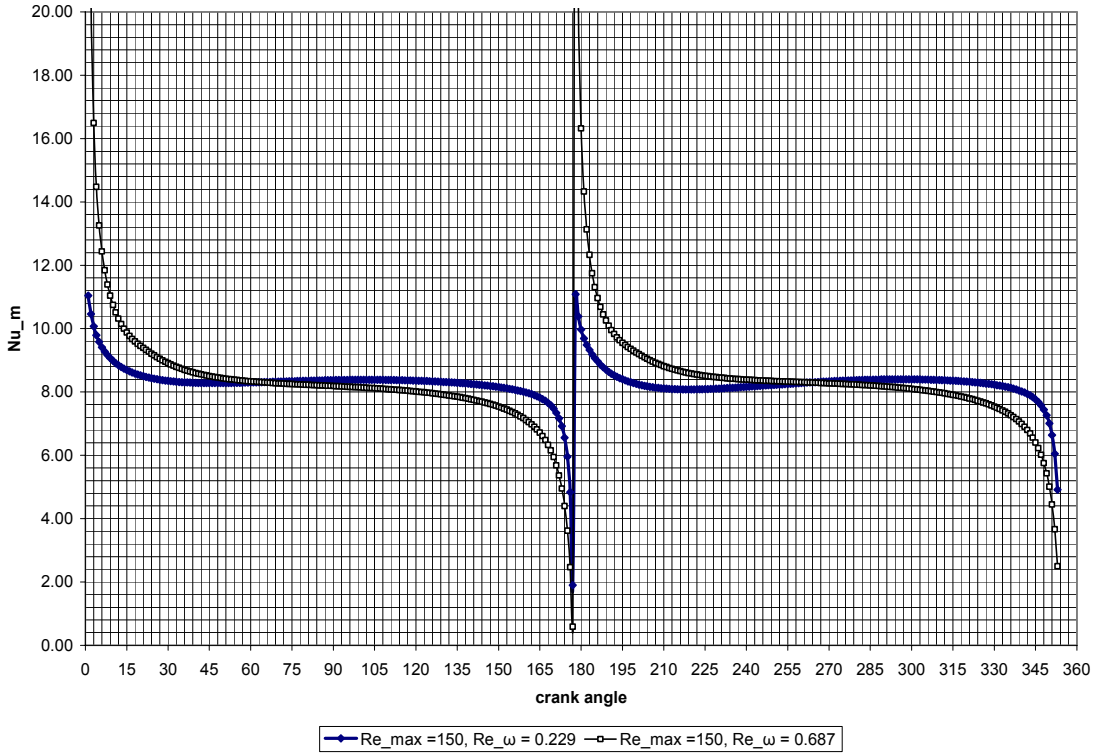

Figure 6.33.—Mean Nusselt number comparison between the base case (Re_{max} = 50, Re_{ω} = 0.229) and the increased-oscillation-frequency case (Re_{max} = 150, Re_{ω} = 0.687).

A 14% reduction in the axial conduction took place while an increase (by a factor of 7.8) in the enthalpy flux occurred when compared to the base case. The net effect is about a factor of 5.0 increase in the regenerator axial heat loss. Again, the reduction in axial conduction is attributed to the higher heat flow from gas to metal due to the higher instantaneous gas mass flow. This resulted in heating the solid faster in the axial direction and, thus, lower (instantaneous) axial heat conduction resulted.

6.7.2.5 Effect of Changing the Solid Material

The impact of solid-material properties on performance are of interest. Pure metals are known to have higher conductivity than alloys. Nickel was chosen for fabrication of the prototype test regenerator, due to limitations of cost and time—since a nickel regenerator could be fabricated via LiGA alone. However, nickel has a higher conductivity than stainless steel (the preferred material) by about 5.5 times (see table 3.10). For this comparison of nickel and stainless steel materials, the contact between layers has been set to infinite thermal contact resistance (TCR); thus the reference stainless-steel case for this material study was not the base case (which had zero TCR). Figure 6.34 compares the friction-factor behavior and, as expected, no change in the friction factor has been detected upon changing the material from stainless steel to nickel. Figure 6.35 shows the behavior of the mean Nusselt number upon changing the material. Because of the higher conductivity of the nickel the wall temperature profile was flatter than that for stainless steel for the length of one layer, between two interfaces of infinite thermal contact resistance. That should cause a change in the heat transfer. Note that figure 6.35 compares the cases of nickel with infinite TCR (adiabatic contact), stainless steel with infinite TCR (adiabatic contact) and the case of stainless steel with zero TCR (perfect contact, the base case).

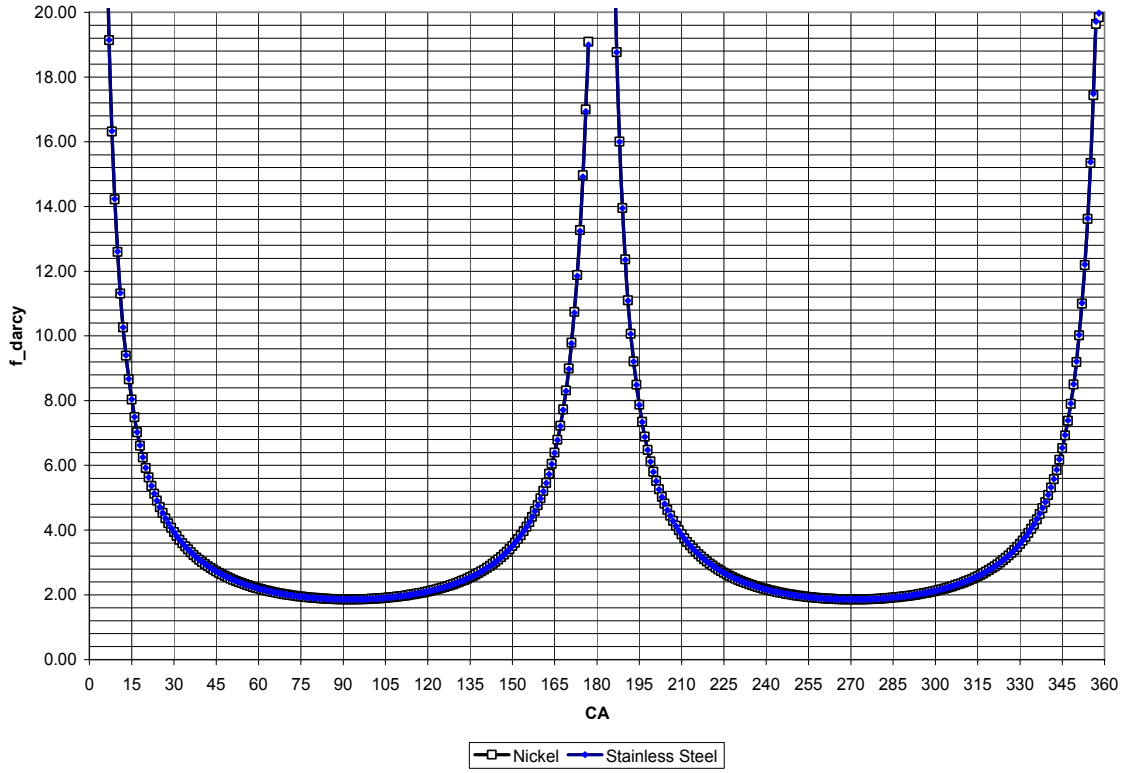

Figure 6.34.—Friction-factor comparison between nickel and stainless steel materials, both with infinite TCR between layers (adiabatic contact).

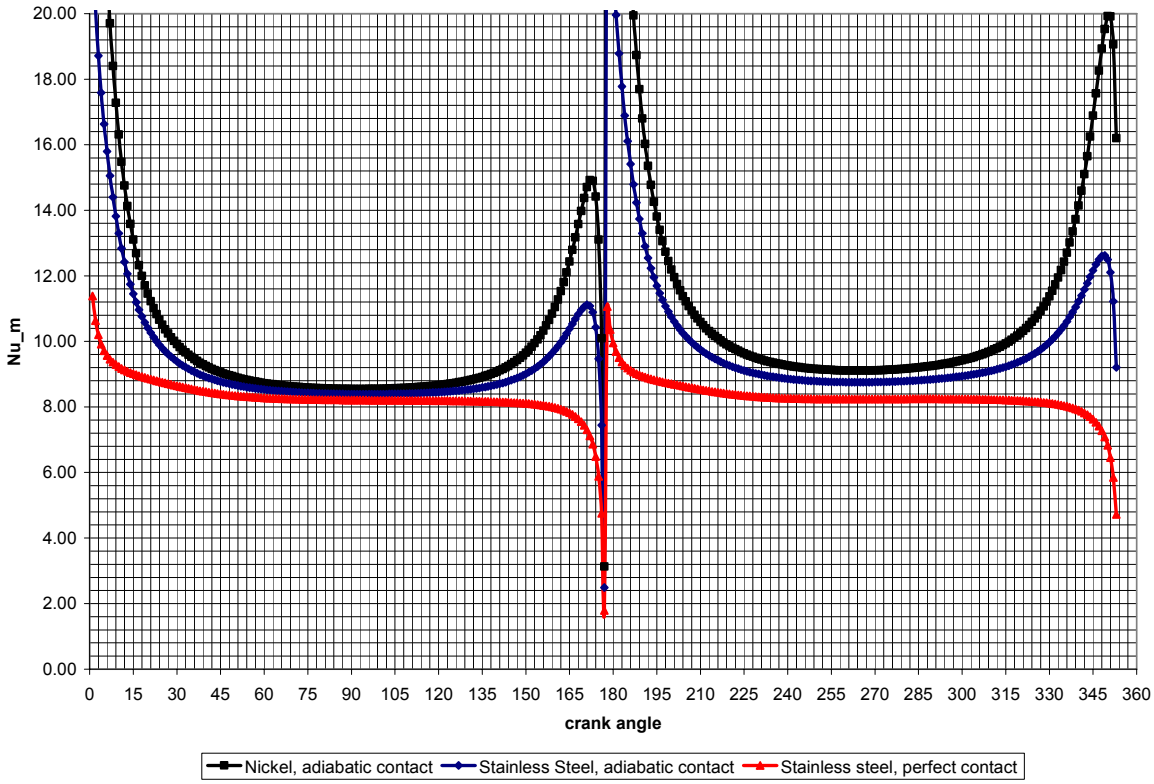

Figure 6.35.—Mean Nusselt number comparison between nickel and stainless steel, both with infinite TCR (adiabatic contact) between layers, and the base case (stainless steel, zero TCR or perfect contact).

The results show that, for infinite TCR between sections, the mean Nusselt number has increased overall for nickel compared to that for stainless steel, especially at low Reynolds numbers (i.e., near flow reversals at ~180° and 360°). Again, this is explained by the fact that within a given layer the temperature profile is flatter resulting in higher temperature differences between the wall and the fluid. The lower conductivity material can maintain a steeper temperature profile within one layer. This steeper profile is closer to the bulk-temperature profile of the fluid, leading to smaller temperature differences between fluid and solid. A comparison of the axial heat losses for nickel and stainless steel is given in table 6.16 (both with infinite TCR or adiabatic contact at the interfaces between layers).

TABLE 6.16—HEAT LOSS COMPARISON BETWEEN STAINLESS-STEEL AND NICKEL MATERIALS, BOTH WITH INFINITE TCR (OR ADIABATIC CONTACT) AT INTERFACES BETWEEN LAYERS (OR DISKS)

	Enthalpy loss, W	Change	Conduction loss, W	Change	Total loss, W	Change
Infinite TCR and SS	1.960		0.531		2.491	
Infinite TCR and Nickel	1.862	-5.1%	0.724	+36.3%	2.586	+3.8%

In this case a 36.3% increase in the axial conduction took place while a decrease (by 5.1%) in the enthalpy flux occurred when nickel is compared with stainless steel, both cases with infinite TCR between layers. The net effect is about a 3.8% increase in the regenerator heat loss using nickel. The increase in the axial conduction is attributed to the higher thermal conductivity of nickel (compared to stainless steel).

6.8 Results of 3-D CFD Straight-Channel-Layers Approximation of Involute-Foil Layers

The focus of this section is the presentation and discussion of the results for the 3-D straight-channel-layers (fig. 6.10) simulations. As mentioned earlier, two types of 3-D simulations were developed. One is the 3-D straight-channel (an approximation of an involute-foil) and the other is the 3-D involute-foil channel. The grid for the involute-foil problem is quite dense and it was not feasible for use in oscillatory-flow simulations. The 3-D straight channel grid was subjected to oscillatory flow boundary conditions and the results are to follow.

As with the actual microfabricated involute-foil geometry, the flow channels alternate in orientation from layer to layer. Figure 6.10 shows that at the entrance, the channels are horizontal for this view and on the second layer, the channels are vertical. This results in a small contact area between layers. However, the walls of the second layer disturb the flow leaving the first layer by forcing the flow to reorient itself to the new channels. That should result in an increase of friction factor. However the heat transfer should improve because of the boundary-layer disturbance. The question of how the thermal contact between the layers affects the heat transfer is again important. Allowing maximum solid conduction (zero TCR) through the interfaces between layers again forms the base case for these straight-channel simulations. The effect of setting an infinite thermal contact resistance between the layers is then studied and compared with the base case and also with the 2-D simulation. Table 6.17 shows the conditions, or study matrix, for the 3-D simulations performed using the straight-channel geometry.

TABLE 6.17—SUMMARY, OR STUDY MATRIX, FOR 3-D STRAIGHT-CHANNEL-LAYERS RUNS

Case examined	Material	Transient or steady	Layer thermal-contact resistance (TCR)	Re_{max}	Re_{ω}
Comparison with literature	SS	steady	Zero	50	0.0
Base case		oscillatory flow	Zero	50	0.229
Effect of thermal contact resistance		oscillatory flow	Infinite	50	0.229

6.8.1 Steady-Flow Simulation (3-D Straight-Channel Layers)

A 3-D steady-state simulation at a Reynolds number of 50 was performed in order to compare with the literature and with the 2-D results. In order to compare with the 2-D results, and with the literature, the Darcy friction factor is plotted against the hydrodynamic axial coordinate, x^+, which is dimensionless. The same correlation from Shah (1978), discussed earlier, is used. In the 2-D simulation, the Shah correlation was below the 2-D CFD results in the entry section and then matched well with the results. Figure 6.36 compares these 3-D steady-flow results with the 2-D results and the correlation from Shah.

As can be seen in figure 6.36, the 3-D results agree well with the 2-D results for the first layer. Upon entering the second layer, the flow encounters some resistance from the perpendicularly-oriented second layer. That is where the friction factor goes up and departs from the agreement with the 2-D results. Then the flow tries to settle again until it encounters another geometry change upon entry into the third layer. As it moves through the stack of layers, the behavior of the fluid flow settles into periodicity, with small increases in friction factor upon entering each layer and with an average value above the 2-D prediction. This behavior was expected and the simulation provided an answer regarding the magnitude of the friction factor increase.

In order to characterize the heat transfer, the mean Nusselt number is plotted with respect to the dimensionless thermal axial coordinate, x^*, in figure 6.37 and is compared to the results from the 2-D simulations and the correlation developed by Stephan (1959). As discussed earlier, the alternating orientation of the layers is expected to improve the heat transfer, relative to 2-D and uniform-channel flow. That should result in higher 3-D Nusselt number values at each flow-channel discontinuity; this can be observed in figure 6.37 .

As can be seen in figure 6.37, the 3-D results agree well with the Stephan (1959) correlation and the 2-D simulation for the first layer. However, the Nusselt number increases for the following layers. This is expected because of the disturbance in the thermal boundary layer introduced by the changing orientation

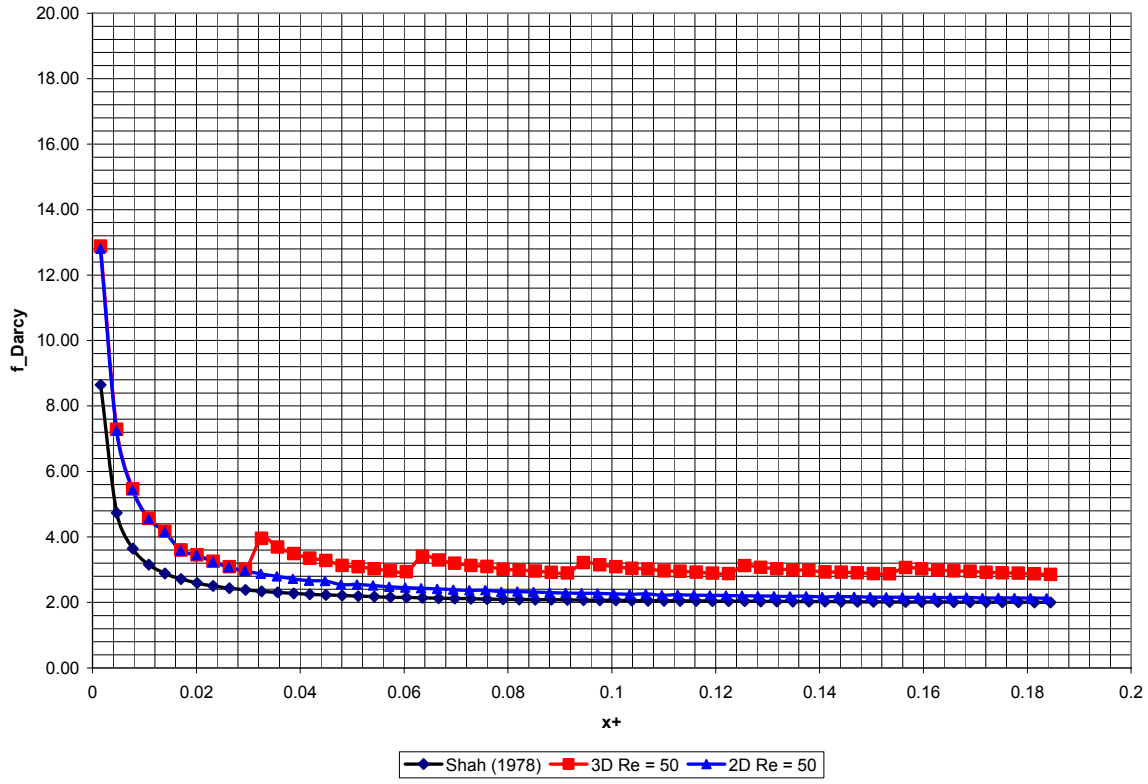

Figure 6.36.—3-D straight-channel-layers, steady-flow, friction-factor comparisons with 2-D results and Shah (1978) literature correlation—all at Reynolds number, Re = 50.

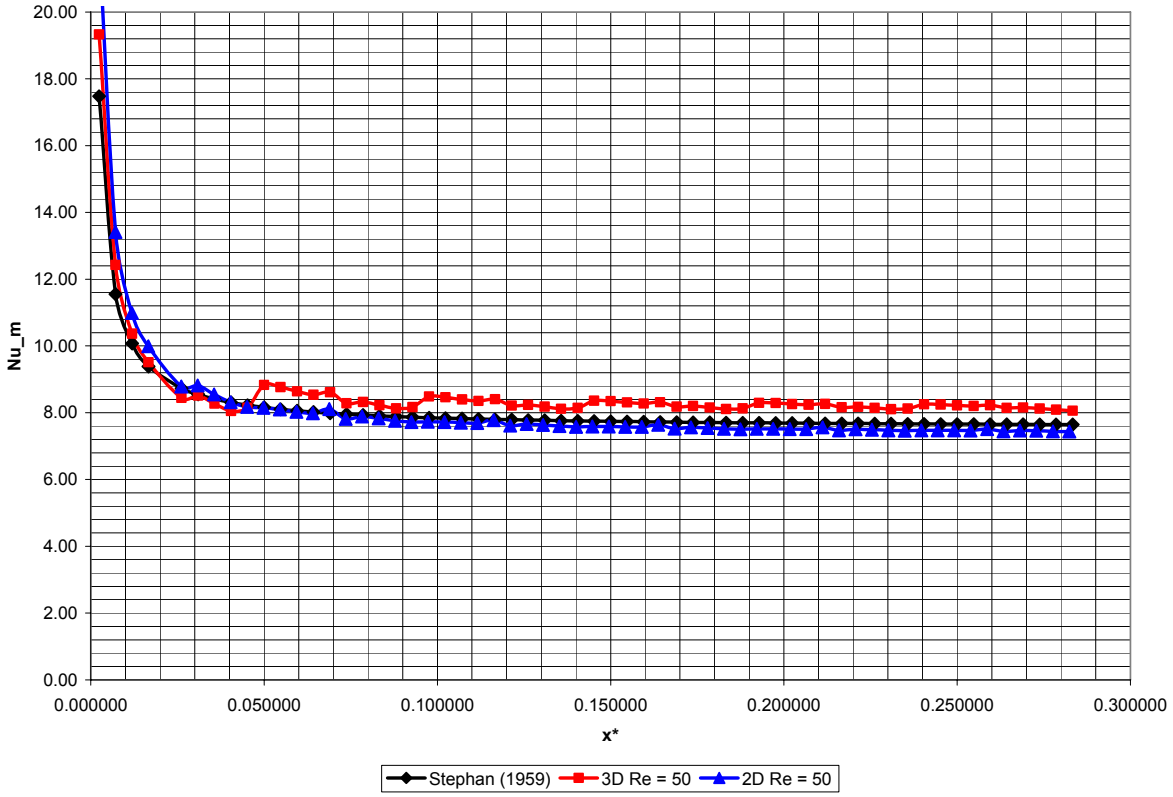

Figure 6.37.—3-D straight-channel-layers, steady-flow, mean-Nusselt-number comparisons with 2-D results and Stephan (1959) literature correlation—all at Reynolds number, Re = 50.

of the channels. After several layers, the heat transfer settles into a periodic behavior with an average Nusselt number higher than the 2-D simulation. The small irregularities in the 3-D and 2-D results represent interpolation error due to the location of the data extraction planes with respect to the grid. The CFD software stores data at the centers of cells. If data are requested at a location between the cell centers, the software performs a linear interpolation, which introduces a small error.

6.8.2 Oscillatory-Flow Simulation (3-D Straight-Channel Layers)

6.8.2.1 Base-Case 3-D Oscillatory Flow

For the 3-D straight-channel oscillatory-flow simulations, the same forcing-function for the mass flux as in the 2-D simulations was used (see eq. (6.12)). As in the 2-D simulations, it took about 10 cycles to establish cycle-to-cycle convergence. The expectation is again that both the friction factor and the Nusselt number would be higher.

As for the 2-D simulations, the friction factor is plotted (see fig. 6.38) against the crank angle in degrees and compared to the 2-D case and the experimental correlation for involute-foil by Gedeon (eq. (6.10) or (3.2)).

As expected, the 3-D friction-factor values are higher than the 2-D results at all crank angles and are more in line with the experimental involute-foil correlation values from Gedeon (eq. (6.10) or (3.2)). The mean-Nusselt-number results determined from the 3-D simulation are compared (see fig. 6.39) with the 2-D results and the experimental involute-foil correlation from Gedeon (eq. (6.11) or (3.4)). As mentioned earlier, the correlation from Gedeon averages the Nusselt number over the length of a stack of layers while the present work uses only the length of one layer to obtain the mean Nusselt number. As expected, the Nusselt number values are higher than the values for the 2-D parallel-plate simulation and also higher than the Gedeon correlation given by equation (6.11) or (3.4).

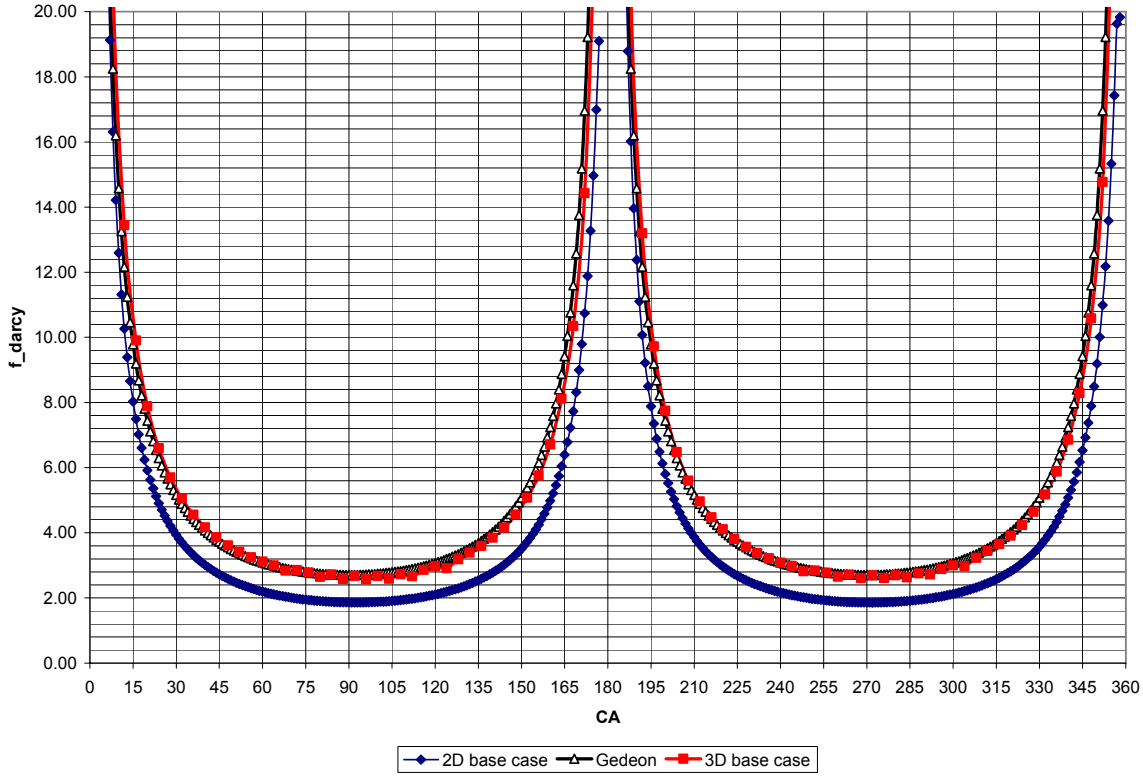

Figure 6.38.—3-D straight-channel-layers, oscillatory-flow, friction-factor comparison to 2-D base-case oscillatory-flow results and the Gedeon (eq. 6.10) experimental involute-foil correlation.

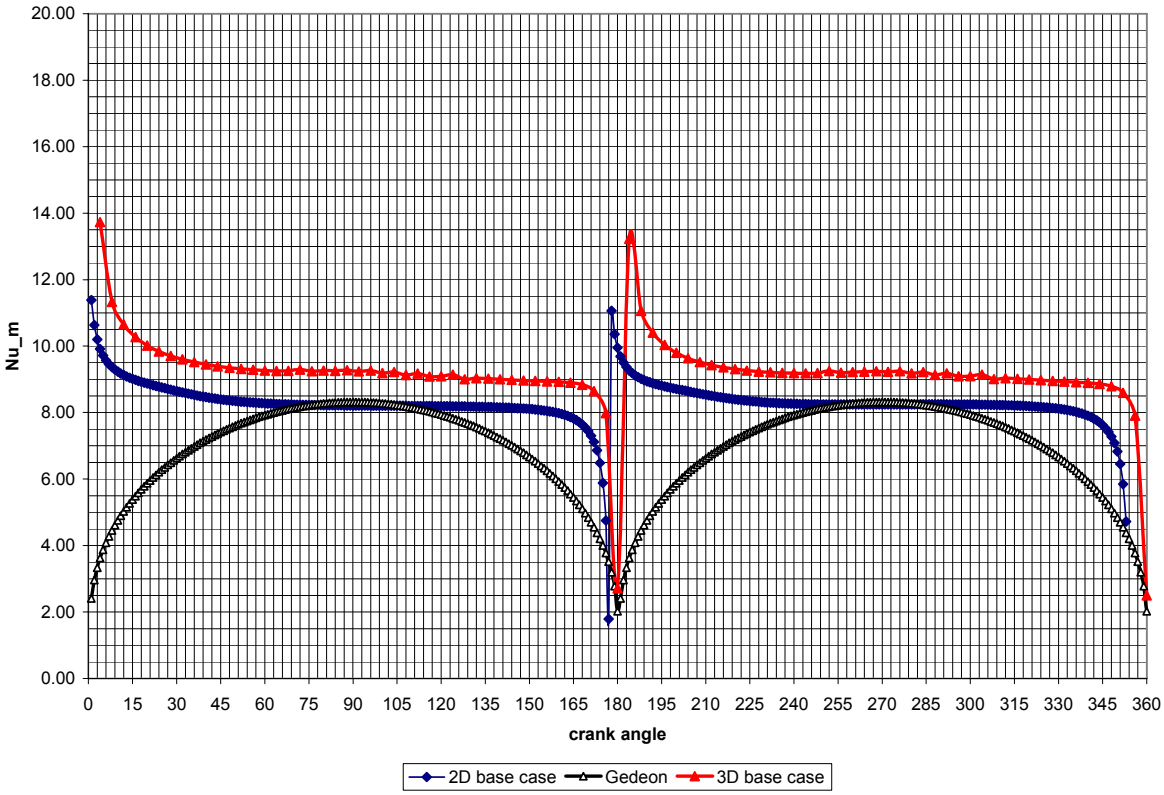

Figure 6.39.—3-D straight-channel-layers, oscillatory-flow, mean-Nusselt-number comparison to 2-D base-case oscillatory-flow results and the Gedeon (eq. (6.11) or (3.4)) experimental involute-foil correlation.

6.8.2.2 Effect of Changing the Thermal Contact Resistance (3-D Straight-Channel-Layers)

As in the 2-D work, in order to study the effect of thermal contact resistance between the layers, an infinite thermal-contact-resistance (TCR) condition was imposed at the interfaces between the layers (replacing the zero-TCR of the base case). The expectation is that the friction factor will not change when compared with the perfect contact case. However, the mean Nusselt number should behave similar to how it behaved when the same condition was imposed in the 2-D study. That is, the Nusselt number should increase overall, especially at the low Reynolds numbers that are encountered when the flow switches direction (near 180° and 360°). Figure 6.40 shows a comparison of the mean-Nusselt-number behavior among the 3-D zero-TCR (perfect contact) and the infinite-TCR (adiabatic contact) cases and the infinite-TCR (adiabatic contact) 2-D case. When compared to the 3-D zero-TCR case (i.e., perfect contact), the infinite-TCR (adiabatic contact) case has higher mean Nusselt number, especially in the regions of lower Reynolds numbers close to where the flow reverses. This was expected and it is similar to what happened in 2-D when the infinite thermal contact resistance condition was imposed.

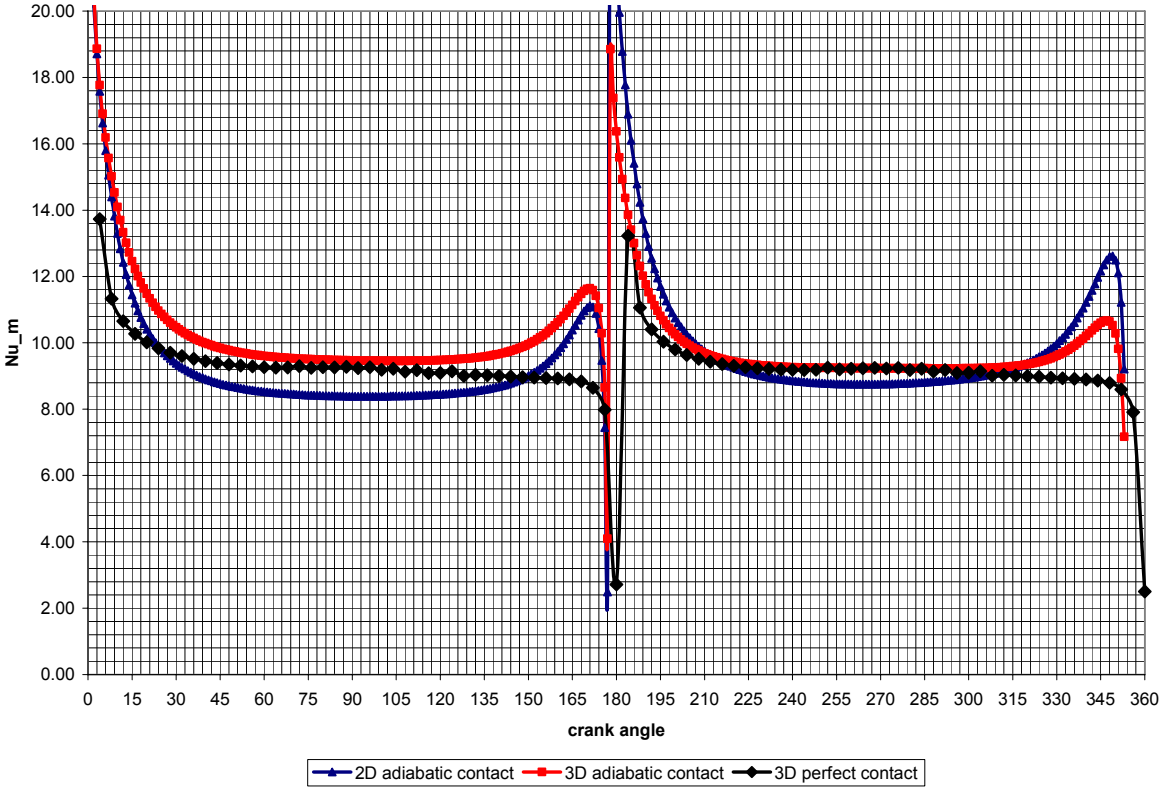

Figure 6.40.—Mean-Nusselt-number comparison for 3-D straight-channel-layers, oscillatory-flow cases, with zero-TCR (perfect contact) and infinite-TCR (adiabatic contact) between layers—and for the 2-D oscillatory-flow infinite-TCR (adiabatic contact) case.

6.9 Results, 3-D Steady-Flow Simulation of Involute-Foil Layers

In this section, the results for the 3-D involute-foil-layer simulations are presented and discussed. This 3-D computational domain resembles more closely the actual microfabricated design in terms of the shape of the channel. However, the attempt to capture the geometry of the channel better resulted in a dense grid. Even after reducing the length of the stack to only two layers, the cell count was close to 2.7 million. As explained earlier, one can use a two-layer-long unit repeatedly by taking the velocity and temperature profile from the outlet and applying it back to the inlet in order to simulate a longer stack. The drawback of this technique is that oscillatory-flow simulation is not possible. Instead of one oscillatory-flow run, simulations have been performed using steady-state conditions at several Reynolds numbers.

6.9.1 Summary of 3-D Involute-Foil Runs

The 3-D involute-foil grid actually consists of two types of grids, one half layer for the entry and a repeating unit consisting of a one-half-layer entry, a full layer, and a one-half-layer exit (see fig. 6.9). Cutting the first layer in half allows for the two grids to line up properly when passing the boundary conditions (profile) from one grid to the other. By the same token, two repeating units will line up properly so that the boundary profile can be passed, where the geometry is continuous. As shown in figure 6.9, the grid captures one full involute-foil channel in the middle. The other channels are also simulated as full because of the periodic boundary conditions applied to the sides. In fact, when periodicity is considered, this grid simulates a full ring of channels. The contact between the layers is perfect; the thermal contact resistance is zero.

Meshing this geometry presented a considerable challenge. Even though the channels were insured to line up properly, in order not to get discontinuities when passing the boundary profile, one has to ensure that the cell coordinates of the exit face match the cell coordinates of the inlet face. The ends of the channel with their round shape did not allow for a structured mesh and an unstructured mesh had to be employed. However, the generation of the unstructured mesh is harder to control when it comes to matching cell coordinates between inlet and outlet faces. This required linking the inlet and the outlet faces, which is a tedious process. Table 6.18 shows a summary of simulations performed using the 3-D involute-foil grid.

TABLE 6.18.—SUMMARY, OR STUDY MATRIX, OF 3-D STEADY-FLOW INVOLUTE-FOIL SIMULATIONS

Geometry	Material	Transient or steady	Layer thermal contact	Re no.
3-D Involute-foil channel	SS	Steady	Zero	50
				94
				183
				449
				1005
				2213

When the 2-D steady-flow simulations were performed, it was necessary to impose boundary conditions, as summarized in table 6.19.

TABLE 6.19—INLET BOUNDARY CONDITIONS FOR THE SIMULATED REYNOLDS NUMBERS, RE, OF TABLE 6.18

Case	B.C. in CFD	Inlet temp, K	Wall temp, K	Velocity inlet, m/s	Re no.
1	Velocity-inlet	660	673	4.7	50
2				8.9	94
3				17.3	183
4				42.4	449
5				94.9	1005
6				209.0	2213

6.9.2 Steady-State, Re = 50, Friction-Factor and Nusselt Number Comparisons

As for the 2-D parallel-plate and the 3-D straight-channel-layers, a 3-D involute-foil-layers simulation at Reynolds number 50 was performed. In order to compare with the 2-D results and with the literature, the Darcy friction factor is plotted (see fig. 6.41) against the dimensionless hydrodynamic axial coordinate, x^+. The same literature correlation, Shah (1978), is used.

The 3-D involute-foil-layers simulation shows a variation in friction factor (the saw shape) similar to the 3-D straight-channel layers, as expected. One thing to keep in mind is that the length of the involute-foil layer is 15 μm longer in the flow direction than the 3-D straight-channel layer. While work was in progress on this project it was learned that the actual fabricated layers were shorter than originally intended. The 3-D straight channel was adapted to the shorter length and simulations were performed that way. However the 3-D involute-foil layer length simulated was kept at the original length. The above comparison captures this difference graphically by showing that the layer-to-layer rise in friction factor for the 3-D involute-foil layers happens after the rise shown by the 3-D straight-channel layers.

In order to characterize the heat transfer, the 3-D involute-foil mean Nusselt number is plotted in figure 6.42 with respect to the thermal axial coordinate and is compared to the results from the 2-D simulation, 3-D straight-channel simulation, and the correlation developed by Stephan. The variation in mean Nusselt number, Nu_m, is similar to that encountered for the 3-D straight channel grid. The out of step layer to layer transition is again explained by the difference in the length of the layer.

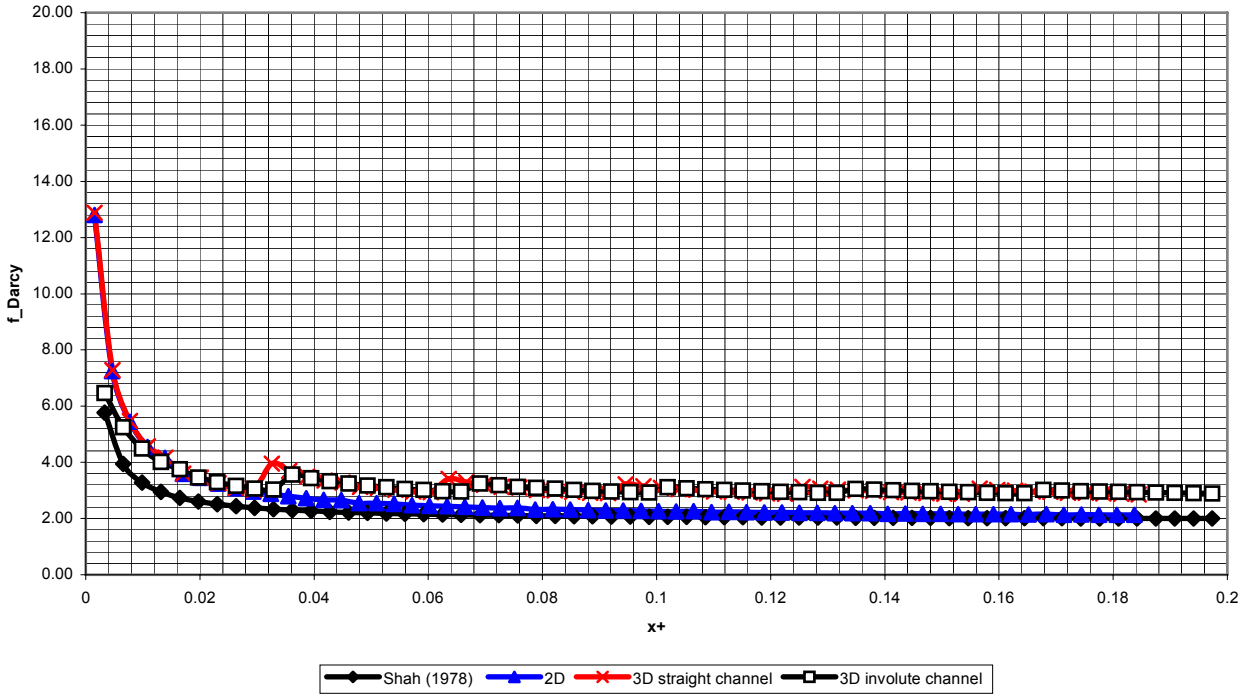

Figure 6.41.—Steady-state friction-factor comparison at Reynolds no., Re = 50 as a function of dimensionless length . Calculated via the 3-D involute-foil and straight-channel layer simulations, the 2-D parallel-plate simulation—and compared with the Shah (1978) correlation.

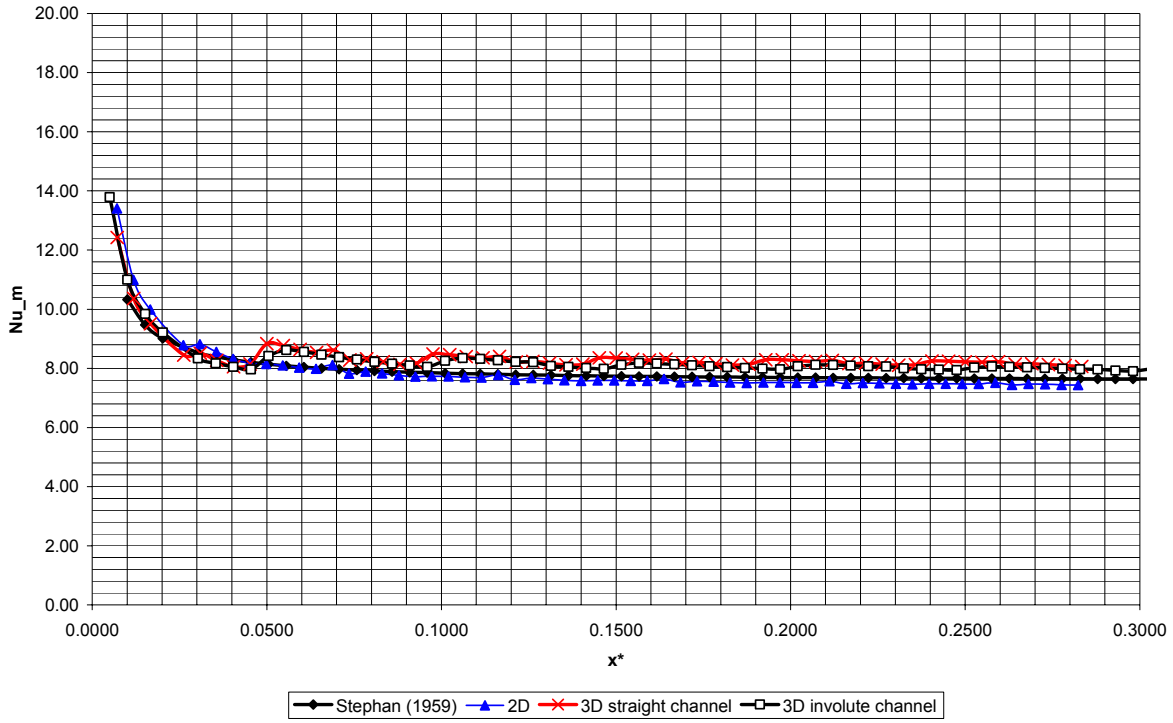

Figure 6.42.—Steady-state mean-Nusselt-number comparisons at Reynolds number, Re = 50 as a function of dimensionless length. Calculated via the 3-D involute-foil and straight-channel layer simulations, the 2-D parallel-plate simulation—and compared with the Stephan (1959) correlation.

6.9.3 Summary: Steady 3-D Involute-Foil Friction-Factor Results for All Reynolds Numbers

Simulations at other values of Reynolds numbers have been performed in order to determine the variation of the friction factor with the Reynolds number. A total of six Reynolds numbers have been attempted. The results are presented in groups of three from lowest to highest.

Figure 6.43 compares the variation of the friction factor at Reynolds numbers 50, 94, and 183. The friction factor is lower at higher Reynolds numbers, as expected. As in previous simulations, the regular friction factor increases observed at the transition from layer to layer are present at the other Reynolds numbers. The fact that the transitions don't line up is an artifact of the plotting versus the dimensionless axial coordinate, $x+$, which includes the Reynolds number in the denominator. Figure 6.44 presents the variation of the friction factor versus the actual axial coordinate in meters. One can see that the transitions between the layers line up now. However such a representation in terms of the actual dimension is not useful when a comparison with other work or an experiment is to be done. The results for the next three Reynolds numbers are presented in figure 6.45. Similar to the previous three Reynolds number simulations, the friction factor decreases as the Reynolds number increases. Another important observation is that as the Reynolds number increases, it takes more layers for the friction-factor variation to flatten out. In the case of Reynolds number = 2213 the simulation has been run up to 14 layers while for Reynolds number = 50 only six layers appear to be enough for the friction-factor trend to flatten. Averages of the friction factor have been taken from the last layers and plotted against the Reynolds number and compared with results from experiments and correlations in figure 6.46.

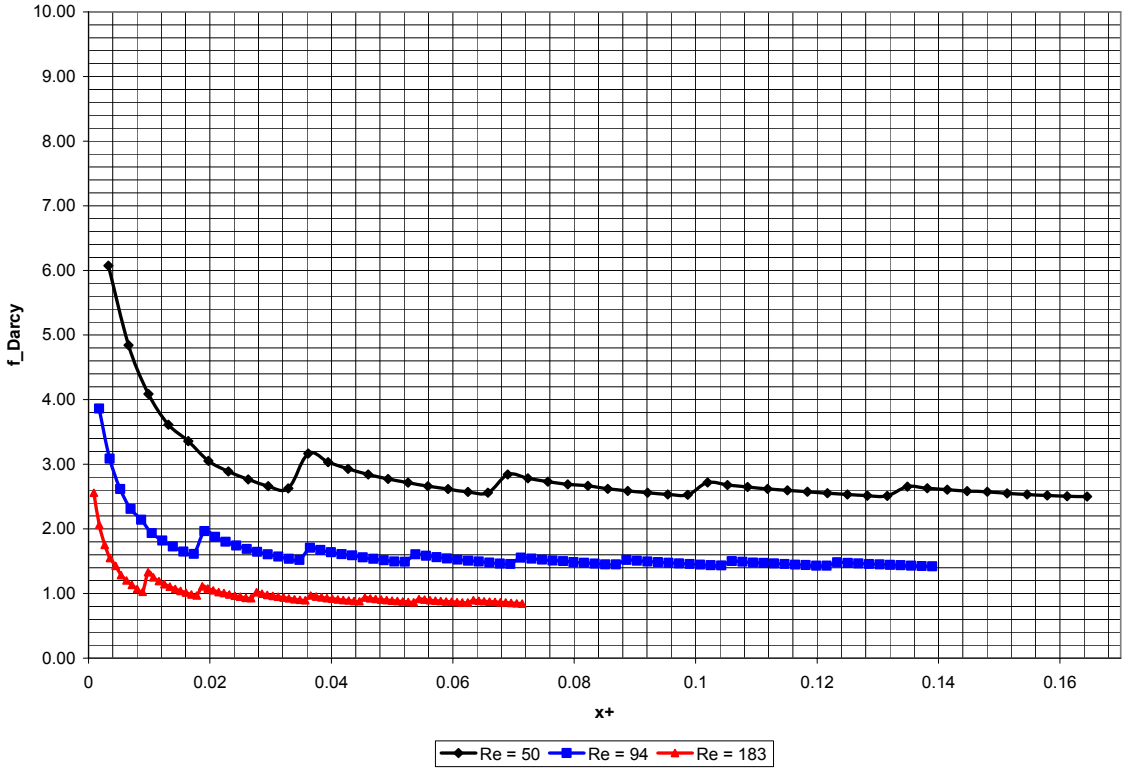

Figure 6.43.—Steady 3-D involute-foil simulation friction-factor at different Reynolds numbers, Re = 50, 94, and 183—as a function of the dimensionless length, x^+.

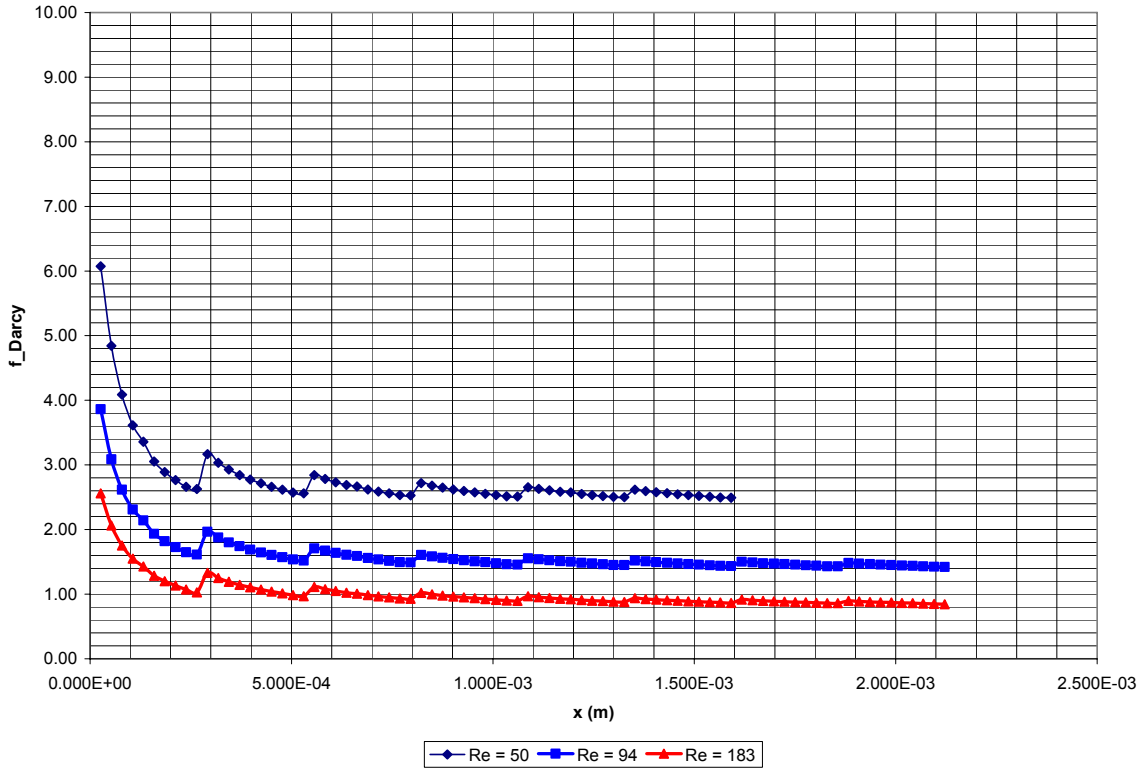

Figure 6.44.—Steady 3-D involute-foil simulation friction-factors at different Reynolds numbers, Re = 50, 94, and 183—as a function of the actual length, x.

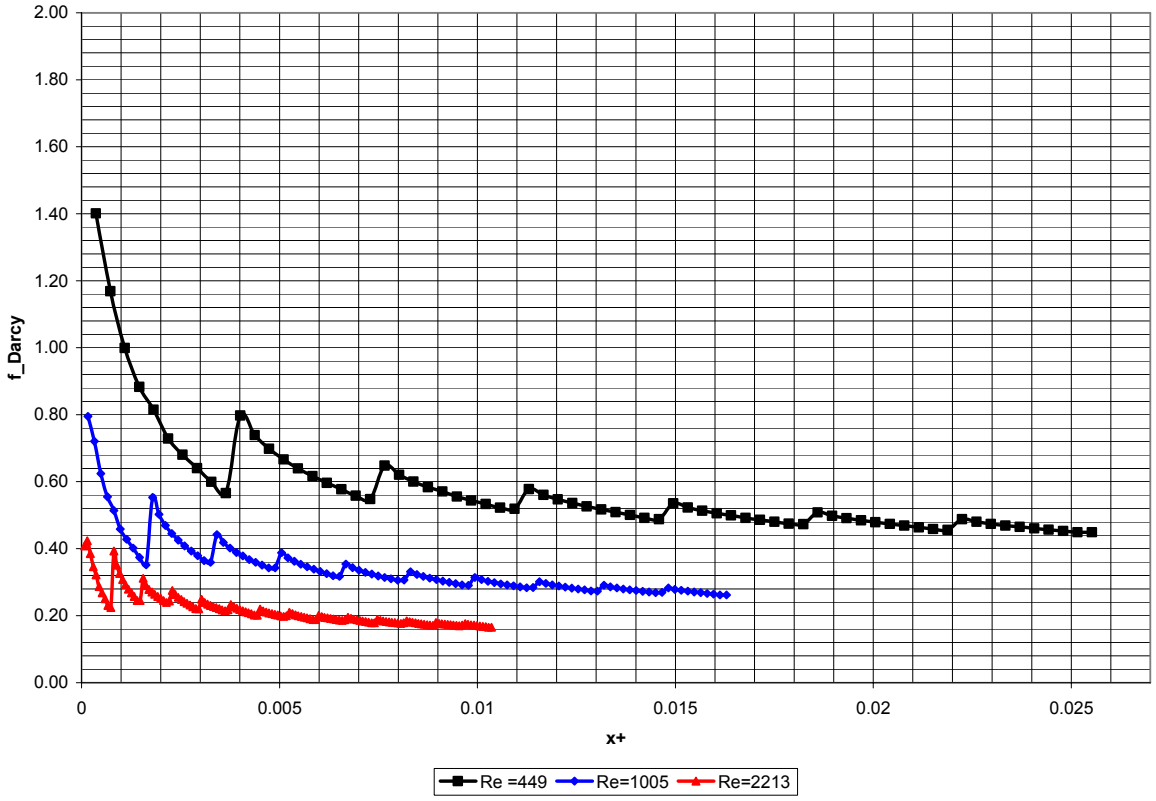

Figure 6.45.—Steady 3-D Involute-foil simulation friction factors at different Reynolds numbers, Re = 449, 1005, and 2213—as a function of the dimensionless length, x^+.

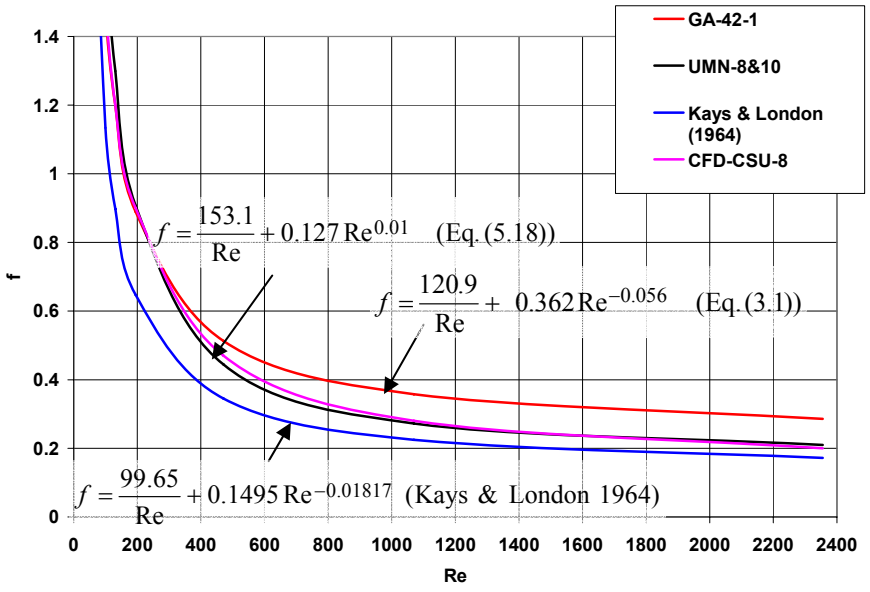

Figure 6.46.—3-D involute-foil-simulation friction factor (CFD-CSU-8) compared with UMN large-scale measurements (8 and 10 layers), Gedeon involute-foil experimental correlation (GA-42-1, eq. (3.1), original stacking) and Kays and London (1964) staggered-plate correlation.

In figure 6.46, the results obtained from the 3-D involute-foil simulations have been compared with experiments done by the University of Minnesota (UMN) on eight- and ten-layer large-scale stacks (see section 5.3.5). The same graph contains a correlation developed by Kays and London (1964) for staggered-plate heat exchangers and a correlation developed by Gedeon (eq. (3.1), for original stacking) based on involute-foil experiments performed in the NASA/Sunpower oscillating-flow test rig. The results from the current simulations match very well with the UMN experiments. Both the CFD and UMN data match very well with equation (3.1) at the low end of the Reynolds number range (~100 to 200). However equation (3.1) provides higher f values at the high end of the Reynolds number range (~1000). This is attributed to the roughness associated with the EDM cutting process, shown earlier in figure 3.7.

6.9.4 Summary: Steady 3-D Involute-Foil Mean-Nusselt-Number Results for All Reynolds Numbers

The steady 3-D involute-foil simulations performed at the six Reynolds numbers were also analyzed for heat transfer. The mean Nusselt number was plotted versus the dimensionless thermal axial coordinate, x^*, which also includes the Reynolds number in the denominator. This causes the plots to appear compressed in the axial direction, as Reynolds number increases. Figure 6.47 shows the mean Nusselt number variation for the first three Reynolds numbers, 50, 94, and 183. The mean Nusselt number increases as the Reynolds number increases. There is a good match for the first layer where the graphs appear to overlap. However, for the following layers, the mean Nusselt number, Nu_m, settles at higher values for increased Reynolds numbers. The plots appear to flatten as they advance axially and that can be associated with the flow reaching a more thermally-developed condition. As with the friction factor, at higher Reynolds numbers it takes more layers for the plot to flatten. Figure 6.48 shows the results for the next three Reynolds numbers, 449, 1005, and 2213. The behavior of the mean Nusselt number follows the same behavior of being the same in the first layer but increasing as the Reynolds number increases.

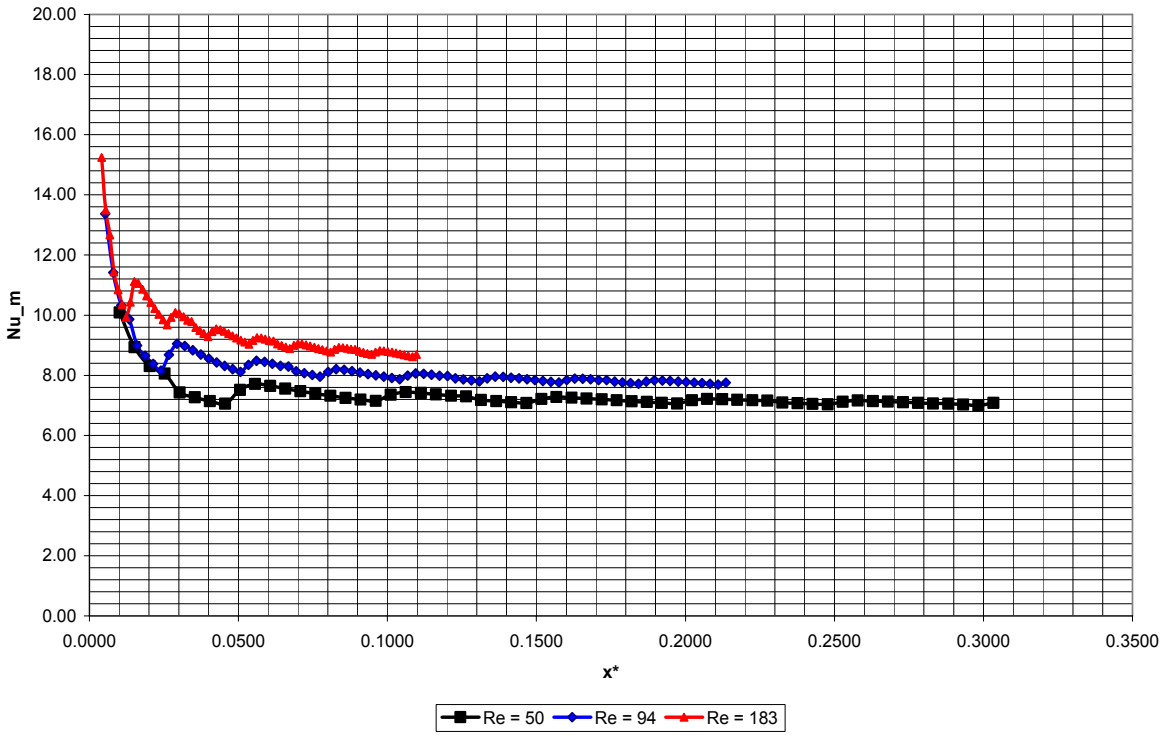

Figure 6.47.—Steady 3-D involute-foil simulation mean-Nusselt-numbers at different Reynolds numbers, Re = 50, 94, and 183—as functions of dimensionless length, x^*.

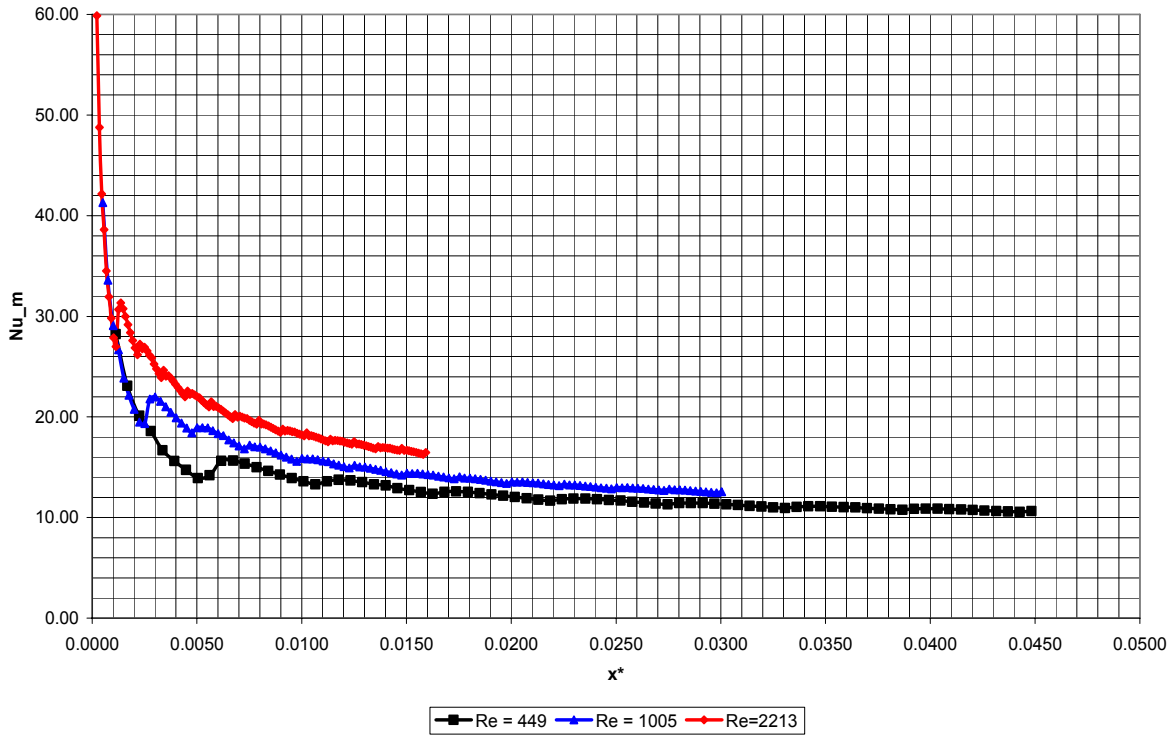

Figure 6.48.—Steady 3-D involute-foil-simulation mean Nusselt numbers at different Reynolds numbers, Re = 449, 1005, and 2213—as function of dimensionless length, *x**

6.10 CFD Simulation Conclusions

This section provides the conclusions to the work described in the previous CFD sections (Starting with section 6.0 "Analysis Tools and CFD Results"). A multitude of simulations were run using three main geometric representations of involute foils: 2-D parallel-plate, 3-D straight-channel layers, and 3-D involute-foil layers. Both steady-state and oscillatory-flow simulations were carried out for the 2-D and 3-D straight-channel geometries. Only steady-state simulations were considered practical for the 3-D involute-foil geometry (because of grid size and CPU time required). The results focused mainly on two quantities of interest, the friction factor and the mean Nusselt number. These quantities were compared for various simulation cases, experimental correlations from the literature, and experimental data obtained at UMN (large-scale tests) and Sunpower Inc (actual-scale tests). The simulation results were based upon the whole flow length for the steady-state cases. In the case of the oscillatory-flow simulations, where the computational domain has only six layers, the quantities of interest were averaged only for the length of one layer from the middle of layer three to the middle of layer four.

6.10.1 Conclusions: 2-D Parallel-Plate Simulations (Steady and Oscillating Flow)

The 2-D parallel-plate steady-state simulations showed good agreement with the correlations from the literature. That provided confirmation that the chosen grid refinement is able to resolve the fluid flow and the heat transfer for the laminar flow regime.

A base-line case was chosen for this study using helium as the working fluid at pressure = 2.5E06 Pa (25 atm), and stainless steel solid material with zero thermal contact resistance (TCR) between the 6 layers. The oscillation frequency and amplitude chosen resulted in maximum Reynolds number, $Re_{max} = 50$, and Valensi number, $Re_{\omega} = 0.229$. For this base case the enthalpy loss computed throughout the cycle = 1.722 W while the axial conduction loss = 1.174 W with a total of 2.896 W. This total value must be minimized for optimum regenerator design.

Changing the solid thermal contact resistance from zero to infinity between the layers had no effect on the friction factor, as expected. However, the mean Nusselt number increased overall with the increase more pronounced at the crank angles where the flow switches direction. The infinite thermal contact resistance between the layers blocked solid conduction from layer to layer. That resulted in a higher temperature difference between the solid and the fluid with an increase in the heat transfer, as represented by the higher Nusselt numbers. Comparing the results of this case with the base case, greater than 54.7% reduction in the axial conduction took place (as expected) while an increase (by 13.8%) in the enthalpy loss occurred. The net effect was about a 14% reduction in the regenerator axial heat loss. This confirms the finding of the earlier 1-D analyses shown in section 3.6.5.3., i.e., increasing the TCR between the layers will result in a reduction of the axial conduction accompanied with an increase in the enthalpy heat loss.

Increasing the velocity amplitude of the oscillation (by a factor of 3) resulted in lower friction factors. The increased amplitude means higher maximum Reynolds number (=150) and lower friction factors due to the fact that the friction factor is inversely proportional to the square of the mean velocity. However the increase in amplitude has little effect on the mean Nusselt number. Comparing the results of this case with the baseline case above, an 18.6% reduction in the axial conduction took place while an increase (by a factor of 10.6) in the enthalpy loss occurred. The net effect was about a factor of 6.6 increase in the regenerator axial heat loss. The reduction in the axial conduction is attributed to the higher heat flow from gas to metal due to the higher instantaneous gas mass flow. This resulted in heating the solid faster in the axial direction and thus lower (instantaneous) axial heat conduction.

Increasing the frequency of the oscillation (by a factor of 3), which also has an effect of increasing the velocity amplitude (by a factor of 3), had the effect of decreasing the friction factor upon approaching the flow reversal points and increasing the friction factor right after the flow direction has reversed. The mean Nusselt number curve was also altered by the increase in frequency of the oscillation. As the flow decelerates and approaches the switchover points the mean Nusselt number decreases and when the flow accelerates after the direction change, the mean Nusselt number increases. Comparing the results of this case with the baseline case, discussed above, we see similar results to the case of increasing the amplitude of oscillation. A 14% reduction in the axial conduction took place while an increase (by a factor of 6.9) in the enthalpy loss occurred. The net effect was about a factor of 5.8 increase in the regenerator heat loss. Again, the reduction in the axial conduction is attributed to the higher heat flow from gas to metal due to the higher instantaneous gas flow.

Increasing the thermal conductivity of the solid material (by changing the solid material from stainless steel to nickel) did not have an effect on the friction factor as expected. However, the mean Nusselt number showed an overall increase with a more pronounced rise at low Reynolds numbers. It should be noted that in this case infinite thermal contact resistance was applied between layers. Therefore, this case was compared with the results of the stainless steel material discussed above (not with the base case). In this case, a 36.3% increase in the axial conduction took place while a decrease (by 5%) in the enthalpy loss occurred. The net effect is about 3.8% increase in the regenerator heat loss. The increase in the axial conduction is attributed to the higher thermal conductivity of nickel (compared to stainless steel).

6.10.2 Conclusions: 3-D Straight-Channel-Layer Simulations (Steady and Oscillating Flow)

For the 3-D straight-channel-layer steady-state simulation, both the friction factor and the mean Nusselt numbers depart from agreement with the 2-D simulation values upon entering the second layer. That is where the 3-D effects become obvious and they persist as the axial coordinate advances. At the entrance of every layer, the forced reorientation of the flow results in small rises of both the friction factor and the mean Nusselt number with subsequent decreases as the flow settles into each new layer. Overall the plots of the friction factor and the mean Nusselt number tend to flatten out as the flow reaches a fully developed condition.

For the oscillatory-flow simulations of the 3-D straight channel layers, the friction factor shows an overall increase compared to the 2-D oscillatory-flow simulation and good agreement with the

experimental involute-foil correlation from Gedeon. The mean Nusselt number also shows an overall increase compared to the results from the 2-D simulation. It also shows a higher value when compared to the correlation from Gedeon at maximum Reynolds number. The shapes of both the friction factor and mean Nusselt number curves are similar to the shapes observed in the 2-D simulations. So the effect of going from 2-D to 3-D resulted in shifts upwards of both friction factor and mean Nusselt number curves, as might be expected since the 2-D simulations do not include the flow perturbations resulting from flow around the ends of the foil layer.

Changing the thermal contact resistance from zero to infinite between the solid layers in the 3-D straight-channel layers with oscillating flow had no effect on the friction factor, as expected. However the mean Nusselt number increased overall but with a more pronounced increase at the crank angles near where the flow switches direction. The same behavior was encountered in the 2-D simulations. Although the actual values for the mean Nusselt number are higher in the 3-D simulations, the more expedient 2-D simulations capture well the behavior of the mean Nusselt number as the thermal contact resistance is changed.

6.10.3 Conclusions: 3-D Involute-Foil-Layer Simulations (Steady Flow Only)

Simulations at several Reynolds numbers in the laminar-flow regime were performed and the friction-factor and the mean-Nusselt-number results were quantified as functions of their respective dimensionless axial coordinates. For Reynolds number 50, comparisons were performed for the 2-D and the 3-D straight-channel simulations. The friction-factor variations with Reynolds number were compared to experiments and two theoretical correlations. Several conclusions can be drawn:

As with the 3-D straight-channel layers, the simulations for the 3-D involute-foil layers show increases in both friction factor and mean Nusselt number at the geometric transitions between the layers. Furthermore, at Reynolds number 50, these increases are similar for the 3-D straight-channel and the 3-D involute-foil simulations. From this similarity one can infer that using a simpler grid such as that used for the 3-D straight-channel layers can capture to a good extent the steady-state three-dimensional effects of the 3-D involute-foil layers for low Reynolds numbers. This is important in terms of the practicality of doing CFD simulations. Although more computing power is available now than ever, the researcher still must compromise between computing time and accuracy.

The friction factor matched well the experimental results. That lends credence to the simulations performed for the 3-D involute-foil layers. The detailed work that went into constructing the grid, running the CFD simulations, and post processing the data provided meaningful results, validated by experiment. By their nature, the simulations can in a more expedient way go beyond what the experiments can do and provide further predictions for optimization or comparison with other designs.

The technique of analyzing a repeating unit recursively has also been validated. That allows for steady-state simulations of a stack consisting of a large number of layers by using a repeating unit that is only two layers thick. That, in turn, not only saves on computation time and resources but also makes the simulation of a large stack feasible.

6.10.4 Future CFD Work

The CFD involute-foil simulations reported here revealed many insights into how the fluid flow and the heat transfer occur in the microfabricated involute-foil-design regenerator. However, the study could be usefully extended in two main directions. The first direction consists of varying parameters that result in having to modify the grids. Such geometric parameters could be the length of the layer, the hydraulic diameter or surface roughness. The second direction consists in changing the boundary conditions and/or the material properties.

As far as boundary conditions are concerned, there are numerous combinations of amplitude and frequency that can be attempted based on the conditions encountered by the regenerator in actual Stirling engines. Furthermore, inlet profiles that better match the conditions at the entry and the exit of the regenerator could be tried. All these new simulations can build upon the present work and save time and money, yet provide ever more advanced knowledge.

CFD simulations for comparison with the experimental jet penetration study done by UMN have been postponed to Phase III. This study will include a slot jet and a round jet to examine the jet spread angle and penetration depth.

7.0 Structural Analysis of Micro-Fabricated Involute-Foil Regenerators (Infinia)

7.1 Summary

This section reports the regenerator structural analysis results which helped demonstrate the feasibility of the design. The results indicate that the proposed regenerator structure has high axial stiffness and the stress level is sensitive to a radial side disturbance. Potential further work is also discussed. It should be noted that in these analyses stainless steel was used (the originally planned microfabrication material) while the thermal test data (friction factor and Nusselt number) discussed earlier was taken using a nickel regenerator.

7.2 Introduction

To have high heat storage capacity, regenerators are constructed of high-porosity material that readily conducts heat radially and has a high surface area. Most current space-power regenerators are made from random fibers, which are somewhat difficult to manufacture in a precisely repeatable manner and are susceptible to deformation; these problems can lead to performance losses. The CSU NRA regenerator microfabrication contract team proposed a microfabricated involute-foil regenerator to potentially replace random-fiber and wire-screen regenerators. Figures 7.1 and 7.2 illustrate the geometry of the annular rings and the involute sections of the regenerator. Early analysis showed the potential for significant gains in performance efficiency and reductions of manufacturability variability while improving structural integrity (Qiu and Augenblick, 2005).

To ensure that the stiffness and the stress levels meet the design criteria, linear stress analysis was carried out on this proposed new regenerator. This section presents the results of finite element analysis of the microfabricated, involute-foil regenerator under 44 N (10.0 lb) axial force and 4.4 N (1.0 lb) side disturbance force.

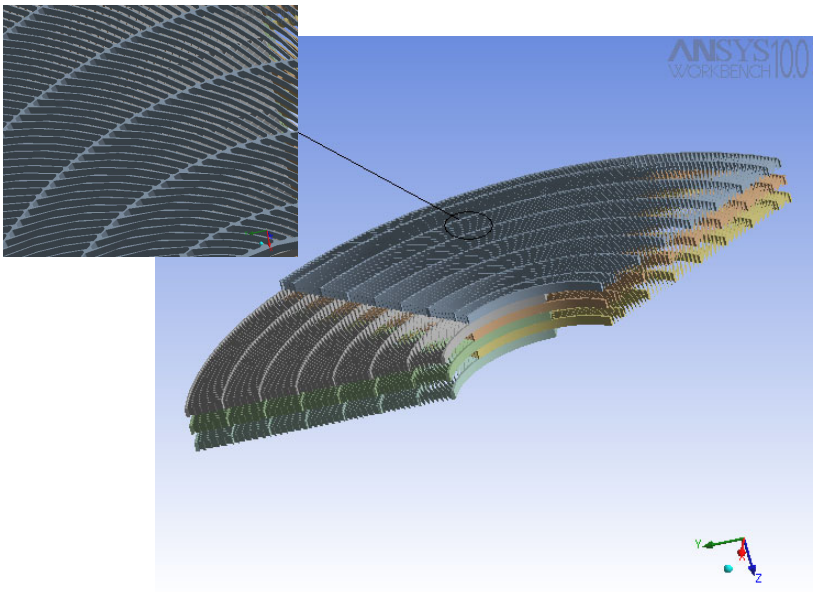

Figure 7.1.—Partial of the solid model.

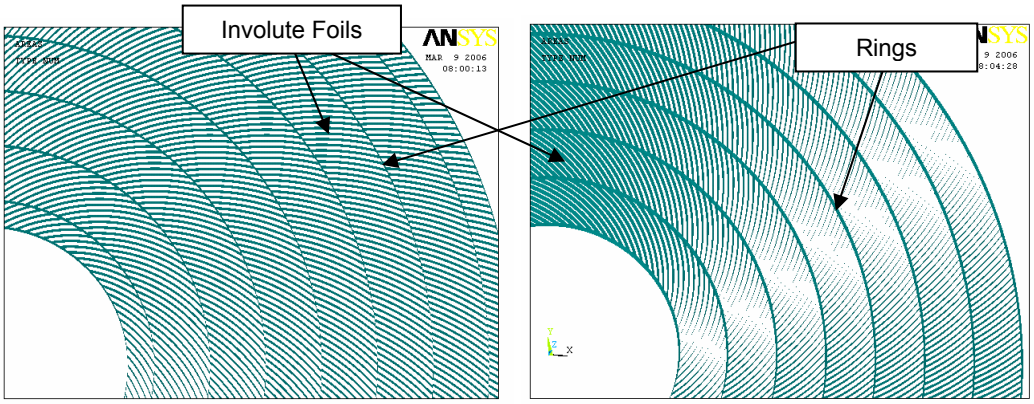

Figure 7.2.—Geometry of layers.

7.3 Finite Element Analysis

A finite-element-analysis (FEA) model was created to represent the geometric characteristics and three load cases were applied to the finite-element model to examine the stiffness and the stress levels.

Without using symmetry or periodic-symmetry conditions, all 360° of the geometry was included in the finite-element model. The thicknesses of the annular rings and the involute segments were much smaller than the other 2 dimensions. To allow the model to be handled by the computer power available, the FEA model was simplified as surfaces in 3D space with 4 layers in axial direction. ANSYS shell element *shell63* was used in the FEA to reduce the size of the model. The regenerator was made from stainless steel 316L and the assumption that the material properties were not sensitive to temperature change was used in the analysis.

7.3.1 Material Properties of Stainless steel 316L Used in FEA

Young's modulus	=	1.9×10^{11} N/m^2 (2.796×10^7 psi)
Poisson's ratio	=	0.3
Tensile strength	=	4.97×10^8 N/m^2 (7.21×10^4 psi)
Yield strength	=	1.8×10^8 N/m^2 (2.61×10^4 psi)

7.3.2 Geometric Model

Thicknesses of the involute sections, inside annular rings, and the outside annular ring are 12.7 μm (0.0005 in.); 25.4 μm (0.001 in.), and 127 μm (0.005 in.), respectively. Total box volume was about 270 mm^3 (0.0165 in.^{3}); the mass volume was about 44.5 mm^3 (0.0027163 in.^{3}). The porosity was about 84%. Individual disk thickness (axial direction) was 250 μm. The FEA was based on the preferred stainless-steel material, even though nickel was chosen for convenience in early testing of the performance of the involute-foil geometry.

7.3.3 FEA Model

ANSYS 3D shell element *shell63* with 6 DOF at each node was used. The total number of elements was 136422. The total number of nodes was 170220.

7.3.4 Boundary and Loading Conditions

7.3.4.1 Case 1 (Axial Compression)

It is extremely important that the regenerator be properly fixed within the heater head, as any relative movement between the regenerator and the heater head can lead to regenerator structural oscillation and failure. Axial compression and a slight press-fit mechanism are currently used by Infinia to stabilize their regenerators within the heater head. A 44 N (10 lb) axial force was uniformly distributed on the top

surface to simulate the axial fit and the bottom-face surface was constrained from translation in the axial direction. In order to avoid rigid-body motion in the FEA, the minimum constraint condition *Ux = Rx = Ry = Rz = 0* and *Uy = Rx = Ry = Rz = 0* were used on 2 nodes of the inside circle as in the following figures.

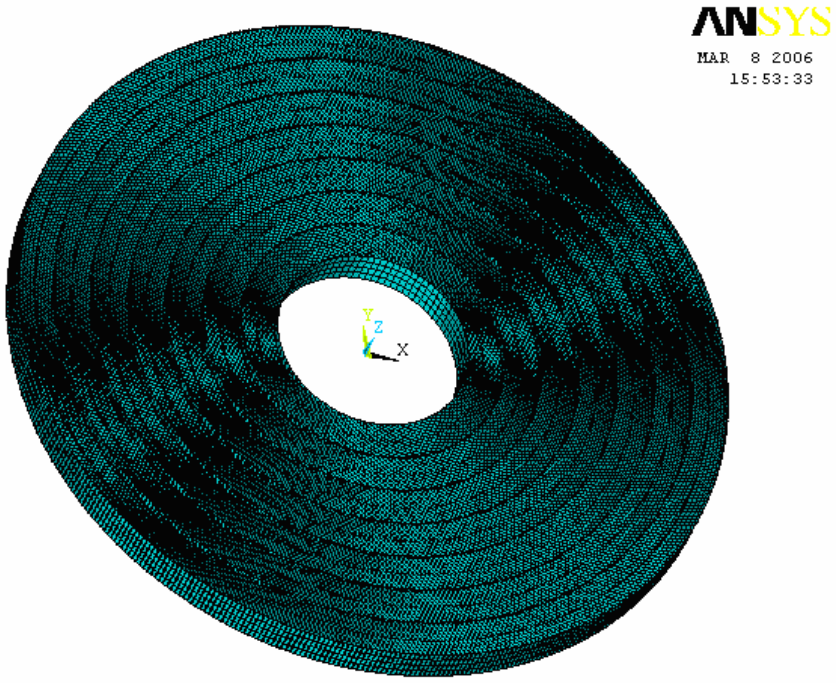

Figure 7.3.—FEA model (note 4 layers are modeled).

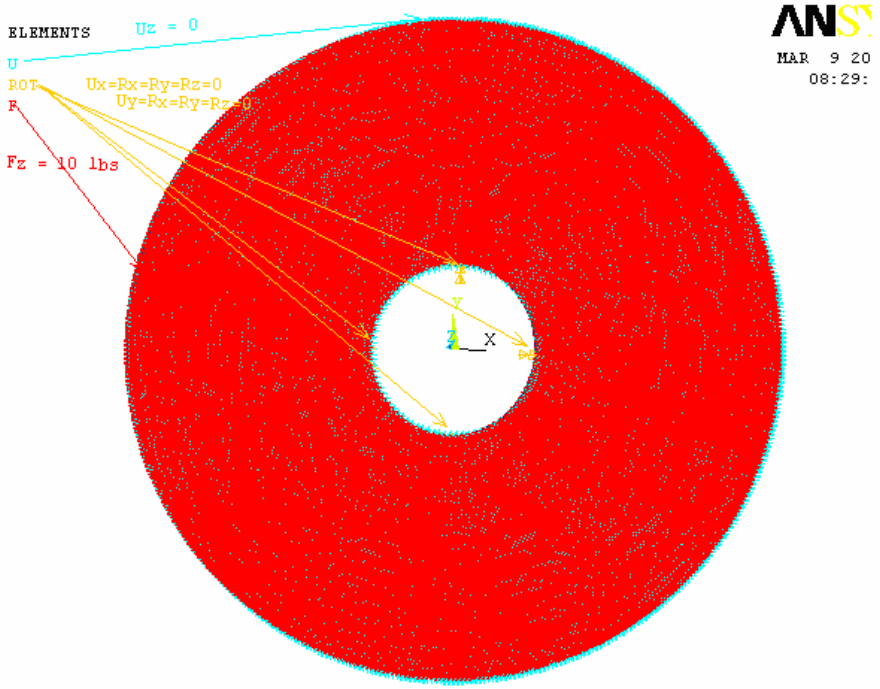

Figure 7.4.—Boundary and axial compression loading condition (Case 1).

7.3.4.2 Case 2 (Radial Side Load)

During installation, the regenerator ought to be installed so that it is under axial compression with no side loading. To simulate the disturbance from a side load, a 4.45 N (1 lb) side force acting on about 0.047% of the top layer outside annular ring was added to Case 1 to investigate the side load effect. The bottom-face surface was constrained in the axial direction and the inside circle of the bottom face was fixed in rotation and translation directions to avoid the rigid-body motion.

7.3.4.3 Case 3 (Distributed Radial Side Load)

This load case was created to investigate the stress sensitivity with respect to the side-load acting-area. The boundary condition and the load conditions were similar to the Case 2 except that a 4.45 N (1 lb) radial side load acted on 10% of the top layer outside annular ring.

7.3.5 FEA Results for Cases 1, 2 and 3

The FEA results for Cases 1, 2 and 3 are summarized in table 7.1 and plotted in figures 7.7 through 7.21.

TABLE 7.1—MAXIMUM DISPLACEMENT AND VON MISES STRESS FOR LOAD CASES 1, 2 AND 3

Load case	Disp. *Ux*, in. {plane of disk}	Disp. *Uy*, in. {plane of disk}	Disp. *Uz*, in. {axial}	Total disp., in.	von Mises stress, psi
Case 1 (axial force)	0.734e-6	0.736e-6	0.646e-6	0.804e-6	1732
Case 2 (rad'l force 1)	0.111e-3	0.148e-3	0.289e-5	0.148e-3	40624
Case 3 (rad'l force 2)	0.462e-4	0.304e-4	0.735e-6	0.462e-4	6374

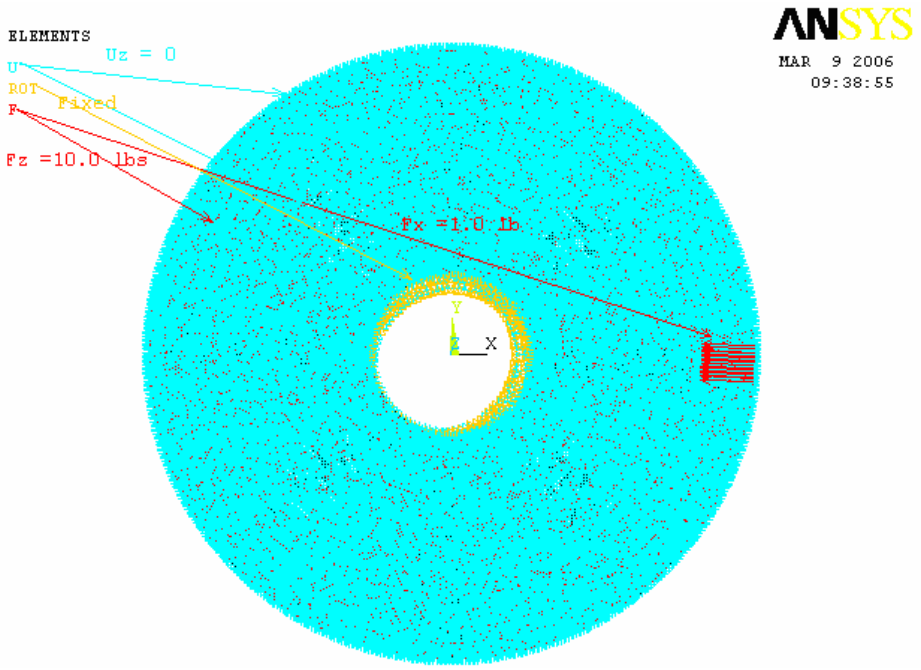

Figure 7.5.—Boundary and radial side-loading condition (Case 2).

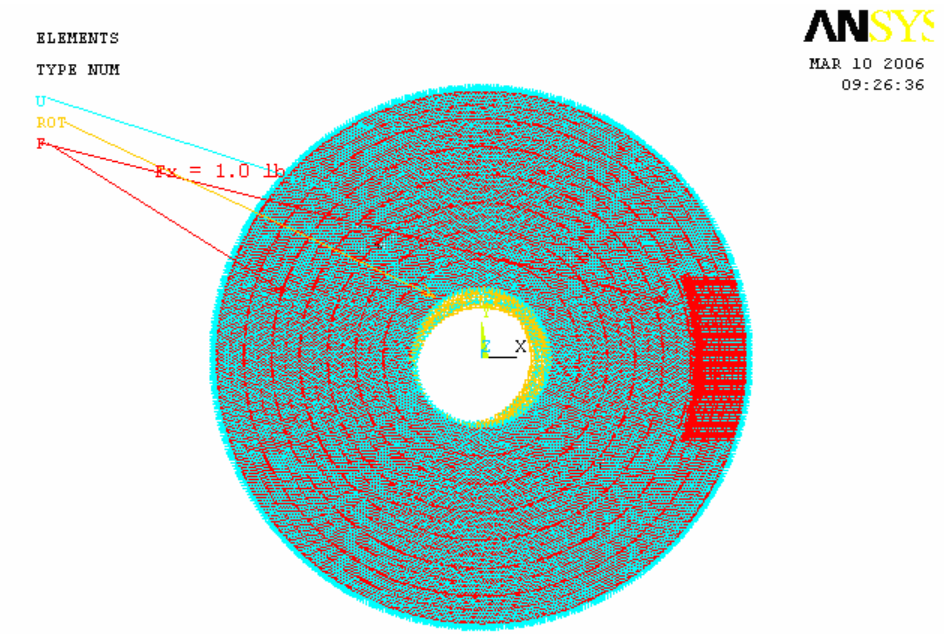

Figure 7.6.—Boundary and distributed radial side loading condition (Case 3).

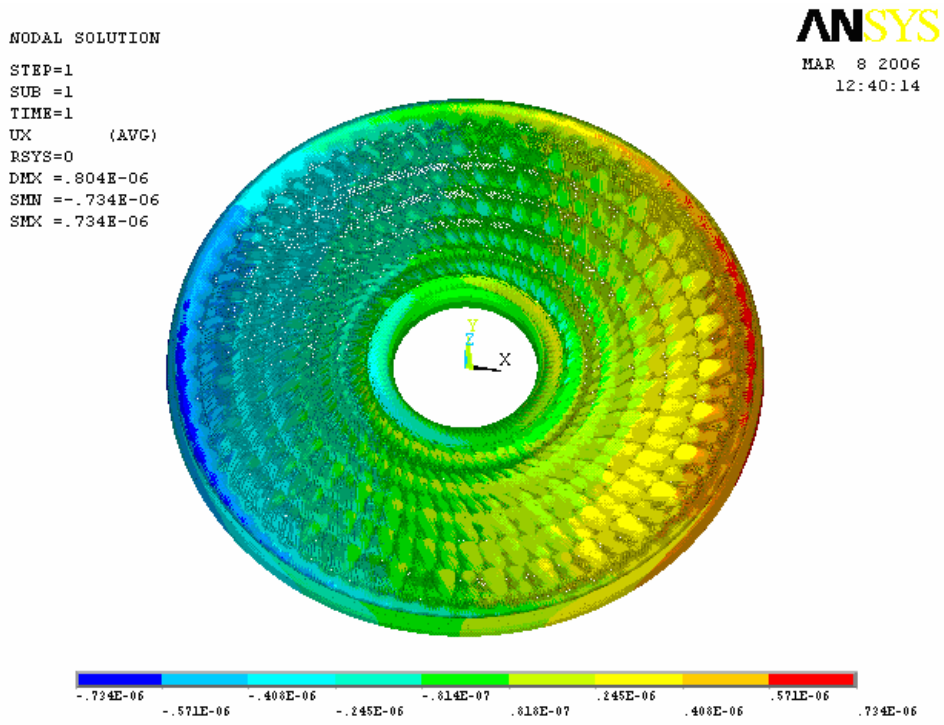

Figure 7.7.—Deformation *Ux* (Case 1).

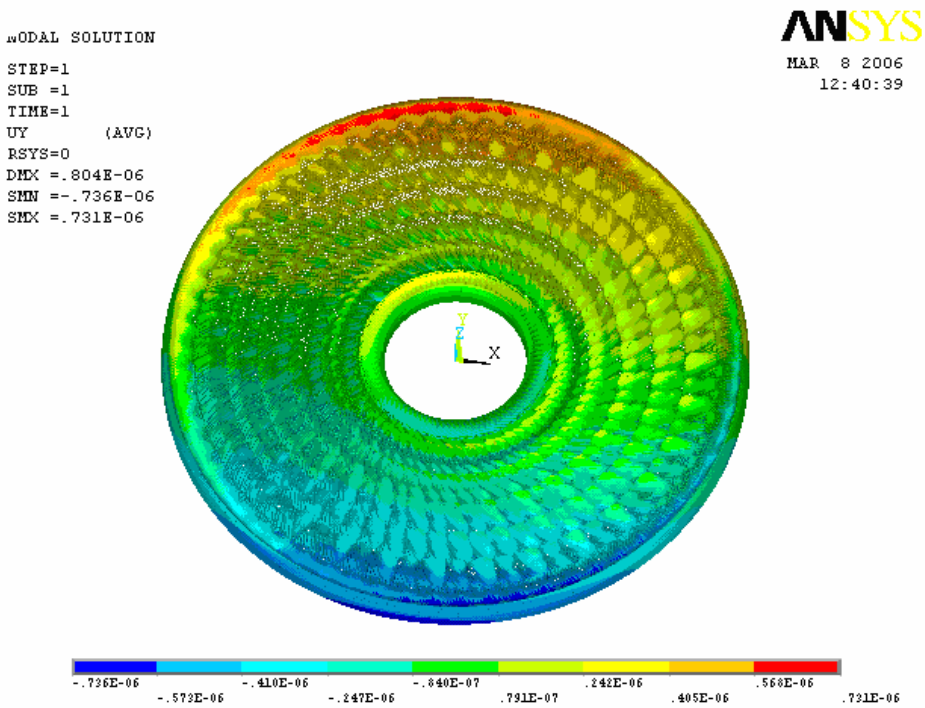

Figure 7.8.—Deformation *Uy* (Case 1).

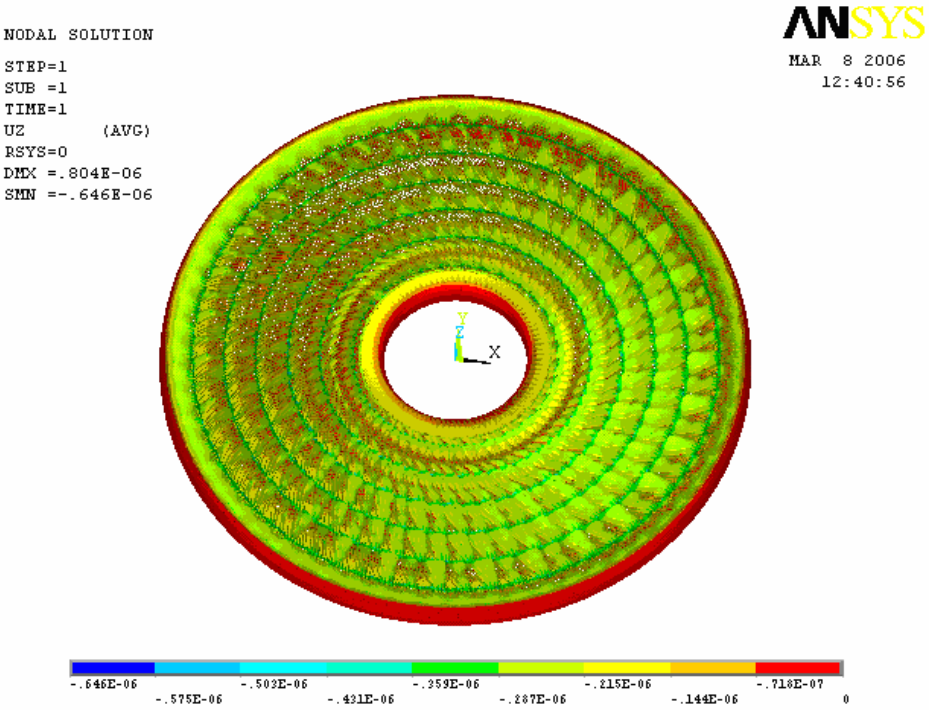

Figure 7.9.—Deformation *Uz* (Case 1).

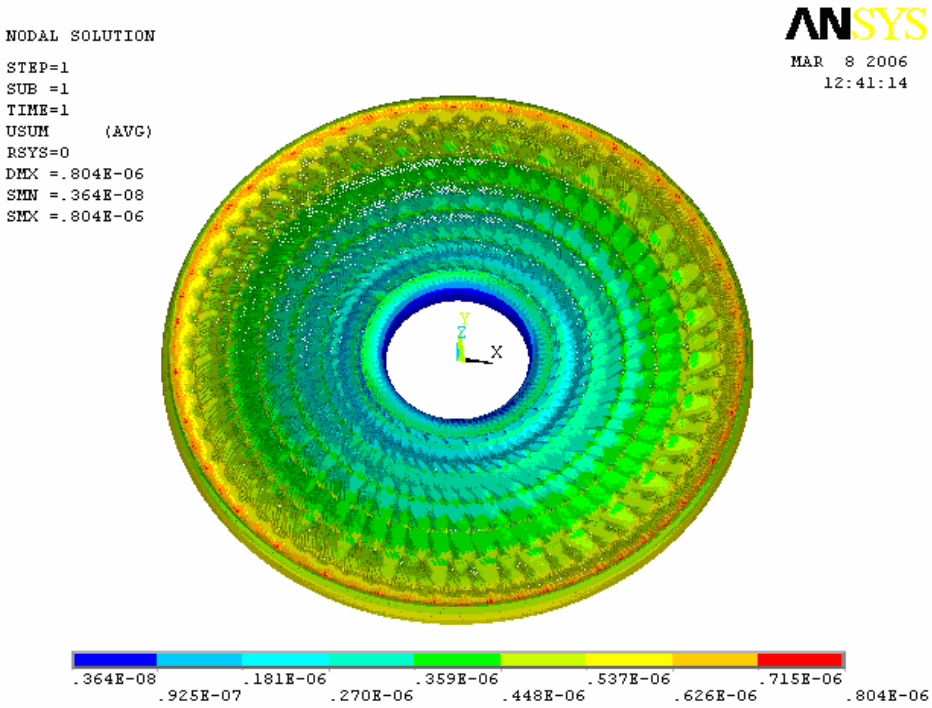

Figure 7.10.—Total deformation (Case 1).

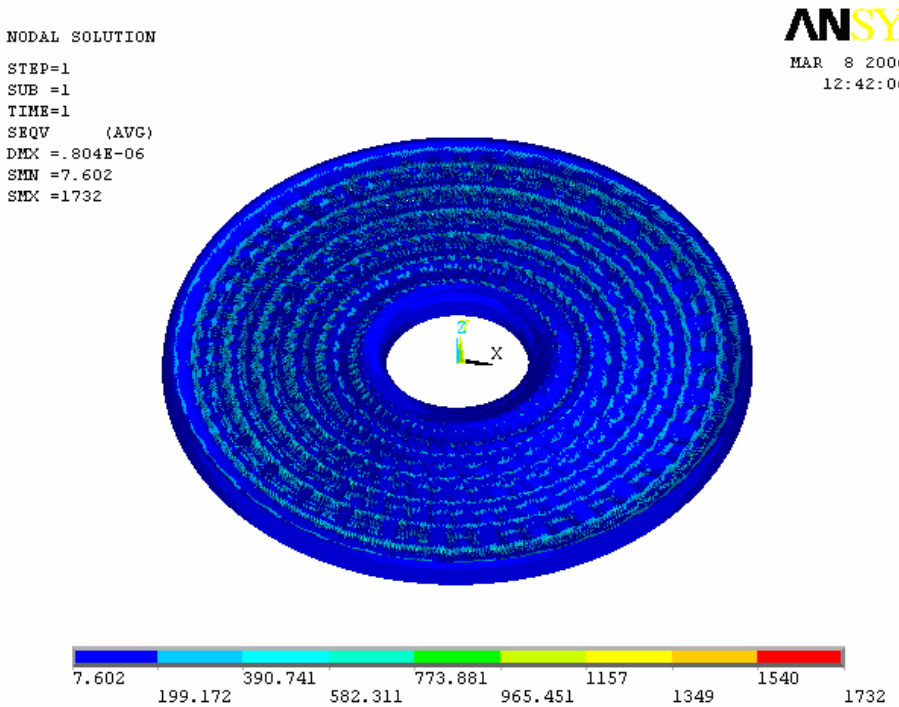

Figure 7.11.—Von Mises stress (Case 1).

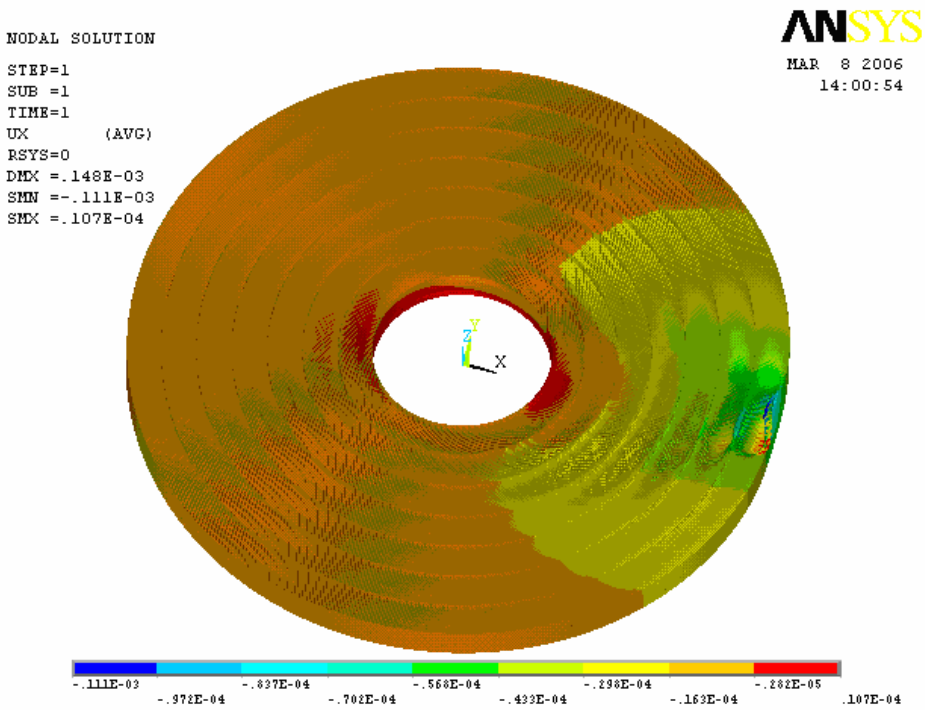

Figure 7.12.—Deformation *Ux* (Case 2).

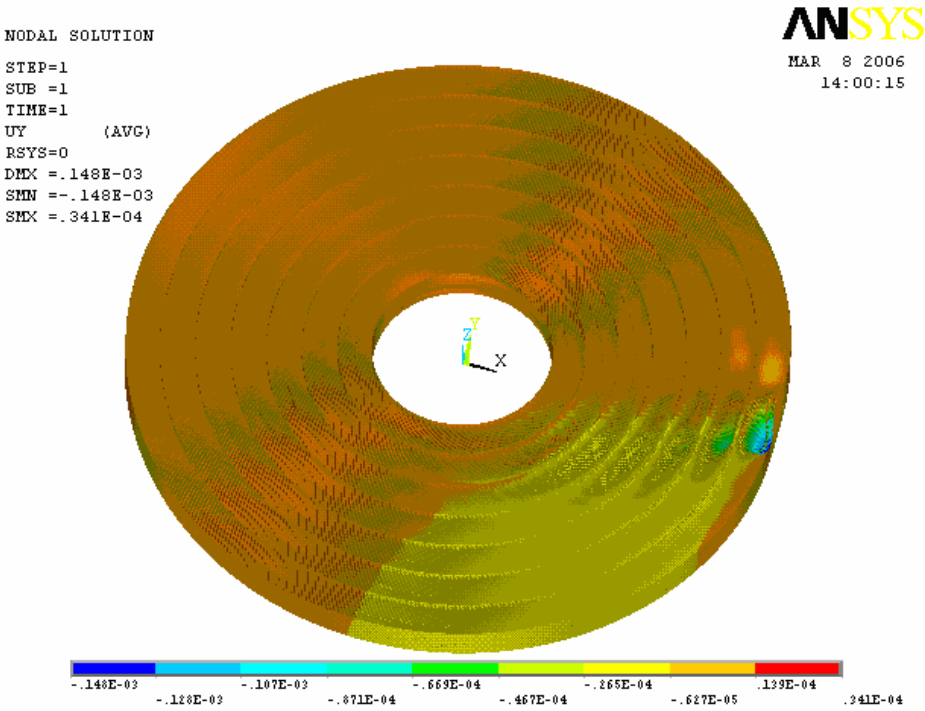

Figure 7.13.—Deformation *Uy* (Case 2).

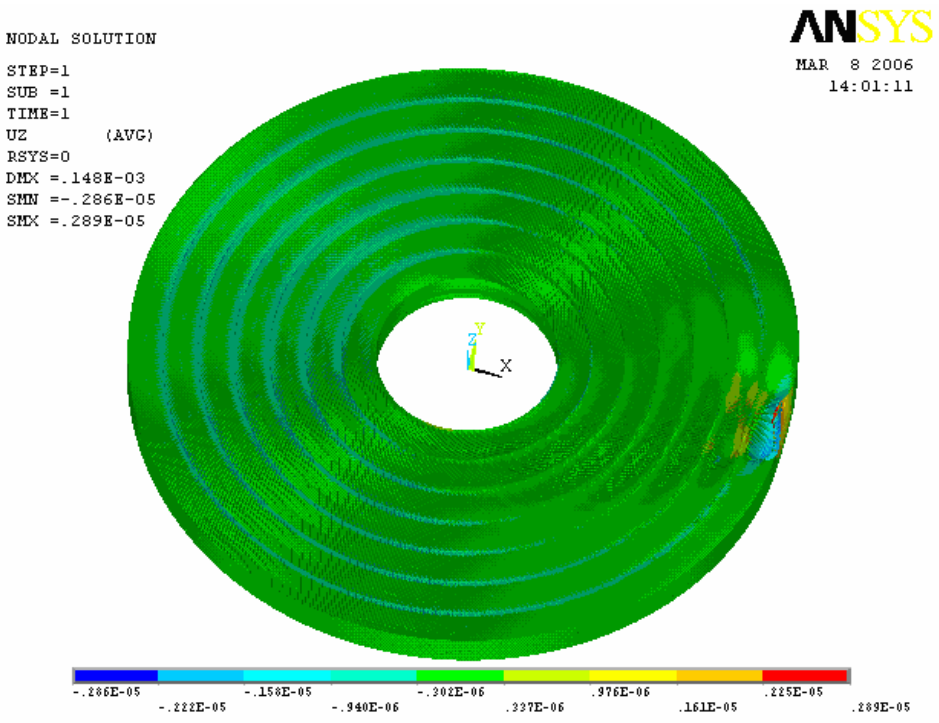

Figure 7.14.—Deformation *Uz* (Case 2).

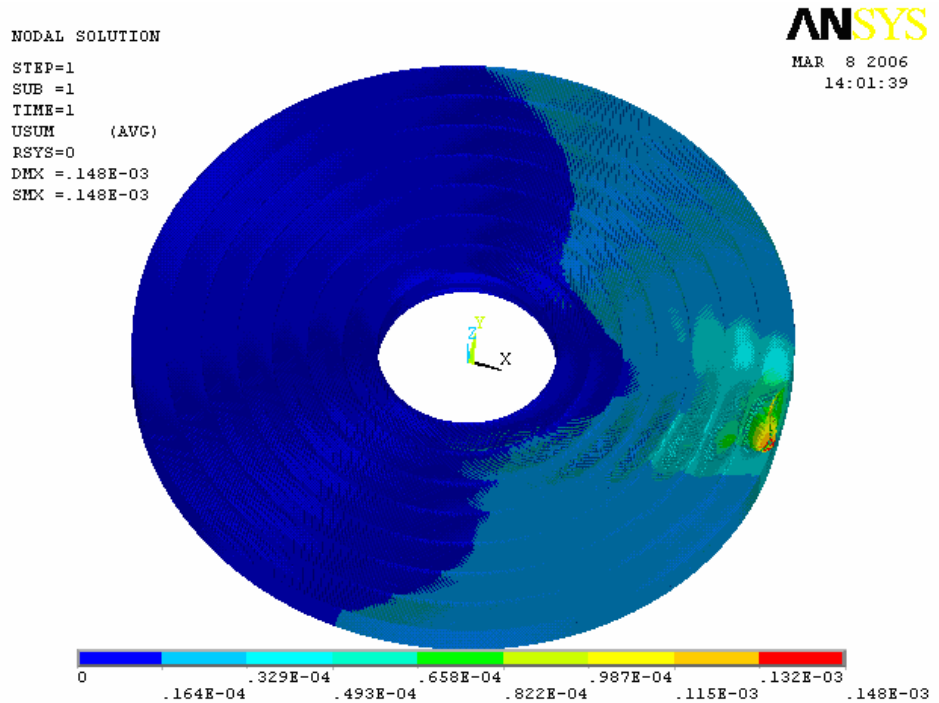

Figure 7.15.—Total deformation (Case 2).

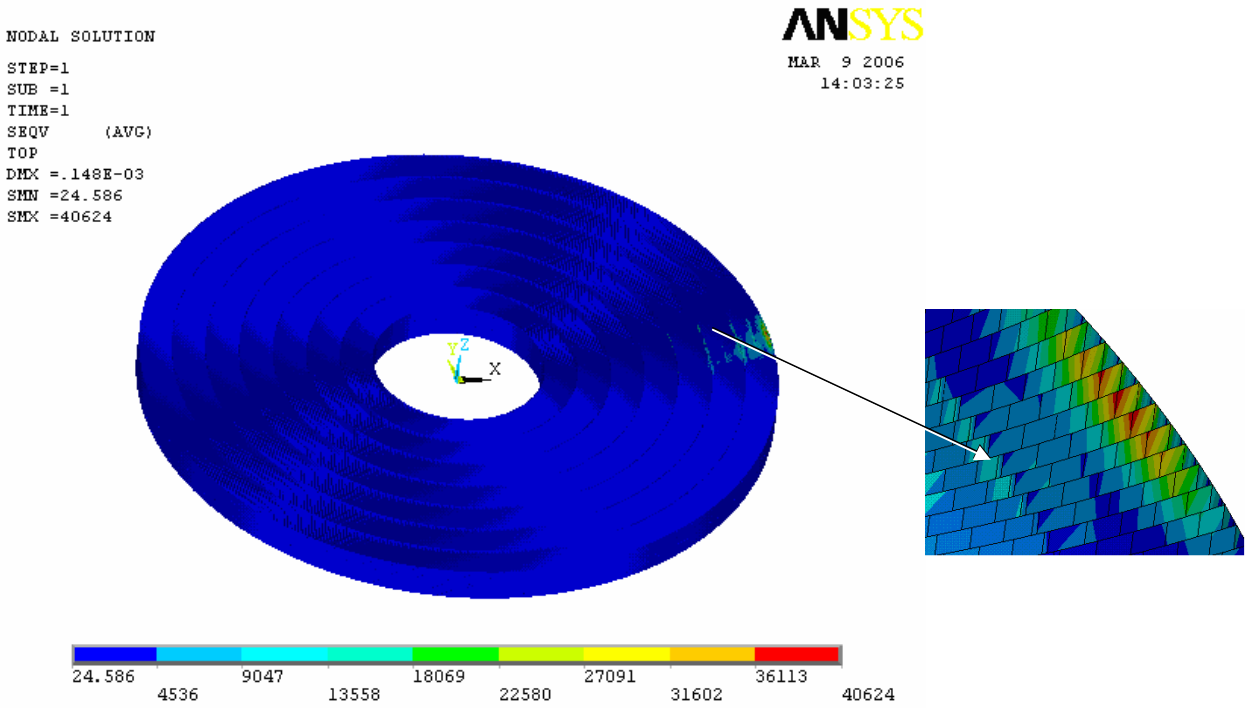

Figure 7.16.—Von Mises stress (Case 2).

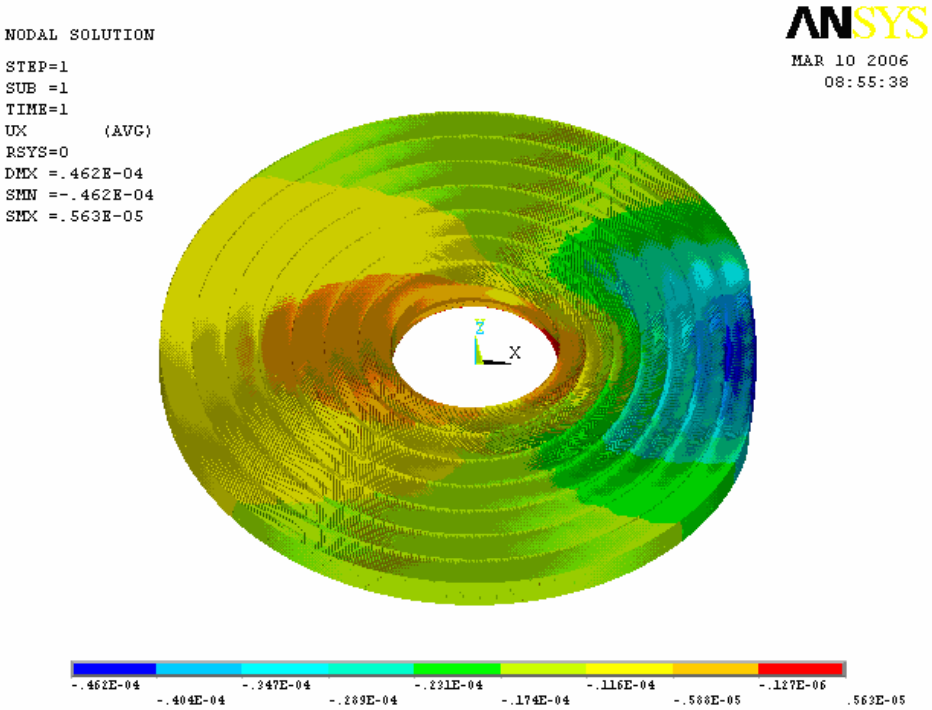

Figure 7.17.—Deformation *Ux* (Case 3).

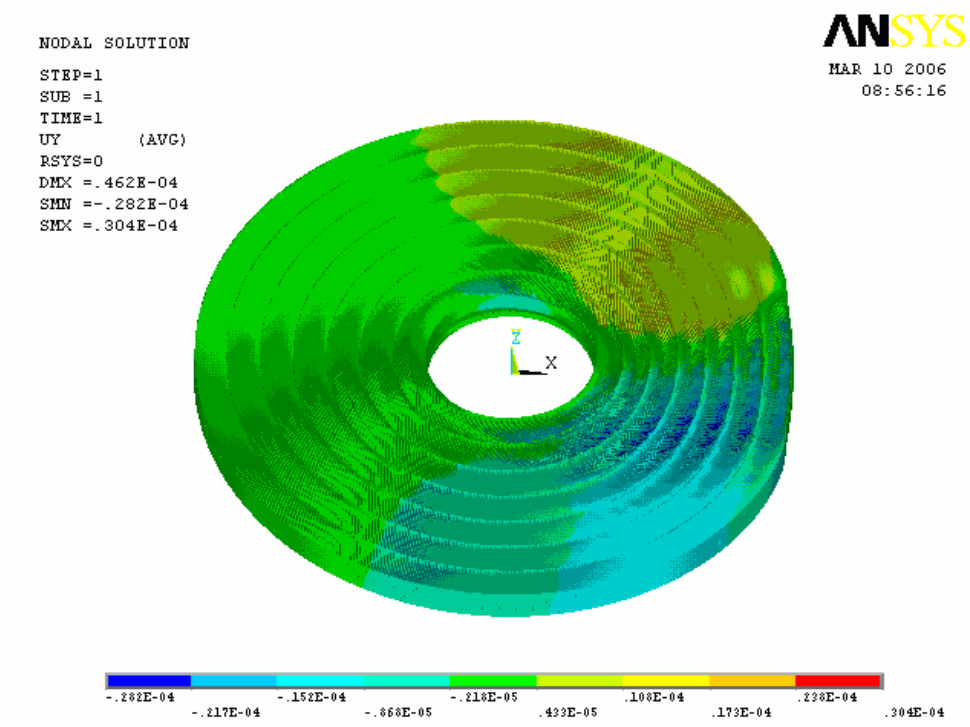

Figure 7.18.—Deformation *Uy* (Case 3).

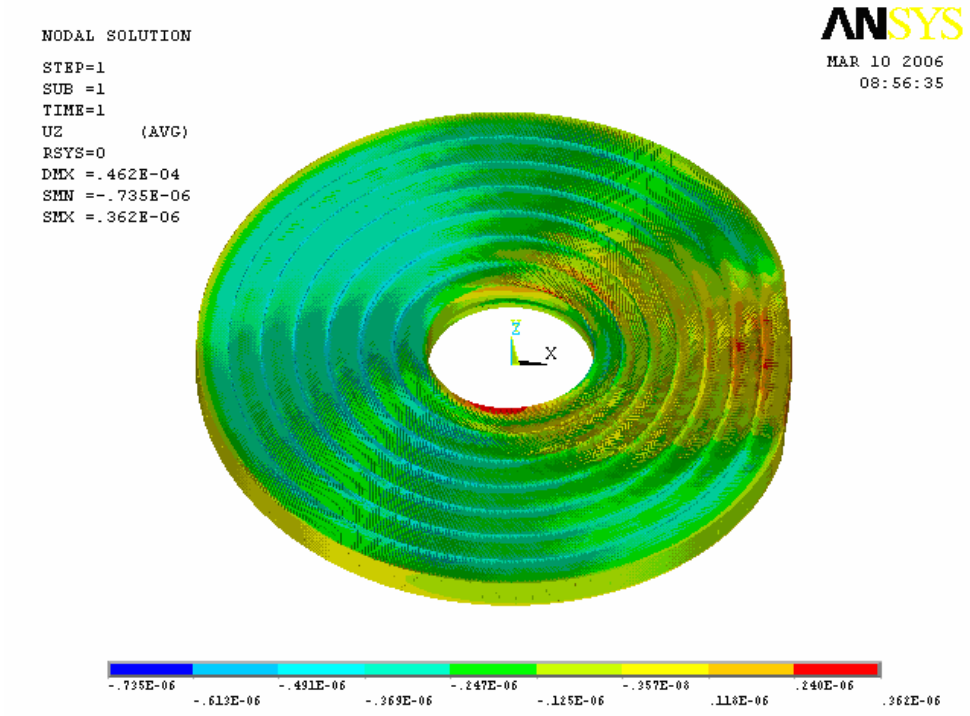

Figure 7.19.—Deformation *Uz* (Case 3).

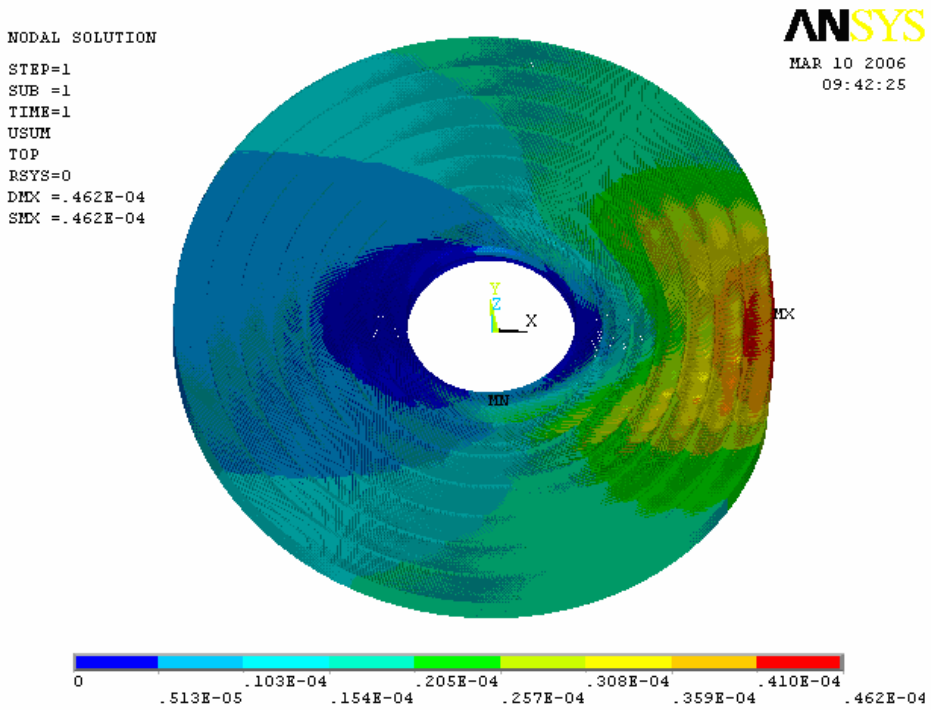

Figure 7.20.—Total deformation (Case 3).

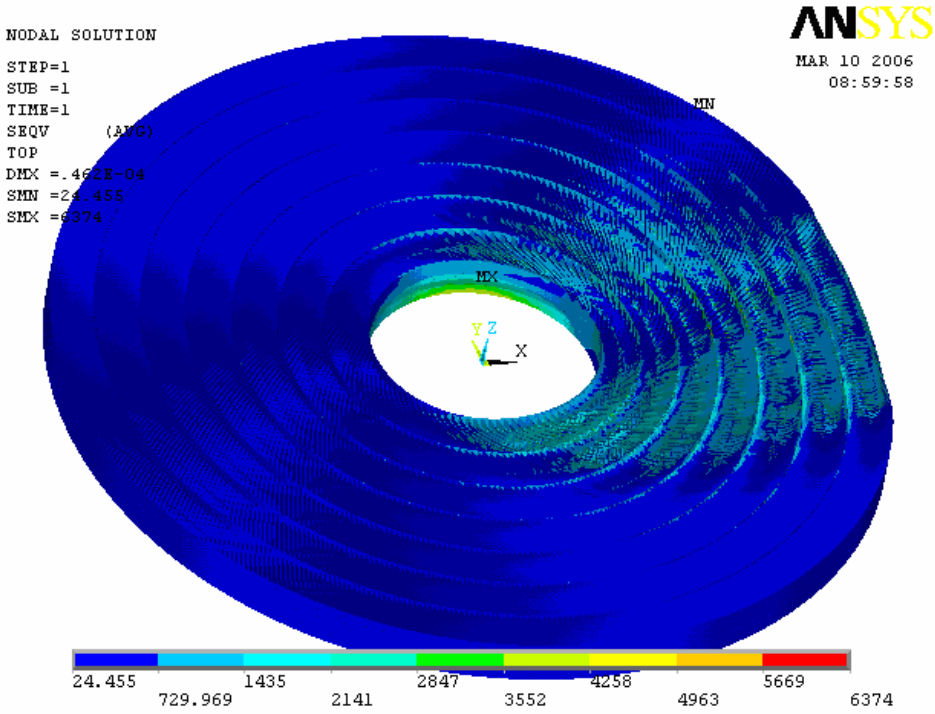

Figure 7.21.—Von Mises stress (Case 3).

7.4 Structural Analysis Summary and Conclusions

Finite element analysis of the microfabricated involute-foil regenerator shows that the regenerator had very high average axial direction stiffness (3.75e7 lb/in.). Without any radial side disturbance, the stress level was much lower than the material yielding strength. If the radial side disturbance such as misalignment was localized in a small area, as in Case 2, Von Mises stress was beyond the material yielding strength and permanent deformation could occur in that area, which may decrease the Stirling efficiency. In order to prevent local permanent deformation, the radial side load must be small or the disturbance area must be large, as in Case 3.

In summary, the proposed microfabricated involute-foil regenerator has high axial stiffness. The stress level is sensitive to the radial side disturbance, which therefore requires special cautions and appropriate processing during installation to prevent lateral permanent deformation.

7.5 Further Structural Analysis Work

To enhance the structure of the regenerator in the radial direction and to decrease the likelihood of performance degradation should be the main goals of further structural analysis of the microfabricated involute-foil regenerator. The stress caused by radial side loading is a function of variables, such as the length, the angle, the thickness, the number of the ribs in each involute section, and the number of the annular rings. Geometric optimization could be performed to decide the optimum values of the above variables for reducing stress.

8.0 Phase II Conclusions and Recommendations for Future Work

During Phase II an actual-size regenerator comprised of a stack of 42 disks, 19 mm in diameter and 0.25 mm thick (in the flow direction)—with microscopic involute-shaped flow channels—was microfabricated and tested in an oscillating-flow test rig. The geometry resembles an assembly of sections of uniformly-spaced parallel plates, except that the plates are curved. The curved sections of plates, or "involute foils," are incorporated in annular portions of the disks which are separated by concentric rings. Two types of disks alternate in the stack, so that the angles between the foils or plates in adjacent disks are close to 90º. Each disk was made from electro-plated nickel using the LiGA process. This process involved x-radiation of a photoresist through a mask, dissolving portions of the irradiated photoresist, then electroplating of nickel on a copper substrate within remaining photoresist channels, etc. This regenerator had feature sizes close to those required for an actual Stirling engine, but the overall regenerator dimensions were sized for the NASA/Sunpower oscillating-flow regenerator test rig. Examination by scanning electron microscope showed the disks were an accurate rendition of the design specification, except for a few flaws of types which are expected to be eliminated in the future via improvements to the manufacturing process. Testing in the oscillating-flow test rig showed the regenerator performed extremely well, producing the highest figures of merit ever recorded for any regenerator tested in this rig (since its fabrication about 20 years ago). Other regenerator materials recently tested in this rig include random-fiber, wire-screen and etched-foil materials.

Progress was also made in understanding the detailed fluid dynamics and heat transfer in the regenerator by computational fluid dynamic (CFD) analysis at Cleveland State University and large-scale testing at the University of Minnesota. In general, the conclusions from the CFD and large-scale testing results reinforced those from the actual-size test results and revealed some important details about the microscopic flows responsible for the overall regenerator behavior.

A Phase III effort is now underway to microfabricate a stack of involute-foil disks to form a regenerator for testing in a modified Sunpower FTB (Frequency Test Bed) engine. This engine was originally designed for a random-fiber regenerator and will not be reoptimized for the new involute-foil regenerator—though some modifications will be made to the engine. The Phase III effort includes testing of this involute-foil equipped FTB (with hot-end temperature of 650 °C).

Beyond this Phase III effort, the microfabrication process needs to be further developed to permit microfabrication of higher temperature materials than nickel (Pure nickel is too soft a material for practical use even in the 650 °C FTB engine). For example, DOE, NASA and Sunpower are currently developing an 850 °C engine for space-power applications. And a potential power/cooling system for Venus applications would need regenerator materials capable of ~1200 °C. Early Mezzo attempts to "EDM" stainless-steel using a LiGA developed EDM tool involved a burn time (dependent on EDM machine setting) that was much too large to be practical. Some possible options for further development of a microfabrication process for high-temperature involute-foils are: (1) Optimization of an EDM process for high temperature materials that cannot be processed by LiGA only; burn times can be greatly reduced by higher-power-EDM-machine settings than originally used in Phase I by Mezzo; but "overburn," i.e., the gaps between the EDM tool and the resulting involute-foil channels, increases with higher powers; (2) development of a LiGA only process for some high temperature alloy, or pure metal, that would be appropriate for the regenerator application (pure platinum would work but has very high conductivity, which would tend to cause larger axial regenerator losses, and it is very expensive), or (3) microfabrication of an appropriate ceramic material for high-temperature regenerators (structural properties of ceramics, which tend to be brittle, would be a concern).

References

Adolfson, D., "Oscillatory and Unidirectional Fluid Mechanics Investigations in a Simulation of a Stirling Engine Expansion Space," M.S. thesis, Mechanical Engineering Department, University of Minnesota, 2003.

Gedeon, D., Sage Stirling-Cycle Model-Class Reference Guide, 3rd edition, Gedeon Associates, Athens, OH, 1999.

Gedeon D. and Wood, J.G. "Oscillating-Flow Regenerator Test Rig: Hardware and Theory with Derived Correlations for Screens and Felts," NASA CR–198442, 1996.

Kays, W. and London, A., Compact Heat Exchangers, Second edition, 1964, McGraw-Hill, Inc. p. 213.

Kays, W.M. and London, A.L., Compact Heat Exchangers, Third edition, 1984, McGraw-Hill, Inc.

Mala, M.G., Li, D, "Flow characteristics of water in micro-tubes, International Journal of Heat and Fluid Flow," vol. 20, pp. 142–148, 1998.

Munson, B., Young, D., and Okiishi, T., Fundamentals of Fluid Mechanics, Second edition, 1994, John Wiley & Sons, Inc., p. 506.

Niu, Y., Simon, T.W., Ibrahim, M.B., Tew, R.C., and Gedeon, D., 2003, "Jet Penetration into a Stirling Engine Regenerator Matrix with Various Regenerator-to-Cooler Spacings," Paper no. AIAA-2003-6014, 2003 International Energy Conversion Engineering Conference, Portsmouth, VA.

Niu, Y., Simon, T.W., Ibrahim, M.B., Tew, R. and Gedeon, D., 2003, "Measurements of Unsteady Convective Heat Transfer Rates within a Stirling Regenerator Matrix Subjected to Oscillatory Flow," Paper no. AIAA-2003-6013, 2003 International Energy Conversion Engineering Conference, Portsmouth, VA.

Organ, A.J., (2000), "Two Centuries of Thermal Regenerator," Proceeding of the Institute of Mechanical Engineering, Part C, Journal of Mechanical Engineering Science, 214(NoC1): pp. 269–288.

Qiu, S., and Augenblick, J., "Thermal and Structural Analysis of Micro-Fabricated Involute Regenerator," The Space Technology and Applications International Forum, STAIF2005, Albuquerque, NM, February 2005.

Qu, W. and Mudawar, I., "Analysis of three-dimensional heat transfer in micro-channel heat sinks," International Journal of Heat and Mass Transfer, vol. 45, pp. 3973–3985, 2002.

Qu, W. and Mudawar, I., "Experimental and Numerical Study of pressure drop and heat transfer in a single-phase micro-channel heat sink," International Journal of Heat and Mass Transfer, vol. 45, pp 2549–2565, 2002.

Seume, J.R., Friedman, G., and Simon, T.W., "Fluid Mechanics Experiments in Oscillating Flow Volume I-Report," NASA CR–189127, 1992.
Shah, R.K., "A correlation for laminar hydrodynamic entry length solutions for circular and noncircular ducts," Journal of Fluids Eng. 100, 177–179, 1978.
Shah, R.K. and London, A.L., Laminar Flow Forced Convection in Ducts, Academic Express, 1978.
Siegel, R. and Howell, J., Thermal Radiation Heat Transfer, Second Edition, Hemisphere, 1981.
Simon, T. and Seume, J., "A Survey of Oscillating Flow in Stirling Engine Heat Exchangers," NASA CR–182108, 1988.
Stephan, K., "Warmeubergang und druckabfall bei nicht ausgebildeter Laminarstromung in Rohren und in ebenen Spalten," Chem.-Ing.-Tech. 31, 773–778, 1959.
Tiselj, I., Hetsroni, G., Mavko, B., Mosyak, A., Pogrebnyak, E., Segal, Z., "Effect of axial conduction on the heat transfer in micro-channels," International Journal of Heat and Mass Transfer 47, pp. 2551–2565, 2004.
Wakeland, R.S. and Keolian R.M., "Effectiveness of parallel-plate heat exchangers in thermoacoustic devices," J. Acoust. Soc. Am., 115 (6), pp. 2873–2886, June 2004.

Appendix A—Detailed Derivation of Radiation Heat Flux Through a Tube With a Small Cross-Section (Gedeon Associates)

Problem: Evaluate the radiation heat flux $q(\xi)$ through the tube cross-section $A(\xi)$ as the sum of the heat flows from the two ends and the two wall surfaces before and after point ξ. For each part base the calculations on the configuration factors for radiation heat transfer tabulated in appendix C of Siegel and Howell. With the assumption that ends and walls are black-body emitters there is no reflected radiation to consider and the analysis is relatively straight forward.

A.1 Negative End Contribution

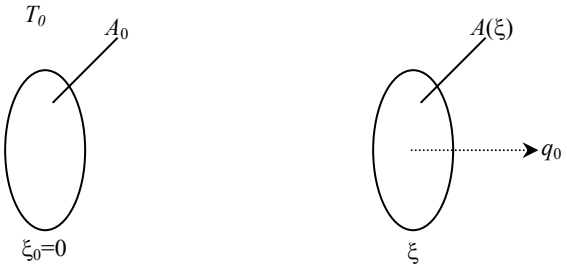

q_0 is the radiation flux leaving surface A_0 that passes through surface $A(\xi)$. It may be written as

$$q_0 = \sigma T_0^4 F_{0-\xi} \tag{A.1}$$

where $F_{0-\xi}$ is the configuration factor for the fraction of the total radiation leaving A_0 that arrives at $A(\xi)$. From case 21 p. 826 Siegel and Howell

$$F_{0-\xi} = \tfrac{1}{2}\left(G - \sqrt{G^2 - 4}\right) \tag{A.2}$$

where

$$G = 2 + 4\xi^2 \tag{A.3}$$

A.2 Positive End Contribution

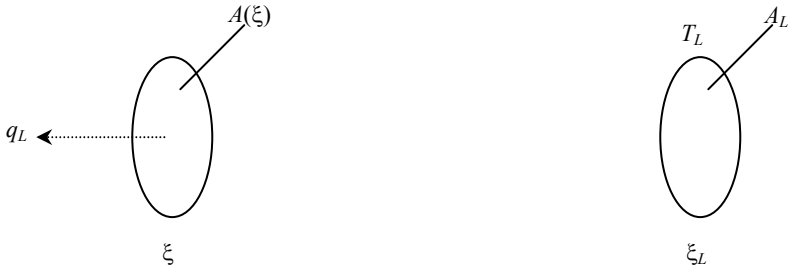

q_L is the radiation flux leaving surface A_L that passes through surface $A(\xi)$. It may be written as

$$q_L = -\sigma T_L^4 F_{L-\xi} \tag{A.4}$$

where $F_{L-\xi}$ is the configuration factor for the fraction of the total radiation leaving A_L that arrives at $A(\xi)$. Similar to the previous case

$$F_{L-\xi} = \frac{1}{2}\left(H - \sqrt{H^2 - 4}\right) \tag{A.5}$$

where

$$H = 2 + 4(\xi_L - \xi)^2 \tag{A.6}$$

A.3 Negative Wall Contribution

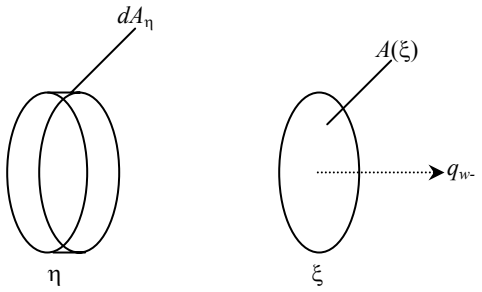

q_{w-} is the radiation flux leaving the wall surface $\eta < \xi$ that passes through surface $A(\xi)$. Integrating the contributions of differential elements dA_η it may be written as

$$q_{w-} = \frac{1}{\pi a^2}\sigma \int_0^\xi T(\eta)^4 \; F_{\bar{d}\eta-\xi} dA_\eta \tag{A.7}$$

Substituting for the wall area element

$$dA_\eta = 4\pi a^2 \, d\eta \tag{A.8}$$

this becomes

$$q_{w-} = 4\sigma \int_0^\xi T(\eta)^4 \; F_{\bar{d}\eta-\xi} d\eta \tag{A.9}$$

$F^{-}_{d\eta-\xi}$ is the configuration factor for the fraction of the total radiation leaving dA_η that arrives at $A(\xi)$. From case 30 p. 829 Siegel and Howell

$$F^{-}_{d\eta-\xi} = \frac{(\xi-\eta)^2 + \frac{1}{2}}{\sqrt{(\xi-\eta)^2 + 1}} - (\xi - \eta) \tag{A.10}$$

A.4 Positive Wall Contribution

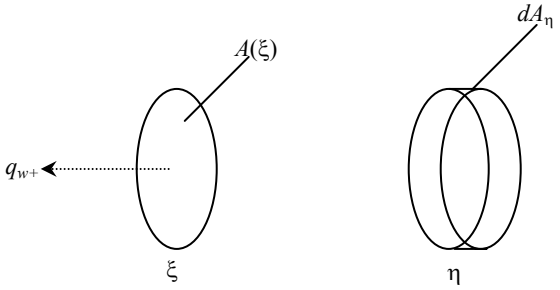

q_{w+} is the radiation flux leaving the wall surface $\eta > \xi$ that passes through surface $A(\xi)$. Similar to the previous case:

$$q_{w+} = -4\sigma \int_{\xi}^{\xi_L} T(\eta)^4 \; F^{+}_{d\eta-\xi} d\eta \tag{A.11}$$

$F^{+}_{d\eta-\xi}$ is the same configuration factor as the previous case except with ξ and η switched

$$F^{+}_{d\eta-\xi} = \frac{(\eta-\xi)^2 + \frac{1}{2}}{\sqrt{(\eta-\xi)^2+1}} - (\eta-\xi) \tag{A.12}$$

A.5 Normalization

Dividing the 4 heat flux contributions by $q_{\max} = -4\sigma(T_L^4 - T_0^4)$ converts them to normalized radiation heat fluxes

$$\frac{q_0}{q_{\max}} = \frac{-(T_0/T_L)^4 \, F_{0-\xi}}{1-(T_0/T_L)^4} \tag{A.13}$$

$$\frac{q_L}{q_{\max}} = \frac{F_{L-\xi}}{1-(T_0/T_L)^4} \tag{A.14}$$

$$\frac{q_{w-}}{q_{\max}} = \frac{-4\int_0^{\xi} (T(\eta)/T_L)^4 \; F^{-}_{d\eta-\xi} \, d\eta}{1-(T_0/T_L)^4} \tag{A.15}$$

$$\frac{q_{w+}}{q_{\max}} = \frac{4\int_{\xi}^{\xi_L} (T(\eta)/T_L)^4 \; F^{+}_{d\eta-\xi} \, d\eta}{1-(T_0/T_L)^4} \tag{A.16}$$

For a linear temperature variation the temperature ratio $T(\eta)/T_0$ may be expressed as

$$\frac{T(\eta)}{T_L} = \frac{T_0}{T_L} + \left(1 - \frac{T_0}{T_L}\right)\frac{\eta}{\xi_L} \tag{A.17}$$

A.6 Programming

Custom Delphi program RadiationDownTube.pas performs the above calculations and sums all the radiation contributions to produce the results plotted above (Excel does the actual plotting of data). An adaptive quadrature routine does the required integrations. The program was tested for two test cases with known solutions, (1) the radiation flow in the limit of zero tube length and (2) the radiation flow for a step temperature distribution with $T = T_0$ up to point ξ and $T = T_L$ beyond. For both cases $q/q_{max} = 1$.

Appendix B—Regenerator Figure-Of-Merit Degradation With Intra-Regenerator Flow-Gap Variations (Gedeon Associates)

To: Regenerator Research Team
From: D. Gedeon
January 7, 2004

The intra-regenerator flow streaming results for parallel foil regenerators is used to estimate the degradation in our regenerator figure of merit as a result of gap variations between sections.

B.1 Background

We have settled on this formula for calculating the figure of merit for preliminary ranking of regenerator matrices[2]

$$F_M = \frac{1}{f\left(\frac{\mathrm{Re}\,\mathrm{Pr}}{4\mathrm{Nu}} + \frac{N_k}{\mathrm{Re}\,\mathrm{Pr}}\right)}$$

For a foil-type regenerator $f = 96/\mathrm{Re}$, Nu = 8.23 and $N_k = 1$. When plotted as a function of Reynolds number (assuming Pr = 0.7) the figures of merit for a foil regenerator, as well as a few other regenerators of interest, look like the chart below.

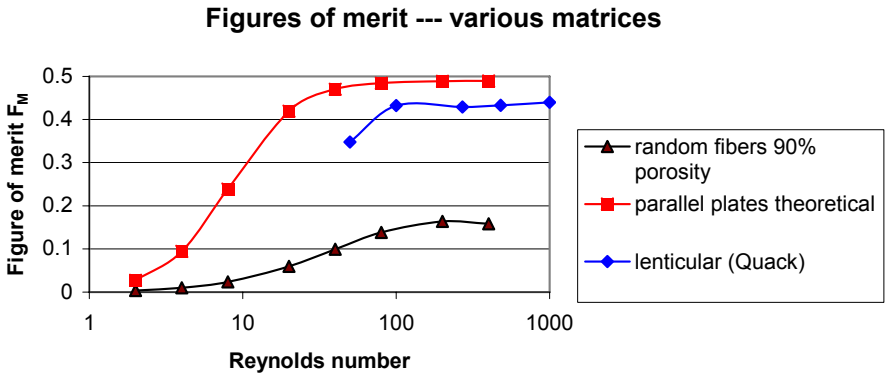

B.2 Effects of Gap Variations

A foil regenerator is split into two parts. The flow gap in one is increased while decreased in the other. This gives rise to DC flow circulations between the two parts and a degradation in overall engine efficiency, as previously documented.[3]

Not previously reported was the effect of the gap variations on combined-regenerator pumping loss W_f (Sage output AEfric) and cycle-average enthalpy flow $\dot{H}$ (Sage output HNeg or HPos) . Because W_f relates to friction factor and $\dot{H}$ relates to Nusselt number, this information can be used to estimate the effective figure of merit as a function of gap variations. Specifically, friction factor is directly

[2]D. Gedeon, *Regenerator figures of merit*, August 6, 2003, (CSUmicrofabFiguresofMerit.tex)
[3]D. Gedeon, *Intra-regenerator flow streaming produced by nonuniform flow channels*, Jan 5, 2004 (CSUmicrofabIntraRegenFlows.doc)

proportional to W_f. So the effective friction factor for the gap-perturbed regenerator is greater (or less) than the friction factor for the baseline regenerator by the factor

$$\frac{f}{f_0} = \frac{W_{fA} + W_{fB}}{\left(W_{fA} + W_{fB}\right)_0}$$

where the 0 subscript refers to the baseline (equal flow gap) regenerator and subscripts A and B refer to the two regenerator parts. Because the Nusselt number is inversely proportional to $\dot{H}$, the effective Nusselt number for the gap-perturbed regenerator is related to Nusselt number for the baseline regenerator by the factor

$$\frac{\mathrm{Nu}}{\mathrm{Nu}_0} = \frac{\left(\dot{H}_A + \dot{H}_B\right)_0}{\dot{H}_A + \dot{H}_B}$$

The effective f and Nu thereby computed can be substituted into the formula for figure of merit with Reynolds number taken as the baseline regenerator mean value Re = 62. The result is two curves of figure of merit degradation as a function of relative gap variation, one for the case where the two regenerator parts are in good thermal contact and one for the case of no thermal contact. The latter case is worse because of the temperature skewing effect of DC flow which amplifies the DC flow if not suppressed by thermal contact between the two parts, as shown in the following plot:

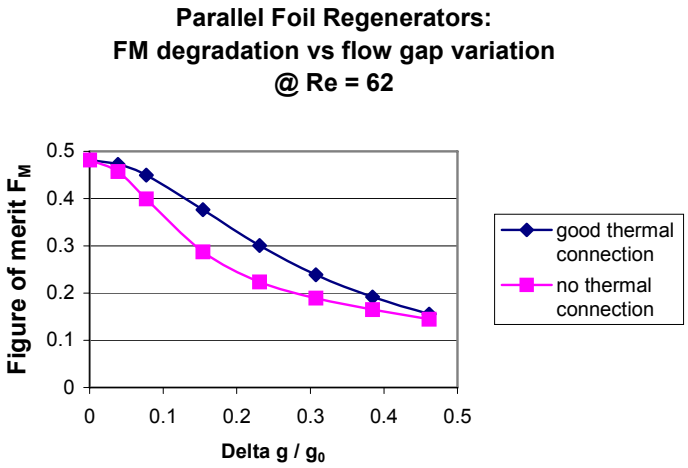

The "Delta g / g_0" represents the amount by which the gap is higher in part A and simultaneously lower in part B, compared to the baseline gap. A gap-variation *amplitude*, in other words. The curve labeled "good thermal connection" corresponds to gap variations between regenerator parts in good transverse thermal contact—e.g., between adjacent foil layers or nearby in the same layer. The curve labeled "no thermal connection" corresponds to gap variations between distant parts of the regenerator, as might occur when all the layers on one side of an annulus are crammed together and spread apart on the other side due to some systematic assembly error or misalignment between inner and outer canisters.

It is seen that in either case it does not take too much gap variation to significantly reduce a foil regenerator figure of merit. Increased cyclic enthalpy flow (sum for both parts) is mainly responsible for the degradation. Flow frictional loss hardly changes, even decreases a bit. At a gap variation of $\pm 45\,\%$ the figure of merit is down in the vicinity of random fibers at 90% porosity ($F_M = 0.14$). This is for a Stirling engine regenerator. The figure of merit degradation for a cryocooler regenerator would be much faster, based on the conclusions of the January 5, 2004, memo.

It is reasonable to apply the above plot to the general case of any channel-type regenerator, such as the honeycomb type. In that case hydraulic-diameter variation would replace flow-gap variation, but the resulting curves should be quite similar.

So, based on the above, what should we specify for an allowable gap variation (hydraulic diameter variation) for a microfabricated regenerator? Maybe a $\pm 10\,\%$ variation would be reasonable. That should keep us above $F_M = 0.4$ for both localized variations and systematic gap variations. If systematic variations (over large distances) are not a problem then we might go as high as $\pm 15\,\%$. Maybe a bit more. But not too much more lest we wind up in the unenviable position of producing an "improved" regenerator that performs as well as random fibers at many times the cost.

Appendix C—Potential 6 to 9% Power Increase for a Foil-Type "Microfab" Regenerator in the Sunpower ASC Engine (Gedeon Associates)

To: Regenerator Research Team
From: D. Gedeon
March 26, 2004

Gary Wood has been wondering if the previous estimates for the benefits of a microfabricated regenerator (see: August 25, 2003 memo) might have been optimistic considering the regenerator length was excessive (133 mm) and foil solid conduction was discounted. Solid conduction multiplier Kmult was set to 0.1 as an approximation to the interrupted and convoluted solid conduction path we were considering for the lenticular matrix design.

This memo addresses these concerns. A foil-type is inserted into the canister of the most recent Sunpower ASC engine Sage model (D25B3.stl) and the foil spacing is optimized, with length constrained first to 70 mm, then 60 mm. The foil is assumed to be 15 μm thick stainless steel with the full solid conductivity accounted for in the model.

After re-optimization the result is a 6.6% increase in PV power for the same heat input for 70 mm long foil, compared to the baseline random fiber regenerator. A 5.5% increase for 60 mm long foil. Details follow.

C.1 Details

One of the two Sage files created for this study is named **D25B3FoilRegen**. It has an optimization structure much like that described in a December 23, 2003 memo "Sage Model for ASC Optimization" (SunpASCOptimizationFile.doc), except the acceptor length is constrained to 25 mm and the regenerator matrix type is foil. Regenerator length is constrained to 70 mm. A second Sage file named **D25B3FoilRegenL60** is identical except regenerator length is constrained to 60 mm.

When these Sage files are optimized all of the basic engine dimensions get adjusted to best serve the foil regenerator, subject to all the dimensional constraints that have so-far evolved for the ASC engine design. The objectives were to see how well a foil regenerator would do compared to the baseline random fiber regenerator and get some idea of the trades for reduced regenerator length. Foil gap was optimized but foil thickness held constant at 15 μm.

The table below provides the some key results and dimensions for the two foil regenerator optimizations, compared to the baseline random-fiber regenerator.

	Baseline random fiber regenerator D25B3	Foil regenerator 70 mm long D25B3FoilRegen	Foil regenerator 60 mm long D25B3FoilRegenL60
Heat input (W)	230.0	230.0	230.0
PV power (W)	111.8	119.2	118.0
Percent increase	—	**6.6**	**5.5**
Foil gap (μm)	—	97.2	92.6
Canister area (cm^2)	2.83	2.25	2.06

So once again there are significant benefits to foil regenerators, even at reduced length. Note that the regenerator canister area went down for the two foil cases resulting in a slightly more compact engine with reduced pressure-wall conduction loss.

For the 60 mm case the foil solid conduction averaged over the regenerator represents about 6.7 W out of 230 W heat input. This would be worth another 3% of efficiency (power increase for given heat input) if eliminated. For the batch-mode EDM'ed regenerator plates we are considering there would be an interrupted solid conduction path allowing us to eliminate some of the 6.7 W conduction loss. So the original estimate of a potential benefit on the order of 9% for a microfabricated regenerator continues to appear reasonable.

Appendix D—EDM Regenerator Disks: Concentric Involute Rings (Gedeon Associates)

To: Microfab Team
From: D. Gedeon
April 13, 2004

In which involute foils are packaged in a cylindrical form within concentric rings.

D.2 Packing a Cylinder

Thinking ahead to the test regenerator we are planning to build in year 3, we need to come up with a matrix that fits within a 19 mm diameter cylindrical form. What should it look like?

The involute-foil idea is tempting, except that the only way to *completely* fill a cylinder with an involute is with the extreme case of a single foil, wound in spiral fashion. This will not do because it is not geometrically similar to the multi-foil involute structure we would use for a thin annular regenerator (space power engine) and it results in a long unsupported length of foil, more like a watch spring than a regenerator matrix.

Both problems can be solved by packing the involute elements into concentric rings, each ring separated by a thin wall. Each ring may contain a different involute family (different generating circle) so they may all be geometrically similar to "thin annular" involutes. The ring walls also serve as support points for individual involute elements, thereby increasing their stiffness.

The illustrations on the following page show two ways one might package involutes into concentric rings. In the picture labeled "geometric spacing" the rings are defined by circles with successive diameters in the same ratio. The advantage of geometric spacing is that the involutes in all rings have about the same angle relative to the cylinder radius and are therefore fluid-dynamically and structurally similar insofar as those things matter. The disadvantage is that the ring spacing decreases toward the center, resulting in shorter elements (shorter aspect ratios for the flow channels). In the picture labeled "uniform spacing" the rings are defined by circles with successive diameters in constant increments. The advantage of uniform spacing is that the lengths of the involute elements do not vary as much. The disadvantage is that the radius-angle of the involute elements increases toward the center, possibly resulting in fluid-dynamic or structural differences between inner and outer rings.

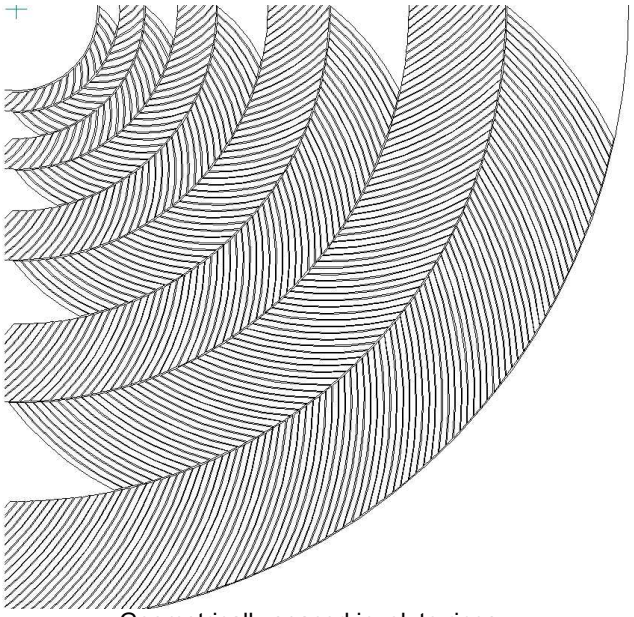

Geometrically spaced involute rings.

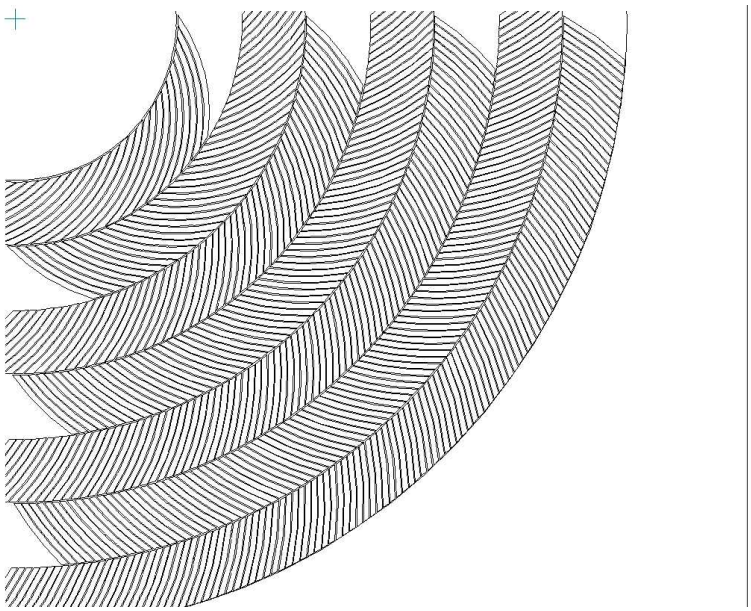

Equally spaced involute rings.

D.2 Dimensions

The illustrations show cross-section views of regenerator disks created with the Solid-Edge CAD software. Only about ¼ of the disks are cut into the involute patterns so-as not to bog down the tiny brain of Solid-Edge in computing all the little features. Common dimensions for the two regenerator disks are

Outer diameter	19.05 mm
Involute channel width (gap)	86 μm
Wall thickness between involutes	≈14 μm
Wall thickness between rings	20 μm
Disk thickness	500 μm

The involute channel widths are exact, as these things go, with the wall thickness varying slightly to accommodate the approximate circular profiles used instead of true involute profiles. The error so created is estimated later on.

D.3 Central Holes

In each case there comes a point toward the center of the matrix where continuing the pattern becomes absurd and one can either change to another type of foil pattern or just stop and fill the central hole with an insulating stuffer. For purposes of the test regenerator it should be acceptable to go with the insulating stuffer. For the geometrically-spaced matrix the central hole diameter is 2.6 mm. For the equally-spaced matrix it is 5.0 mm.

D.4 Alternating Sense Involutes

As illustrated, the angular sense of the involutes alternates in successive rings. This results in a herringbone pattern. It would also be possible to maintain the same angular sense in each ring. In either case the idea would be to flip alternating regenerator disks so the angular sense changes with each layer. This way there should be no need for rotational alignment between layers and the solid conduction path

between involute wall elements is interrupted. The opportunity for flow distribution between layers is also maximized.

The structural and flow advantages to the herringbone pattern, if any, are not completely clear. On possible item of consequence is that any radial flow in a plenum at the discharge end of such a herringbone matrix would tend to get mixed because the flow coming from successive involute ring would tend to swirl in opposite directions. A good thing, I suppose.

D.5 EDM

Based on my current understanding of the Mezzo EDM process the illustrated regenerator disks should be possible to make. One concession to EDM might be to round the corners where the involute elements attach to the circular walls between rings which would result in somewhat greater axial thermal conduction loss.

D.6 Structural Analysis

In principle one could perform a finite-element stress analysis of a complete involute-ring regenerator disk, but I have not done that. The important things to understand would be the axial load required to buckle a regenerator comprising a stack of such disks and the resistance to deformation of the individual involute wall elements.

The axial buckling load is important if we decide to hold the stack in place by compression. I have some hope that the axial bucking strength will be adequate because each involute flow channel forms a structural cell consisting of side walls integrally connected to end walls. Each structural cell should be relatively stiff, compared to foil layers unconnected at the ends. And there are a large number of such cells to distribute the load.

The resistance to deformation of the individual wall elements is important to maintaining uniform spacing. If nothing else the walls should be stiff enough so that internal stresses relieved by the EDM process do not result in significant spacing variations. I am not sure, but it seems that the curved shapes of the involute walls will help in this regard. The radius of curvature cannot change too much without affecting the separation between endpoints, which is constrained by the end walls (inter-ring walls). Were the elements straight (e.g., radial spokes) they could deflect much more for the same end constraints. Obviously we need to think more about this.

Appendix E—Involute Math (Gedeon Associates)

Gathered together here are some useful formulas and suggestions for generating involute patterns in CAD software.

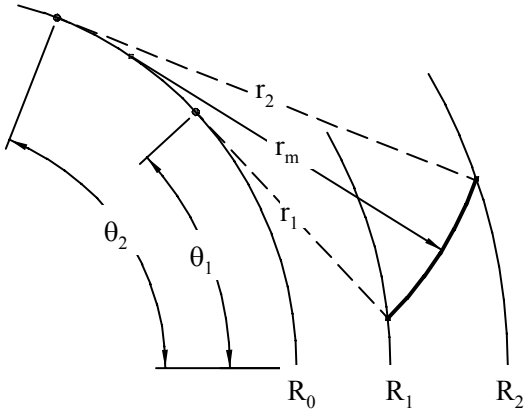

Each ring of flow channels is a circular pattern of elemental flow channels. At the center of each elemental flow channel is a segment of an involute curve defined by a generating circle and two boundary circles, as illustrated in this sketch.

The generating circle has radius R_0 and the two boundary circles have radii R_1 and R_2. The involute segment is the curved arc between R_1 and R_2. By definition it is generated by the mathematical equivalent of a string unwinding from the generating circle. Dotted lines indicate the position of the string at the beginning and ending of the arc. The exposed lengths of the string at the two endpoints of the involute segment are just the arc lengths along the generating circle subtended by angles θ_1 and θ_2 or

$$r_1 = R_0\theta_1$$

and

$$r_2 = R_0\theta_2$$

r_1 and r_2 are also the local radii of curvature of the involute segment at the two endpoints. By drawing some right triangles it is easy to conclude that r_1 and r_2 are geometrically related to the various circle radii by

$$r_1 = \sqrt{R_1^2 - R_0^2}$$

and

$$r_2 = \sqrt{R_2^2 - R_0^2}\ .$$

A circular pattern of N involute segments can be made by rotating the original involute by angular increments $2\pi/N$ (in radians) about the center of the generating circle. This pattern can also be thought of as being made by shortening the string by increments s_0 equal to the circumference of the generating circle divided by N, or

$$s_0 = \frac{2\pi R_0}{N}$$

The advantage of this point of view is that s_0 is evidently the normal spacing between involute elements. Solving the previous equation for N, the number of involute elements spaced by distance s_0 is

$$N = \frac{2\pi R_0}{s_0} \tag{1}$$

The arc drawn in the above illustration is not actually a true involute curve but rather just an ordinary circular arc centered on the generating circle with radius

$$r_m = (r_1 + r_2)/2 \tag{2}$$

The normal spacing between the circular arcs is therefore not exactly s_0. It varies as

$$s \approx s_0 \cos\alpha \tag{3}$$

where α is the rotation angle of radius r_m relative to its angle at mid segment. This can be seen from the following illustration which shows two successive circular "involute" arcs drawn with their centers vertically aligned on the generating circle. The reason for the approximately-equals symbol in the previous equation is that s_0 is the arc length between two successive center-positions along the generating circle, not exactly the cord length.

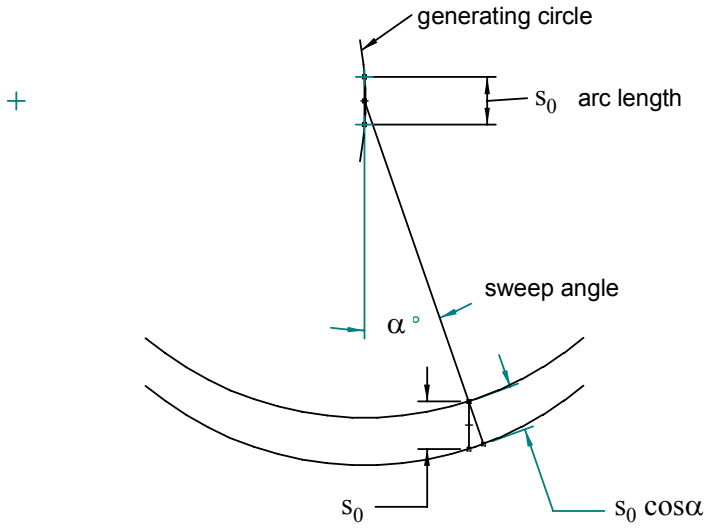

E.1 Involute Cutouts

As mentioned, the "involute" arc segments so generated lie at the centers of the flow channels. The way the flow channels are generated is to offset the arc segments toward each side by small increments (concentric arcs) to create cutout boundaries, as in this illustration of a single flow channel between two boundary circles:

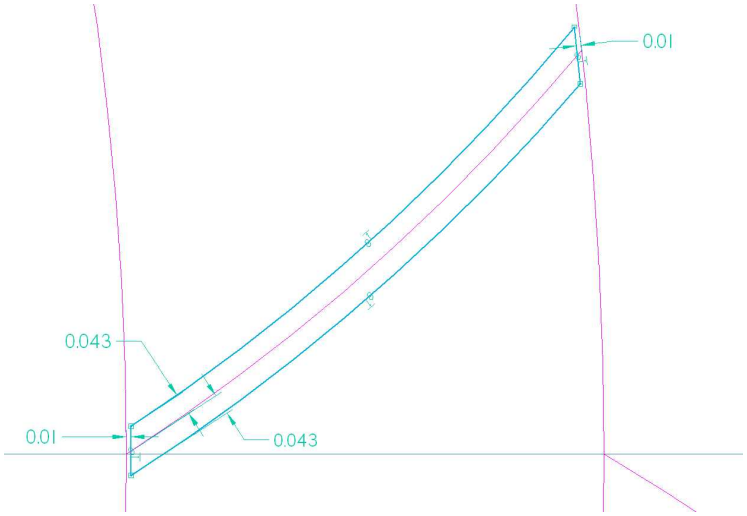

The "involute" arc segment and boundary circles are colored pink and the cutout boundaries are colored blue. In this case the involute arc segment is offset 43 μm toward each side forming a channel of width 86 μm. The cutout ends are offset 10 μm from the inter-ring boundary circles, consistent with 20 μm thick walls between ring sections. The normal distance separating true involute arc segments in the circular pattern is 100 μm. With 86 μm channel widths, this leaves 14 μm for the side wall thickness. Actually the side walls vary in thickness slightly because of the circular-arc approximation to true involute segments and the resulting error in normal spacing that results. That error affects only the side wall thickness. The channel width is exact, to within the limits of the CAD software.

E.2 Spreadsheet Calculations

Generating the involute channels requires a sequence of boundary circles and a sequence of generating circles. In principle the two sequences could be different but it is easiest if the same sequence of circles is used for both purposes. In other words, given an arbitrary sequence of circles C_i, for $i = 0 \ldots M$, with diameters D_i in increasing order, circle C_0 is the generating circle for the involute arc segments between C_1 and C_2, circle C_1 is the generating circle for the involute arc segments between C_2 and C_3 and so forth. Then the only remaining choice is the spacing between the diameters D_i. The options of geometrical spacing (D_i / D_{i-1} = constant) or arithmetic spacing ($D_i - D_{i-1}$ = constant) have already been illustrated and their properties discussed. We might eventually want to look at other options too.

To automate the process I wrote a spreadsheet that calculates circle sequences and other useful information for the 19.05 mm diameter regenerator disks illustrated earlier. Two spreadsheets actually, *Involute19DiamCyl.xls* for geometrically-spaced rings and *Involute19DiamCylEqualSpaced.xls* for equally-spaced rings. The spreadsheets generate a sequence of circles spanning the desired diameter range, then for each concentric ring of the structure calculate the following items, based on the desired normal spacing s_0 between involute channels:

- Number N of elements in the circular pattern (eq. (1) to nearest integer)
- Radius of curvature of the approximate-involute arc segment from equation (2)
- Sweep angle α in radians $(\theta_2 - \theta_1)$
- Relative spacing error at endpoints $1 - \cos\alpha/2$ based on equation (3)
- Spacing error due to roundoff of N

The last two items are handy for estimating the variation in wall thickness between involute channels. For example, the spreadsheet calculated values for the equal-spaced rings are:

Circle diameters D_i, mm	Number elements in pattern N	Radius of involute arcs r_m, mm	Sweep angle α, radians	Relative spacing error at endpoints	Relative spacing error due to N roundoff
19.05					
17.05	472.00	4.92	0.24	0.007	-0.002
15.05	409.00	4.62	0.27	0.009	-0.002
13.05	347.00	4.29	0.30	0.011	0.000
11.05	284.00	3.94	0.34	0.014	-0.001
9.05	221.00	3.55	0.40	0.020	-0.002
7.05	158.00	3.11	0.51	0.033	-0.004
5.05	95.00	2.60	0.76	0.072	-0.009
3.05					

Note that the relative spacing error for the inner ring is relatively large (0.072). This times s_0 is the approximate amount by which the wall thickness is thinned down near the channel endpoints. For the present case of s_0 = 100 μm the absolute wall thickness error is about 7 μm. When everything is accounted for in Solid Edge the actual wall thickness for the inner ring varies from about 10 μm at the ends to 19 μm at mid chord. The wall thickness is much more uniform for subsequent rings.

Appendix F—Implications of Regenerator Figure of Merit in Actual Stirling Engines (Gedeon Associates)

Re: NASA/CSU Regenerator Microfabrication Contract NAS3-03124
From: David Gedeon
January 27, 2006

Our regenerator figure of merit measures the heat transfer per unit flow resistance of a regenerator matrix. But what does that mean in the context of an actual stirling engine? (or cooler) The question can be answered by imagining a fixed stirling engine into which regenerators of variable figure of merit F_M are substituted. It turns out (derived below) that the figure of merit is inversely proportional to the product of regenerator pumping loss W_p thermal loss Q_t and the square of regenerator mean flow area A_f:

$$F_M \propto \frac{1}{W_p Q_t A_f^2}$$

For regenerators with the same flow areas the figure of merit is inversely proportional to the product of pumping loss and thermal loss. So a high figure of merit will correspond to a low pumping loss, a low thermal loss or both. But depending on the relative sizes and importance of the two losses in an actual engine the overall benefit to engine efficiency will vary. It is even logically possible that a regenerator with higher figure of merit will result in lower actual engine efficiency if it reduces one of the two losses that is not very important while allowing the other, that *is* important, to increase a bit. Or if it reduces the engine power density because of a larger void volume.

F.1 Figure of Merit Reformulation

The figure of merit we have adopted comes from an earlier memo [1]:

$$F_M = \frac{1}{f\left(\frac{\mathrm{R_e P_r}}{4\mathrm{Nu}} + \frac{N_k}{\mathrm{Re\,Pr}}\right)} \tag{1}$$

where,

f	Darcy friction factor
Nu	Nusselt number hd_h / k
N_k	effective gas conductivity due to thermal dispersion as a fraction of molecular conductivity
Re	Reynolds number $\rho u d_h / \mu$
Pr	Prandtl number $c_p \mu / k$
d_h	hydraulic diameter

In equation (1) the two terms in the denominator measure the effects of heat transfer and thermal dispersion, respectively. Another memo [2] discusses the equivalence between mean-parameter enthalpy flows produced by heat transfer and microscopic enthalpy flows produced by thermal dispersion.

So what does the figure of merit have to do with the losses in a regenerator? To answer that question it is convenient to start with the expressions for time average thermal energy transport (enthalpy + dispersion) per unit void flow area q_t and pumping power per unit regenerator void volume w_r given in the 1996 regenerator test rig contractors report[3], appendix C.

$$q_t = - k \frac{\partial T}{\partial x}\left\{\frac{\mathrm{Pe}^2}{4\mathrm{Nu}} + N_k\right\} \tag{2}$$

and

$$w_r = \frac{1}{2d_h}\left\{f\rho u^2|u|\right\} \tag{3}$$

where {} stands for time average and Peclet number Pe is shorthand for Re Pr. Multiplying q_t by regenerator void flow area A_f converts it to total thermal energy transport Q_t

$$Q_t = -kA_f \frac{\partial T}{\partial x}\left\{\frac{\mathrm{Pe}^2}{4\mathrm{Nu}} + N_k\right\} \tag{4}$$

Multiplying w_r by the regenerator void volume $A_f L$ converts it to total pumping power W_p

$$W_p = \frac{A_f L}{2d_h}\left\{f\rho u^2|u|\right\} \tag{5}$$

For reasons that are about to become clear it is convenient to express pumping power in terms of F/Re by introducing the factor 1 in the form $\rho|u|d_h/(\mu\,\mathrm{Re})$, which results in

$$W_p = \frac{A_f L\rho^2}{2\mu}\left\{\frac{f}{\mathrm{Re}}u^4\right\} \tag{6}$$

One can already see signs of the figure of merit (1) in the preceding equations. It is even clearer by writing the figure of merit in the form

$$F_M = \frac{\mathrm{Pr}}{\left(\frac{f}{\mathrm{Re}}\right)\left(\frac{\mathrm{Re}^2\,\mathrm{Pr}^2}{4\mathrm{Nu}} + N_k\right)} \tag{7}$$

Ignoring time averages and constants (since we are only interested in proportionalities), representing the temperature gradient as $\Delta T/L$ and after a little simplification the figure of merit can be reduced to the form

$$F_M \propto \frac{\rho^2 c_p \Delta T(uA_f)^4}{A_f^2}\frac{1}{W_p Q_t} \tag{8}$$

What does it mean? In the first factor on the right all of the quantities in the numerator are constant for any given stirling machine.

fixed gas and charge pressure	$\Rightarrow$	c_p and ρ are fixed
fixed hot and cold temperatures	$\Rightarrow$	ΔT is fixed
fixed piston, displacer volumetric flow rates	$\Rightarrow$	uA_f is fixed

So assuming all of the above the figure of merit reduces to

$$F_M \propto \frac{1}{W_p Q_t A_f^2} \tag{9}$$

Or solving for the pumping-work thermal-energy-transport product

$$W_p Q_t \propto \frac{1}{F_M A_f^2} \tag{10}$$

Hmm. This interesting result suggests that large regenerator flow areas are good. For two regenerators with the same F_M the one with the larger flow area will have a lower $W_p Q_t$ product. I suppose that makes sense given the dependence of pumping power on velocity to the fourth power in equation (6). This may be one reason F_M does not track overall engine efficiency so closely when comparing regenerators of different matrix structures (e.g., parallel plates vs random fibers).

A cautionary remark in applying equation (10) too literally is that it does not take into account to total void volume of the regenerator. The pressure amplitude and therefore power density of the engine will vary inversely with the regenerator void volume, though not in direct proportion because there are other volumes in the total engine. The implication is that if one measures the $W_p Q_t$ product relative to the square of the engine power then the A_f^2 factor may be somewhat canceled out. But if one is comparing two regenerators with the same void volume then this concern vanishes.

References

1. D. Gedeon, *Regenerator figures of merit*, (CSUMicrofabFiguresofMerit.tex), memorandum August 6, 2003.
2. D. Gedeon, *Digression on regenerator figure of merit calculations*, (CSUMicrofabFMeritConsistency.tex), memorandum December 12, 2003
3. D. Gedeon and J.G. Wood, *Oscillating-flow regenerator test rig: Hardware and theory with derived correlations for screens and felts*, NASA Contractor report 198442, February 19964

Appendix G—Random Fibers Correlations with Porosity Dependent Parameters—Updated with New 96% Porosity Data (Gedeon Associates)

Re: NASA/CSU regenerator improvement grant NNC04GA04G
From: D. Gedeon
November 1, 2006

Since the previous memo on this topic[4] additional testing of a 96% porosity random-fiber half-length sample "A" produced a lower figure of merit compared to the tests of the full-length 96% porosity sample. Recent full-length re-testing suggested that the original full-length data was bad for the 50 bar helium test case.[5]

This memo updates the porosity-dependent master correlations for f, Nu and N_k based on heat transfer data for the 96% porosity half-length sample, which is believed to be more reliable.

I am planning to go ahead and insert these latest master correlations into the development version of Sage because the peak figure of merit for 96% porosity random fibers has dropped significantly from about 0.43 down to about 0.28. This will have an effect for *far-out* regenerator investigations but should have minimal impact for analysis of conventional regenerators with porosities on the order of 90%. There is a table of relative errors produced by the master correlations near the end of this memo.

G.1 Master Correlations

The updated correlations are in the same form as before

$$f = \frac{a_1}{\mathrm{Re}} + a_2 \,\mathrm{Re}^{a3}$$

$$\mathrm{Nu} = 1 + b_1 \mathrm{Pe}^{b2}$$

$$N_k = 1 + b_3 \mathrm{Pe}^{b2}$$

Re is the Reynolds number based on hydraulic diameter. Pe = Re Pr is the Peclet number. What has been updated is the porosity dependence embedded in the individual coefficients, as follows: ($x = \beta/(1-\beta)$, where β is porosity)

$$a_1 = 22.7x + 92.3$$

$$a_2 = 0.168x + 4.05$$

$$a_3 = -0.00406x - 0.0759$$

$$b_1 = (0.00288x + 0.310)x$$

$$b_2 = -0.00875x + 0.631$$

$$b_3 = 1.9$$

[4] August 19, 2006 memo *NASARandomFiberMasterCorrelations.doc*)
[5] Details in October 20, 2006 memo NASARandomFiberMysteryLengthDep.doc and November 1, 2006 memo NASARandomFiberReasonsLengthDep.doc).

G.2 Figure of Merit

The overall figure of merit still increases with increasing porosity, but not as much as before. It now peaks at a value of about 0.28 at 96% porosity, down from about 0.43 previously.

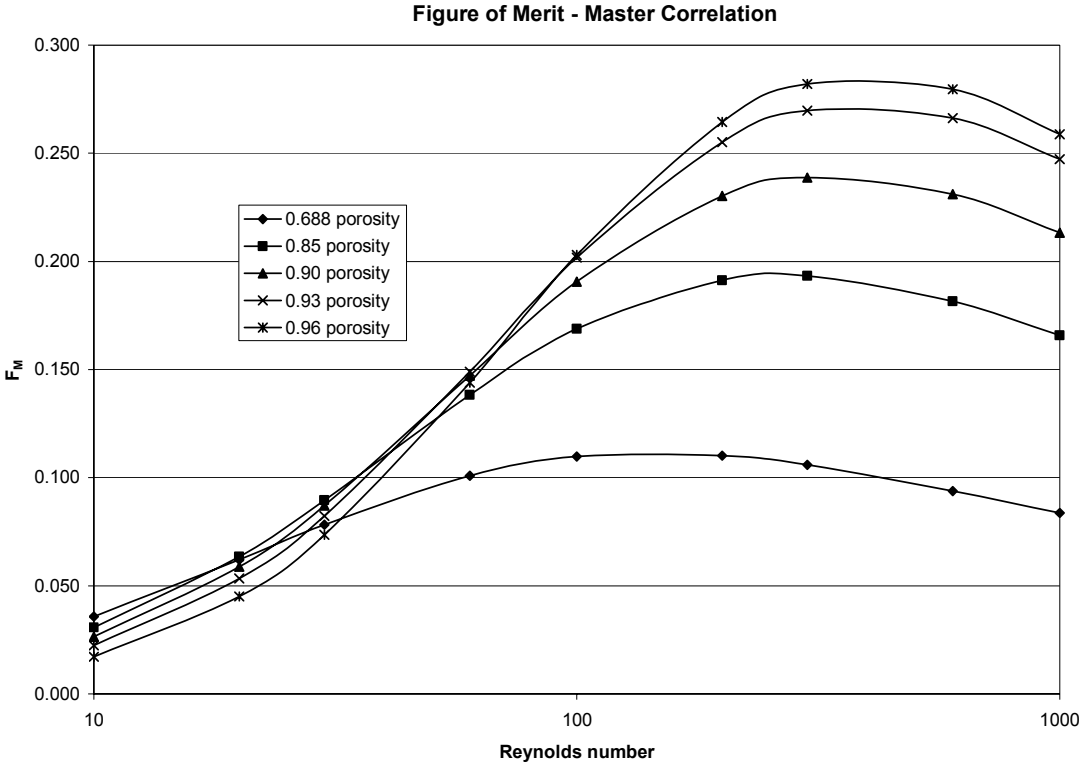

G.3 Correlating Porosity

The above F_M plot and the material in this section is derived from the revised spreadsheet *RandomFiberPorosityDependence.xls*.

The data-modeling parameters for the individual regenerator tests are listed in the following table. The only changes compared to the table in the August 19, 2006 memo are for the 0.96 porosity Nu and N_k parameters, which are now based on tests for half-length sample "A" .

		f parameters			Nu, N_k parameters		
B	β /(1-β)	a1	a2	a3	b1	b2	b3
0.688	2.205	128.8	3.858	-0.063	0.499	0.635	3.787
0.820	4.556	248.5	4.889	-0.071	0.945	0.632	2.157
0.850	5.667	233.8	4.15	-0.082	1.552	0.539	1.113
0.897	8.709	211.2	5.139	-0.151	1.287	0.600	1.026
0.900	9.000	321.4	5.138	-0.108	2.323	0.534	0.583
0.930	13.29	380.3	9.906	-0.195	7.447	0.424	1.983
0.960	24.00	651.5	6.627	-0.135	8.600	0.461	2.498

The individual parameters are plotted below along with their trend-lines.

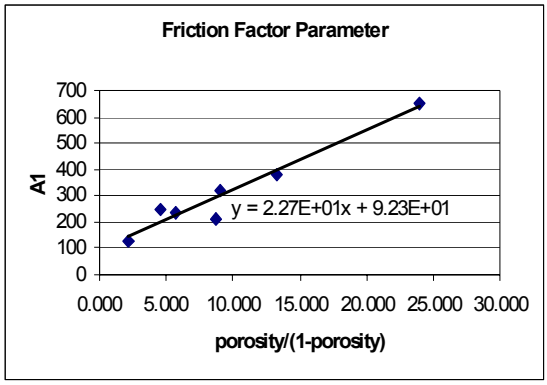

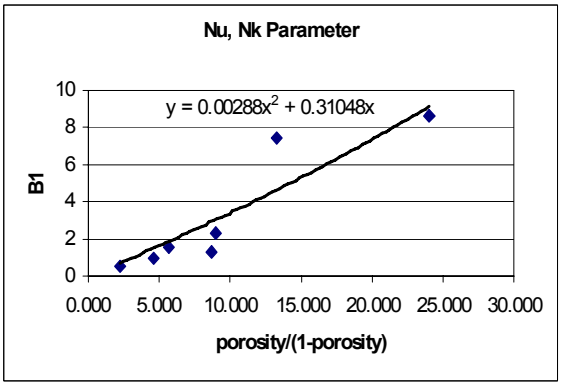

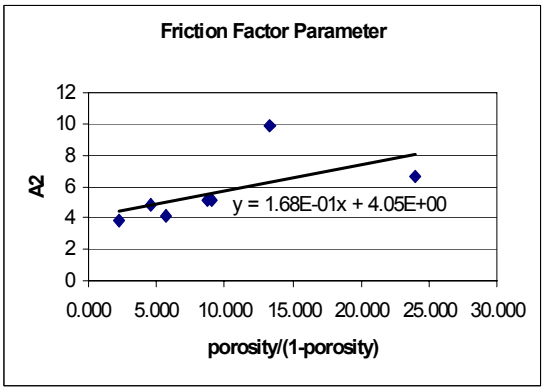

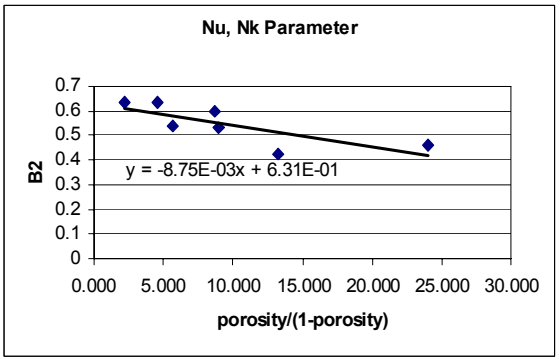

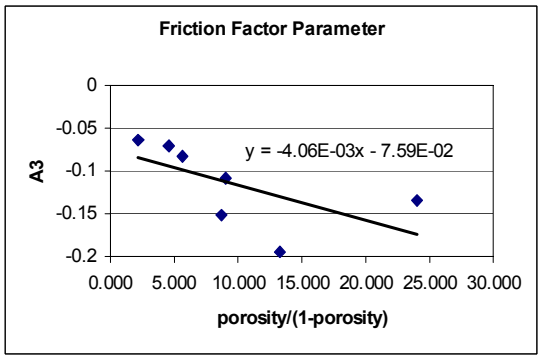

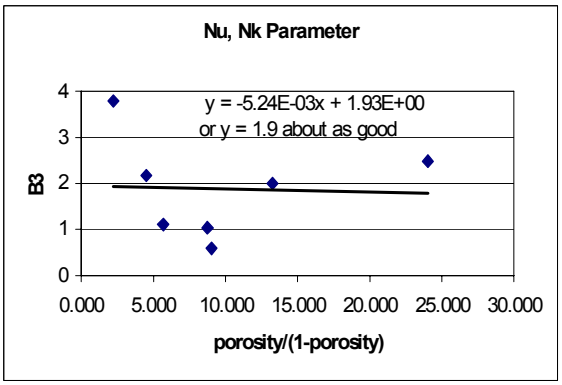

The previous quadratic curve fit (trend-line) for the b_1 heat-transfer parameter (Nusselt number coefficient) is no longer obviously necessary but it does reduce relative errors for the individual correlations, compared to a linear trend line, and also results in a more uniform progression of increasing figure of merit with porosity. The y-intercept remains zero so that the implied heat-transfer coefficient does not diverge at zero porosity ($h \propto \mathrm{Nu}\,(1-\beta)/\beta$) as argued in the August 19, 2006 memo.

The following table gives the updated table of correlated vs individual ratios for various quantities of interest, averaged over the Reynolds number range from 10 to 1000. Values for individual correlations are indicated by zero subscripts. F_M is the overall figure of merit.

	Master correlation relative errors Averaged over Re = 10 to 1000			
β	f/f_0	Nu /Nu_0	N_k /N_{k0}	F_M/F_{M0}
0.688	1.05	1.22	0.47	1.35
0.820	0.83	1.28	0.75	1.52
0.850	1.03	1.40	1.95	1.09
0.897	1.35	1.80	1.47	0.99
0.900	0.99	1.39	3.09	0.99
0.930	0.97	0.93	1.40	0.94
0.960	0.98	0.89	0.66	1.12

Compared to the table in the August 19, 2006 memo (including 0.93 porosity data) the figure-of-merit ratios in the range of porosities 0.688 to 0.85 are substantially higher. There is not much change at porosity 0.90 and a bit more pessimism at 0.93. The correlation at porosity 0.96 is based on new data.

G.4 Data Files

The derived data files used for parameter modeling were:

Sample	Tested	Porosity	DP file	HX file
2 mil Brunswick	1992–93	0.688	P06-29Scaled	H11-21Scaled
1 mil Brunswick	1992–93	0.82	P11-04Scaled	H11-18Scaled
30 µm Bekaert	2006	0.85	DP_85Porosity	HX_85PorosityTrunc
12 µm Bekaert	2003	0.897	BekD12P90DPRetestScaled	BekD12P90HXScaled
30 µm Bekaert	2006	0.90	DP_90Porosity	HX_90PorosityTrunc
30 µm Bekaert	2006	0.93	DP_93Porosity	HX_93PorosityTrunc
30 µm Bekaert	2006	0.96	DP_96Porosity	HX_96PorosityHalfA

REPORT DOCUMENTATION PAGE	Form Approved OMB No. 0704-0188

1. REPORT DATE *(DD-MM-YYYY)*	2. REPORT TYPE	3. DATES COVERED *(From - To)*
01-12-2007	Final Contractor Report	

4. TITLE AND SUBTITLE
A Microfabricated Segmented-Involute-Foil Regenerator for Enhancing Reliability and Performance of Stirling Engines
Phase II Final Report for the Radioisotope Power Conversion Technology NRA Contract NAS3-03124

5a. CONTRACT NUMBER
NAS3-03124

5b. GRANT NUMBER

5c. PROGRAM ELEMENT NUMBER

6. AUTHOR(S)
Ibrahim, Mounir; Danila, Daniel; Simon, Terrence; Mantell, Susan; Sun, Liyong; Gedeon, David; Qiu, Songgang; Wood, Gary; Kelly, Kevin; McLean, Jeffrey

5d. PROJECT NUMBER

5e. TASK NUMBER

5f. WORK UNIT NUMBER
WBS 138494.04.01.01

7. PERFORMING ORGANIZATION NAME(S) AND ADDRESS(ES)
National Aeronautics and Space Administration
John H. Glenn Research Center at Lewis Field
Cleveland, Ohio 44135-3191

8. PERFORMING ORGANIZATION REPORT NUMBER
E-16191

9. SPONSORING/MONITORING AGENCY NAME(S) AND ADDRESS(ES)
National Aeronautics and Space Administration
Washington, DC 20546-0001

10. SPONSORING/MONITORS ACRONYM(S)
NASA

11. SPONSORING/MONITORING REPORT NUMBER
NASA/CR-2007-215006

12. DISTRIBUTION/AVAILABILITY STATEMENT
Unclassified-Unlimited
Subject Category: 20
Available electronically at http://gltrs.grc.nasa.gov
This publication is available from the NASA Center for AeroSpace Information, 301-621-0390

13. SUPPLEMENTARY NOTES

14. ABSTRACT
An actual-size microfabricated regenerator comprised of a stack of 42 disks, 19 mm diameter and 0.25 mm thick, with layers of microscopic, segmented, involute-shaped flow channels was fabricated and tested. The geometry resembles layers of uniformly-spaced segmented-parallel-plates, except the plates are curved. Each disk was made from electro-plated nickel using the LiGA process. This regenerator had feature sizes close to those required for an actual Stirling engine but the overall regenerator dimensions were sized for the NASA/Sunpower oscillating-flow regenerator test rig. Testing in the oscillating-flow test rig showed the regenerator performed extremely well, significantly better than currently used random-fiber material, producing the highest figures of merit ever recorded for any regenerator tested in that rig over its ~20 years of use.

15. SUBJECT TERMS
Stirling; Regenerator; Foil regenerator; Heat exchanger

16. SECURITY CLASSIFICATION OF:			17. LIMITATION OF ABSTRACT	18. NUMBER OF PAGES	19a. NAME OF RESPONSIBLE PERSON
a. REPORT	b. ABSTRACT	c. THIS PAGE			STI Help Desk (email:help@sti.nasa.gov)
U	U	U	UU	177	19b. TELEPHONE NUMBER *(include area code)* 301-621-0390